FRONT-END METHODS FOR ENHANCING THE ANALYTICAL POWER OF MASS SPECTROMETRY

PETER PAUL LIUNI

A DISSERTAITON SUBMITTED TO
THE FACULTY OF GRADUATE STUDIES
IN PARTIAL FUFILLMENT OF THE
REQUIREMENTS
FOR THE DEGREE OF
DOCTOR OF PHILOSOPHY

GRADUATE PROGRAM IN CHEMISTRY
YORK UNIVERSITY
TORONTO, ONTARIO

December 2015

Abstract

The analytical power and versatility of mass spectrometry can be enhanced by adding 'front-end' devices, which provide additional functionality before, during or immediately after ElectroSpray Ionization (ESI). Such devices can include Ion mobility spectrometry (IMS) and Time-Resolved ElectroSpray Ionization (TRESI) which provide enhanced analysis of illicit compounds, protein folding, enzyme kinetics, and catalysis-linked dynamics. With respect to IMS, this work describes implementation of a hybrid Trace Compound Detector (TCD) system that combines IMS and MS to allow for rapid front-end mobility separation, followed by characterization and identification of analytical markers of seized opium by mass spectrometry. Ultimately, this device provides an avenue for rapid prosecution based on simultaneous detection and unambiguous identification of illicit drugs. TRESI is used to extend Mass Spectrometry (MS) to millisecond-timescale reaction studies. In the first instance, we combine TRESI with Travelling Wave Ion Mobility Spectrometry (TWIMS) to compare equilibrium and kinetic unfolding intermediates of cytochrome c, showing a high degree of correlation between all species populated under these substantially different regimes. We then combine TRESI with Hydrogen Deuterium Exchange (TRESI-HDX) to elucidate the relationship between structural fluctuations (conformational dynamics) of enzymes and their catalytic activity. The results of this work include a new model for catalysis-linked dynamics, in which the nature of the conformational landscape explored by an enzyme is independent of catalysis, but the rate at which the landscape is explored is enhanced for catalytically active species.

Acknowledgements

You know, I have a confession to make. Keep your hearts in your chests because this data's all real. But really, a true confession. And that is, I was a failing high school chemistry student.

Now, if it had been up to my guidance counselors, parents, friends, and family; my journey would have ended back in high school. Full stop. But the question that remained inside me was why? Why if you are so passionate about a subject, so vividly enthralled by everything about it, why should you be told you can't continue to learn it? So I enrolled in College. No knock to College, but when all your friends and family sail off to University – there's this nagging voice inside your head that wants to keep telling you one thing. You are lesser. And maybe I needed to be told that, because my 1st year of College was humbling to say the least – I failed Chemistry yet again. The voice was right, or so it seemed.

Sometime during the winter of 2003 I came to realise I was a poor student; something I never admitted to myself. It sank in deep, and what erupted was outright rage. How could I let MY dream, MY goal, just slip away? How could I lie to my 4 year old self, who drew a picture of a Scientist, proclaiming that is what he wanted to be when he grew up on his Senior Kindergarten Graduation Day? That thought right there, changed me forever. I channeled it into pure blind determination. And I studied. Harder than I ever had in my life. I would never accept failure again, and I'd go even further, I wouldn't accept it in my closest friends. I studied hard for them too, because I knew they had dreams. And no one should ever be told by anyone – even themselves – to give up on their dreams.

The quest for knowledge that is a Ph.D. is a long journey for the most part made in solitude, but also in companionship. The names here represent people who have enriched and made a meaningful - however large or small - contribution to my life from start to end of this Ph.D.

Teresa and Pietro Liuni, my parents, thank you for your unwavering support and love throughout my long 12 years of post-secondary education, for every step I thought I took alone, you were behind me, ready to catch me if I fell. To my Family, Pupo and Liuni, you are my backbone and my blood, thank you for being there for me and reminding me what family is all about. Carmine and Jeanine, my best friends, you have always been there for me, a ray of light for when I was in the darkest of places, even when all other lights had gone out.

Derek Wilson, my advisor and mentor, thank-you for letting me play in your lab. The creative space you gave me made me feel like a child again; free to create and explore in my ideas. To my Committee members, Dasantila Golemi-Kotra, Sergey Krylov, Gerald Audette, Vivian Saridakis, and Grary Shaw; your valuable wisdom and suggestions have made this dissertation possible.

John Van Nostrand, for teaching me mass spectrometry and for being a good friend. Greg Koyanagi, for your ability fix nearly everything and being a good friend. Diethard Bohme, for your essential advice and criticisms of my work. Vlad Romanov, for teaching me how to be confident. Voislav Blagojevic, for giving me hope that this whole thing's going to eventually pan out. Tamanna Rob, for being the lab mom, my confidant and friend. Yanfang Liang, for always making it sound easy. Declan Williams, for showing me true work ethic, and Resistance. Shaolong Zhu, for being the better version of me. Diana

Resetca, for teaching me work ethic and vodka can definitely mix. Preet Gill, for those late night talks bro. Cristina Lento, for being the only Italian in the lab – relate. Kereene Brown, for being an upbeat presence and the Catan box. Bin Deng, for your versatility and modesty. Diefei Sun, for your useful discussions and help. Marlee Ng, for making everything memorable and being a great friend. Karan Hingorani, for your inspiration and love of science and beer.

I leave this poem as a final ode to my life as a student, it has given me strength and inspiration; my hope is that it does the same for you.

All that is gold does not glitter,

Not all those who wander are lost;

The old that is strong does not wither,

Deep roots are not reached by the frost.

From the ashes a fire shall be woken,

A light from the shadows shall spring;

Renewed shall be blade that was broken,

The crownless again shall be king.

-J.R.R Tolkein

List of Publications

1. **Liuni, P.**; Deng, B.; Wilson, D. J. Comparing Equilibrium and Kinetic Protein Unfolding Using Time-Resolved Electrospray-Coupled Ion Mobility Mass Spectrometry. *Analyst* 2015, 140 (20), 6973–6979.
2. **Liuni, P.**; Romanov, V.; Binette, M.-J.; Zaknoun, H.; Tam, M.; Pilon, P.; Hendrikse, J.; Wilson, D. J. Unambiguous Characterization of Analytical Markers in Complex, Seized Opiate Samples Using an Enhanced Ion Mobility Trace Detector-Mass Spectrometer. *Anal. Chem.* 2014, 86 (21), 10772–10779.
3. **Liuni, P.**; Zhu, S.; Wilson, D. J. Oxidative Protein Labeling with Analysis by Mass Spectrometry for the Study of Structure, Folding, and Dynamics. *Antioxid. Redox Signal.* 2014, 21 (3), 497–510.
4. **Liuni, P.**; Olkhov-Mitsel, E.; Orellana, A.; Wilson, D. J. Measuring Kinetic Isotope Effects in Enzyme Reactions Using Time-Resolved Electrospray Mass Spectrometry. *Anal Chem* 2013, 85 (7), 3758–3764.
5. **Liuni, P.**; Jeganathan, A.; Wilson, D. J. Conformer Selection and Intensified Dynamics During Catalytic Turnover in Chymotrypsin. *Angew. Chem*. 2012, 124 (38), 9804–9807.
6. Rob, T.; **Liuni, P**.;Gill, P.K.; Zhu, S.; Balachandran, N.; Berti, P.J.; Wilson D.J. Measuring Dynamics in Weakly Structured Regions of Proteins Using Microfluidics-Enabled Subsecond H/D Exchange Mass Spectrometry. *Anal. Chem.* 2012, 84 (8), 3771-3779.
7. **Liuni, P.**; Wilson, D. J. Understanding and Optimizing Electrospray Ionization Techniques for Proteomic Analysis. *Expert Rev. Proteomics* 2011, 8 (2), 197–209.
8. **Liuni, P.**; Rob, T.; Wilson, D. J. A Microfluidic Reactor for Rapid, Low-Pressure Proteolysis with on-Chip Electrospray Ionization. *Rapid Commun. Mass Spectrom.* 2010, 24 (3), 315–320.

Table of Contents

Abbreviations

ADH – Yeast Alcohol Dehydrogenase
AMU – Atomic Mass Units
APCI – Atmospheric Pressure Chemical Ionization
API – Atmospheric Pressure Interface
APPI – Atmospheric Pressure Photoionization
ATPase – Adenosine Triphosphatase
BIRD – Blackbody Infrared Dissociation
CAD – Collisionally Activated Dissociation
CD – Circular Dichroism
CBSA – Canada Border Services Agency
CE – Capillary Electrophoresis
CEM – Chain Ejection Model
CI – Chemical Ionization
CID – Collision Induced Dissociation
CPMG – Carr-Purcell-Meiboom-Gill
CRM – Charged Residue Model
CV – Compensation Voltage
Da – Dalton
DC – Direct Current
DESI – Desorption Electrospray Ionization
DLI – Direct Liquid Injection
ECD – Electron Capture Dissociation
EDC – Enhanced Duty Cycle
EESI – Extractive Electrospray Ionization
ESI – Electrospray Ionization
ETD – Electron Transfer Dissociation
FAB – Fast Atom Bombardment
FD – Fused Droplet
FTICR – Fourier Transform Ion Cyclotron Resonance
FWHM – Full Width Half Maximum
GC – Gas Chromatography
HDX – Hydrogen Deuterium Exchange
HESI –Heated Electrospray Ionization
HPLC- High Performance Liquid Chromatography
ICP – Inductively Coupled Plasma
IEM – Ion Evaporation Model
IMS – Ion Mobility Spectrometry
kDa – Kilo Dalton
KIE – Kinetic Isotope Effect
kV – Kilovolts
LC – Liquid Chromatography
LTQ – Linear Ion Trap Quadrupole
MALDI – Matrix-Assisted Laser Desorption/Ionization
MCP – Multichannel Plate Detector
MDa – Mega Dalton
MS – Mass Spectrometry
NMR – Nuclear Magnetic Resonance
NAD – Nicotinamide adenine dinucleotide
PDB – Protein Data Bank
PETN - Pentaerythritol Tetranitrate
pNP – para-Nitrophenylate
pNPA – para-Nitrophenyl Acetate
QIT – Quadrupole Ion Trap
QLIT – Quadrupole Linear Ion Trap
QTOF – Quadrupole Time of Flight
QQQ – Triple quadrupole
SAXS – Small-angle X-ray Scattering
SESI – Secondary Electrospray Ionization
SID – Surface Induced Dissociation
SV – Separation Voltage
TCD – Trace Compound Detector
Th - Thompsons
TLC – Thin Layer Chromatography
TOF – Time of Flight
TRESI – Time Resolved Electrospray Ionization
TWIMS – Travelling Wave Ion Mobility Spectrometer
UPLC – Ultra Performance Liquid Chromatography
UV – Ultra Violet
XIC – Extracted Ion Chromatogram

List of Tables

List of Figures

Chapter 1

Introduction

A version of this chapter was published in Expert Review of Proteomics:

Liuni, P.; Wilson, D. J. Understanding and Optimizing Electrospray Ionization Techniques for Proteomic Analysis. Expert Rev. Proteomics 2011, 8 (2), 197–209.

1.1 Mass Spectrometry

1.1.1 Current Perspectives

Mass spectrometry, as the science of measuring atomic or molecular mass, has existed since the turn of the 20th century, initiated by J.J. Thompsons historic works on *Rays of Positive Electricity and Their Application to Chemical Analyses*.[1] Mass Spectrometers are truly remarkable instruments that have the unique ability to accurately determine the mass of a substance by ionization, transfer into the gas-phase and subsequent manipulation with electric and/or magnetic fields.

Fundamental improvements to ionization, ion sampling, and ion detection over a 100-year span have given mass spectrometry an unprecedented range of analytical applications. Development of an atmospheric pressure, 'direct-from-liquid-phase' soft ionization method, saw John Fenn and Koichi Tanaka win the Nobel prize in chemistry for electrospray (ESI) and matrix-assisted desorption ionization (MALDI) of biomolecules; expanding the analytical space of mass spectrometers into the realm of biology.[2] Mass spectrometers have gone from detecting small molecules, to analyzing large biological protein complexes and viruses in excess or > 1 MDa in matter of a few decades.[3,4] At present, mass spectrometers have evolved into critical components in analytical science, facilitating giant leaps in the fields of biology[5], medicine[6], and chemistry[7].

1.1.2 Soft Ionization Methods

1.1.2.1 Matrix Assisted Laser Desorption/Ionization

Matrix-assisted laser desorption/ionization is a soft ionization method that enables the detection of non-volatile biological samples such as peptides, proteins and nucleic acids.[8] It typically utilizes a narrowly tuned laser (N_2 337nm, ND:YAG 355nm and 266nm) pulse

(1-10 ns) to trigger ionization of a sample on a surface, generating a hot plume of ionized material that enters the mass spectrometer for detection.[9] Ion formation is highly complex and dependent on a number of primary and secondary ionization processes, those of which are outlined elsewhere.[9,10] Critical to the MALDI method is matrix composition; typically a low molecular weight organic acid that absorbs laser radiation along with additives and solvents, which are highly dependent on the target analyte.[11] MALDI mass spectrometry excels in proteomics[12], glycomics[13], lipidomics[14], identifying post-translationally modified peptides[15], intact protein identification[16], and biological imaging applications[17]; all with intact molecular ions being the most dominant species (with the occasional 2^+ and 3^+ ions as well). A downside to the method is that no single MALDI matrix or sample preparation protocol is suitable for all analytes; a list of commonly used MALDI matrices can be found here.[8] MALDI also suffers from irreproducibility[18], as well as unwanted side-reactions caused by the irradiation process.[19]

1.1.2.2 Electrospray Ionization

ESI is a second soft-ionization technique that has a number of advantages over MALDI. Ionization is initiated directly from bulk solution, which allows for straightforward 'online' integration of solution phase sample-handling processes, such as high-performance liquid chromatography (LC)-based separations and purifications.[20–22] ESI is also multiply charging commonly producing 1^+ or greater molecular ions. In a typical electrospray ion source (Figure 1), solution containing the analyte(s) of interest is passed through a thin metal capillary, which is held at high electric potential (±2-±6 kV).[23] In positive ion mode, positive potentials generate an electric field at the capillary tip driving positively charged solutes towards the meniscus, creating an excess of positive charge at the liquid/air

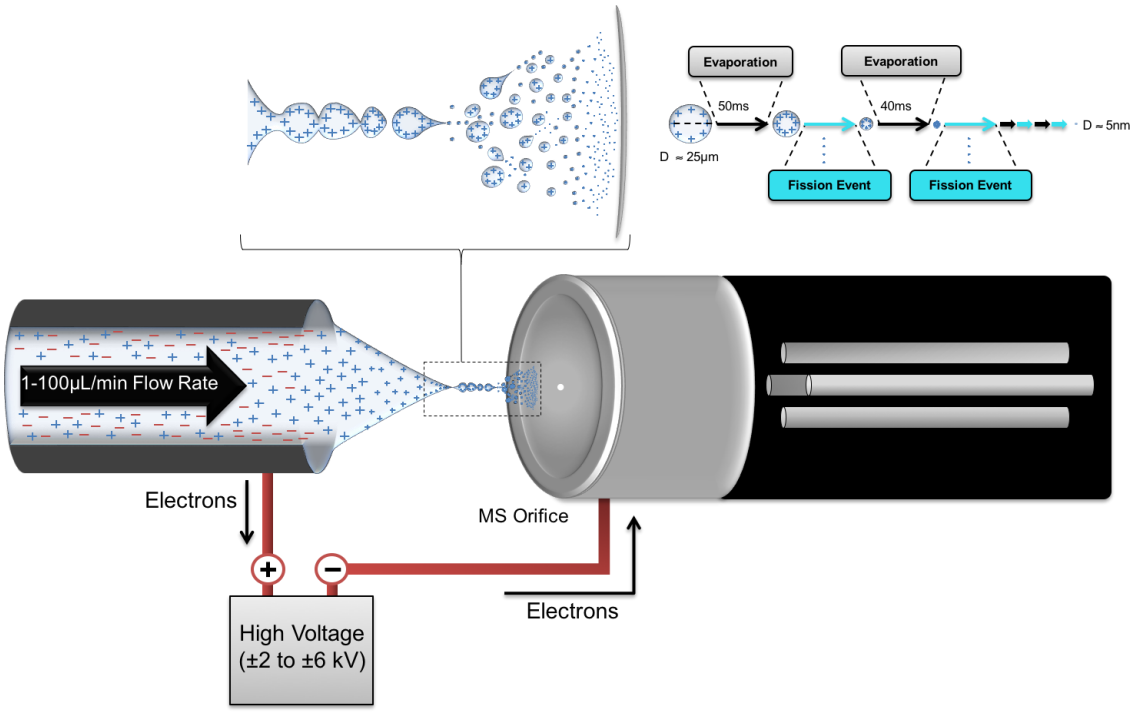

Figure 1. A representation of the electrospray process. Shown to the left is a thin metal capillary containing analyte solution where high electric field potentials cause the formation of a Taylor cone. In positive ion mode, positively charged particles congregate at the tip of the Taylor Cone, resulting in the ejection of positively charged parent droplets at the liquid-air interface, while negatively charged particles align to the outer walls of the capillary (the opposite occurs for negative ion mode). Droplet sizes depend on analyte flow rates (typically 1-100µL/min for ESI) and the electric field strength. Seen in the above inset, the parent droplets fly towards the oppositely charged curtain plate of the mass spectrometer. Solvent evaporation, initially lasting for ~50ms causes the droplet to shrink until the charge-charge repulsions are too great for the surface tension of the droplet to maintain. At this point a coulomb 'jet' fission event occurs, with the parent droplet expelling smaller progeny droplets. Subsequent evaporation and jet fission events continue at an increasingly rapid rate until the droplet (which started at ~25µm in diameter) reaches a diameter of ~5nm, whereby the remaining analyte molecule(s) are transferred into the gas phase.

interface.[24] The effects of the electric field, coulombic repulsion between positive charge carriers, and surface tension combine to form a conical liquid structure known as a Taylor cone[25], which extends up to several millimeters from the capillary tip.

At the distal end of the Taylor cone, coulombic repulsion overcomes surface tension, forming a narrow jet from which charged droplets are ejected. As the droplet shrinks, the charge-to-volume ratio increases until coulombic repulsion destabilizes the droplet structure. At this point, which is typically 10-20% below the 'Rayleigh limit' (where charge balances surface tension[26]), the droplet becomes a 'parent', forming a jet from which small ([proportional to]10% diameter of parent[27]), highly charged 'progeny' droplets are emitted.[28,29] Parent and progeny droplets undergo numerous evaporation/jet fission cycles, losing 5-20% of their charge and approximately 2-5% of their mass[24] with each 'jet fission' event, until a radius of approximately 5-10 nm is reached.[23] Analyte molecules within these nanodroplets are transferred into the gas phase with excess charge via one (or both) of the mechanisms described in the following section.

1.1.2.3 Electrospray Ionization Mechanisms

Analyte ionization in electrospray is thought to occur via two mechanisms, namely the 'Charged Residue' model (CRM), first generally suggested by Dole and colleagues[30] and later described by Rollgen et al.[31], and the 'Ion Evaporation' model (IEM) introduced by Iribarne and Thomson[32]. These mechanisms are not mutually exclusive, and there is considerable experimental and computational evidence to support the validity of both.[33–35] The current consensus is that smaller analytes ($\leq$ 3000 Da[34]) favor ion evaporation, whereas larger analytes are mainly ionized via the charged residue mechanism.[24] Of interest for bottom-up and middle-down proteomics studies is that larger

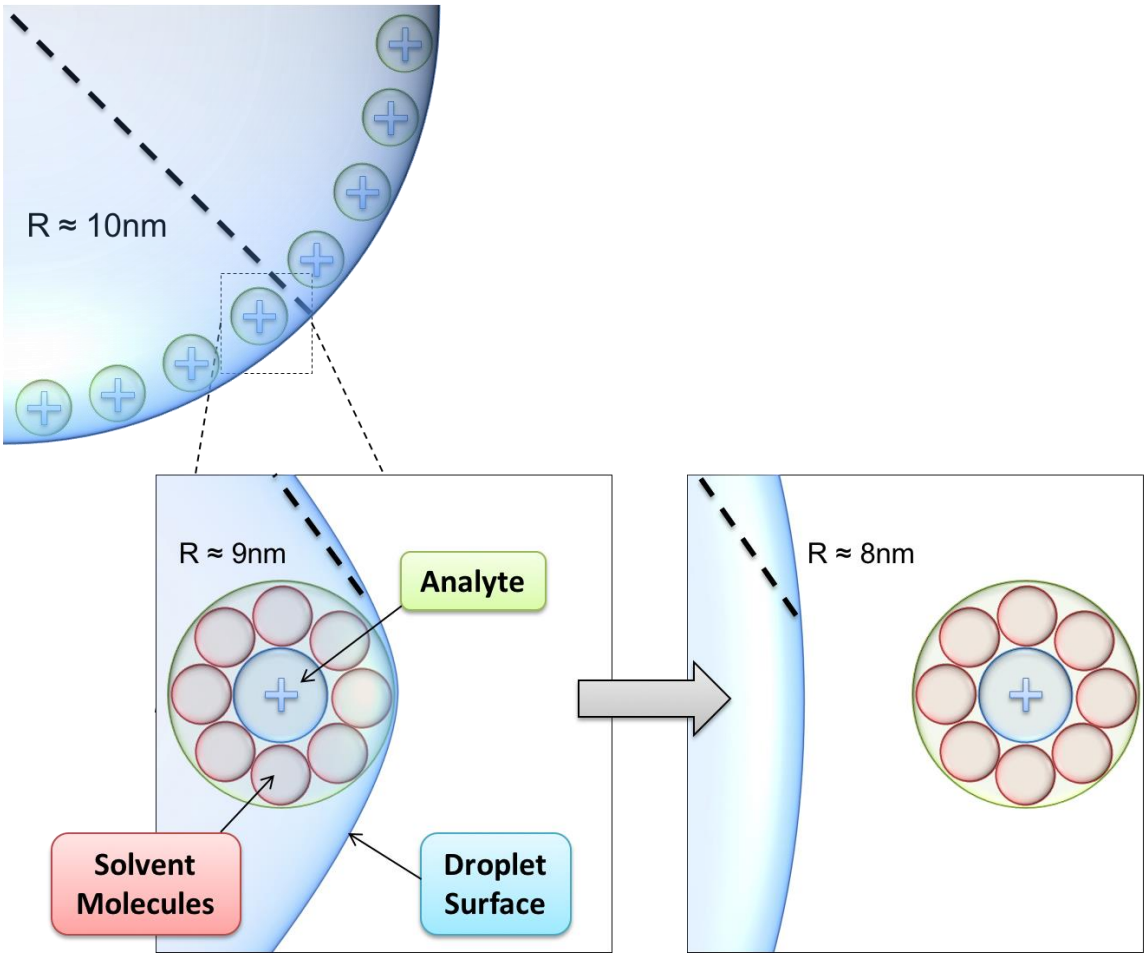

Figure 2. Shown is an IEM regime where a droplet of ~10nm in diameter (reduced in size from multiple evaporation-jet fission cycles) has positively charged analyte ions orienting at the surface. The removal of charge, primarily observed as Coulomb fission at larger droplet radii is replaced by Ion Evaporation. The inset depicts the onset of Ion Evaporation as the droplet approaches a 'transition state', where the repulsive Coulomb forces generated by neighboring analyte ions equal the short-range attractive forces caused by droplet polarization. To the right, the leaving ion is ejected from the droplet as it continues to evaporate, and enters the gas phase. Reproduced from Liuni et. al.[36]

peptides from proteolytic digests may fall within the substantial 'gray area' between clearly dominant CRM or IEM ionization. In this case, it may be that both mechanisms operate simultaneously, or that ionization occurs via a hybrid process.[37] A chain ejection model (CEM) has recently been proposed by the Konnerman group, where disordered polymers are ejected as long chains from charged droplets, accounting for experimentally observed charge-state distributions of unfolded proteins generated from ESI.[38]

The IEM was the first ESI mechanism to be described in detail.[39] In this model, droplets with very small radii ([less than or equal to]10 nm diameter) 'field evaporate' solvated analyte ions, rather than undergoing jet fission to relieve coulombic repulsion. Ions generated in this way acquire excess charge locally as they are ejected from the droplet, which limits the expected amount of charging. The IEM also predicts more efficient ionization of species with higher evaporation rates, which, for peptides, is dominated by hydrophobicity-driven surface activity.[40] Thus, the ESI signal response for peptides in aqueous solution scales quite well with hydrophobicity.[41] There are two pieces of qualitative evidence against the IEM for large analytes. First, proteins acquire more charge than would be expected from local charge acquisition on evaporation from the nanodroplet.[42,43] Second, ESI mass spectra of proteins sometimes include aggregates not present in solution whose formation would be promoted by a charged residue mechanism, but not an ion evaporation mechanism.[44] A schematic depiction of ionization via the IEM is provided in Figure 2.

In the CRM, very small droplets (≤ 10 nm diameter) continue to undergo jet-fission/evaporation cycles until the remainder of the solvent is removed by evaporation, leaving a 'residue' of charge on the (now gas-phase) analyte.[27] This mechanism would

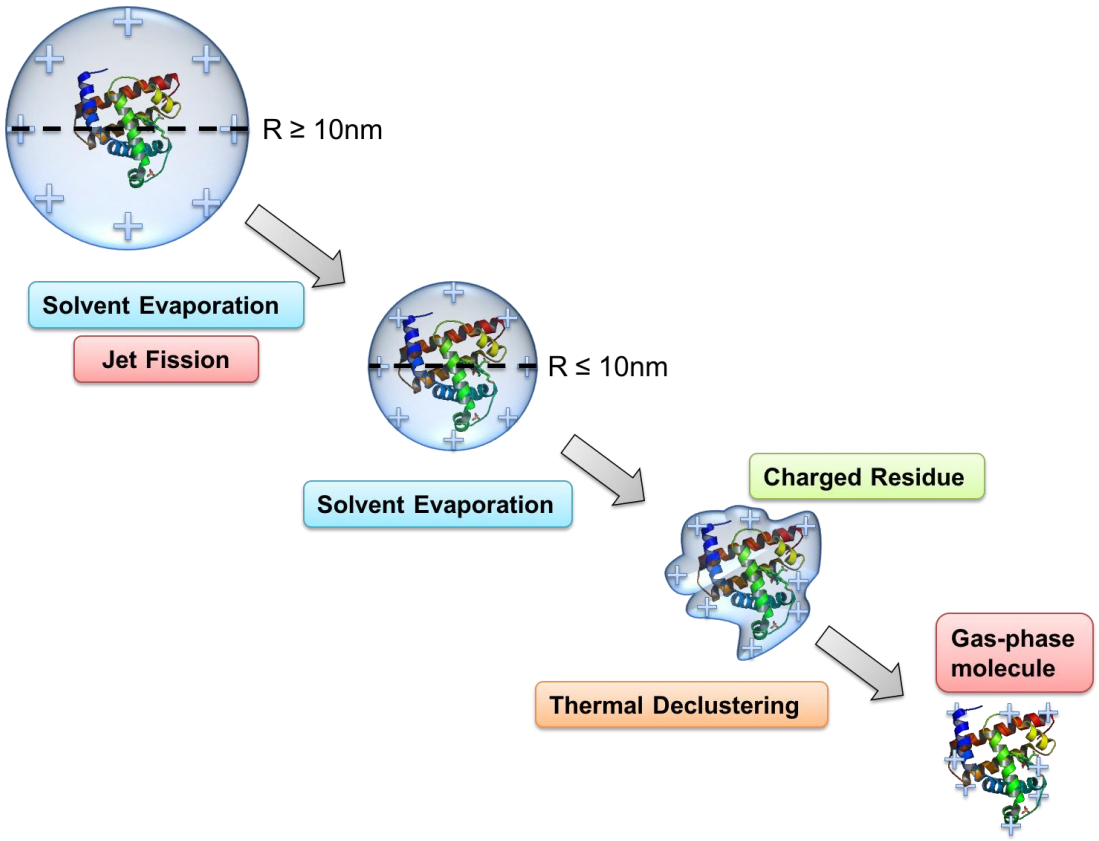

Figure 3. The Charged Residue Model (CRM) is depicted here showing the progressive loss of solvent due to evaporation on a droplet containing a single globular protein. The onset for this mechanism occurs in droplets with diameters ~10nm or less. In the final evaporation stage, charge present in solution is transferred to the protein through a 'charged residue' state. Upon further thermal declustering and clean-up in the mass spectrometer, a gas phase molecule with charge transferred to the surface of the protein is observed. Reproduced from Liuni et.al.[36]

explain the large amount of charge carried by protein analytes into the gas phase, since in principle the entire charge complement of the droplet after the last jet fission event can contribute to the charge residue. The CRM predicts that analyte charge should correlate with analyte surface area, and for most proteins (particularly those that are nicely globular) over a wide range of masses, this has been demonstrated experimentally to be the case.[45] Deviations from the classical interpretation of the CRM occur when solvent mixtures are used (probably because the more volatile solvent evaporates prior to the final jet fission event[46]) or when the protein analyte cannot be approximated as a solid sphere.[42]

With the CRM, it is mainly the nature of the charged residue, and its effect on post-ionization factors such as declustering and ion transmission, that most strongly influences signal response. Thus, the nature of the solvent that forms the charged residue, especially the presence of non-volatile salts, is a crucial factor. For the analyte, physicochemical properties affecting the charged residue, such as overall shape (globular vs extended), number of accessible basic residues and accessible hydrophobic surface (which determines the 'stickiness' of the solvent in the charged residue), have the greatest influence on the observed signal intensity. A schematic depiction of ionization via the CRM is provided in Figure 3.

1.1.2.4 Nano-Electrospray Ionization

Conventional ESI involves pressure-driven flow rates in the µl/min range. Under these conditions, initial droplet sizes are of the order of tens or even hundreds of µm and the electrospray process can take hundreds of ms.[27] Thus, modern electrospray sources incorporate in-line heating[47] and collateral gas flows[48] to hasten evaporation. Even with

these additions, however, a substantial fraction of potential analytes is lost due to insufficient time for desolvation prior to discharge at the counter-electrode.

An alternative approach is to use much lower flow rates, which can be achieved by capillary action alone (i.e., in the nL/min range) and narrow-bore 'pulled' capillaries, which results in initial droplet diameters in the hundreds of nm range. Under these 'nanospray' conditions, ionization occurs within tens of μs.[24,45,49] The advantages of nanospray in proteomics are low sample consumption, generally better signal response and a higher tolerance for solvent impurities due to less solute concentration during droplet shrinkage.[50] Nanospray is also less prone to ionization bias due to differential liquid-to-gas transfer rates among analytes[51,52], a feature that is particularly important in quantitative studies. Drastically reduced sample consumption sparked the first major application of electrospray MS in proteomics, coupling nanospray with 2D polyacrylamide gel electrophoretic separations.[53] Improved signal response is also frequently associated with nanospray, and there is evidence that ion generation is enhanced by as much as 500-fold under nL/min flow conditions.[54]

Liquid chromatography-coupled electrospray mass spectrometry (LC/ESI-MS), discussed in the following section, is often carried out under a flow regime that is part-way between classical nanospray and electrospray (i.e., in the order of 100 nL/min). This regime was originally called microspray[55,56], but is now more often described as 'nanospray' or 'nanoflow electrospray' when it is used.

1.2 Pre-Ionization Technologies and Methods

A ‘Pre-ionization’ method refers to any experimental procedure applied upstream from the ionization source of a mass spectrometer. Brief discussion of GC-MS, CE-MS, and

microfluidics is given, with primary focus on LC-MS and hydrogen/deuterium exchange mass spectrometry.

The coupling of mass spectrometry to chromatographic techniques is a desirable union of two technologies due to the enhanced degree of separation while also increasing sensitivity through MS detection. Gas chromatography mass spectrometry (GC-MS) was developed in the 1950's[57] to exploit the gaseous separating power of GC, with accurate mass detection by mass spectrometry. Surprisingly, as both being gas-phase techniques, early GC-MS's suffered from low detection limits caused by a poor GC-to-MS interface[58] and differential operating pressures (GC = 760 Torr, MS = 10^{-6} Torr).[59] Modern-day mass spectrometers and low effluent GC flows now provide a sensitive direct GC-to-MS connection[60] where qualitative and quantitative information on a variety of compounds such as pesticides, hydrocarbon fuels, flavors, oils, and drugs; while amino acids, steroids, and non-volatile drugs require some derivatization to increase their volatility.[61] Non-volatile compounds that cannot be vaporized or structurally decompose during the vaporization process are not amenable to GC or GC-MS.

Capillary electrophoresis-mass spectrometry (CE-MS) introduced in 1987 by Richard Smith and co-workers[62], involves the separation of analyte ions in an electrical field, and subsequent detection by mass spectrometry.[63] More information on CE separation mechanisms is provided elsewhere.[64] CE-MS ionization includes fast-atom bombardment (FAB)[65], inductively-coupled plasma (ICP)[66], matrix-assisted laser desorption/ionization (MALDI)[67]atmospheric pressure chemical ionization (APCI)[68], desorption electrospray ionization (DESI)[69], with CE-ESI being the most common. Buffer incompatibility between CE (usually non-volatile) and ESI (volatile)[70] lead to development of supplemental fluid

(sheath-flow[71]) and sheathless interfaces.[72,73] NanoESI coupling to CE with sheathless interfaces now offer the highest sensitivity at nanolitre per minute flow rates.[74] Extensive use of CE-MS can be seen in proteomics[75], glycoproteomics[76], metabolomics[77], intact protein analysis[78], protein-ligand interactions[79] characterization of biopharmaceuticals[80], pesticides analysis[81], and small molecule analysis.[82]

Microfluidics is a multidisciplinary field that began in the early 1990's.[83,84,85] Often touted as "labs-on-a-chip"; microfluidic devices can carry out complex 'nano' and micro–scale experimental procedures, including on-chip capillary electrophoresis[86,87] and liquid chromatography.[88] with mass spectrometric detection.[89,90] Early glass devices were cumbersome, requiring coatings[91], derivitization[92], or pneumatic assistance[93] to improve signal from electrospraying 'off-chip'.[92,91] Inserted capillary ESI emitters provided a substantial improvement[94,95], however, generate considerable dead volume which is problematic for integrated microfluidic separation stages.[96] Polymer-based substrates[97,98,99] were a robust, low cost, alternative to glass substrates showing comparable sensitivity to commercial nanospray ESI sources[100] even offering commercial high throughput analysis with direct coupling to mass spectrometers.[101,102] Immobilized enzyme microfluidic reactors make it possible for full bottom up style proteomic[103], protein characterization[104], protein folding[98], and protein dynamic[105,106] workflows integrated on a single platform. Rational manipulation of discrete droplets on a patterned electrode grid by Digital microfluidics displays the wide breadth of lab on a chip technology, and has various applications in cell-based assays, protein profiling, and enzyme assays.[107]

1.2.1 Liquid Chromatography – Mass Spectrometry

Liquid chromatography-Mass spectrometry (LC-MS) and it's successors High Performance Liquid Chromatography (HPLC) and Ultra Performance Liquid Chromatography (UPLC) have major advantages over GC and CE such that less sample cleanup is required, volatile buffers are commonly used, no derivatization is necessary, and thermal decomposition of analytes is not a problem. Briefly, liquid chromatography involves the liquid-phase adsorption and separation of components in a mixture through high-pressure interactions with a packed stationary phase (column). Typical reversed-phase separation involves a non-polar column packing (C_{20}, C_{18}, C_{16}) with a polar aqueous mobile phase (Methanol, Acetonitrile, Water); while normal phase utilizes the opposite configuration – nonpolar mobile phase with polar stationary phase.

Direct LC-to-MS interfaces developed over a number of years, the first of which was in 1968 using a direct liquid injection (DLI).[108] Chemical ionization (CI) sources were also developed, but suffered from poor LC flow rates, low signal-to-noise, and spectra complexity caused from ion clustering.[109] Thermospray was the first to facilitate the direct LC-to-MS vaporization of a liquid as it flowed through a heated capillary tube[110], allowing for commercial instrumentation utilizing thermospray sources. Atmospheric Pressure based ionization methods such as electrospray ionization (ESI)[111,112] and chemical ionization (APCI)[113] were a godsend to the LC-MS community, because not only did they increase sensitivity, but they also made LC-MS analysis applicable to biological fluids.[114,115,116]

A typical whole-cell lysate might generate a mixture containing tens of thousands of peptides with and without post-translational modifications, a much greater number than could be analyzed based on MS alone, even with ultra-high-resolution mass analyzers.[117]

The widespread use of LC-MS in proteomics has strongly influenced ESI source design and optimization[118], mass spectrometer design[119], and newer LC methods such as multidimensional LC[120] and more recently ultra-performance[121] varieties. Widespread use of Atmospheric Pressure Interface(API)-based LC-MS methods can be seen in pesticide analysis[122,123], environmental applications[124,125], drug discovery and development[126,127], metabolomics[128,129], lipidomics[130,131], proteomics[132,133,134], protein dynamics[135,136], identifying post-translational modifications[137], glycoproteomics[138], and nucleic acids.[139]

1.2.2 Hydrogen/Deuterium Exchange – Mass Spectrometry

Hydrogen/Deuterium Exchange (HDX) is a simplified solution-phase labeling technique that substitutes labile hydrogens on backbone amides in a protein for deuterium, when the surrounding solvent environment is primarily comprised of D_2O. Deuterium incorporation is dependent on conformational fluctuations of the protein, and thus can be used to directly probe structure and dynamics. Traditional HDX methods involve two-dimensional NMR spectroscopy; which is considered a 'gold-standard' because it provides a high resolution amino acid 'residue-by-residue' map of deuterium uptake and reaction rate.[140] More detailed information on NMR-based HDX methods can be found elsewhere.[141,142] Critical limitations to NMR-based HDX methods involve the inability to characterize transient intermediate populations in large proteins (~40 kDa or greater)[143], lengthy acquisition times, and high analyte concentrations. Contrary to NMR is Hydrogen/Deuterium exchange mass spectrometry (HDX-MS)[144]; which was determined from it's onset to be highly sensitive to protein concentrations in the nM-µM range, and a practically unlimited protein size range.[145] These advantages over NMR has largely shifted

the field towards an HDX-MS-based approach, with recent developments showing near single amino acid resolution is possible.[146]

1.2.2.1 Fundamentals of Hydrogen/Deuterium Exchange

Hydrogen atoms on O-H, N-H, and S-H groups in a protein are considered labile, and can exchange with the surrounding bulk solvent. The exchange reaction itself is both acid (D_3O^+) and base (OD^-) catalyzed (Figure 4) with a minimal contribution from water catalysis.[147] The acid catalyzed exchange reaction mechanism is rather complex.[148] Initially thought to occur only by protonation of the amide N-H [149], evidence has shown that protonation of the carbonyl oxygen, resulting in an imidic acid intermediate and subsequent return to the amide via protenation of the amide nitrogen (essentially the reverse reaction) is a second possible pathway.[150] In the base catalyzed reaction, abstraction of the amide proton by deuterium oxide is followed by deuteration of the amide nitrogen by D_2O.[151]

The rate constant for exchange (k_{ex}) is the sum of the acid (k_a), base (k_b), and water (k_w) catalyzed reaction rates, and is described in the following equation:

$$k_{ex} = k_a[\mathrm{H}^+] + k_b[\mathrm{OH}^-] + k_w \quad (1)$$

The pH-dependence of the reaction-rate can also be shown as (2) and (3):

$$k_{ex} = k_a 10^{-\mathrm{pH}} + k_b 10^{(\mathrm{pH}-\mathrm{p}K_w)} + k_w \quad (2)$$

$$\log(k_{ex}) = \log(k_a[\mathrm{H}^+] + k_b[\mathrm{OH}^-] + k_w) \quad (3)$$

Hydrogen/Deuterium exchange rate constants for small unstructured dipeptide, tripeptide, and polypeptide molecules have been measured as a function of pH by NMR.[152] Figure 5 depicts the relationship between log (k_{ex}) vs pH for a number of exchangeable sites.[153] Backbone amide protons exhibit minimal k_{ex} at pH 2.5, with overall base-catalyzed exchange being ~8 orders of magnitude larger than acid-catalyzed exchange. Shifts in

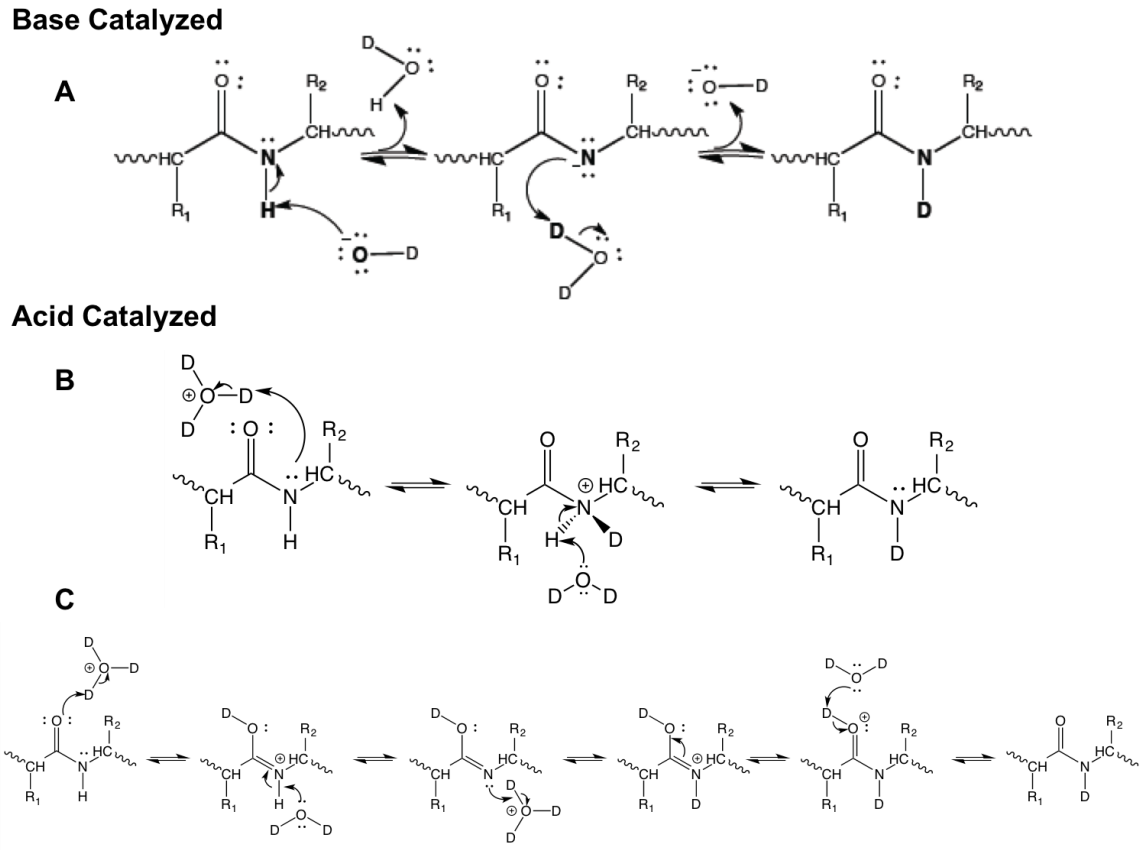

Figure 4. Base-catalyzed and acid-catalyzed amide backbone hydrogen/deuterium exchange mechanisms. (A) The base catalyzed mechanism proceeds through deprotonation of the amide by a deuterium hydroxide.[154] Typically, HDX labeling is carried out under neutral conditions (pH 7) where the base-catalyzed mechanism dominates. (B) N-protonation mechanism for acid-catalyzed H/D exchange. (C) O-protonation mechanism for acid-catalyzed H/D exchange.[154] Amides near electron withdrawing R groups (ie: Asparagine) tend to exchange by O-protonation, and electron donating (ie: Phenylalanine) promote N-protonation.[155] Adapted from Resetca[156] and Tüchsen et. at.[154]

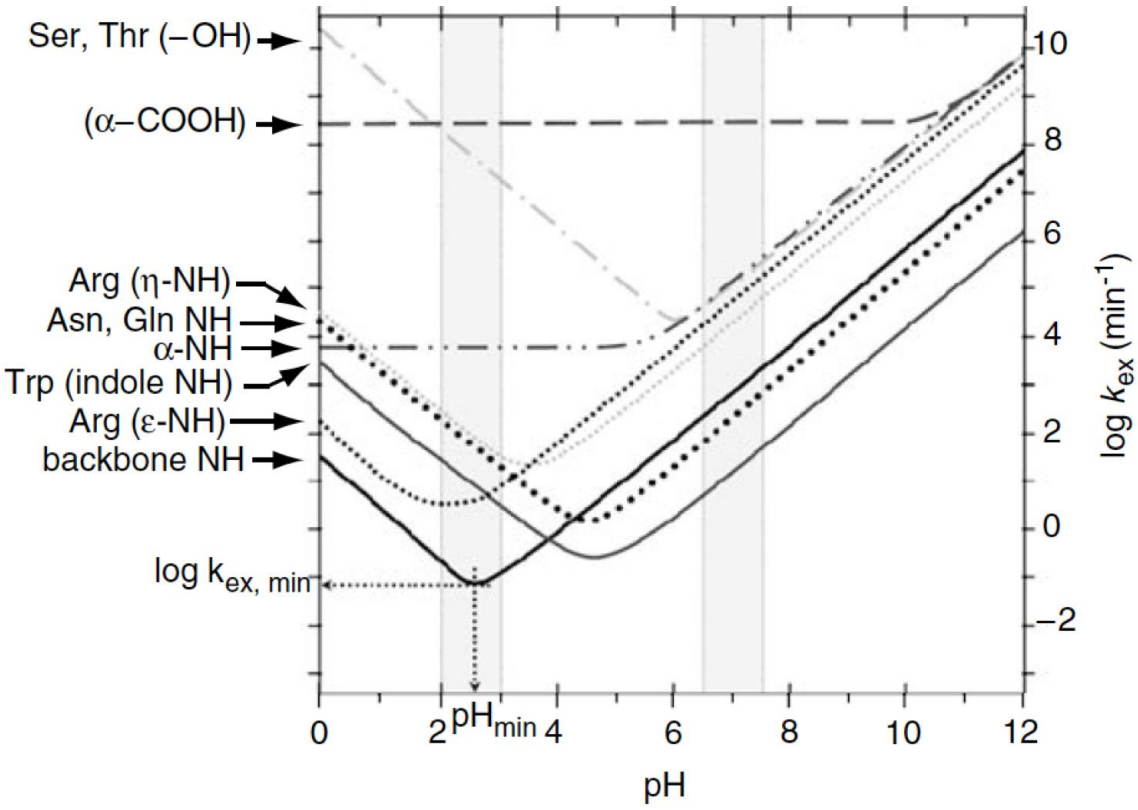

Figure 5. A chevron plot depicting exchange rates (logk_{ex}; 25°C) for amide and side-chain hydrogens as a function of pH. Shaded regions indicate typical pH values for labeling (~pH 7) and for quenching (~pH 2.5). The pH minimum reflects the lowest exchange rate for amide backbone hydrogens, 10^4 times slower than k_{ex} at pH 7. At 0°C, k_{ex} decreases by another order of magnitude, allowing retention of the deuterium label with minimal back-exchange for LC-MS workflows. Adapted from Morgan and Engen.[153]

pH_{min} caused by sequence-dependant inductive and electrostatic contributions from neighbouring side chains. Polar and positively charged side-chains withdraw electron density from the labile N-H group, increasing its pKa and base-catalysed HDX rate, while negatively charged groups do the opposite.[152,157] Non-polar side chains primarily lower both acid and base catalyzed HDX rates due to steric and hydrophobic effects.[152]

HDX rates are also influenced by temperature and can be estimated for each acid-, base-, and water-catalyzed rate constant for a constant temperature, $k_x(T)$, using the following formula:

$$k_x(T) = k_x(293°K)\exp\left(-\frac{E_a}{R}\left[\frac{1}{T}-\frac{1}{293°K}\right]\right) \quad (4)$$

where $k_x(293°K)$ corresponds to the reference rate constant at 20°C, R is the gas constant ($1.985x10^{-3}$ kcal mol^{-1} K^{-1}) and E_a corresponds to the reference energy of activation (E_a^{acid} = 14 kcal mol^{-1}, E_a^{base} = 17 kcal mol^{-1}, E_a^{water} = 19 kcal mol^{-1}).[152] Small model dipeptide, and tripeptide systems fall completely under the considerations of the above information, however, understanding and interpreting HDX in larger polypeptide chains and proteins requires further awareness of higher-order biophysical phenomena.

1.2.2.2 Hydrogen/Deuterium Exchange in Proteins

Proteins in their native state will exhibit transient thermal fluctuations, known as 'breathing' motions, that briefly break some H-bonds making them readily available for exchange with solvent D_2O. This can be described mechanistically as:[143]

$$N-H_{closed} \underset{k_{cl}}{\overset{k_{op}}{\rightleftarrows}} N-H_{open} \xrightarrow[D_2O]{k_{ch}} N-D_{open} \underset{k_{op}}{\overset{k_{cl}}{\rightleftarrows}} N-D_{closed}$$

where k_{op} is the rate constant for the 'open' state for an amide H-bond, k_{cl} is the hydrogen bonded 'closed' state for the same amide hydrogen, and k_{ch} is the rate constant for conversion of N-H to N-D. The availability of a labile hydrogen to undergo H->D transfer in a protein is governed by several factors, first and foremost is whether or not it is involved in a hydrogen bond. Intramolecular hydrogen bonding usually in secondary structure elements such as alpha-helices and beta sheets, can effectively block deuterium exchange from occuring.[158] Solvent accessibility is also of fundamental importance, as amide protons may seldom become available for exchange if locked in the hydrophobic core of a protein.[159] The inductive effects from neighboring and close-contact side chains must also be considered. These combined factors tend to slow the observed HDX rate of backbone amide hydrogens in a protein, relative to those in small peptide models or unstructured polypeptides. This ratio can be defined as a protection factor (P), such that:

$$P = {k_{ch}}/{k_{HDX}} \tag{5}$$

where k_{HDX} is the observed rate of exchange for a particular amide, and k_{ch} is the intrinsic rate of exchange for the same amide.[148] Protection factors can vary substantially in native proteins ($2\text{-}10^5$ for amides in ubiquitin)[160], where high P values are associated with 'structure' and low P values are associated with 'disorder'.[161] Molecular dynamics simulations of protein dynamics have recently placed P-value analysis under heavy scrutiny, as intermediate P-values may not completely describe crystallographically relevant protein structures, owing to poor choice of models for k_{ch} and a partially incomplete understanding of the full HDX mechanism.[162] Very high and very low protection factors do however corroborate quite well to presence and absence of structure, as seen in heavily characterized protein ubiquitin.[162]

The breathing motions of proteins are similarly described by equation (6), and under steady-state conditions, the observed rate of exchange (k_{HDX}) for a protein is given by:

$$k_{HDX} = \frac{k_{op}k_{ch}}{k_{op} + k_{cl} + k_{ex}} \quad (6)$$

With the assumption that a native protein is stable ($k_{cl} >> k_{op}$), equation (6) is reduced to:

$$k_{HDX} = \frac{k_{op}k_{ch}}{k_{cl} + k_{ex}} \quad (7)$$

where k_{cl} for a sequence of amino acids can be calculated independently.[141] From the equation there are two possible regimes under which HDX occurs. The first is where the closing rate is much faster than the rate of exchange ($k_{cl} >> k_{ch}$). In this scenario, referred to as EX2, the protein must visit its open state multiple times in order to increase the probability of labeling, and can be expressed as:

$$k_{HDX} = \frac{k_{op}}{k_{cl}} k_{ch} \quad (8)$$

The equilibrium constant for opening, $K_{op} = k_{op}/k_{cl}$, can be used to characterize the thermodynamics of a protein, specifically the free energy of the opening event ($\Delta G°$):[163]

$$\Delta G° = -RTlnK_{op} = -RTln(k_{HDX}/k_{ch}) \quad (9)$$

The second scenario, EX1, occurs when the protein visits the open state and has a much slower rate of refolding relative to the rate of exchange ($k_{ch} >> k_{cl}$). In this case, the protein becomes labeled for an extended period before reverting back to the closed state, and can be expressed as:

$$k_{HDX} = k_{op} \quad (10)$$

And thus, HDX of the protein in this regime is entirely reflective of the kinetics of the opening events. The pH dependence on k_{ch} imposes limits to EX1 and EX2 HDX regimes.[141] HDX is predominantly base-catalyzed and k_{ch} tends to be much slower than k_{cl} below neutral pH. EX2 exchange generally occurs at low pH, while EX1 tends to occur at higher pH.

1.2.2.3 HDX for Characterizing Protein Dynamics by Mass Spectrometry

Electrospray ionization mass spectrometry coupled with hydrogen/deuterium exchange typically measures protein dynamics by monitoring the exchange reaction as a function of time.[144] This is classically done in a 'contiinuous labeling' experiment, where protein in a native buffer is diluted with D_2O, initiating the labeling reaction (Figure 6B). Deuterium content is usually 50% or greater in order to favour the labeling process, which is halted or 'quenched' by aliquoting at various times and lowering the pH to ~2.5 and reducing the temperature to 0°C. The quenched solution is sprayed directly into the mass spectrometer where mass–shifts of deuterated protein can be resolved. Pulsed labeling is another type of experiment that introduces deuterium at fixed times, and is usually employed for detecting protein folding intermediates.[164] Monitoring deuterium uptake for an intact protein reveals dynamics measured on a 'global' scale (Figure 6A) which characterizes global changes in protein structure, stability[165], and ligand binding[166].

In order to localize dynamic changes to specific areas of secondary structure, acid quenching is followed by digestion of the protein by an acid protease such as pepsin.[145] Typically, the peptides that follow are separated using reversed phase LC prior to MS, mirroring 'bottom-up' workflows used extensively in proteomics.[167] Proteomic fragmentation methods such as CID are incapable of increasing spatial resolution of

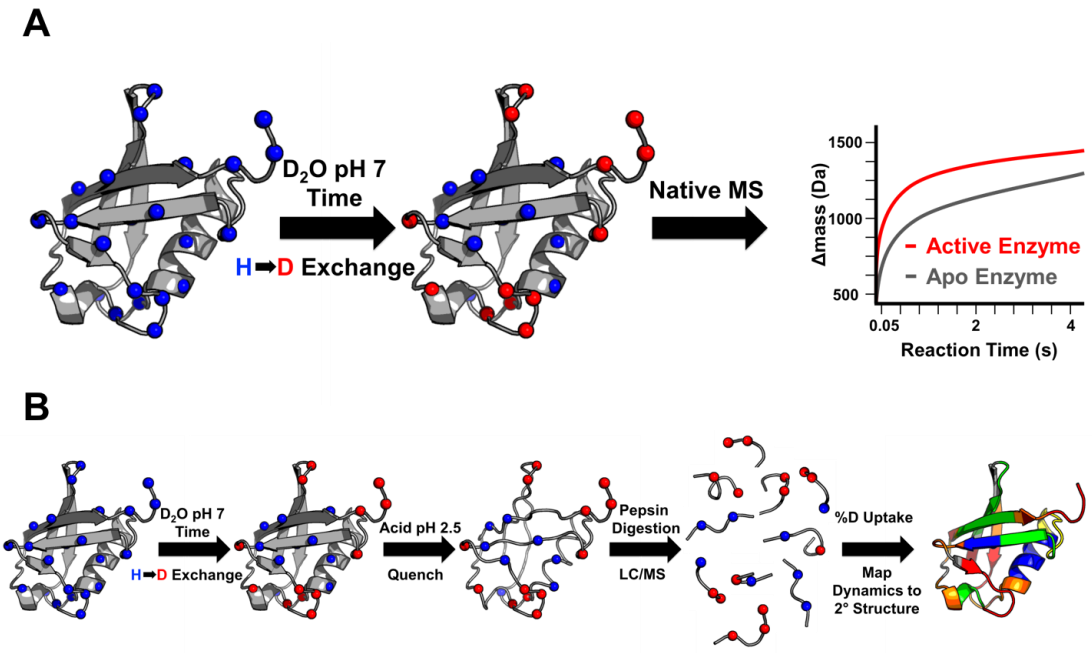

Figure 6. Hydrogen/Deuterium Exchange Experiments. (A) In a 'Global' HDX experiment the protein in solution is exposed to D2O under native conditions (pH 7) and exchanges for a set time. As time is increased, dynamic amides exchange causing the mass of the protein to increase, which results in a shift to higher *m/z* when monitored by ESI-MS. This type of experiment can be used to interrogate the dynamic effects of small-molecule inhibition[168], and catalysis-linked dynamics.[169] (B) In a 'Bottom-up'-style HDX experiment, protein exchanges under native conditions for a set period of time, and then quenched to pH 2.5 to hold the deuterium label in place, reducing D->H exchange (back exchange). Pepsin digestion followed by LC-MS separation and detection of deuterated peptides yields a high spatial resolution map of dynamic regions of the protein, which are typically displayed on x-ray crystal structures.

deuterium labelled peptides due to deuterium scrambling, resulting in loss of solution-phase dynamics information.[170] Non-ergotic fragmentation methods such as electron capture dissociation (ECD) and electron transfer dissociation (ETD) are non-scrambling, and can thus provide near amino-acid resolution on peptides and proteins.[171]

1.3 In-Ionization Technologies and Methods

In-ionization is a term that refers to analytical methodologies that are applied during and or immediately after electrospray ionization, but prior to entering the orifice of the mass spectrometer. In-ionization methods make up a large variety of analytical techniques in mass spectrometry, encompassing the field of ambient ionization mass spectrometry[172] as well as filtering ion mobility methods. With minor modifications to existing commercial ESI sources, and/or the interfacing of new ESI sources implementing in-ionization methodologies, surprisingly simplistic methods offer enormous benefits when analyzing highly complex samples. Electrospray methods such as fused-droplet (FD), extractive electrospray ionization (EESI), Field Asymmetric Ion Mobility Spectrometry (FAIMS), and Differential Mobility Spectrometry (DMS) are also discussed.

1.3.1 Fused-Droplet and Extractive Electrospray Ionization

Developing new protocols for detecting analytes in complex matrices is critically important for environmental, forensic, and proteomic applications. Recently reported fused-droplet (FD)[173] and extractive electrospray ionization (EESI) permit the analysis of samples with complex matrixes such as untreated urine[174], breath[175], milk[176], reaction mixtures[177,178,179], honey[179], olive oil[179,180], and intact proteins and peptides.[173,181,182]

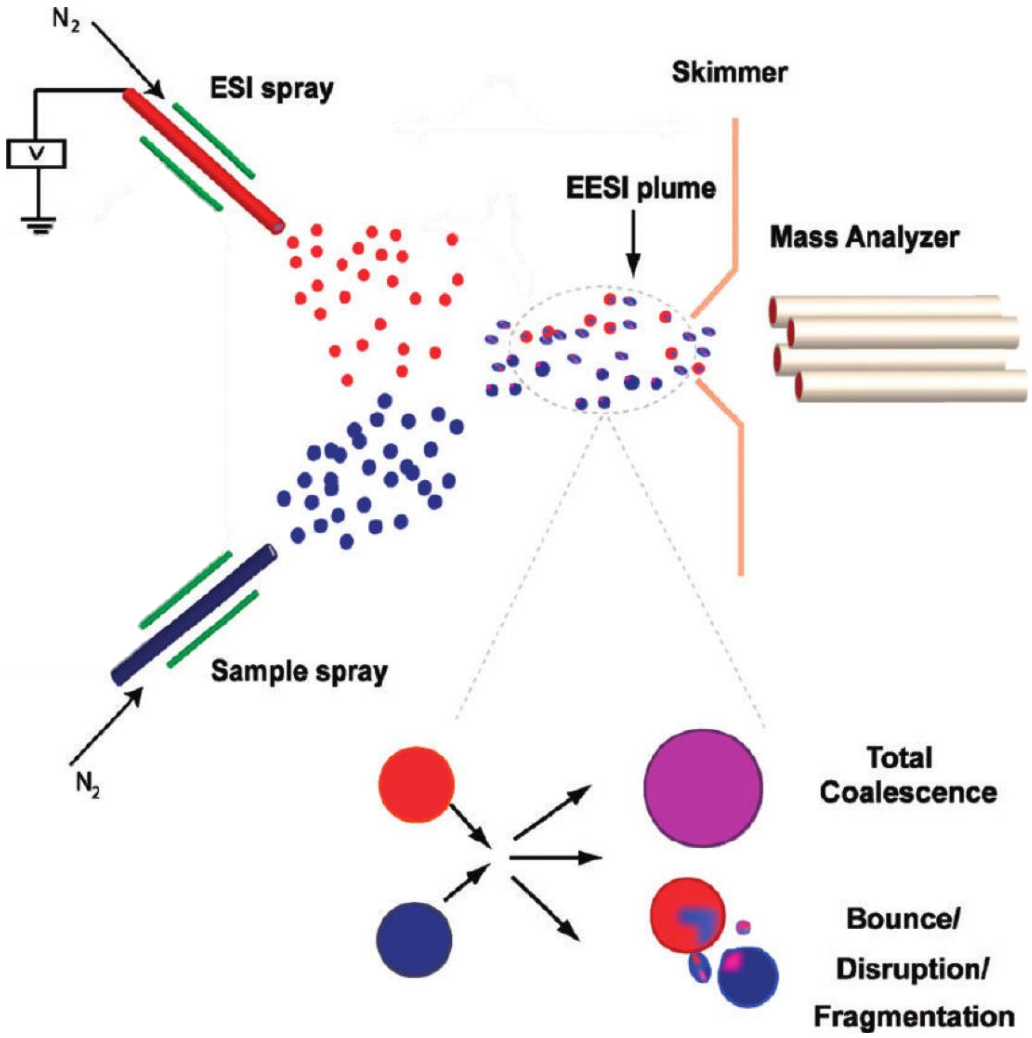

Figure 7. Schematic of an Extractive Electrospray Ionization (EESI) source. Neutral sample is sprayed using N2 or other nebulizing gasses and is ionized by charged solvent droplets prior to entering the mass spectrometer. Possible processes for liquid-phase interactions (ie: droplet coalescence) is seen on the bottom. Adapted from Law et. al.[183]

The technique involves two separate sprayers; one that nebulizes neutral sample solution, while the other produces charged solvent through ESI (Figure 7). The sprayers positioning allows the droplet plumes to intersect, where neutral sample droplets collide with charge solvent droplets. Once droplet coalescence occurs, similarities in solubility allow for selective extraction between the charged ESI droplets and the neutral analyte, followed by ion formation through traditional electrospray mechanisms.[181,184,183]

Conventional FD-ESI / EESI interfaces have adopted a two-sprayer arrangement as seen in Figure 7. The first FD-ESI interface by Chang et. al. relied on a glass reaction chamber to facilitate collisions between charged and neutral droplets, using high sample solution flow rates of 300-500 μL/min.[173] An updated design used an APCI probe with a pneumatic nebulizer, delivering sample at more realistic ESI flow rates (1-50 μL/min), along with better spray geometry and no reaction chamber.[181] The Cooks and Zenobi groups later refined the "two-sprayer" interface, and renamed the technology as extractive electrospray ionization.[174,175] More recently, quantitative analysis of drugs at the picomolar level was achieved using a heated EESI source, which showed remarkable increases in sensitivity with the application of heat while spraying from 25mM TRIS buffer.[185]

1.3.2 Field-Asymmetric Ion Mobility Spectrometry and Differential Mobility Spectrometry

Emerging ion-filtering technologies are critical for applications that require separation ions of similar mass, reduction of chemical noise, increased mass accuracy, or enhanced spectral quality.[186] technologies such as DMS and FAIMS 'pre-filter' ions based on differences between their high-field and low-field mobilities. DMS and FAIMS devices can further separate analytes by using modifier gasses (isopropanol, methanol, ethyl

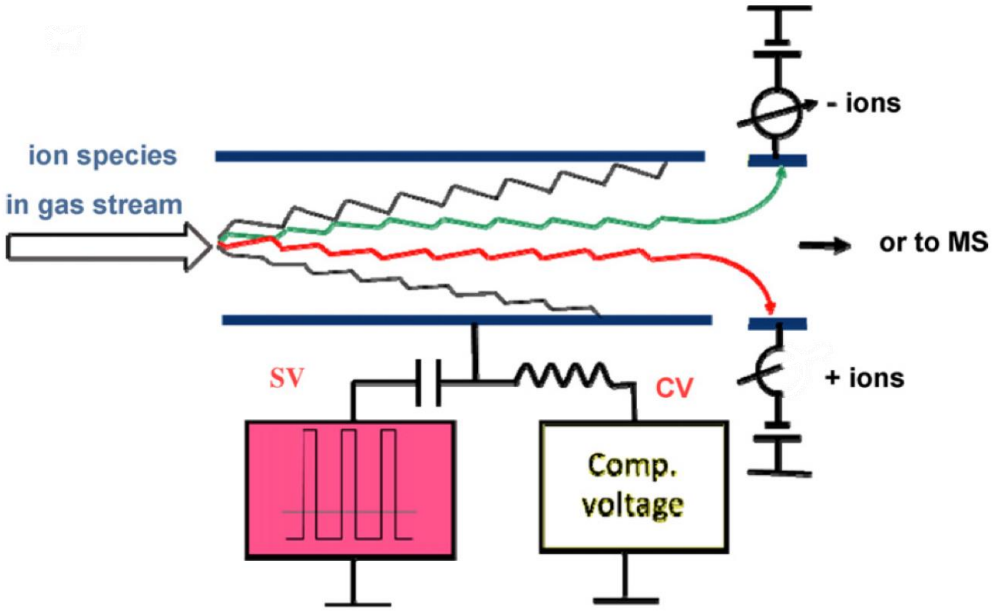

Figure 8. Schematic of a FAIMS/DMS ion filter. Transport gasses carry ions at atmospheric pressure where they interact with a separation voltage (SV), and compensation voltage (CV). Ions are detected by Faraday plates as well as a mass spectrometer. Adapted from Schneider et. al.[186]

acetate, acetonitrile, ect.), although this can complicate quantitative analysis for molecules larger than 1000 Da.[187188]

Devices are based on a system of two parallel plates, and when voltages are applied, the direction of the ion stream can be manipulated (Figure 8). Separation of ions can be described in a two-part process: (1) The application of a radio frequency separation voltage (SV) to the upper plate causes ion trajectories to "wiggle" in a stepwise time-dependent manner towards one of the plates, whereupon the ion discharges. This is caused by the waveforms asymmetry – which consists of a high field portion that directs ions to one plate, and a low field portion of opposite polarity that directs ions to the other. (2) A specific DC offset called the compensation voltage (CV) can be applied to counteract SV ion trajectories, allowing the ion to traverse between the two plates unimpeded and exit the mobility spectrometer for detection.[189]

Initial FAIMS/DMS device designs used planar electrodes as in Figure 8, but have since evolved into cylindrical[190], dome[191], and cube electrodes[192], as well as having decreased in size substantially as seen with the microchip-sized ultraFAIMS devices.[193194] Originally, DMS and FAIMS relied on ^{63}Ni ionization, but have since utilized atmospheric pressure photoionization (APPI)[195] and the more widely adopted ESI for coupling to mass spectrometry.[196] These ion-filtering devices have found widespread use in environmental analysis[197], explosives detection[198], drug discivery[199,200], clinical diagnostics[201], separation of isomers[202], metal speciation[203], protein conformational analysis[204,205], proteomics[191], and food inspection[206].

1.4 Post-Ionization Technologies and methods

Post-ionization techniques are in effect, any manipulation of an ion that occurs between the MS orifice and the detector. The type of post-ionization experiments available is determined by the type of mass spectrometer being used, thus, mass spectrometers combining several types of mass analyzers and filters are often advantageous to the end-user, as they increase experimental versatility.

1.4.1 Hybrid Mass Spectrometers

Hybrid mass spectrometers are denoted by their symbolized designations, which refers to the combination of mass analyzers and mass filters in order of appearance along the ion path. Configurations such as the triple quadrupole (QQQ), quadrupole ion trap (QIT), quadrupole linear ion trap (QLIT or LTQ), Quadruple Time of Flight (QTOF), TOF-TOF, Fourier-transform ion cyclotron resonance (FTICR), and LTQ-Orbitrap, are common mass spectrometers; each having their own distinct components and analytical characteristics. The advantages and disadvantages for each hybrid instrument in proteomics, imaging, and tandem mass spectrometry can be found in these excellent reviews.[207,208,209]

The median length of a protein in the eukaryotic proteome is 361 amino acids, which is much higher than in bacteria (267 amino acids) and higher still than in archaea (247 amino acids).[210] A Protein Data Bank (PDB) query on protein oligomeric states shows that the majority of proteins identified are dimers or larger.[211] To examine these proteins directly requires a mass analyzer with a very high mass range. Time-of-flight (TOF) mass analysers have a theoretically unlimited *m/z* range which makes them suitable for high-mass intact protein analysis.[212] Although quadrupoles have a limited *m/z* range of about 4000 Thompsons (Th), their arrangement in tandem with a TOF enables them to act as a

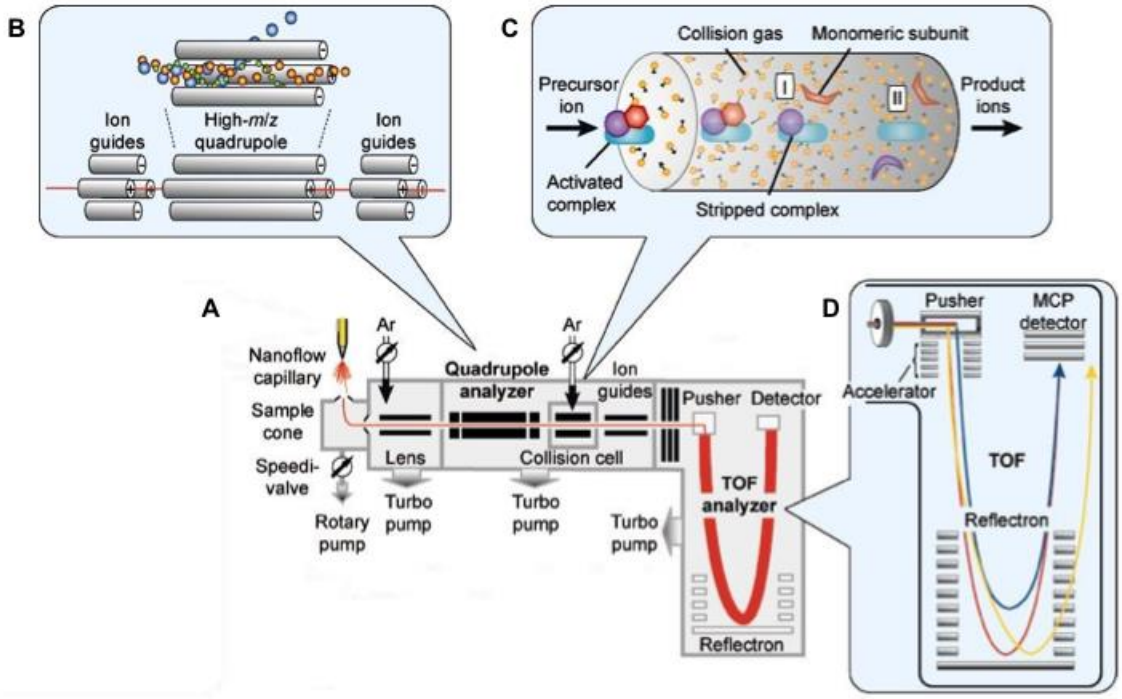

Figure 9. Schematic of quadrupole time-of-flight (QTOF) hybrid mass spectrometer for the analysis of protein complexes. (A) Ions formed by nanoESI or ESI enter into the MS by differential pumping and potential gradients. The red line indicates the ion path from entry to detection in the TOF mass analyzer. (B) The quadrupole mass filter. Modulation of radio frequency and direct currents applied to the rods allow transmission and or selection of ions with a specific *m/z* value. Orange circles represent ions selected for transmission, while blue and green circles are not transmitted. (C) Fragmentation of protein complexes in the collision cell by CID. The precursor ion selected via the quadrupole undergoes collisions with the collision gas (orange), increasing the internal energy of the complex, causing subunits (red and purple) to dissociate at measurable energies. (D) The time-of-flight mass analyzer showing ions with different *m/z* values and their parabolic trajectories towards the multi-channel plate (MCP) detector. Ions with identical *m/z* values but different velocities are represented by the red and blue lines, the yellow line represents an ion that is not detected. Adapted from Sharon et. al.[213]

mass filter, as well as a collision cell.[214] A typical quadrupole TOF mass spectrometer (Figure 9) will require some modifications to allow for efficient transmission of intact proteins. Higher pressures in the Q0 region by way of throttling vacuum lines assist with focusing, as well as low frequency high *m/z* quadruples for decelerating high-mass ions that require more time for desolvation.[215] QTOF instruments are also capable of numerous ion activation techniques, which can induce fragmentation of the protein ion, gaining insight on higher order structure.[216] A majority of ion activation experiments on proteins have been done using collision-induced dissociation (CID – also known as CAD – collisionally activated dissociation), where ions of interest collide at controllable energies with neutral gas molecules to produce fragmentation.[217] Other fragmentations techniques such as surface induced dissociation (SID)[218], blackbody infrared dissociation (BIRD)[219] and electron capture dissociation (ECD)[220] have all be successfully applied to large proteins and protein complexes. Another interesting addition to the QTOF is an ion mobility cell. When positioned directly after the first quadrupole, mass-selected ions can be separated in time, giving detailed information on their size.

1.5 Ion Mobility Spectrometry Mass Spectrometry

The coupling of ion mobility spectrometry (IMS) and mass spectrometry falls into the category of pre-ionization, post-ionization, or both depending on the order. In this dissertation, two separate ion mobility mass spectrometry projects are presented: one pertaining to atmospheric pressure ion mobility – mass spectrometry (Chapter 2), and the other on low-pressure ion mobility mass spectrometry (Chapter 3). The specific experiments for these two types of IMS-MS are explained in their respective chapters. The

aim of this section is to provide a current and historical account of ion mobility spectrometry, along with its basic theoretical principles.

1.5.1 Current and Historical Perspectives

Ion mobility spectrometry (IMS) is a method that was developed to study the behavior of gaseous ions at under the influence of a uniform electric field.[221] Briefly, it works by measuring the time it takes an ion to traverse a region of space under the influence of an electric field while it collides with neutral gas particles. This measurement is the ion's "mobility", but also the process has a moderate degree of separating power, thus different ions can give different mobilities – and as such ion mobility has become a stand-alone method for detecting volatile and semi-volatile compounds. Stand-alone IMS instruments have seen widespread use in explosives and narcotics detection[222,223], air and food quality analysis[224,225], and environmental analysis.[226] For a more comprehensive historical introduction and developmental timeline, we direct the reader to the following text.[227]

In the 1970's ion mobility spectrometry adopted the name "plasma chromatography", and immediately from its inception it was thought that ion mobility could greatly benefit from coupling to mass spectrometry.[228] This is because IMS lacks the capability to separate ions by mass, and vice versa mass spectrometry is unable to separate ions by size. Thus ion mobility and mass spectrometry represent highly complementary and orthogonal analytical techniques. At present, ion mobility spectrometers have successfully been interfaced to triple quadrupole,[229,230] TOF,[231,232] QTOF,[233] QIT,[234] FTICR,[235] and LTQ mass spectrometers.[236] Present-day IMS's are also equipped with a variety of techniques for introducing vapor, semi-volatile, aqueous, and solid samples – many of which are compatible with the ion sources available to mass spectrometers. At first, the most common

ionization method in an IMS-MS system was a ^{63}Ni radioactive ion source[237], but others such as corona discharge ionization,[238] photoionization,[239] and low-temperature plasma[240] have also been implemented. The coupling of these methods allowed for characterization of ion chemistries in standalone IMS systems used in explosive trace detection and detection of narcotics.[230,241,242]

With the introduction of soft-ionization sources like ESI and MALDI, many IMS-MS systems shifted towards analyzing biological materials.[243,244] Since it's fist application to bioanalysis,[245] IMS-MS has seen an explosion in this area of research.[246–249] Much of the pioneering work was done by the Clemmer group, who demonstrated that ion mobility mass spectrometry was capable of separating protein conformers in the gas phase.[250] The Bowers group also showed that by using MALDI and IMS they could identify a protonated structure of bradykinin that fit with an experimental model.[245] Other applications include high-throughput proteomic screening[251], obtaining structural insights on large protein assemblies,[252] and multidimensional IMS coupled to mass spectrometry techniques for the separation of proteins and peptides.[253,254] The commercial availability of standalone instruments (Smiths Detection IONSCAN series,[255] GE Itemiser,[255] and others[256]) and hybrid IMS-MS systems (Waters Synapt TWIMS-MS, Sciex, Agilent) has ensured IMS as a mainstay analytical technique that is experiencing rapid adoption and widespread use.

1.5.2 General Principles of Ion Mobility

Traditional ion mobility spectrometry is based on a drift tube – a gas-filled cylindrical channel where ions are introduced under the influence of a weak electric field. (Figure 10) The theoretical framework governing most ion mobility techniques can be related back drift-tube ion mobility theory. Briefly, as an ion cloud traverses the drift region, it interacts

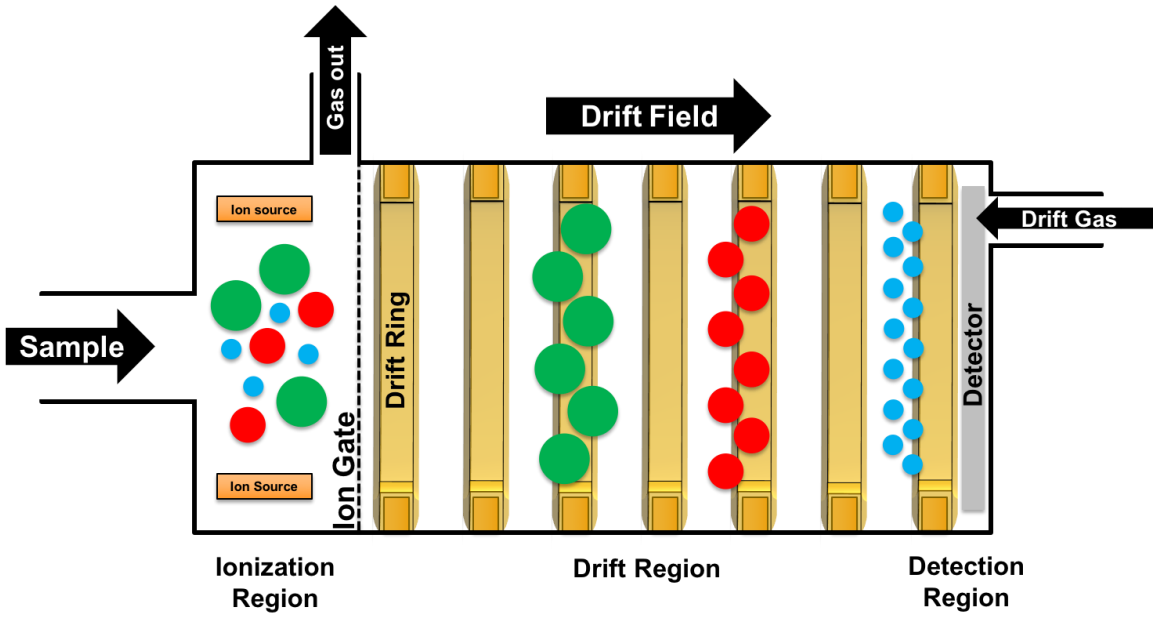

Figure 10. Schematic of a drift-tube ion mobility spectrometer. Samples are ionized (green, blue and red spheres) and trapped for a period of time behind an ion gate. Once the potential on the gate is dropped, samples enter the drift region and undergo separation, each migrating at different drift velocities to the detector. Adapted from Cumeras et. al.[257]

with a uniform electric field whereby it undergoes a continuous round of acceleration-deceleration events caused by collisions with drift gas molecules; acquiring an average drift velocity (v_d). Drift velocities are measured using the time it takes an ion cloud to cross the distance between the point of entry into the drift tube and the detector; which is described by the following equation:

$$v_d = {}^{d}/_{t_D} \tag{11}$$

where t_D is the drift time and d is the distance. The constant of proportionality that relates drift velocity (v_d) to the electric field (E) is K, also known as the mobility coefficient.

$$K = {}^{v_d}/_{E} \tag{12}$$

And is only true if the constant composition of gas, pressure and temperature are all held constant. Thus it is easier to convert the measured mobility, K, into a reduced mobility coefficient, K_0 to account for changes in pressure, temperature and gas composition.

$$K_0 = \frac{L^2}{t_D V} \times \frac{273.15}{T} \times \frac{P}{760} \tag{13}$$

where L corresponds to the length of the drift region, V is the voltage applied across it, P is the gas pressure in Torr, T is the gas temperature in kelvin.[221] When all parameters are normalized, this is the best available measurement that relates the physical properties of an ion swarm and it's mobility. Reduced motilities can vary as a function of E/N (units of Townsends [Td]) where N is the number density of the buffer gas, and as such, most reliable mobility measurements are made in the low-field regime.[258] Theory characterizes drift-tube processes very well, but for other ion mobility techniques such as FAIMS and DMS, processes governing the separation of ions at high and low fields are not yet fully understood and represent an active area of research.[259]

Drift-tube IMS is also capable of measuring an ions physical size. Experimental average cross-sections measured by IMS have been reported for a number of biological molecules using helium drift gas and low pressure with a high degree of accuracy when compared to crystal structures.[260] Drift time measurements are converted into average collision cross sections by the following formula:

$$\Omega = \frac{(18\pi)^{1/2}}{16} \cdot \frac{ze}{(k_B T)^{1/2}} \left[\frac{1}{m_I} + \frac{1}{m_B}\right]^{1/2} \cdot \frac{t_D E}{L} \cdot \frac{760}{P} \cdot \frac{T}{273.15} \cdot \frac{1}{N} \tag{14}$$

where *ze* corresponds to the charge of the ion, k_B is the Boltzman constant, *N* is the number density of the buffer gas, m_I is the mass of the ion, and m_B is the mass of the buffer gas.[261]

Differentiating between protein conformational states as well as structural isomers requires a high-resolution ion mobility method. The theoretical resolving power of a drift-tube is approximately given by:[262]

$$\frac{t}{\Delta t} = \left(\frac{LEze}{16 k_B T ln2}\right)^{1/2} \tag{15}$$

where $t/\Delta t$ is the resolution at full width half-maximum (FWHM), L is the length of the drift tube, E is the electric field, k_B is the Boltzman constant, and T is the temperature in Kelvin. Lower temperatures, higher electric fields, and longer drift tubes can provide high resolution measurements for covalent and ionic bound small-molecules, however, complications arise when attempting to analyze large polyatomic structures like proteins.[263] High-electric fields require increased gas pressure to avoid gas discharge, however, this raises the injection voltage required to transmit the ion from the ion source to the ion mobility cell. Proteins subjected to higher injection voltages can undergo gas-

phase unfolding, and in some cases fragmentation, destroying any prospect of probing native-like conformational states.[264]

1.5.3 Traveling-Wave Ion Mobility Spectrometry – Mass Spectrometry

The relatively new Traveling-Wave Ion Mobility Spectrometry (TWIMS) method developed by Waters[265] for their Synapt series QTOF commercial IMS mass spectrometer has experienced widespread adoption in the amongst mass spectrometrists, providing insights in the structures of peptides[266], proteins[267], protein complexes[268], as well as small molecules[269]. Briefly, the traveling-wave portion consists of a set of stacked ring ion guides which propels ions in "waves" by using a repeating sequence of DC pulses on adjacent rings (Figure 11). A more detailed description of the process is provided elsewhere.[265] Recently the Ruotolo group have shown TWIMS's capability to characterize protein binding stoichiometry and oligomer state for high-throughput drug-based screening.[270] Larger protein complexes such as the rotary ATPase measured with IMS by the Robinson group have uncovered key mechanistic details on the modulation of small molecules on the operation of this molecular machine.[271] TWIMS-MS usefulness relies on its ability to accurately measure collision cross sections (Ω) of ions, with comparable accuracy to conventional drift-tube measurements. Ω measurements (nm^2) in helium and nitrogen were done for ions with masses ranging from 0.5 to 800 kDA, consisting of a series of native and denatured proteins and peptides.[260] It was found that errors of 5% or less (when compared to conventional drift-tube measurements) are achieved when the analyte of interest is flanked by calibrants which are of slightly less mass and slightly more mass than the analyte of interest. Calibration of a TWIMS has been described elsewhere in detail[268], but briefly observed drift times are corrected by the following equation:

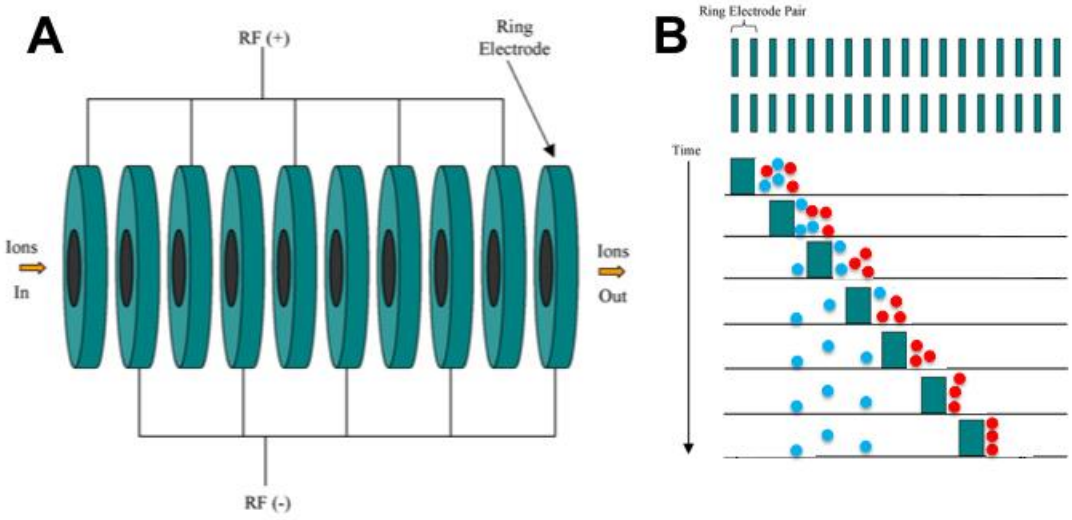

Figure 11. (A) Schematic of a stacked-ring ion guide. (B) Traveling-wave ion mobility separation in a traveling-wave ion guide. A single separation cycle is shown, where red ions are unable to surmount the DC pulse voltage or 'wave' and propelled towards the detector. Blue ions require multiple cycles to reach the detector. Adapted from Pringle et. al.[272]

$$t'_D = t_D - \left[\frac{c\sqrt{m/z}}{1000}\right] \quad (16)$$

where t'_D is the corrected drift time in ms, t_D is the experimental drift time in ms, *m/z* is the observed mass-to-charge ratio of the ion, and c is a constant determined from the enhanced duty cycle delay coefficient of the mass spectrometer itself. Database Ω values in helium are corrected (Ω') for charge (z) and reduced mass (μ):

$$\Omega' = \frac{\Omega_{Database}\sqrt{\mu}}{z} \quad (17)$$

Plotting the slope of the line ln(Ω') vs ln(t'_D) gives an exponential factor X which can be used to further correct drift times:

$$t''_D = {t'_D}^X \left(\frac{z}{\sqrt{\mu}}\right) \quad (18)$$

where t''_D is the final corrected drift time. A plot of database Ω values as a function of final corrected drift times gives a TWIMS-calibrated collision cross section.

1.6 Time-Resolved Electrospray Ionization – Mass Spectrometry

1.6.1 Current and Historical Perspectives

The ability to probe fleeting states in chemical reactions has always been a difficult task. With the arrival of ESI, mass spectrometry's inevitable push into the realm of bimolecular analysis has brought with it the prospect of studying these molecules with unprecedented detail. Some of the first ESI-MS spectra of proteins showed without a doubt a dependence on a proteins charge state distribution with respect to its folded state.[273] How

proteins transition from the folded to unfolded state represents a question long sought after by biologists and chemists alike.[274] Analytical techniques that can detect transient intermediates under pre-equilibrium conditions are critical for assessing and solving this problem. This entails that mixing, reacting and measuring must all take place within the span of microseconds to milliseconds. Stopped-flow and quench-flow rapid mixing apparatuses using UV or fluorescence detection have accomplished such feats.[275] Briefly, in stopped-flow two solutions are mixed at high flow into an observation cell for detection. Although highly sensitive, selectivity is poor for detecting multiple species simultaneously, as well as validation of interferences in protein structure caused by the chromophore itself.[276] Circular dichroism (CD) utilizes a proteins inherent chromophoric ability and is able to detect changes in secondary and tertiary structure.[277] Evidence from a combined stopped-flow and CD study showed folding and refolding of the yeast transcriptional activator GCN4 obeys a two-state model.[278] Unfortunately methods like CD can only observe global large-scale folding events, making it difficult to pinpoint local amino-acid level conformational changes. Much of the efforts to integrate a stopped-flow-like system for studying time-resolved reactions on a mass spectrometer came from the Konermann group.[279] A continuous flow mixer with an interchangeable ESI needle for fixed reaction times was used to study the refolding of cytochrome c by ESI-MS (Figure 12A).[280] Improvements were made when Wilson and Konermann developed a continuous-flow setup with an adjustable reaction chamber (Figure 12B).[281] The concentric capillary design allowed for uninterrupted adjustment of reaction times while facilitating rapid mixing from a notch cut 2mm from the distal end of the inner capillary. As a functioning ESI source, reactions could be monitored in two separate modes: (1) spectral mode, where the reaction

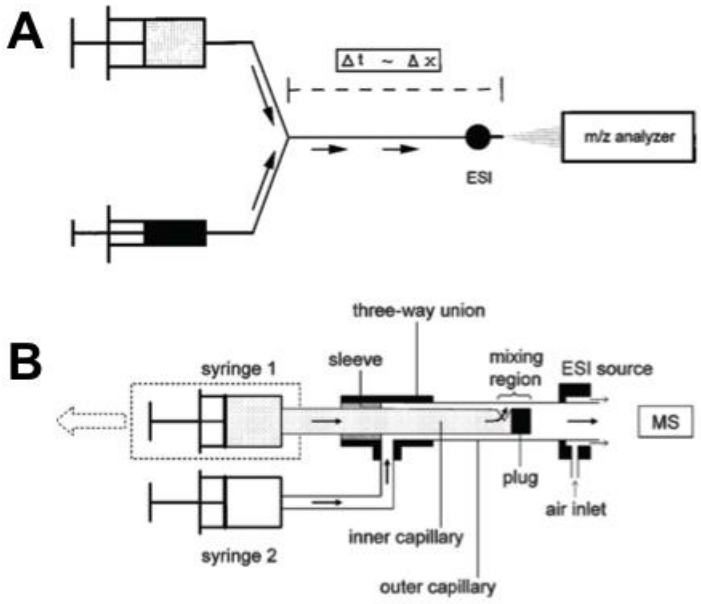

Figure 12. (A) First-generation Time-resolved electrospray ionization (TRESI) source. Solutions are infused via syringe pumps and mixed in a T-junction. Reacted times were defined by the length of the ESI capillary. Reaction time-courses were generated by changing the capillary with others of various length. (B) Second-generation TRESI source with an adjustable reaction region. Adapted from Lento et. al.[282]

volume is held at specific points and discrete reaction times are monitored. (2) Continuous mode, where the reaction volume is increased at a constant uninterrupted rate allowing for "lossless" monitoring of the reaction. This device was used extensively in this dissertation for studying a multitude of biochemical processes and systems, those of which are highlighted below.

1.6.2 Monitoring Enzyme Reactions by TRESI-MS

TRESI-MS is uniquely suited for monitoring enzymatic reactions because it is able to detect subtle changes in substrate, intermediate and product populations as a function of reaction time and mass-to-charge.[283] Accurate determination of rate constants for individual steps in an enzymes catalytic cycle depends on establishing a pre-steady-state, which refers to the period where enzyme intermediates become significantly populated. Steady-state measurements provide information on rate-limiting steps and yield rate parameters such as K_M and k_{cat} which are meaningful, but do not provide fundamental information regarding the multitude of enzyme sub-states that contribute to the mechanism.[284] Initial time-resolved measurements for xylanase in the pre-steady state detected the presence of a covalently-bound enzyme-substrate intermediate.[285] This was also established for the chymotrypsin-catalysed hydrolysis of para-nitrophenyl acetate (pNPA), which monitored subsequent depletion of chymotrypsin and the rise of 42 *m/z* covalently-bound acyl-enzyme intermediate (Figure 13).[283] The reaction serves as a model system for characterizing pre-steady state enzyme kinetics by optical stopped-flow spectroscopy as the p-nitrophenylate (p-NP) release product provides an intense yellow colour.[286] Rate constants for the acylation strep were reported 3.2±0.3 s^{-1} and 3.7±0.3 s^{-1} for both alpha- and delta-chymotrypsin respectively with high correlation to measured

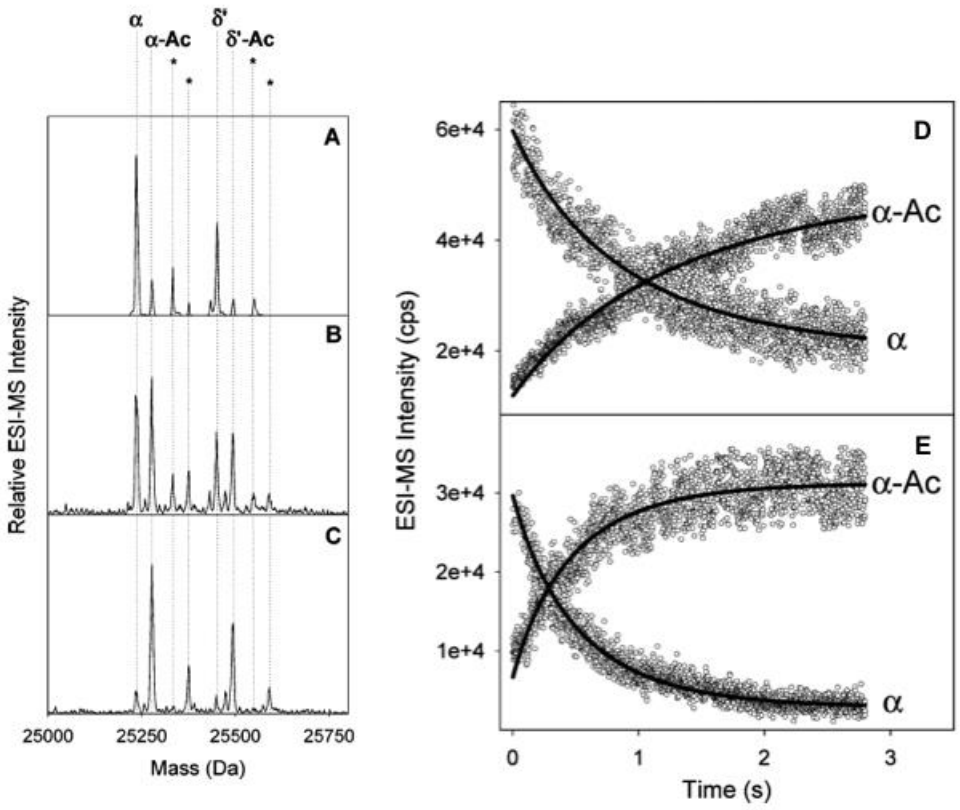

Figure 13. Monitoring the hydrolysis of p-nitrophenyl acetate by chymotrypsin by time-resolved ESI-MS. Deconvoluted mass spectra of α- and **δ**'-chymotrypsin and their respective acyl-enzyme species at A) 30 ms, (B) 700 ms, and (C) 3 s reaction time. Asterisks denote an unidentified 98 Da adduct. Pre-steady state reaction progress curves for the 12+ charge state of chymotrypsin for p-NPA concentrations of (D) 1 mM and (E) 5 mM. Adapted from Wilson et. al.[283]

values in the same study (3.6±0.2 s^{-1}) and elsewhere.[287] Notably, mass spectrometric detection was able to deconvolve two separate forms of chymotrypsin in the same solution, providing individual pre-steady state rates, which would not have been a simple task for optical methods.

1.6.3 Measuring Kinetic Isotope Effects by TRESI-MS

Revealing the mechanistic details of catalysis also depends on knowing the positions of key functional groups in the active site at the transition state.[284] Isotopic substitution has played a large role in elucidating enzyme reaction mechanisms.[288] The differences in observed rate constants for an enzyme as it turns over unlabeled substrate (k_{light}) versus a labeled substrate (k_{heavy}) gives rise to a kinetic isotope effect (KIE) expressed as the ratio of rates:[289]

$$\text{KIE} = {}^{k_{light}}\Big/_{k_{heavy}} \tag{19}$$

KIEs can give insights into the nature of rate-limiting steps, and transition state structure from quantifiable changes in reaction rates.[290] Differences in vibrational frequencies of the light and heavy bond result in differences in their zero point energies between the ground state and the transition state, with the heavy isotope lower in energy than the light. Their energy for activation will be different and will be reflected in their measured rates; using this information transition-state bond lengths and geometry may be inferred.[291] If the isotope is near the site undergoing "bond-breaking", a small secondary isotope effect is observed. When the isotope is directly involved in the bond making/breaking step, a larger primary isotope effect is detected.[292] Measuring KIEs has often relied on optical spectroscopy and scintillation counting.[293] Using radioisotopes such as ^{3}H can be

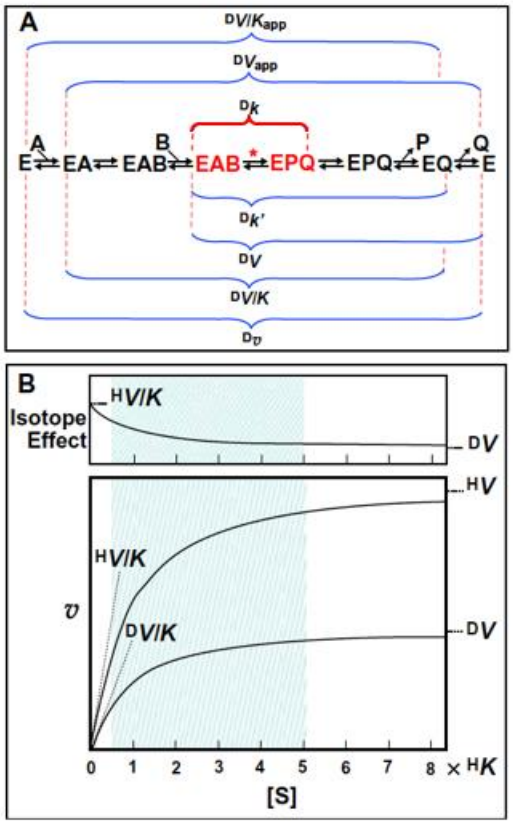

Figure 14. The steady-state and pre-steady state dependence of deuterium isotope effects. (A) An ordered ternary complex mechanism, where E is the enzyme, A is substrate, and B is cofactor, P is product, and Q is cofactor, is used as an example to illustrate the various types of measureable isotope effects. The magnitude of the observed isotope effect is highest for the intrinsic step involving isotopic substitution (Red bracket) and is often only measureable in the pre-steady state. Steady-state parameters (blue brackets) are collections of rate constants often based on Michaelis constants (K_m), maximal velocities (V_m) or specificity constants (V_m/K_m). (B) A steady-state plot of reaction velocity V versus [S] is necessary to obtain key rate parameters. Shaded regions mark areas where typical initial-rate enzyme kinetic measurements are made. Adapted from Purich.[290]

hazardous; while spectroscopic techniques rely on chromophores which are not always amenable to a majority of enzyme substrate reactions. Distinguishing multiple isotopes simultaneously with high sensitivity makes mass spectrometry well suited to the study of isotope effects. Isotope ratio mass spectrometers can accurately measure the relative abundances of labeled and unlabeled substrates[294]; however the numerous sample handling steps involved, along with using dated magnetic sector instruments make isotope ratio mass spectrometers quite cumbersome. Since enzyme mechanisms are invariable multi-step processes, isotope effects can be measured on steady-state parameters (V_{max}, K_M) as well as pre-steady state rate parameters (Figure 14).[295] TRESI-MS provides the time resolution necessary to observe enzymatic reactions in both the pre-steady state and steady-state regime. By measuring KIEs in the enzymatic pre-steady state comprehensive information on the actions of catalytically active functional groups can be obtained.[296,297]

1.6.4 TRESI-Hydrogen/Deuterium Exchange-MS for Studying Protein Conformational Dynamics

Enzymes undergo thermally driven conformational fluctuations that are inherently linked to catalytic efficiency.[298] The association between conformational dynamics and catalytic activity in enzymes is well known[299,300], and established primarily from Carr-Purcell-Meiboom-Gill (CPMG) relaxation dispersion NMR methods.[301] CPMG relaxation dispersion allows for the site-specific characterization of the kinetic and thermodynamic properties of nuclei on the microsecond-millisecond timescale as they sample different environments during conformational exchange.[298] Several models for catalysis-linked dynamics have been discovered using this extremely powerful technique; however, it is

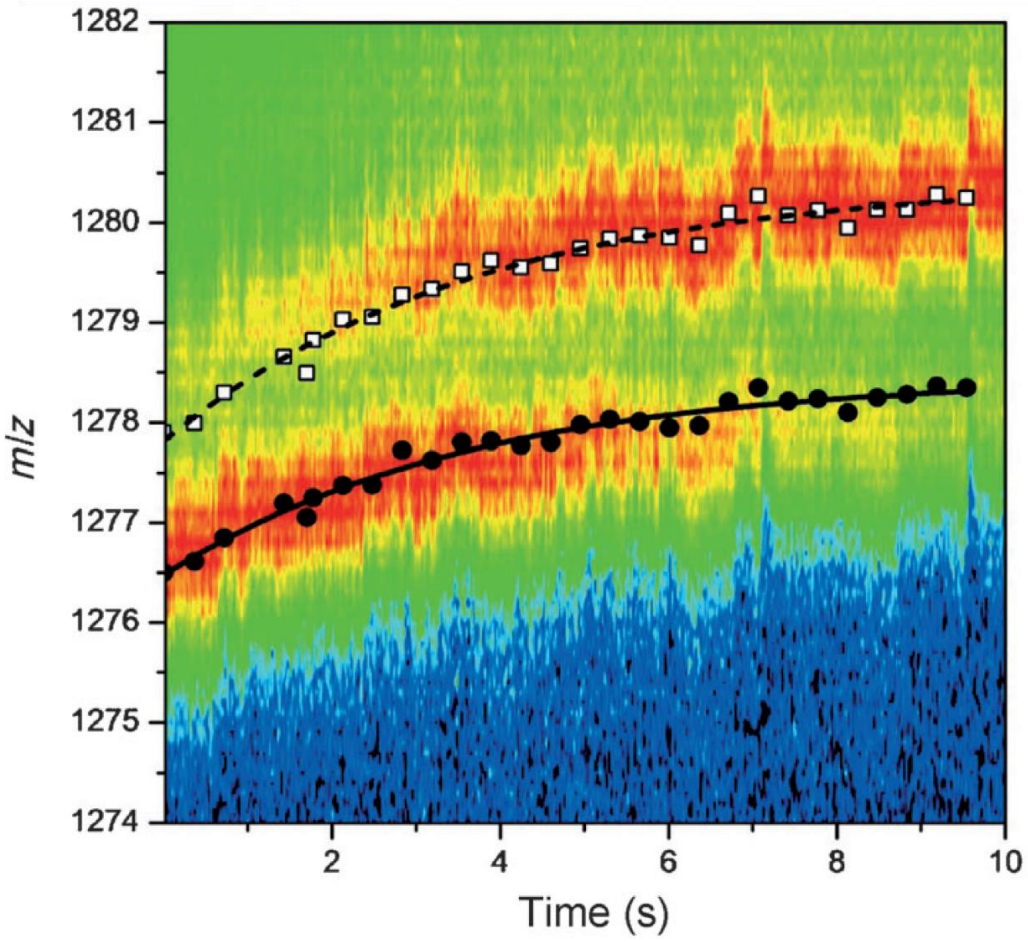

Figure 15. A heat map showing catalysis and HDX for the 20^{+} charge state of chymotrypsin. Catalysis is observed as decreasing (free enzyme) or increasing (acyl-enzyme) heat while the rate of shift to higher *m/z* gives the global HDX kinetics. Fits to the HDX kinetics were obtained by plotting the peak centroid position as a function of time for each *m/z*. Closed circles represent the free protein while the open squares correspond to the acyl-enzyme intermediate. A global exchange rate constant of 0.17±04 s^{-1} for the free enzyme (filled circles and gray triangles) and 0.29±0.03 s^{-1} for the acylated species (open squares). Reproduced from Liuni et. al.[169]

limited in its application to a small subset of enzymes.[302] TRESI-MS in combination with sub-second Hydrogen/Deuterium exchange (HDX) labeling is emerging as straightforward, broad-spectrum alternative to NMR for measuring dynamics in proteins[303], protein-ligand interactions[304], and catalytically active enzyme systems.[305] TRESI-MS was used to characterize the dynamics of catalytically active chymotrypsin by employing a deuterium labelling method simultaneously as the enzyme hydrolysed p-nitrophenyl acetate.[169] Both the free-enzyme and acyl-enzyme species were monitored in the pre-steady state, and individual rates of deuterium exchange were measured. Significantly higher HDX rates for the acyl-enzyme species relative to the free-enzyme were observed, reflecting a higher rate of conformational sampling (Figure 15). Overall deuterium uptake for both species were the same, suggesting the conformational space explored by both enzymes is relatively the same. A new model for catalysis-linked dynamics was developed, which describes conformer selection followed by intensified conformational searching during catalysis. This "intensified" conformational searching is a unique feature that does not agree with the conformer selection model, where the frequency of conformational exchange is independent of catalysis, nor with "hybrid" models that include directed conformational searching after substrate binding.[306,307] Employing these methodologies along with spatially resolved HDX measurements is promising and may provide new insights on the fundamental 'never-before-seen' underlying mechanisms involved in enzyme catalysis.

1.7 Research Objectives

Front-end analytical methods combined with mass spectrometric detection can provide unparalleled modes of analysis. In Chapter 2, we attempt to identify a series of compounds in seized opium samples observed on standalone trace-compound detector (TCD) ion mobility spectrometers for the Canada Border Services Agency. This is accomplished by building a front-end atmospheric pressure TCD-IMS coupled to MS, and then using the unique operating modes of the instrument to mass-identify mobility peaks of interest.

In Chapter 3 we aim to identify differences between acid-induced cytochrome c unfolding intermediates populated by equilibrium perturbation or by kinetic unfolding. We use a front-end time-resolved ESI device to unfold cytochrome c on the millisecond timescale, coupled to a traveling-wave IMS-MS to detect both equilibrium and kinetic unfolding intermediates.

In Chapter 4, we aim to measure kinetic isotope effects in both chymotrypsin and yeast alcohol dehydrogenase using a novel time-resolved ESI-MS approach. Time-resolved ESI initiates enzyme catalysis in the pre-steady state where enzyme intermediates become significantly populated, while the sensitivity of the mass spectrometer allows us to measure a $^{12}C/^{13}C$ isotope effect and a $^{1}H/^{2}D$ isotope effect.

In Chapter 5, we attempt elucidate the link between catalysis and dynamics by first measuring a kinetic isotope effect as yeast alcohol turns over unlabeled and deuterium labeled ethanol by TRESI-MS. We then use global hydrogen/deuterium exchange in both regimes to identify differences in dynamics associated with catalytic turnover.

Chapter 2

Unambiguous Characterization of Analytical Markers in Complex, Seized Opiate Samples Using an Enhanced Ion Mobility Trace Detector-Mass Spectrometer

A version of this chapter was published in Analytical Chemistry:

Liuni, P.; Romanov, V.; Binette, M.-J.; Zaknoun, H.; Tam, M.; Pilon, P.; Hendrikse, J.; Wilson, D. J. Unambiguous Characterization of Analytical Markers in Complex, Seized Opiate Samples Using an Enhanced Ion Mobility Trace Detector-Mass Spectrometer. *Anal. Chem.* **2014**, *86* (21), 10772–10779.

2.1 Summary

Ion Mobility Spectrometry (IMS)-based Trace Compound Detectors (TCDs) are a powerful and widely-implemented tool for the detection of illicit substances. They combine high sensitivity, reproducibility, rapid analysis time and resistance to dirt with an acceptable false alarm rate. The analytical specificity of IMS instruments for a given analyte depends strongly on a detailed knowledge of the ion chemistry involved, as well as the ability to translate this knowledge into field-robust analytical methods. In this work, we introduce an enhanced hybrid TCD-Ion Mobility Spectrometer-Mass Spectrometer (TCD-IMS-MS) that combines the strengths of ion-mobility based target compound detection with unambiguous identification by tandem MS. Building on earlier efforts along these lines (Kozole et. al., 2011), the current instrument is capable of positive and negative-mode analyses with tightly controlled gating between the IMS and MS modules and direct measurement of ion mobility profiles. We demonstrate the unique capabilities of this instrument using four samples of opium seized by the Canada Border Services Agency (CBSA), consisting of a mixture of opioid alkaloids and other naturally occurring compounds typically found in these samples. Although many analytical methods have been developed for analyzing naturally occurring opiates, this is the first detailed ion mobility study on seized opium samples. This work demonstrates all available analytical modes for the new IMS-MS system including ‘single-gate’, ‘dual-gate’, MS/MS and precursor ion scan methods. Using a combination of these modes, we unambiguously identify all signals in the IMS spectra, including previously uncharacterized minor peaks arising from compounds that are common in raw opium.

2.2 Introduction

Cross-border transport of illicit materials is a continuing threat to public safety and a persistent challenge to border protection and law enforcement agencies. Global production of opium averaged 4,600 tons in 2013[308], with opium drug seizures totaling to 179 kg in Canada in the same year.[309] Opium is a partially dried extract of the poppy plant *Papaver Somniferum*. Morphine, codeine, thebaine, papaverine and noscapine are all present in opium in high abundance, on average between 1% to 10% of dry mass.[310,311] Many analytical techniques have been developed for detection of opium using these markers, such as thin-layer chromatography (TLC)[312–316], gas chromatography (GC)[317,318], liquid chromatography (LC)[310,319–321], capillary electrophoresis[322,323], radioimmunoassay[324], ion mobility spectrometry (IMS)[325–327], and mass spectrometry (MS)[328–331]. In the field, more than 15,000 Trace-Compound Detectors (TCDs) have been deployed at security checkpoints worldwide in order to combat international trafficking of illicit materials, and to enhance national security.[25,26] These systems are ideal for the on-site detection of a wide array of specific targets at trace levels, as they combine straightforward operation and field-robustness with limits of detection in the picogram to nanogram range.[334] However, the Ion Mobility Spectrometry (IMS) technologies that underlie these devices operate at relatively low resolution and provide limited capabilities in terms of de-novo compound identification.[335] In the present study, we introduce an improved TCD-IMS-MS instrument that combines high TCD sensitivity with mass spectrometric selectivity, allowing for the unambiguous identification of virtually all peaks within a complex IMS profile generated by seized opiate samples.

Ion mobility emerged early on as a detection method for narcotics[336], and developed rapidly as a field technique for illicit drug detection.[337] In these early investigations, sample vapors were introduced in a "gas chromatography-like" manner, where a wire, syringe, flask, or tube was heated at high temperature to volatilize the analyte of interest into the ion mobility spectrometer.[338,339] Thermal desorption remains the volatilization method of choice for in-field ion mobility analysis because it is fast, compact, requires no complex sample preparation, and is able to vaporize residues collected from human skin and aqueous media with relative ease.[340,341] Gas-phase ions can then be generated through a series of ion/molecule reactions using a ^{63}Ni radioactive source, and subsequently separated by IMS.[332] Most TCDs use a drift-cell IMS design in which compounds are identified based on the time required for an ion to traverse a fixed-length cell containing an inert buffer gas at near-atmospheric pressure under the influence of a constant electric field. Drift-time measurements are often normalized to standard gas density, giving the reduced mobility constant K_0.[342,343]

There have been a number of studies involving narcotics characterization by IMS-MS, with substantial contributions by Karasek and Hill[344] in the 1970s and the Lawrence group in the 1980s.[338,340,345] Sample introduction and ionization methods such as corona discharge[346], photoionization[347], secondary electrospray ionization (SESI)[348], laser desorption[349], MALDI[350,351], desorption ESI[352], and electrospray ionization[353] have all been used for IMS-MS analysis of narcotics. Hill and coworkers have demonstrated separation of opiates and their primary metabolites using a state-of-the-art, high-resolution ESI-IMS-MS instrument, but the main focus was limited to purified morphine, codeine and their metabolic products.[325] To our knowledge, no detailed IMS-MS study is available on the

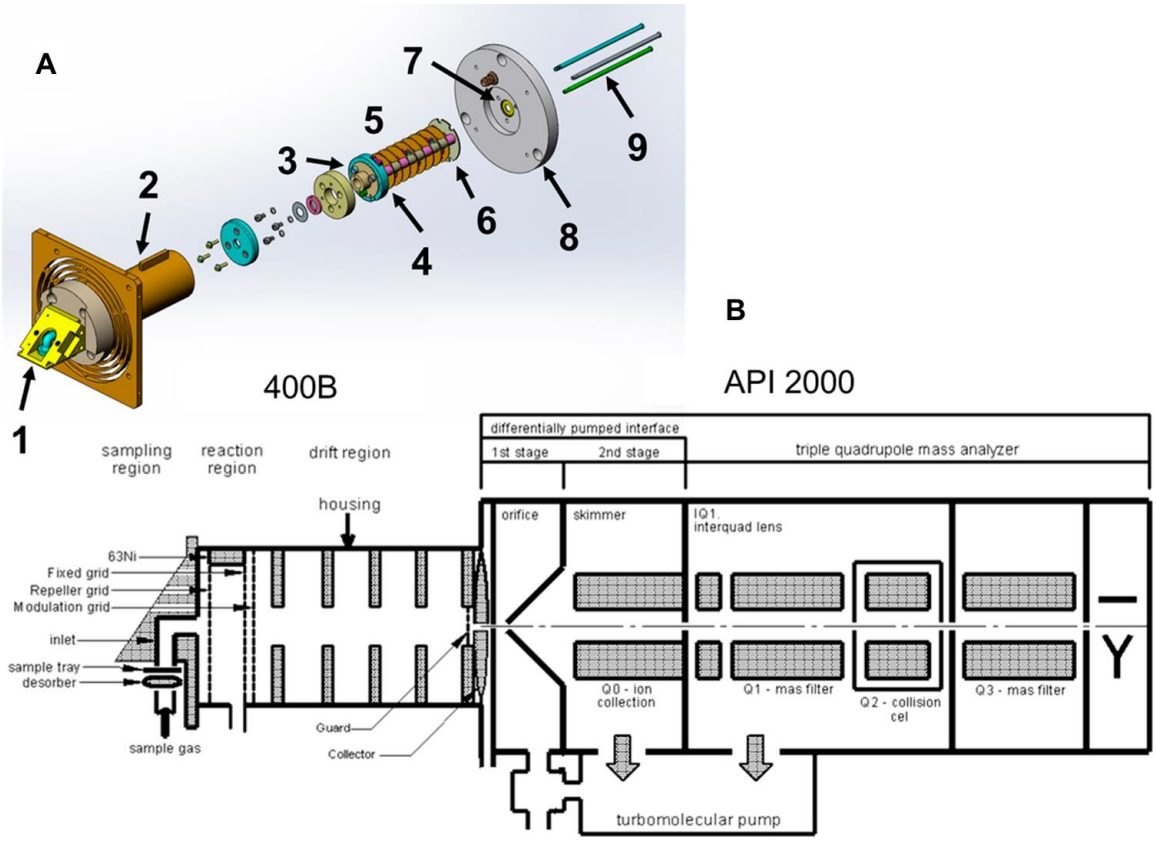

Figure 16. (A) SolidWorks® exploded-view design of the modified 400B IMS cell with the interface to the API 2000. 1− heated inlet; 2 − IMS chamber; 3 − ^{63}Ni; 4−first ion gate; 5 − drift region; 6 − guard; 7 − collector/second ion gate; 8 − interface flange; 9 − threaded supporting rods. (B) Schematic depiction of the hybrid TCD-IMS-MS instrument.

complex mixtures of opiates that are regularly seized by law enforcement.

The aim of this work is to improve selectivity in IMS-based TCDs by direct coupling to an API 2000 triple quadrupole mass spectrometer (Figure 16) and to provide a detailed TCD-IMS-MS characterization of 'real-world' narcotics samples.[354] The instrument design draws on previous work by Kozole and co-workers[355], but incorporates a ten-fold increase in sensitivity for ion detection by IMS, the ability to generate mobility spectra by native Faraday plate detection and the capacity for positive ion-mode measurements. We demonstrate that the new TCD-IMS-MS system enables unambiguous identification of compounds contributing to virtually all ion mobility peaks in complex samples. Our results represent a significant step towards the development of 'field-ready' TCD-IMS-MS instrumentation, and the newly identified IMS peaks can ultimately be incorporated into improved detection algorithms for contraband detection, thus reducing the false alarm rate.

2.3 Experimental

2.3.1 Sample Preparation

Diluted solutions of seized opium samples were obtained from the CBSA. Seized opium samples were dissolved in one-part methanol and three-parts chloroform. The same solvent system was used for the alkaloid standards as well as for comenic, meconic and pyroglutamic acids standards. All samples were prepared by depositing 1µL of diluted solution of opium and alkaloid standards onto a NOMEX swab (Smiths Detection, Mississauga, Ontario, Canada) and allowed to dry for at least 30 seconds prior to analysis. Typical concentrations of the compounds of interest varied from 100 ng/µL to 2000 ng/µL based on the response of the IMS-MS system.

2.3.2 Instrumentation

In the IONSCAN 400B (Smiths Detection, Mississauga, Ontario, Canada), ions are generated using APCI driven by fast electrons produced from radioactive decay of ^{63}Ni. This ionization mechanism produces positively and negatively charged analytes, with an efficiency that is dependent on the absolute difference in proton affinity between the analyte and the activated reagent gas. Ions are then pulsed into the drift cell and detected using a Faraday plate.[355,356] For this study, ion mobility spectra of all compounds were recorded on a standard IONSCAN 400B system as described previously.[357,358] Swabs were introduced into the IONSCAN 400B IMS system and heated to 224°C, thermally desorbing the analytes Samples were analyzed for a total of 8 s (positive ion mode) and 7.5 s (negative ion mode), and acquired using the standard 400B software.

All IMS-MS experiments were performed on a 400B IMS that was mounted directly in front of the orifice of an AB SCIEX API 2000 Triple quadrupole mass spectrometer. The custom-made mechanical interface between the two systems was similar to the interface described by Kozole, but with a number of changes (Figure 16).[355] Details on hardware modifications can be found in Appendix A.

2.3.3 Ion Mobility Mode (standard operation of IONSCAN 400B)

In the ion mobility mode (IMS mode), the first of two ion gates was opened for 200-μs to allow a packet of ions to move into the drift region of the IMS instrument and towards the Faraday plate. The Faraday plate was used to measure current signal. Earlier designs of IMS-MS instruments have made use of Faraday plate ion detection[359–361], however the previous IONSCAN 400B – Triple quadrupole MS system relied on the mass spectrometer in ion transmission mode to record a mobility spectrum.[355] This allows for the acquisition

of '*m/z* selective' mobility spectra, and is an option on our setup, but results in a significant (i.e., roughly factor of 10) loss of sensitivity.[355]

Apart from where stated otherwise, the IONSCAN was operated under standard conditions in both standalone and IMS-MS experiments. Specifically, for positive mode: Drift tube temp. = 220 ºC; inlet temp. = 240 ºC; desorber temp. = 225 ºC; drift gas flow = 350 cc/min; drift field = 253 V/cm; drift cell pressure = 760 Torr; and for negative mode: Drift tube temp = 115 ºC; inlet temp = 240 ºC; desorber temp = 225 ºC; drift gas flow = 300 cc/min; drift field = 253 V/cm; drift cell pressure = 760 Torr. The length of the drift cell was 6.8 cm. Background control scans for the 400B were recorded using a blank NOMEX swab with an internal calibrant, nicotinamide, injected with the reagent gas (Figure 17A). The reduced mobility of the nicotinamide was calculated as 1.86 $cm^2V^{-1}s^{-1}$ using the following equation:

$$K_0 = \frac{L}{t_D E} \times \frac{273.15}{T} \times \frac{P}{760} \tag{20}$$

Where L is the drift length (6.8 cm), E is the electric field strength (253 V/cm), T is the temperature of the drift cell (493 K), and P (≈ 760 Torr) is the pressure in the drift region of the IMS instrument.[362] This value was used to calculate all other K_0 values by the following equation:

$$K_0 = \left(\frac{t_d^{cal}}{K_0^{cal}}\right) / t_d \tag{21}$$

Where t_d^{cal} is the drift time of the internal calibrant, K_0^{cal} is the reduced mobility of the internal calibrant, and t_d is the drift time of the ion of interest.[363]

2.3.4 Continuous Ion Flow

In the continuous ion flow mode, both ion gates in the IMS instrument are open continuously. In negative mode the first ion gate is held at -1800 V and the collector which functions as the second ion gate is held at -100 V. The voltages for positive ion mode are 1570 V (gate) and 65 V (collector), permitting the ions formed in the reaction region of the IMS instrument to pass into the mass spectrometer.

2.3.5 Selected Mobility Monitoring Dual Gate

In the selected mobility monitoring mode, the first ion gate is opened for 200 – 1000 μs to allow a packet of ions into the drift region of the IMS instrument while the second ion gate is opened for one ms after a specific time delay. The time delay is selected to permit only a selected portion of the ion packet with a particular mobility range to pass into the mass spectrometer. This mobility-filtered ion population is analyzed by the mass spectrometer. The stopping potentials applied to the first and second gates were - 1824 V and - 120V in negative ion mode and 1590 V and 95V in positive ion mode respectively.

2.3.6 Orbitrap Elite

Samples and standards were analyzed on an Orbitrap elite mass spectrometer (Thermo Scientific, Massachusetts) in both positive and negative modes, using the standard commercial heated electrospray ionization (HESI) source. Spectra were generated using the Orbitrap mass analyzer at 240000 resolution setting. MS^2 and MS^3 experiments were done using the Orbitrap, while the linear ion trap was used for collision-induced dissociation (CID) experiments that required the mass window to start at 50 *m/z*. Ions were subjected to fragmentation using normalized collision energy, with instrument defined setting between 20% and 40%.[358,359]

2.4 Results and Discussion

In order to characterize instrument performance and identify compounds associated with mobility peaks in complex, 'real-world' samples, a set of four seized opium samples (hereafter referred to as Opium A, B, C and D), as well as standard solutions of morphine, codeine, thebaine, papaverine noscapine, meconic acid, comenic acid and pyroglutamic acid were subjected to a full set of IMS-MS experiments. Mobility spectra, open gate, and dual-gate mass spectra were obtained for all opium samples and standards, in both positive and negative modes. Product ion and precursor ion information was also used to confidently identify peaks from their fragmentation patterns of the precursor ions.

2.4.1 Positive Ion Mode.

Mobility spectra of Opium A showed a complex series of signals, with major peaks at K_0 = 0.985, 1.040, 1.142, and 1.443 $cm^2V^{-1}s^{-1}$. The other opium samples produced the same four IMS peaks, but with significantly varying relative signal intensity (Appendix A, Figure A-1), which is to be expected due to their diverse origin. Standards of the most common constituent alkaloids found in opium were also analyzed by an unmodified IONSCAN 400B TCD (Figure 17A). A complete list of reduced mobility values and the resolving powers for each of the standards are reported in Table A-1 of Appendix A. From a cursory analysis of the data shown in Figure 17A, it is evident that thebaine, papaverine and noscapine are present in higher amounts, while morphine and codeine are present in lower amounts in the seized opium samples.

2.4.1.1 IMS-MS Ion Mobility

Alkaloid standards were analyzed by the IMS-MS system to verify that the mobility spectra generated are comparable to those from the standalone IONSCAN 400B (Figure

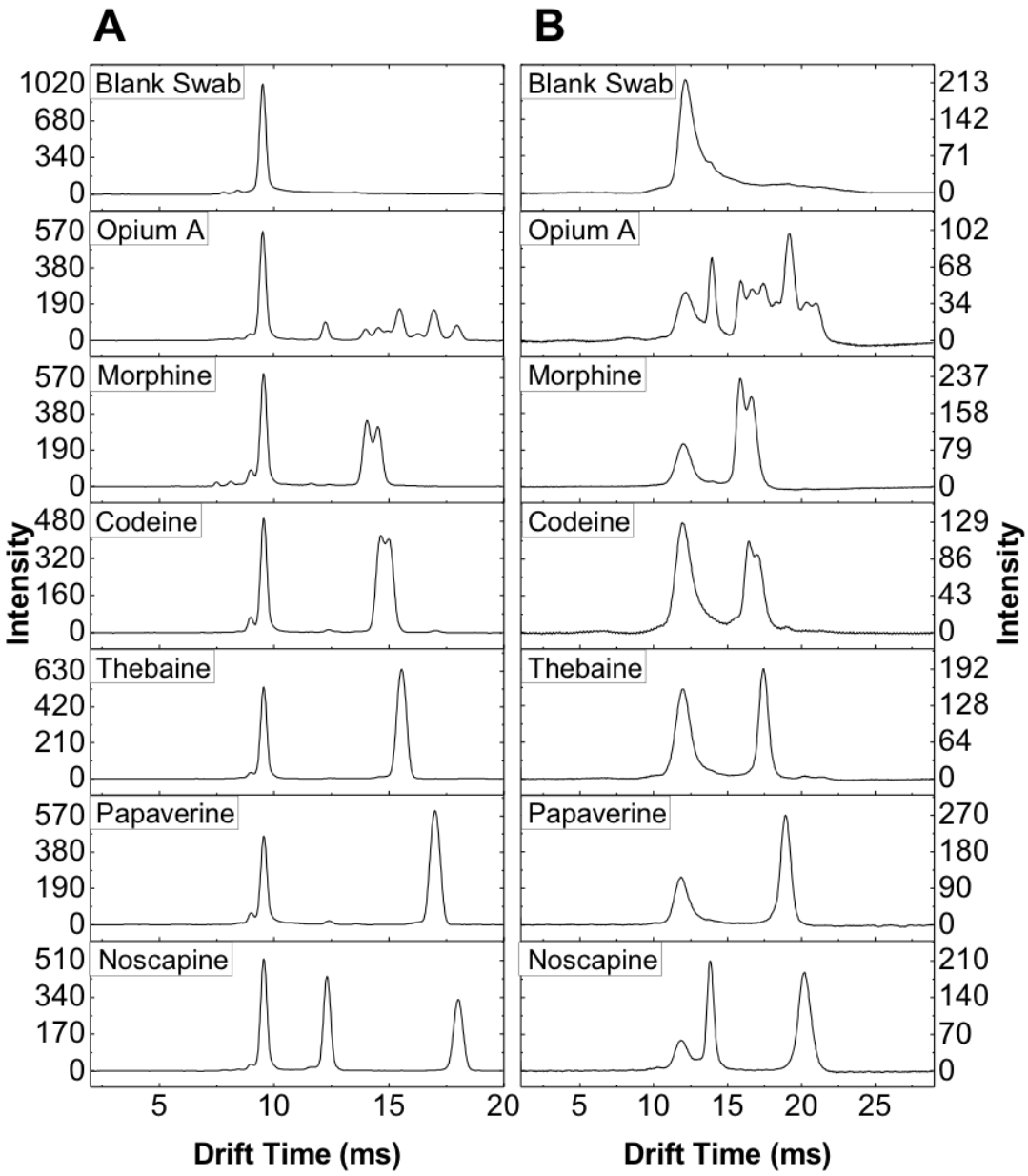

Figure 17. (A) Positive ion mode mobility spectra of the background, swab, seized Opium A and alkaloid standards run on the stand-alone IONSCAN 400B. (B) Positive ion mode mobility spectra obtained on the IMS-MS system. The drift time window was extended to account for the peak broadening.

17B). The IMS spectrum for opium A, shown in Figure 17B, exhibits a peak pattern similar to a spectrum obtained on an unmodified IONSCAN 400B, with slightly lower resolution (a decrease in resolution in positive mode by 25% compared to the stand-alone system) and slightly shifted reduced mobility values. These differences are attributable to the collector-Faraday cup distance being greater than a standard IONSCAN 400B, and a temperature gradient inside the IMS due to the substantial difference in temperature between the drift cell (~ 220°C) and the front end of mass spectrometer (~ 115°C). IMS-MS mobility spectra of the remaining three opium samples can be found in Figure A-2 of Appendix A.

2.4.1.2 Compound Identification

Mass spectra were acquired for all seized opium samples in the open-gate mode. (Appendix A, Figure A-3 to A-6). The spectra were obtained by first delaying desorption for 5 seconds to acquire a baseline background, and then desorbing for 30 seconds afterwards. Standard ions (i.e., those currently used to identify contraband in the 400B based on their mobility profiles) were easily identified and are listed in Table A-1 of Appendix A.

Product ion scans were compared between the seized opium samples and standard solutions of morphine, codeine, thebaine, papaverine, and noscapine using the IMS-MS system. Fragmentation patterns for the opium samples and standards were comparable, and helped identify various peaks from the open-gate MS spectra (Appendix A, Figure A-7 to A11). The MS and MS/MS data obtained from the IMS-MS system were verified with full scan exact mass MS and product ion scans of the opium samples and standards on an Orbitrap instrument (data not shown). Collision induced dissociation experiments for

morphine[364,365], codeine[365], thebaine[364], papaverine[366], and noscapine[367] from the literature were also in good agreement, adding confidence to the peak assignments listed in Table A-2 of Appendix A.

In addition to the pharmacologically active species conventionally used to identify opium, a number of new ions were identified by making use of the scanning capabilities of the API 2000. A precursor ion scan of the peak at 220 *m/z* identified the precursor ion as noscapine. This was confirmed by fragmentation of the 414 *m/z* precursor ion, which showed 220 *m/z* as a major fragment. Both precursor and fragment ions masses have been described before in the literature.[368] Fragmentation (MS/MS) of the peak at 428 *m/z* yields product ions that match the literature for N,N-dimethylnarcotine ($C_{23}H_{26}NO_7$), which was also confirmed by accurate mass measurements on the Orbitrap.[369] The ion at 330 *m/z* has been identified as reticuline ($C_{19}H_{23}NO_4$). MS/MS spectra from both the IMS-MS and FTMS for opium show similar fragment ions when compared to the literature.[370] MS/MS spectra from both the IMS-MS system and Orbitrap identify 370 *m/z* as cryptopine ($C_{21}H_{23}NO_5$), as described before.[371] The relationship between opium poppy and the alkaloids N,N-dimethylnarcotine, reticuline, and cryptopine has been previously established and is not the result of chemical interferences in the seized samples.[372] The peak at 268 *m/z* occurs as a loss of water from morphine[364], and similarly water loss from codeine also accounts for the ion at 282 *m/z*.[373]

2.4.1.3 Dual-Gate Experiments

In dual-gate mode, a second gating pulse is applied at a delay time which transmits ions of precise mobility values to the mass spectrometer, providing the capability to specifically link an ion mobility and *m/z* values. The first gating pulse was set to a width

of 1.0 ms, while the second pulse width was set to 0.5 ms. The delay time between the first and second pulses was set to correspond to mobility peaks with K_0 values of 0.985, 1.040, 1.142, and 1.443 $cm^2V^{-1}s^{-1}$, the results of which can be seen in Figure 18. The peak at K_0 = 0.985 $cm^2V^{-1}s^{-1}$ is monitored at four slightly different delay times, creating a drift time versus intensity 'profile' for the mobility peak. The four mass spectra represent the sum of the ions over a 30 s desorption for each delay time. Measurements taken at 21.9 ms inter-pulse delay identify noscapine (414 *m/z*) as the most abundant ion. As the delay time increases, however, noscapine decreases in intensity while N,N,-dimethlynarcotine at 428 *m/z* increases. Other mobility peaks show even greater complexity. Dual gate mass spectra for the mobility peak at K_0 = 1.040 $cm^2V^{-1}s^{-1}$, for instance, reveal a number of contributing ions with varying intensity, with the most abundant being papaverine (340 *m/z*). A similarly complex mobility peak at K_0 = 1.142 $cm^2V^{-1}s^{-1}$ shows thebaine (312 *m/z*) as the most intense ion whereas the peak at K_0 = 1.443 $cm^2V^{-1}s^{-1}$ is attributable exclusively to the 220 *m/z* fragment of noscapine.

Notably, a number of lower intensity ions are detected by the mass spectrometer, but are not directly observed in the IMS mobility spectrum due to their low abundance in the sample and limited resolving power of IMS. Dual-gate mass spectra can, in some cases accurately assign K_0 values to low-intensity ions by recording the ion intensity at different delay times. As the delay time in the second gate is varied, the ion's intensity will increase or decrease. This trend can be fit to a Gaussian curve, and thereby obtaining a K_0 value from the peak maximum. For example, reticuline (330 *m/z*) is detected in the K_0 = 1.040 $cm^2V^{-1}s^{-1}$ 'scanset' and the K_0 = 1.142 $cm^2V^{-1}s^{-1}$ 'scanset' (Figure 18), with a maximum intensity at an extracted drift time of 19.6 ms. The reduced mobility for reticuline in seized

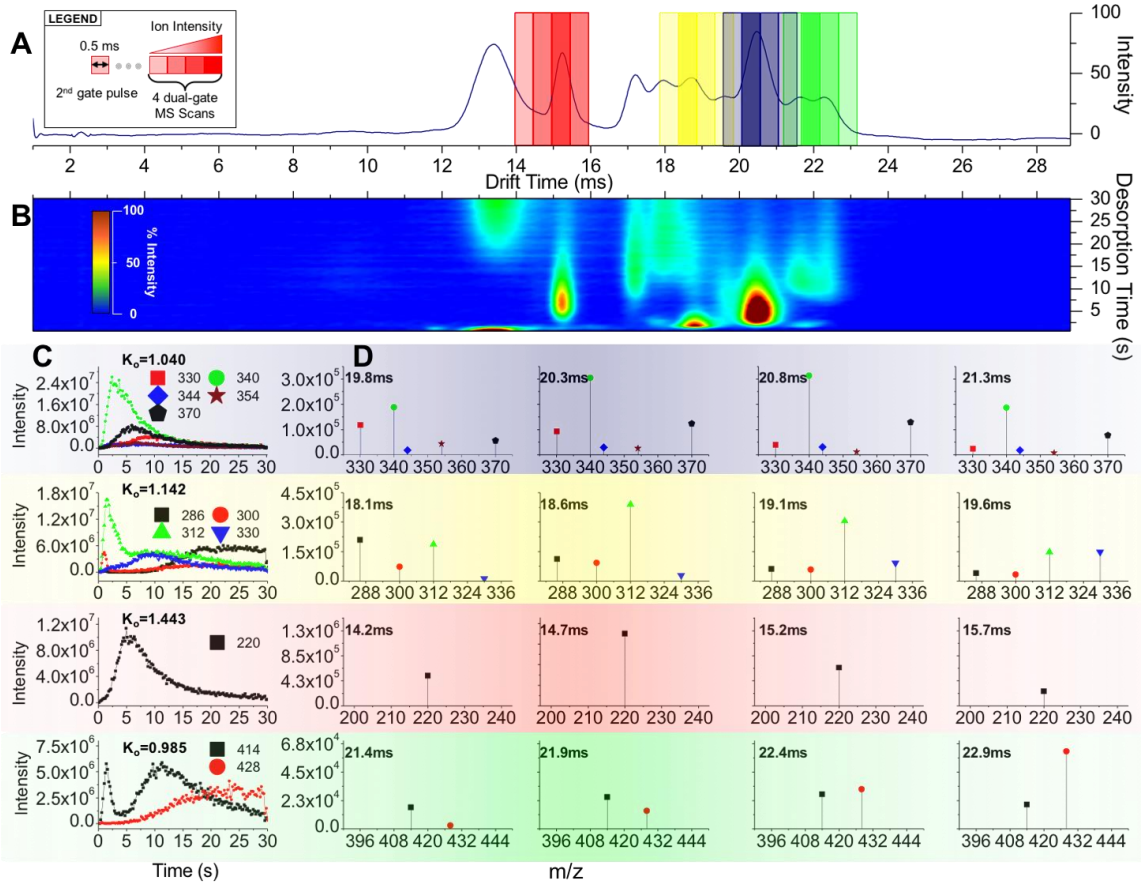

Figure 18. Positive ion mode IMS-MS characterization of Opium A. Each shaded window on the mobility spectrum (A) represents a time-selected slice of the ion packet that is allowed to enter the mass spectrometer−a feature of dual-gate mode. (B) A heat-map of the desorption/mobility profile for Opium A.(C) Time-dependent desorption profiles for ions contributing to specific reduced mobility peaks. (D) Mobility-dependent mass spectra showing the ion composition underlying the shaded regions in panel (A).

opium is therefore reported as K_0 = 1.091 $cm^2V^{-1}s^{-1}$. Similarly, the extracted drift time for cryptopine (370 *m/z*) is 20.6 ms, corresponding to a K_0 of 1.032 $cm^2V^{-1}s^{-1}$.

2.4.2 Negative Ion Mode

In the negative ion mode characterization experiments**,** a unique mobility peak from the seized opium samples was observed, at K_0 = 1.187 $cm^2V^{-1}s^{-1}$.

2.4.2.1 Ion Mobility Spectroscopy

Mobility spectra for opium and alkaloid standards were acquired in the negative mode on the IONSCAN 400B (Figure A-25 and A-26, Appendix A). All opium samples show a major peak at 1.187 $cm^2V^{-1}s^{-1}$, which coincides with the Tetryl-N channel (programmed K_o 1.189 $cm^2V^{-1}s^{-1}$). This negative ion was also present in a seized opium sample analysis conducted by the CBSA using a later version IONSCAN instrument (data not shown). Morphine, codeine, thebaine, papaverine, and noscapine standards did not exhibit the peak seen in the seized samples.

2.4.2.2 Compound Identification

Open-gate mass spectra of opium revealed a number of ions that are unrelated to the common alkaloids seen in the positive mode. Figure 19 shows the open-gate spectrum for Opium A, as well as several CID spectra for the major ions present. The same ions were observed in all other seized opium samples run in negative ion mode. Collision-induced dissociation experiments for the ions at 311, 291, and 284 *m/z* all show the presence of a product ion at 155 *m/z*. In order to confirm 155 *m/z* is the same ion seen in the open-gate mass spectrum, a precursor ion scan of 155 *m/z* was carried out, indicating that it is clustering with 3 of the major peaks: 284 *m/z*, 291 *m/z* and 311 *m/z*. An extensive literature

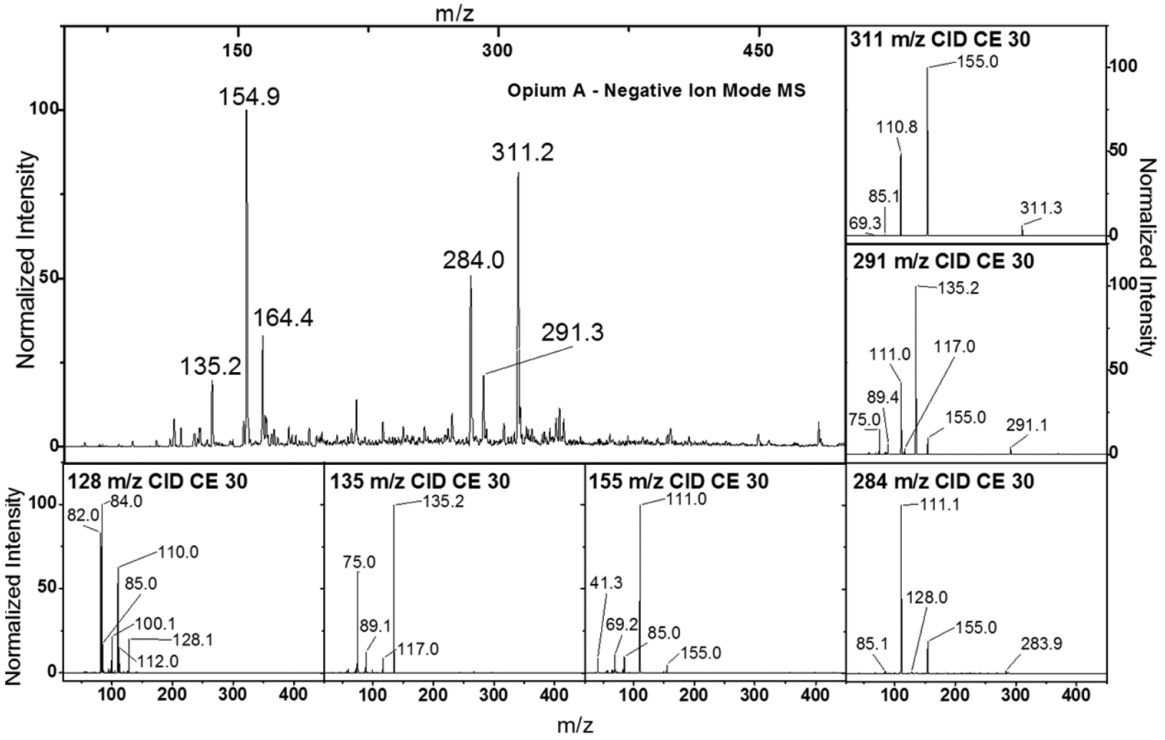

Figure 19. Main panel: negative ion mode open-gate spectra of Opium A. Subpanels show tandem MS spectra of the major MS peaks. MS/MS data from opium was compared to a database, along with tandem MS data from standards, to identify ions of interest.

and database search provided no structural information on the 155 *m/z* ion. Opium samples analyzed via electrospray ionization on the Orbitrap revealed a peak at 154.99854 *m/z*. An empirical formula for the ion ($C_6H_4O_5$) was obtained with mass accuracy of -0.3 ppm, along with tandem MS data identifying it as comenic acid.

Another ion detected at 198.98864 *m/z* ($C_7H_4O_7$, mass accuracy of 1.1 ppm) was a match for poppy acid, also known as meconic acid.[374] CID experiments on meconic acid give a major peak at 155 *m/z*. MS^3 on the 155 *m/z* fragment appearing in meconic acid matches the fragmentation pattern for the MS/MS of 155 *m/z* from comenic acid. The relationship between meconic acid and comenic acid involves the temperature-dependent decarboxylation of meconic acid to produce comenic acid as a major product at 160°C for one hour.[375] Temperatures in the desorber and inlet are set at 224°C and 240°C respectively in commercial IONSCAN 400B instruments operating in Explosives Mode (Negative ion Mode), and may be responsible for the decarboxylation, along with degradation during the opium samples' production, storage and transfer. Nevertheless, the absence of 199 *m/z* in the open-gate spectra for opium on the IMS-MS system, and its presence in the electrospray mass spectrum acquired on the Orbitrap suggests that meconic acid underwent decarboxylation during the desorption process.

Open-gate and CID mass spectra of comenic acid and meconic acid standards were compared to the opium samples, and confirm the origin of a number of ions present in Figure 20B. The ion at 311 *m/z* can now be identified as a comenic acid dimer. MS/MS of 284 *m/z* (Figure 19) shows 155 *m/z* as the major peak with a neutral mass loss of 129 amu. The 128 *m/z* ion is identified with relatively low abundance on the API 2000; therefore CID experiments on 128 *m/z* were performed on the Orbitrap. A database search using

exact mass and MS/MS spectra of 128 *m/z* identify pyroglutamic acid as the ion forming a complex with comenic acid. Pyroglutamic acid is a commonly occurring amino acid derivative of glutamic acid, and can form pyroglutamic acid when heated.[73] Glutamic acid was not observed in the ESI mass spectra of opium in either positive or negative modes, suggesting pyroglutamic acid is naturally occurring in opium, as it is in many other plant species.[376–378] This was confirmed with open-gate and MS/MS of a standard pyroglutamic acid solution on the IMS-MS system and on the Orbitrap, suggesting that the peak at 284 *m/z* is a complex of comenic acid and pyroglutamic acid. Fragmentation of 291 *m/z* shows comenic acid, with a neutral loss of 136 amu (Figure 19). The ion at 135 *m/z* was fragmented in both the IMS-MS and the Orbitrap, and MS/MS spectra match the database for threonic acid. The presence of threonic acid in opium occurs primarily from the degradation and oxidation of long-chain carbohydrates.[379] The peak at 291 *m/z* is identified as complex of comenic acid and threonic acid.

Standards of comenic acid, meconic acid, and pyroglutamic acid were run on a standalone IONSCAN 400B to identify their reduced mobility values (Figure 20A), as well as on the IMS-MS system to characterize their IMS-MS profiles (Figure 20B). Notably, by mixing pyroglutamic acid and comenic acid standard solutions 1:1, a peak with K_0 = 1.18 $cm^2V^{-1}s^{-1}$ was observed in the negative mode, coinciding with the Tetryl-N channel. The PETN-C alarm channel is triggered for the comenic acid dimer at 311 *m/z*. Dual-gate experiments of the opium samples were conducted to confirm 284 *m/z* is related to the peak at 1.18 $cm^2V^{-1}s^{-1}$. To our knowledge, mass-identified reduced mobility values for these compounds are being reported here for the first time. The findings are summarized in Table A-3 of Appendix A.

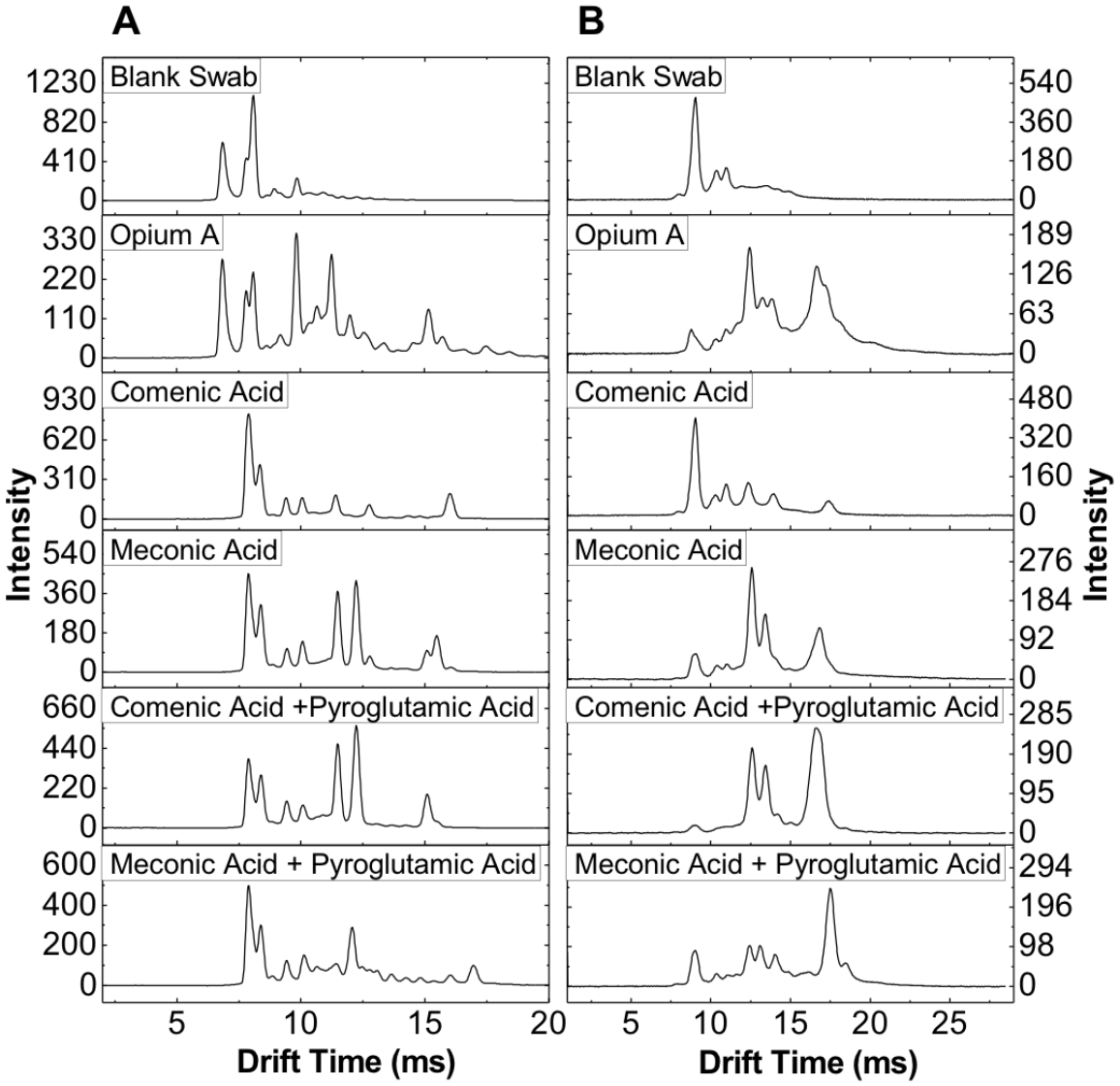

Figure 20. (A) Negative mode mobility spectrum of Opium A showing the peak at 1.18 $cm^2V^{-1}s^{-1}$. Standards of comenic acid, meconic acid and their mixtures with pyroglutamic acid respectively are also shown. The peak of interest is reproduced in the comenic acid pyroglutamic acid mobility spectrum, as well as in the meconic acid pyroglutamic acid mobility spectrum at a lower abundance. (B) TCD-IMS-MS mobility spectra for Opium A and acid standards.

2.4.2.3 Dual-gate Experiments

Dual-gate interrogation of the 1.18 $cm^2V^{-1}s^{-1}$ peak in opium involved five separate acquisitions at 17.3 ms, 17.8 ms, 18.3 ms, 18.8 ms, and 19.3 ms delay times (Figure 21). The same gating conditions used for both positive and negative modes, with the first gate pulse width set to 1 ms and the second gate pulse width set to 0.5 ms. From both the extracted ion chromatogram (XIC) plots acquired in open-gate experiments and the dual-gate spectra, the two most intense ions are 284 *m/z* and 311 *m/z*. The highest intensity for the 284 *m/z* [pyroglutamic acid • comenic acid] cluster occurs at a delay time of 18.3 ms, which lies at the mobility peak maximum K_0 = 1.18 $cm^2V^{-1}s^{-1}$. The highest intensity for the 311 *m/z* comenic acid dimer occurs at a delay time of 18.8 ms, where a small but visible shoulder to the right of the main peak is present. The lower intensity 291 *m/z* and 303 *m/z* peaks could not be analyzed due to their low intensity in the IMS-MS spectrum. We summarize the significant information gained by characterizing opium in negative ion mode in Table A-4 of the Appendix A.

2.5 Conclusions

The use of an enhanced IMS-MS system for the elucidation of spectral detail in IMS spectra has been demonstrated. The system allows unambiguous identification of ions generated from complex mixtures, shown here using seized opium samples. Among the advantages of this tool is the ability to monitor the evolution of the sample during thermal desorption by both ion mobility spectrometry and mass spectrometry. Numerous analytical modes were demonstrated, each providing additional data for conclusive identification of unknown peaks in the mobility spectra. Open-gate MS and MS/MS provided a robust method for identifying compounds in complex spectra generated from ^{63}Ni sources. Single-

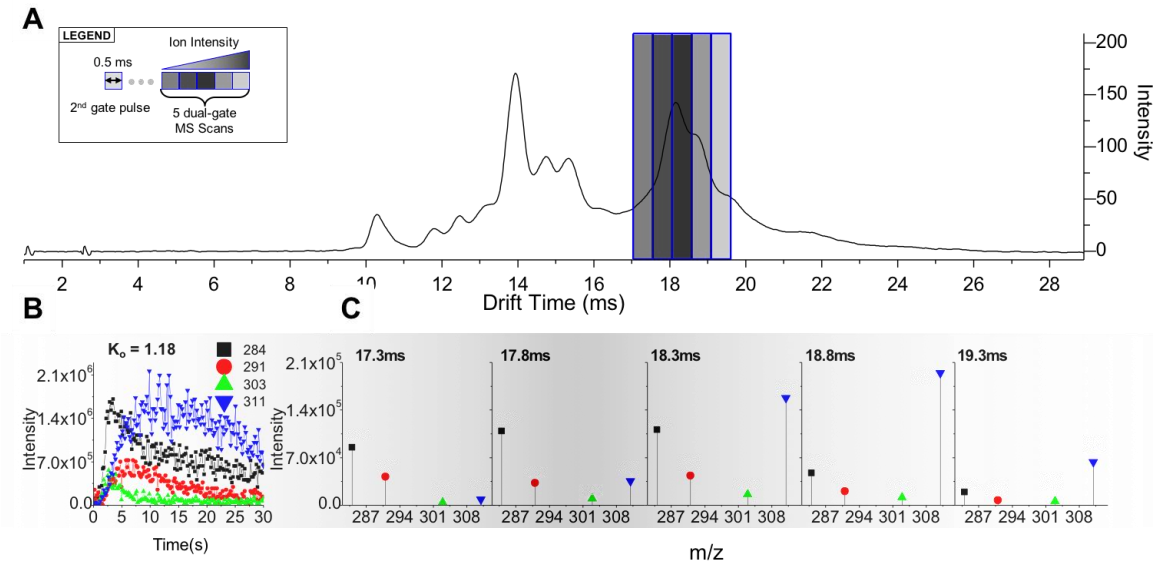

Figure 21. Negative ion mode IMS-MS characterization of Opium A. Each shaded window on the mobility spectrum (A) represents a time-selected slice of the ion beam that is allowed to enter the mass spectrometer. (B) Time-dependent desorption profiles of ions contributing to the K_0 = 1.18 mobility peak. (C) Mobility-dependent mass spectra showing the composition of the shaded region in panel (A).

gate experiments confirmed the relationship between reduced mobilities of the major compounds in opium to those from samples obtained in-the-field. Dual-gate experiments were able to correlate virtually all of the many mobility peaks generated from seized opium with mass spectral data. From these experiments, the four IMS peaks in positive ion mode with reduced mobility values of 0.985, 1.040, 1.142, and 1.443 $cm^2V^{-1}s^{-1}$, were found to correspond to noscapine, papaverine, thebaine, and a fragment of noscapine, respectively. In the negative mode, the peak at 1.18 $cm^2V^{-1}s^{-1}$ is attributed to a [pyroglutamic acid • comenic acid] complex. While confirmation of the presence of analytes known from the literature is shown to be relatively straightforward, identification of novel compounds that evolve only during thermal decomposition can be challenging, requiring a combination of several IMS/MS methods and confirmatory experiments using pure standards.

The ion characterization knowledge acquired from this study can be used to improve the detection algorithms in commercial IMS-based TCDs for enhanced sensitivity and selectivity. In particular, we have characterized the in-source formation of comenic acid from poppy acid, and its subsequent dimerization and complexation with pyroglutamic acid, which represents a unique chemistry and a strong analytical marker for opium in negative mode TCD-IMS. A thorough understanding of the behavior of highly complex drug mixtures using the current trace-detector instrumentation is a feature of the IMS-MS system described. These insights will allow the introduction of novel markers for on-site detection of illicit narcotics and the instrumentation represents a significant step towards unambiguous detection of illegal substances in the field.

Chapter 3

Comparing Equilibrium And Kinetic Protein Unfolding Using Time-Resolved Electrospray-Coupled Ion Mobility Mass Spectrometry

A version of this chapter was published in Analyst:

Liuni, P.; Deng, B.; Wilson, D. J. Comparing Equilibrium and Kinetic Protein Unfolding Using Time-Resolved Electrospray-Coupled Ion Mobility Mass Spectrometry. Analyst 2015, 140 (20), 6973–6979.

3.1 Summary

Protein unfolding intermediates are thought to play a critical role in conformational pathogenesis, acting as a ‘gateway’ to inactivation or pathogenic aggregation. Unfolding intermediates have long been studied either by populating partially-folded species at equilibrium using increasingly denaturing conditions, or by transiently populating ‘kinetic’ intermediates under fully denaturing conditions using a time-resolved approach (e.g. stopped-flow fluorescence). However, it is not clear that the folding intermediates populated under equilibrium conditions are comparable to intermediates transiently populated in kinetic experiments. In this work, we combine time-resolved electrospray (TRESI) with travelling wave Ion Mobility Spectrometry (IMS) for the first time to directly compare equilibrium and kinetic unfolding intermediates of cytochrome c. Our results show a high degree of correlation between all species populated under these substantially different regimes.

3.2 Introduction

The mechanisms of protein (un)folding are a long-standing challenge in structural biology.[380,381] Intermediates that arise along the folding pathway are directly linked to the fundamental question of how proteins adopt their ‘native’ conformations from the initially unstructured polypeptide that is generated from the ribosome.[382,383] Unfolding intermediates are often linked to pathogenesis,[384,385] acting as a gateway between the functional ‘native’ configuration and inactive or amyloidogenic conformations. However, these protein intermediates are challenging to study as they are often transient, weakly populated at equilibrium and spectroscopically similar to the ground-state.[386,387]

Experimental efforts to study unfolding intermediates in vitro typically involve equilibrium perturbation of protein structure over a range of denaturant concentrations.[388,389] The advantage of populating unfolding intermediates in this way is that the sample is at equilibrium, allowing an unlimited time for analysis. Thus, it is possible to apply a wide range of analytical techniques including fluorescence,[390] SAXS[391] and notably NMR,[392] which can sometimes provide a highly detailed structural picture. However, it is not clear that species populated under a range of solvent conditions represent true unfolding intermediates, since each is a reflection of a unique conformational energy landscape.[386,388,393] An alternative is to employ rapid mixing techniques to transiently populate unfolding intermediates under a single set of strongly denaturing conditions. In this case, the unfolding process is driven by a single, rapid change in the conformational landscape (e.g. due to pH jump[393] or rapid addition of denaturant[394]), and proceeds under constant conditions. This 'kinetic' approach may be more likely to generate biologically relevant intermediates, but it also presents substantial analytical challenges, since intermediates appear only for exceptionally short periods (often milliseconds or less) after mixing.[386,387] As a result, analytical options for kinetic experiments are much more limited and the field is dominated principally by fluorescence-based approaches.[395] Time-resolved Electrospray Ionisation Mass Spectrometry (TRESI-MS) was introduced as an alternative to optically-based stopped-flow rapid mixing experiments.[396–398] The principle advantage of TRESI is the ability to monitor virtually all reactive species simultaneously in millisecond time-resolved kinetic experiments.[397] TRESI has been used in a wide range of applications, from simple organic reactions[399] to enzyme catalysis[400] and protein folding.[401–403] In isolation, TRESI provides limited structural information about protein

analytes, although a coarse-grained picture can be achieved by monitoring the electrospray charge-state distribution.[404] A more detailed picture can be achieved by combining TRESI with Hydrogen/Deuterium exchange (HDX),[405,406] however, such experiments are unsuitable for pH-jump unfolding measurements due to the pH dependence of HDX kinetics.

Ion Mobility Spectrometry (IMS) is a relatively new addition to the commercially-available mass spectrometry tool-kit.[407–409] The basic principle of IMS is spatio-temporal separation of gas-phase ions using low-energy collisions with a neutral gas. In most IMS techniques, retardation of ions traversing the IMS cell is directly proportional to their collision cross section, which is function of volume and shape.[407–409] The most straightforward implementation of IMS is the 'drift tube' in which ions traverse a high pressure cylindrical cell under the influence of a constant, relatively weak electric field. In travelling-wave ion mobility setups, ions are 'swept' through a high pressure cell by electric field 'waves' generated by successively applying a potential to a series of ring ion guides. Mobility separation can be optimized by adjusting the wave height and frequency.[410] It is also possible in most cases to calculate collision cross sections from travelling-wave mobility data, often with use of an internal calibrant.[411]

In the present study we combine TRESI-MS with travelling wave IMS to investigate equilibrium and kinetic unfolding intermediates of cytochrome c. Cytochrome c provides an ideal model for this study because it has been extensively characterized by TRESI[401] and IMS-MS[412] independently. Our principal aim is to demonstrate the TRESI-IMS-MS approach as a powerful tool for characterizing kinetic protein (un)folding intermediates and to probe the equivalency of equilibrium vs. kinetic protein folding intermediates.

3.3 Experimental

3.3.1 Reagents and Materials

Cytochrome c (C7752), Ubiquitin (U6253), and Myoglobin (M1882) were all purchased from Sigma Aldrich (St. Louis, MO). Protein solutions were made to 10μM concentrations from 300μM protein stock solutions which were stored at 4°C. Solutions were made in HPLC water (Fischer Scientific) and the pH was adjusted with LCMS-grade ammonium hydroxide (Sigma-44273) and acetic acid 99.7% (Sigma Aldrich,St. Louis, MO).

3.3.2 Ion Mobility Measurements

Mass spectra and traveling–wave mobility spectra were acquired via electrospray ionization on a Waters Synapt G1 (Manchester, UK) equipped with an 8k quadrupole. Nitrogen gas was used for both the source and IMS region, and argon gas was used in the trap region of the mass spectrometer. The traveling-wave mobility separation was calibrated using 10μM ubiquitin and 10μM myoglobin in a 49:49:2 water, methanol, and acetic acid solution.[408] Settings such as capillary voltage, sample cone, extraction cone, trap/transfer collision energy, and trap DC bias voltages were optimized to allow for optimal ion transmission with minimal activation of the protein. It is important to note that a certain degree of ion activation is necessary for transmission, but too much activation can lead to fragmentation and erroneous mobility measurements. Discussion of this topic is beyond the scope of this paper; we direct the reader to the following excellent reviews.[408,413] The resulting source conditions used for the calibration are as follows: Capillary 2.25 kV, sample cone 30 V, extraction cone 1.0 V, source temperature 80°C, desolvation temperature 150°C, desolvation gas flow 200 L/h, cone gas flow 25 L/h. The

pressure in the source region was left unchanged at 200 Pa. The trap and transfer collision energies were set to 10 V each, with a trap pressure of 3.99 Pa.

Protein solutions were infused at a rate of 10 µL per minute using Harvard 11 Elite syringe pumps (Holliston, Massachusetts). Time-of-flight mass spectra were acquired for 3 minutes with a 2 second scan duration with mass-to-charge (*m/z*) range of 500-4000 Th, and showed no fragmentation with excellent transmission of both ubiquitin and myoglobin. Optimal traveling-wave mobility separation was achieved by using a 300 m/s IMS wave velocity and 7.5 V IMS wave height, with an IMS pressure of 48.6 Pa. The pusher frequency of the TOF was set to 90µs, which coincided with a Transfer T-wave velocity of 200 m/s to ensure any "ripples" or "beats" in the mobility spectrum are eliminated.[408] Transfer wave height was held at 8 V. Spectra were acquired for 5 minutes with a 5 second scan duration. Mass and mobility data were processed using MassLynx 4.1 (Waters Ltd. Manchester, UK).

3.3.3 Equilibrium Unfolding

Equilibrium unfolding studies were carried out by running a series of pH adjusted cytochrome c solutions and recording their mass spectrum and mobility separation. A series of solutions of 10µM cytochrome c in water were pH adjusted to pH 2.4, 2.5, 3, 4, 5, 6, 7, 8, 9, 10 and infused into the ESI source of the Synapt at a rate of 10 µL per minute. The same source conditions and settings from calibration procedure were used for these experiments, ensuring no significant error in measured drift times. Spectra were acquired in triplicate for 5 minutes with a 5 second scan duration.

3.3.4 Kinetic Unfolding Using TRESI

Kinetic unfolding of cytochrome c was done using a custom built time-resolved ESI (TRESI) source that interfaces directly to the commercial heated electrospray source of the Synapt (Figure 22). The TRESI interface is acts as an adjustable millisecond timescale reactor, facilitating the mixing of two solutions which are then electrosprayed into the mass spectrometer.[414] Analyte solutions are infused through two separate concentric capillary lines which mix in a small volume region that can be adjusted by pulling back the inner most capillary. The time-resolved interface was constructed as per Liuni et al.[415] with some minor changes. A 33 gauge stainless steel metal capillary (I.D. = 132.6 μm, O.D. = 203.2 μm, length = 18 cm, McMaster-Carr, Aurora, OH) served as both the outer capillary and electrospray capillary. Cytochrome c at 10 μM was infused into the inner glass capillary (I.D. = 40 μm, O.D. = 109.2 μm, length = 40 cm, Polymicro Technologies, Phoenix, AZ) at a rate of 5 μL per minute and a 10% acetic acid solution was infused into the outer metal capillary at a rate of 5 μL per minute. Reaction profiles for the acid-induced unfolding of cytochrome c were acquired by steadily pulling the inner capillary back from end of the outer capillary. For instance, a 1 mm distance between the ends of the inner and outer capillaries corresponds to a reaction time of 136 ms (this reaction time is calculated taking into account laminar flow, see Wilson et al.[398]). To acquire a time-course, the inner capillary is withdrawn in steps of 1 mm, with 5 minute acquisitions at each step.

3.4 Results and Discussion

3.4.1 IMS-MS of Equilibrium Unfolded Cytochrome C

Cytochrome c is among the most-well studied proteins in the context of (un)folding.[416] This is owed principally to the fact that cytochrome c is an exceptionally good analyte,

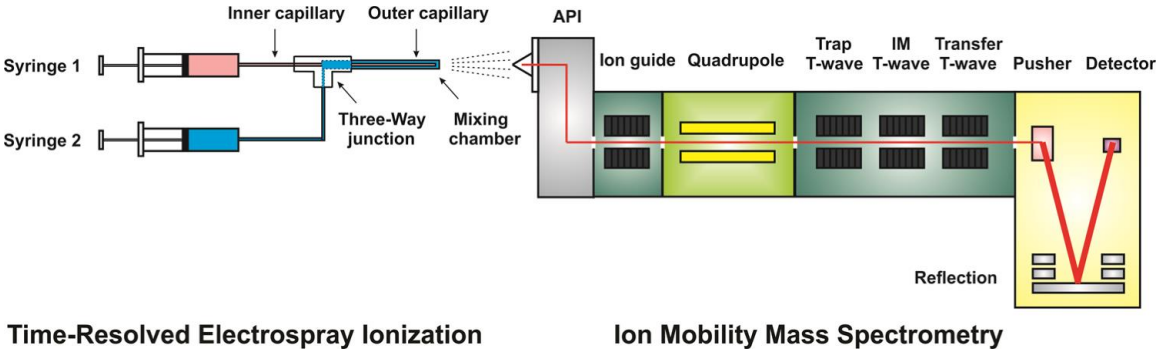

Figure 22. A schematic depiction of the TRESI-IMS-MS apparatus. Rapid mixing of 'folded' cytochrome c (syringe 1) and denaturing solution (10% acetic acid in H_2O, syringe 2) occurs near the end of the inner capillary. Unfolding reaction time is adjusted by withdrawing the inner capillary from the end of the outer capillary, which serves as the electrospray source.

with distinctive chromophoric properties arising from its covalently bound heme group and a tendency to ionize easily in electrospray mass spectrometry. There is consequently a wealth of literature on cytochrome c unfolding, including equilibrium and kinetic studies using optical detection[417] and even TRESI-MS.[98] Cytochrome c was also among the first protein IMS analytes and is now an exceedingly well characterized in terms of IMS collision cross section and other parameters, including equilibrium unfolding.[412] A summary of our equilibrium unfolding data are shown in Figure 23. One interesting feature of these data compared to previous measurements is the persistence of *m/z* peaks corresponding to a partially-folded species at low pH. Even at pH 2.4 (the lowest value attainable with acetic acid), cytochrome c exhibits an equilibrium between the fully unfolded state and a distribution of peaks centred on 8+, which is generally thought to correspond to a molten-globule intermediate. While this molten-globule is often observed as a low-populated species in pH 2.4 cytochrome c mass spectra, its apparent persistence in this case may be attributable to the enhanced sensitivity of z-spray type ion sources for globular species relative to extended (unfolded) species in electrospray.

In general, the observed equilibrium unfolding is in-line with what has been reported previously, consisting of three principle components: a 'folded' species (corresponding to charge states 5^+–7^+, centred on 7^+), an intermediate 'molten globule' species (charge states 8^+–11^+, centred on 9^+) and an 'unfolded' species (charge states 12^+–19^+, centred on 16^+). With the inclusion of IMS, it is possible to observe the extent to which these charge state distributions overlap in terms of the species from which they arise (Figure 24, top row). The 8^+ peak, for instance, includes a significant contribution from the 'folded' species in addition the 'intermediate' species to which it is assigned based on the charge-state

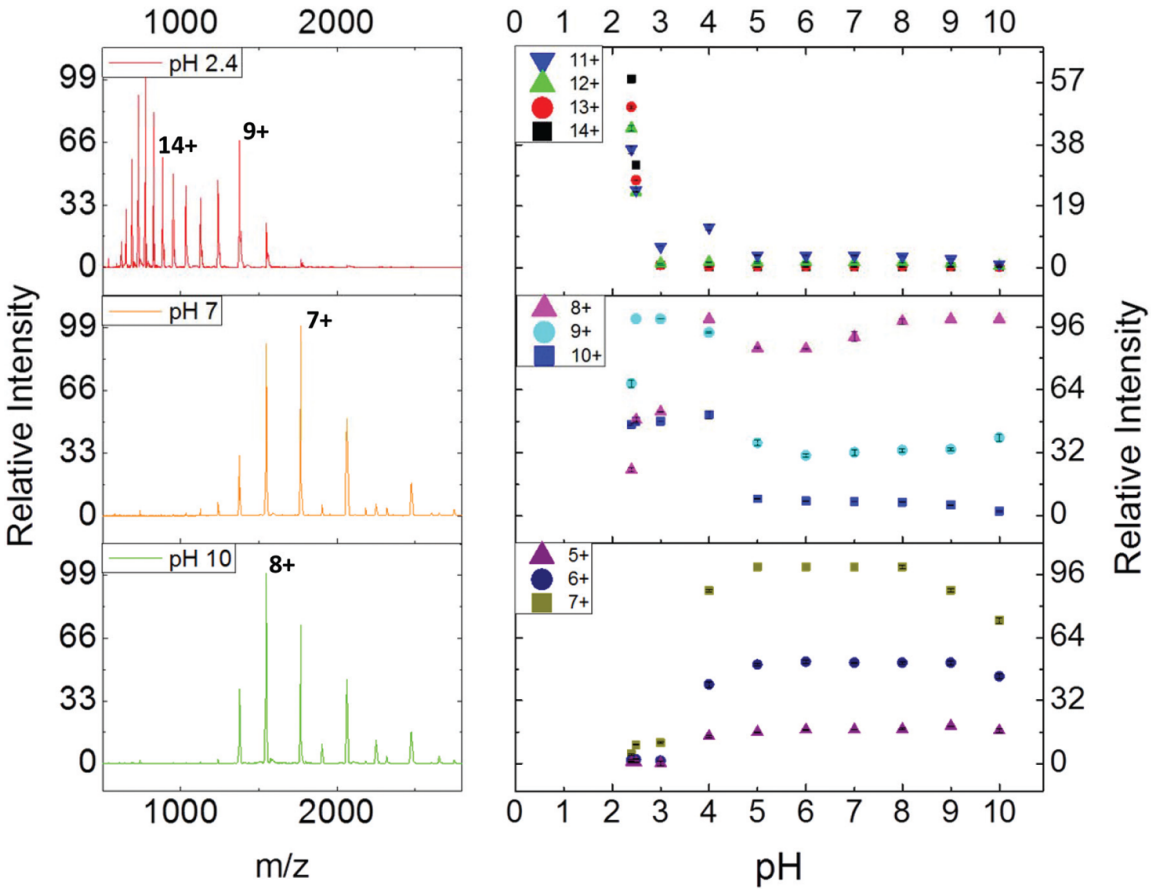

Figure 23. An overview of cytochrome c equilibrium unfolding data. Raw mass spectra show shifts in the charge state distribution associated with unfolding (left). Charge-state specific pH profiles (right) are grouped by dominant contributing species (n = 3).

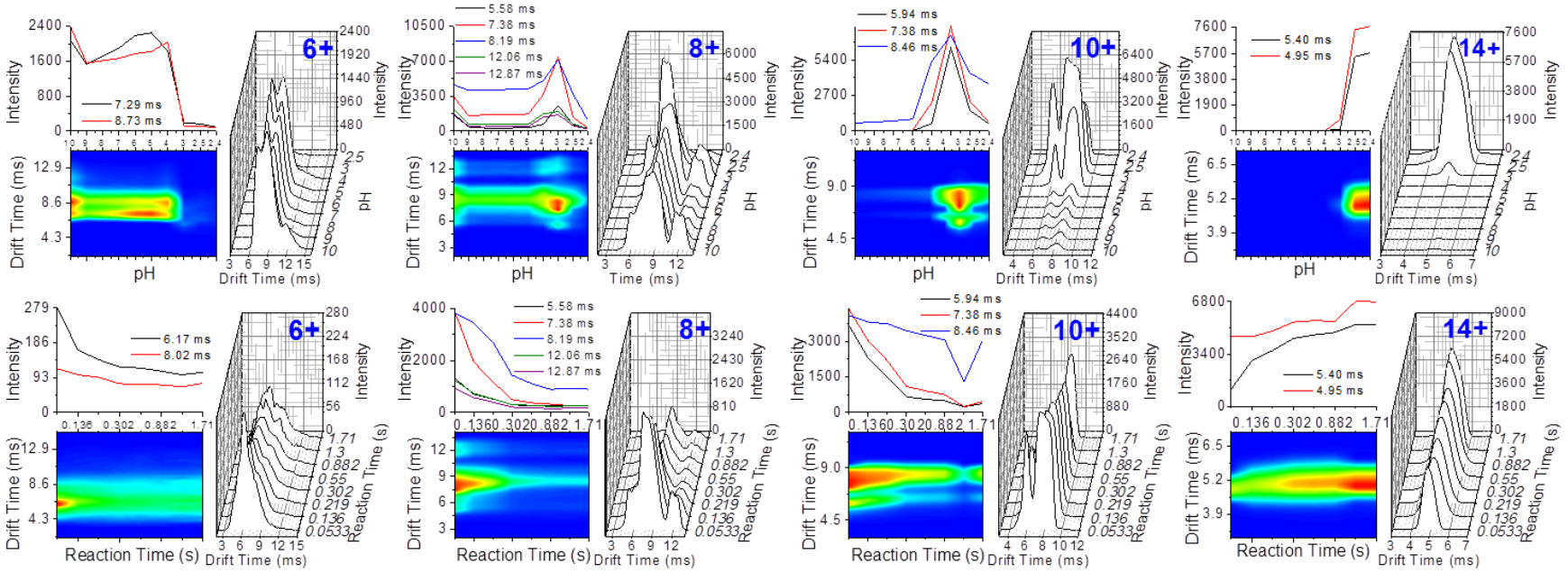

Figure 24. Equilibrium (top row) and kinetic (bottom row) IMS profiles for selected charge states. Each panel includes a spline trace illustrating the pH or time-dependent profiles for specific drift times (top left), a heat map providing a 'top-down' view of the pH or kinetic IMS profile and a 3D view of the pH or time-dependent IMS profile for each charge state.

distribution alone. Similarly, the 10+ peak arises from both ‘intermediate’ and ‘unfolded’ species.

3.4.2 Unfolding Kinetics of Cytochrome C Using TRESI-IMS-MS

TRESI-MS has been used to monitor folding and unfolding kinetics in a number of proteins, including myoglobin,[402] haemoglobin,[418] ubiquitin[419] and inducible nitric oxide synthase.[420] The latter study in particular offers an excellent example of the mechanistic detail that can be derived from TRESI measurements alone, provided that there are changes in mass due to ligand dissociation or complexation. Kinetic cytochrome c unfolding has been monitored by TRESI-MS in the introduction of a TRESI-based microfluidic device. In this study, a kinetic intermediate, identified as a transiently populated species during time-dependent unfolding, was observed in the 9^+ and 10^+ charge states. TRESI-MS data from the current study are summarized in Figure 25. The results are broadly in agreement with those of Rob et al.,[98] except that kinetic intermediate behaviour is also observed in the 8^+ charge state. Here again, the data are indicative of a three-component system, with a ‘folded’ species centred on 7^+, an ‘intermediate’ centred on 9^+ and an ‘unfolded’ species centred on the 16^+ charge state. The transition from the ‘folded’ to ‘intermediate’ charge-state distribution occurs within the dead-time of the TRESI apparatus, so that the observed kinetics are associated with the transition from the ‘intermediate’ to ‘unfolded’ state.

Without IMS, the observed kinetic profile of each *m/z* peak is an average of the individual profiles of all contributing species. In the current study, IMS resolution allows each contributing species to be monitored independently, as shown in Figure 24 (bottom row). What is striking about the temporal profiles of the kinetic mobility data (Figure 24, bottom row, IMS peak intensity vs. reaction-time profiles and heatmaps) is that some IMS- distinguishable species track with the dominant peak in the profile while others do not. For instance, the 10+ profile consists of three

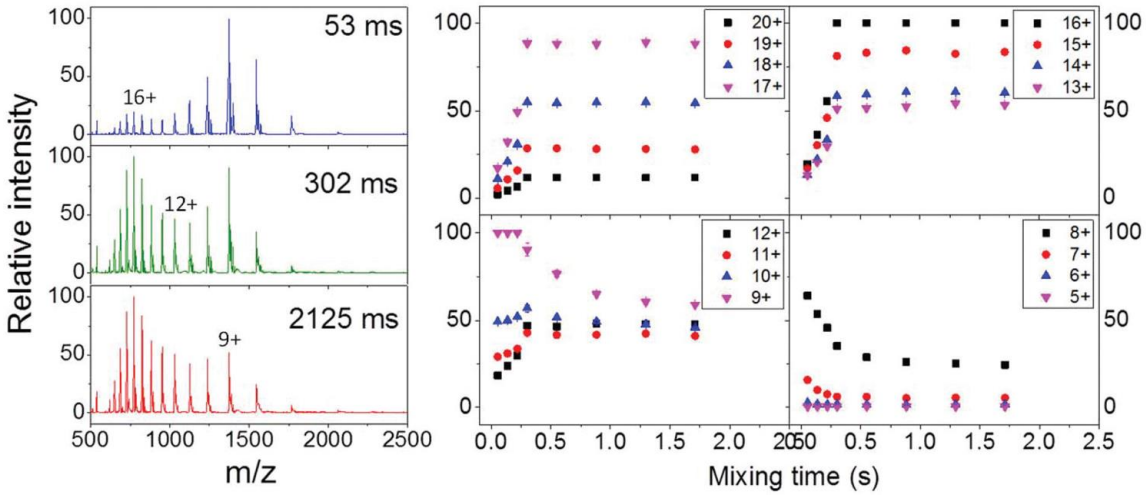

Figure 25. An overview of cytochrome c kinetic unfolding data. Raw mass spectra show shifts in the charge state distribution associated with unfolding (left). Charge-state specific intensity-time profiles (right) are grouped by dominant contributing species.

IMS-distinguishable species (drift times 5.94, 7.38 and 8.46 ms) the former two of which show substantially different kinetic behaviour compared to the dominant IMS peak at 8.46 ms drift time. The many IMS peaks associated with the 8^+ charge state, in contrast, exhibit virtually identical time-dependent behaviour (after adjusting for ion intensity). While both 8^+ and 10^+ species are clearly kinetic intermediates, it may be that the kinetically-distinct species in the 10^+ profile are reflective of true solution-phase structures, while the observed 8+ species are a consequence of gas-phase unfolding during transit through the IMS cell.[421]

3.4.3 Comparison of Equilibrium and Kinetic Unfolding Intermediates

One of the principal objectives of this work was to determine if the intermediates populated during equilibrium and kinetic unfolding of cytochrome c are structurally distinguishable. In both the equilibrium and kinetic unfolding experiments described above, the unfolding process involved 'folded', 'unfolded' and an 'intermediate' species that is presumed to correspond to a well-established molten globule. When the IMS profiles of equilibrium and kinetic unfolding are compared, taking into account the fact that the kinetic data proceed from the 'intermediate' (which is maximally populated at pH 3 under equilibrium conditions), the similarity for all charge-states is striking (Figure 26). The most straightforward profiles correspond to the unfolded species (e.g., 14+), which exhibits a unimodal IMS profile with rapid monophasic exponential decay as a function of pH or time.

Critically, even charge-states with the most complex IMS profiles exhibit precisely the same set of collision cross sections in equilibrium and kinetic unfolding experiments This in itself provides substantial support for the notion that equilibrium and kinetic unfolding intermediates of cytochrome c are structurally identical. Furthermore, the equivalence of the apparent thermodynamic and kinetic stabilities of species populated during cytochrome c unfolding, leading

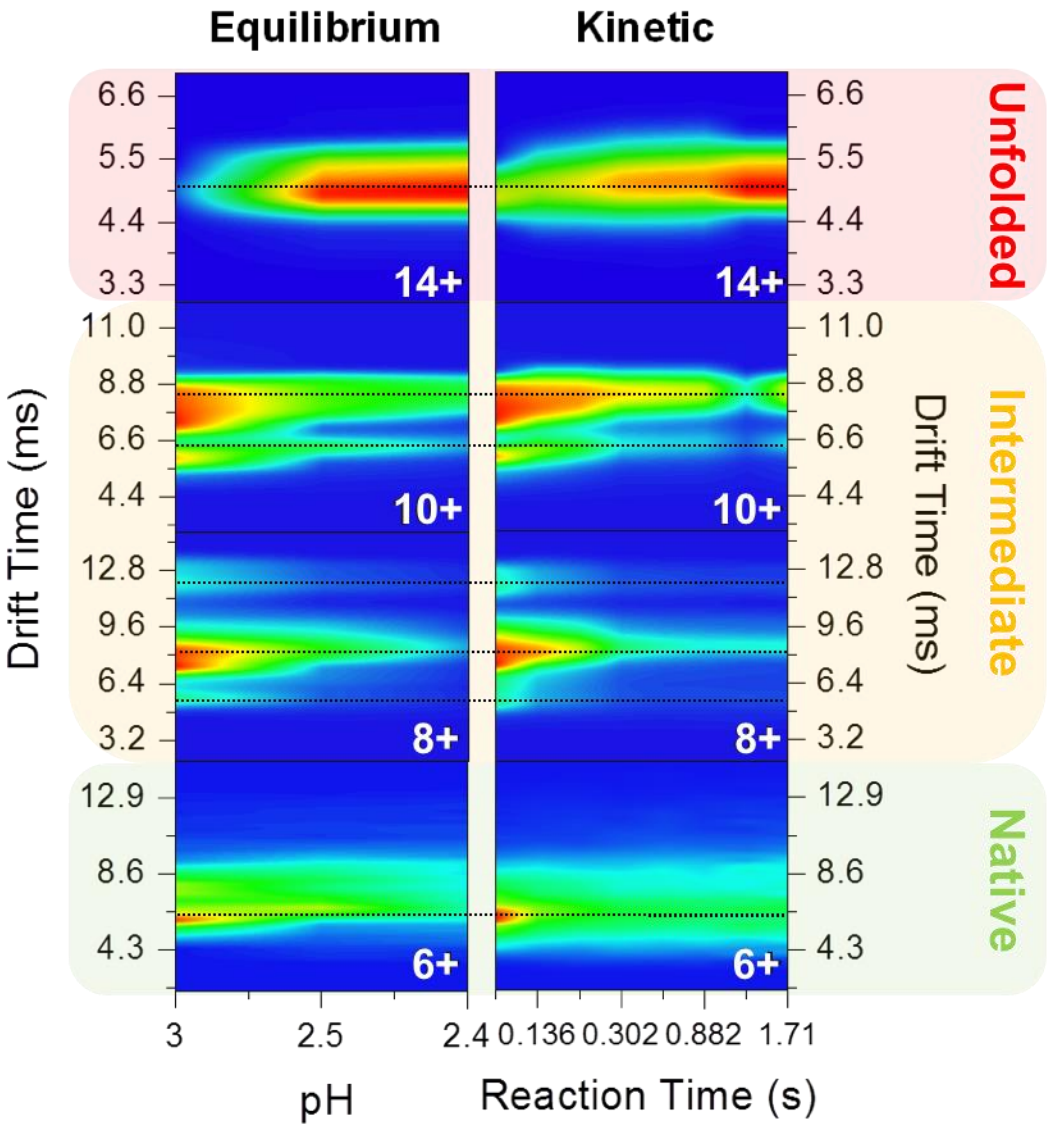

Figure 26. A direct comparison of the pH or time-dependent IMS profiles of selected cytochrome c charge states in the course of unfolding. The pH scale was adjusted to focus on the 'intermediate-to-unfolded' transition that can be directly monitored in the kinetic experiments. All equilibrium species (left column) line up with cross-section corresponding kinetic species (right column) suggesting that the conformations populated during equilibrium and kinetic unfolding of cytochrome c are identical. Moreover, cross-section matched species exhibit similar thermodynamic and kinetic stability profiles.

to qualitatively similar pH-dependent and time-dependent profiles for cross-section-matched species, also points to the equivalence of kinetic and equilibrium unfolding intermediates. Taken together, these data represent substantive evidence that cytochrome c unfolds through a similar mechanism whether in response to progressively increasing denaturant concentrations or time exposed to fully denaturing conditions.

3.5 Conclusions

In this work, we have introduced a new hyphenated mass spectrometry technique, TRESI-IMS-MS, which is suitable for a broad range of applications. Specifically, TRESI-IMS-MS can provide cross-section based structural analysis of species that are transiently populated during (bio)chemical reactions. The elected application in this work was a comparison of equilibrium and kinetic unfolding intermediates of cytochrome c, with the aim of determining if the species populated under equilibrium conditions were identical to those transiently populated during time-dependent unfolding. Our data strongly suggest that these species are indeed equivalent, at least in the sense that they generate identical IMS profiles at each charge state. A more thorough examination of this issue could include hydrogen/deuterium exchange implemented either in solution through the TRESI source or in the gas phase during IMS separation. Ultimately, though, our current data indicate that even when protein folding landscapes are substantially different (due to different solvent conditions), they share common local minima.

Chapter 4

Measuring Kinetic Isotope Effects In Enzyme Reactions Using Time-Resolved Electrospray Mass Spectrometry

A version of this chapter was published in Analytical Chemistry:

Liuni, P.; Olkhov-Mitsel, E.; Orellana, A.; Wilson, D. J. Measuring Kinetic Isotope Effects in Enzyme Reactions Using Time-Resolved Electrospray Mass Spectrometry. *Anal. Chem.* **2013**, *85* (7), 3758–3764.

4.1 Summary

Kinetic isotope effect (KIE) measurements are a powerful tool for studying enzyme mechanisms; they can provide insights into microscopic catalytic processes and even structural constraints for transition states. However, KIEs have not come into widespread use in enzymology, due in large part to the requirement for prohibitively cumbersome experimental procedures and daunting analytical frameworks. In this work, we introduce time-resolved electrospray ionization mass spectrometry (TRESI-MS) as a straightforward, precise, and inexpensive method for measuring KIEs. Neither radioisotopes nor large amounts of material are needed and kinetic measurements for isotopically "labeled" and "unlabeled" species are acquired simultaneously in a single "competitive" assay. The approach is demonstrated first using a relatively large isotope effect associated with yeast alcohol dehydrogenase (ADH) catalyzed oxidation of ethanol. The measured macroscopic KIE of 2.19 ± 0.05 is consistent with comparable measurements in the literature but cannot be interpreted in a way that provides insights into isotope effects in individual microscopic steps. To demonstrate the ability of TRESI-MS to directly measure intrinsic KIEs and to characterize the precision of the technique, we measure a much smaller $^{12}C/^{13}C$ KIE associated specifically with pre-steady state acylation of chymotrypsin during hydrolysis of an ester substrate.

4.2 Introduction

Kinetic isotope effects (KIEs) have a broad range of uses in the study of enzyme mechanisms, providing insights that cannot be obtained by other techniques.[422–425] KIEs have been employed to determine rate limiting microscopic steps,[426–428] link catalysis to dynamics in the active site,[429–432] and structurally characterize transition states.[433–435] However, in spite of their obvious usefulness and a long history development, KIE measurements have not come into widespread use in the broader field of enzymology. There are a number of potential reasons for this, including analytical frameworks that can appear quite daunting even for moderately complex reaction mechanisms, and the ambiguity arises from drawing conclusions about microscopic processes from what are usually steady state measurements.[436,437] This is in addition to the experimental procedure themselves, which are often arduous and expensive.

Scintillation counting was initially the dominant method for measuring KIEs, but the requirement for radioisotopes has resulted in a marked decrease in use. Currently, radiolabeling is used mainly for hydrogen tunneling analyses that compare $^{1}H/^{3}H$ and $^{2}H/^{3}H$ isotope effects, as well as competitive assays for heavy atom KIEs.[438] The majority of KIE measurements are made using optical techniques, but this has severely limited the subset of systems studied due to the requirement for a chromophoric change on turnover. For example, $NAD(P)^{+}$ dependent enzymes represent the overwhelming majority of KIE studies in the literature, partly because of the large isotope effects associated with hydride transfer and a well justified interest in hydrogen tunneling but also because reduction/oxidation of the nicotinate moiety is optically detectable (NADH has a characteristic absorption band at $\lambda = 340$ nm).[427,439–441] Optical analysis by UV/visible absorption or fluorescence also generally precludes competitive assays, since isotopically “labeled” and “unlabeled” species are indistinguishable. More recently, MS- and NMR-based methods have

emerged that address these limitations somewhat.[442,443] NMR approaches that allow for the measurement of KIEs from natural abundance ^{13}C are especially promising since they do not require isotopic labeling.[444–446] However, these techniques bring their own drawbacks which can include the requirement for a large amount of material,[444,446] limited applicability, and lower precision quantitation of reactants and products.

The ability to distinguish multiple isotopes simultaneously at high sensitivity makes mass spectrometry well suited to the study of isotope effects, as exemplified by the well-established field of isotope ratio mass spectrometry.[447] MS-based approaches have been used to measure KIEs in enzyme systems, typically by quenching the reaction midphase and noting the relative quantities of specifically labeled and unlabeled product.[442,443] This approach is in principle broadly applicable but relies on a single time-point measurement and numerous sample handling steps between quenching and analysis, which can make it difficult to achieve the needed level of precision.

In this work, we introduce a new, straightforward approach for measuring KIEs based on time-resolved electrospray ionization mass spectrometry (TRESI-MS). TRESI-MS is an electrospray-coupled rapid mixing technique that enables monitoring of solution phase processes on the ms time scale.[448] The data are analogous to conventional stopped-flow intensity−time profiles except that no chromophore is required and isotopically labeled and unlabeled species are distinguishable by mass. To establish the feasibility of the approach, we first measure a large, well-studied KIE in the yeast alcohol dehydrogenase (ADH)-catalyzed hydride transfer from ethanol to NAD+. We then test the limits of the technique by measuring a small $^{12}C/^{13}C$ isotope effect associated with the pre-steady state acylation of chymotrypsin by the ester substrate para-nitrophenyl acetate (pNPA).

4.3 Experimental

4.3.1 Materials

α-Chymotrypsin, yeast alcohol dehydrogenase, β-nicotinamide adenine dinucleotide, ammonium hydroxide, ammonium acetate, and 4-nitrophenol acetate (p-NPA) were obtained from Sigma-Aldrich (St. Louis, MO). Deuterium oxide, 1,1'-^{13}C acetic anhydride (99%), and 1,1-D_2 ethanol were purchased from Cambridge Isotope laboratories (Andover, MA). HPLC-grade methanol, ethanol, acetonitrile, and hydrochloric acid were purchased from Caledon Laboratories (Georgetown, ON, Canada). Ultrapure water was generated from the in-house Milli-Q system (EMD Millipore, Billerica, MA). All solutions were pH adjusted using the S20 SevenEasy pH meter (Denver Instruments, Bohemia, NY). For all experiments, infusion and continuous pullback of the inner capillary was conducted using Harvard 11+ infusion syringe pumps (Holliston, MA, USA).

4.3.2 Synthesis of ^{13}C-Labeled pNPA

To a solution of p-nitrophenol (1.0 equiv.) in freshly distilled dichloromethane was added a catalytic amount of dimethylaminopyridine (0.05 equiv.) in one portion, followed by a slight excess of acetic anhydride (1.05 equiv.). The reaction was monitored by thin-layer chromatography (TLC) analysis. Once complete, the reaction was diluted with diethyl ether and extracted with water. The ether layer was washed with brine, dried with $MgSO_4$, and concentrated under vacuum. The crude material was purified by column chromatography using silica gel. The final product was characterized by mass spectrometry and UV−vis spectroscopy. ^{13}C-labeled labeled p-nitrophenyl acetate was prepared using the same procedure and using 1,1'-$^{13}C_2$-labeled acetic anhydride.

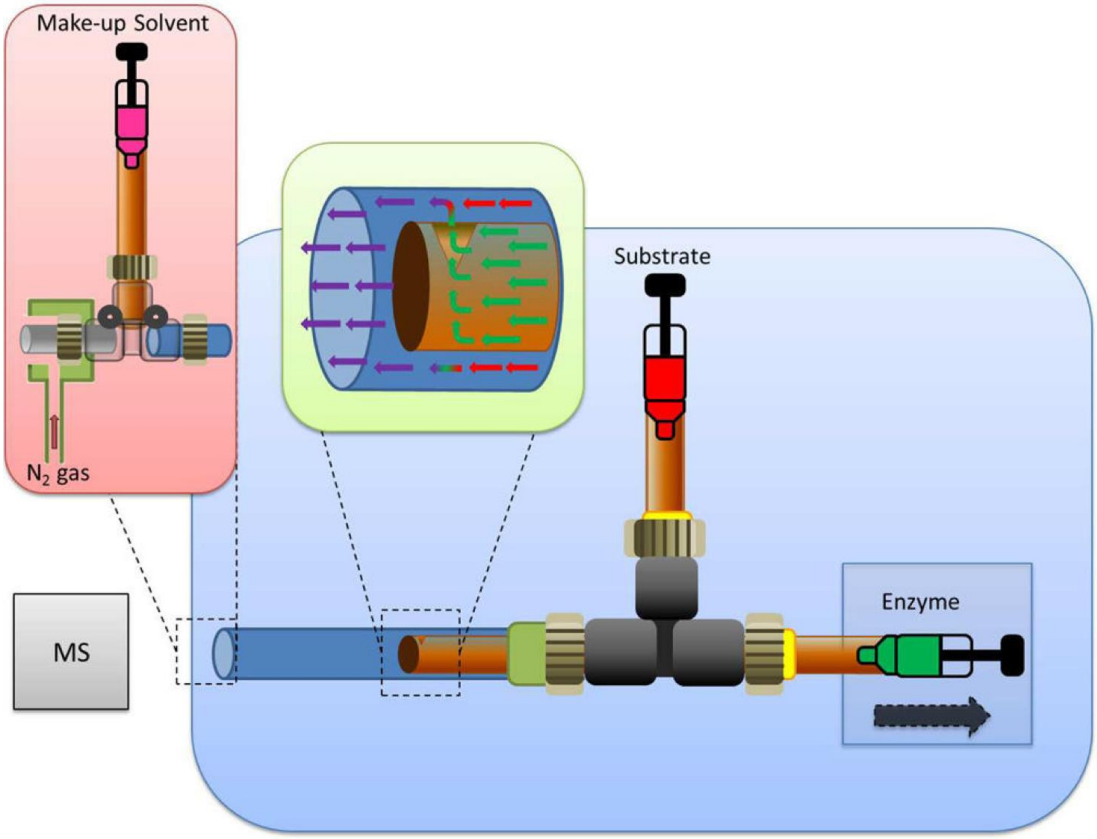

Figure 27. Schematic depiction of the TRESI-MS source.[448] Solution containing enzyme is injected into the "inner capillary" from Syringe 1 (green) via infusion pump. This pump, Syringe 1, and the inner capillary comprise an assembly that can be withdrawn from the source region (gray arrow), resulting in withdrawal of the inner capillary from the end of the outer capillary and a correspondingly increased delay between mixing and ionization. Syringe 2 (red) injects substrate solution through the annular intercapillary space. Mixing occurs when solution from the inner capillary flows into the intercapillary space though a notch cut 2 mm from the end of the inner capillary. Freshly mixed solution then passes into a delay volume which is determined by the position of the inner capillary within the outer capillary and then into a static mixer where electrospray-enhancing "makeup solvent" is added (pink syringe) immediately prior to the onset of ESI.

4.3.3 TRESI-MS

Time-resolved measurements were carried out using an electrospray mass spectrometry-coupled capillary mixer described previously (Figure 27).[448,449] Briefly, the device is based on a concentric capillary design. In both ADH and chymotrypsin experiments, the enzyme solution was injected through the polyimide-coated fused silica inner capillary (Polymicro, Pheonix, AZ). Solutions containing 50% labeled and unlabeled substrate were injected through the stainless steel outer capillary (Small Parts, Logansport, IN). Mixing occurred when enzyme solution was released into the intercapillary space from a notch cut 2 mm from the inner capillary end, with the mixed solution then passing into a delay volume. Reaction profiles were acquired by steadily moving the inner capillary back from the end of the outer capillary, resulting in the acquisition of steadily later reaction times. For chymotrypsin experiments, an additional static mixer was added to the end of the outer capillary in order to supply an electrospray-enhancing "makeup solvent" consisting of 10% (v/v) methanol and 6 mM HCl (pH 2) in water immediately prior to ionization. Kinetics were measured from 42 ms to 22 s of reaction time, corresponding to 30 min of inner capillary withdrawal and data acquisition.

4.3.4 KIE Measurements

For all experiments, isotopically labeled and unlabeled substrates were mixed and reacted simultaneously in an internal competition assay. In alcohol dehydrogenase experiments, syringe 1 contained a 2 μM solution of ADH in 10 mM ammonium acetate (pH 8.4). This was mixed with a series of equimolar ethanol and 1,1-D_2 ethanol solutions, (10 mM-200 mM) each containing 400 μM NAD^+ prepared in 10 mM ammonium acetate (pH 8.4). Samples were injected at a total flow rate of 3.0 μL/min. The intensity of NADH and NADD at 666 *m/z* and 667 *m/z*, respectively, was monitored as a function of time, and kinetic data was acquired from extracted ion currents at their

respective masses. For the purpose of extracting V0, the 667 *m/z* signal was assumed to contain a 20% component from NADH due to the M+1 isotopic peak. For chymotrypsin experiments, a 25 μM chymotrypsin solution at pH 8.4 is loaded into Syringe 1. A solution containing both 2.5 mM ^{12}C-p-NPA and 2.5 mM ^{13}C-p-NPA was prepared in 40% methanol, adjusted to pH 7.0, and loaded into Syringe 2. A 6 mM HCl solution in 10% methanol is loaded into Syringe 3 as a makeup solvent. Samples were injected at flow rates of 3.5 μL/min for all 3 syringes (10.5 μL/min total flow rate). The makeup solvent also acts as a chemical quencher for the reaction; therefore, the dead time for the mixing tee is negligible. Extracted ion current profiles from peaks corresponding to the 12+, 11+, 10+, and 9+ charge states of the free and acyl-enzyme forms of chymotrypsin, respectively, were acquired and used in the calculation of KIEs.

All experiments were conducted with mild-moderate declustering potentials on a QSTAR Elite Qq-TOF mass spectrometer (AB Sciex, Framingham, MA). ESI voltages were optimized between +4500 and +5500 V (positive ion mode) prior to the acquisition of data. The Analyst QS 2.0 software package was used to control, acquire, and view mass spectral information, and protein mass spectra were deconvoluted using the BioAnalyst software suite (AB Sciex, Framingham, MA).

4.4 Results and Discussion

4.4.1 Yeast Alcohol Dehydrogenase Oxidation of Ethanol

KIEs associated with hydride transfer are among the most well-studied isotope effects, serving as a model for hydrogen tunneling[450–452] and catalysis-linked dynamics.[453,454] The ADH-catalyzed hydride transfer from benzyl alcohol to NAD^+ was the first reaction in which evidence of hydrogen tunneling was reported.[452] There remains nonetheless substantial disagreement on the

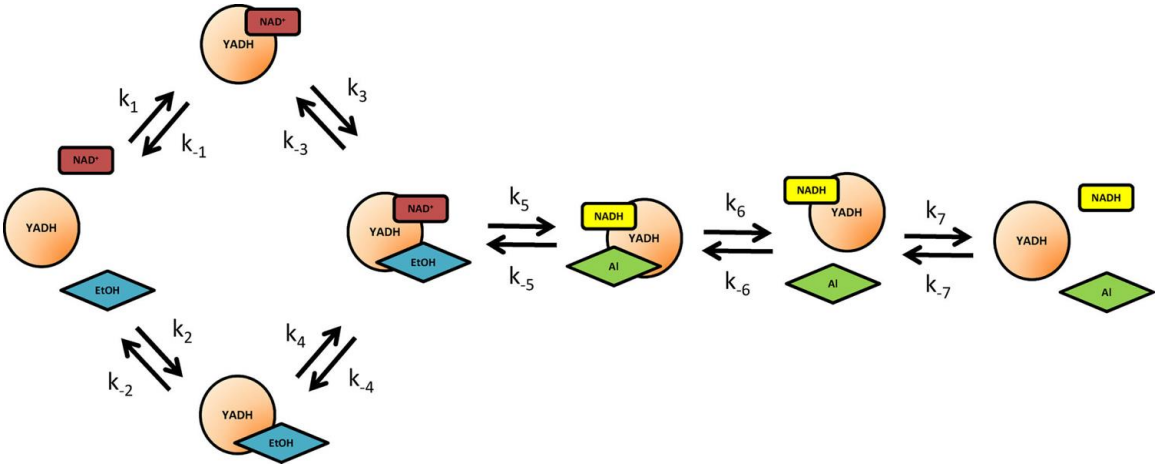

Figure 28. Schematic depiction of the semisequential bi-bi ADH mechanism proposed by Dickinson and Monger in 1973, with release of NADH being the rate-limiting process in the oxidation of ethanol (EtOH) to acetaldehyde (Al).

extent to which hydrogen tunneling can be inferred from the conventional approach of characterizing the pressure or temperature dependence of the KIE.[455] The reliability of KIE-based evidence for the contribution of enzyme dynamics to catalysis has also recently come into question.[437] In the case of ADH, much of the difficulty in interpreting the hydride transfer primary KIE arises from ambiguities in our understanding of the mechanism. Recent studies generally assume the semi-sequential bi-bi mechanism proposed by Dickinson and Monger in 1973 (Figure 28), with the rate limiting step in the "oxidation-of-alcohol" direction being release of the nucleotide product.[456]

ADH has frequently been used as a protein complex standard for electrospray mass spectrometry.[457,458] Under optimal electrospray conditions, the ADH spectrum is dominated by the intact tetramer, shown in Figure B1, Appendix. The addition of saturating concentrations of ethanol has little impact on the quality of the spectrum, and specific binding to the tetramer is detected via a 184 Da mass shift (i.e., 1 molecule per active site). However, mM concentrations of NAD^+ have a strongly deleterious effect on spectral quality, eliminating the possibility of directly monitoring active enzyme complexes in the steady state. Kinetic measurements were therefore carried out by monitoring the product NAD(H/D), with adjustment to the extracted parameters for the ~20% contribution of the NADH M+1 (^{13}C) peak to the monoisotopic NADD peak. Typical reaction progress curves from competition experiments involving 50% labeled ethanol (CH_3CD_2OH) at 10 mM (a) and 200 mM (b) are shown in Figure 29. The insets show the linear portions of the curves used to extract initial velocities V_0 for a steady state analysis.

As expected, these data show a significant KIE, with hydride transfer from the labeled ethanol to form NADD being substantially slower than the formation of NADH from the unlabeled substrate. The average "observed" kinetic isotope effect KIE_{obs} extracted directly from these data

is V_0(NADH)/ V_0(NADD) = 1.8 ± 0.4; however, this analysis assumes that the isotopic substitution has no influence on any microscopic process apart from the "rate limiting" step, which seems unlikely given that hydride transfer (where the isotopic substitution generates a primary KIE) is not rate limiting.[459] The observed KIE is therefore a macroscopic phenomenon which is better defined in terms of the apparent specificity constant:

$$KIE_{spec} = \left[\frac{\left(k_{cat(NADH)}/K_{M(NADH)}\right)}{\left(k_{cat(NADD)}/K_{M(NADD)}\right)}\right] \quad (23)$$

usually abbreviated as ^{D}(V/K).[436] Michaelis−Menten plots showing the initial rates of formation of NADH and NADD as a function of ethanol concentration are provided in Figure 30. With the NAD+ concentration held constant at a saturating level of 20 mM, the V0 vs. [ethanol] profile exhibits classical Michaelis−Menten saturation kinetics. Extracted values of k_{cat} and K_M yield a KIE_{spec} of 2.19 ± 0.05 (R^2 NADH = 0.82, R^2 NADD = 0.88), which is in line with comparable literature values, including the initial measurement by Mahler and Douglas[423] and more recent work by Park et al.[460] The significant difference between KIE_{obs} and KIE_{spec} suggests a substantial shift in one or more microscopic equilibria upon isotopic substitution, but the ADH mechanism is too complex to allow for the determination of specifically which processes are affected from a single macroscopic measurement. Moreover, there are a number of other factors that complicate any attempt at a quantitative interpretation of the observed KIE, in particular an undefined 2° KIE from the deuterium that is not transferred and an untested assumption that catalysis at each active site is fully independent. Random binding of labeled and unlabeled substrate at each active site generates a heterogeneous set of active enzyme complexes, which could distort the observed KIE if the activity of one site is influenced by the activity of another.

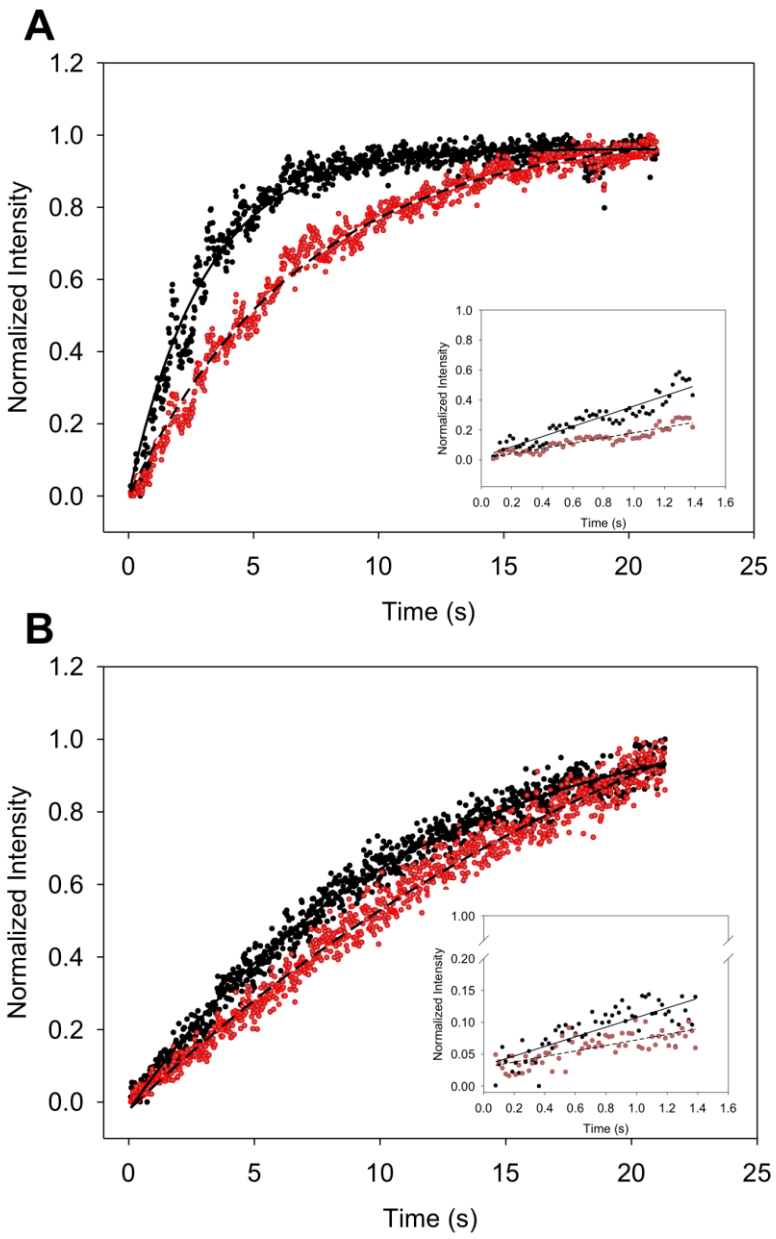

Figure 29. Reaction progress curves for the oxidation of ethanol by ADH at two different ethanol concentrations (A) 200 mM and (B) 10 mM, acquired by monitoring the accumulation of NAD(H/D). Dark circles represent the NADH signal intensity, while gray circles correspond to NADD. Lines are single exponential fits to the data to aid visualization (not used in the analysis). Insets show the linear portions of the progress curves used for the extraction of V_0.

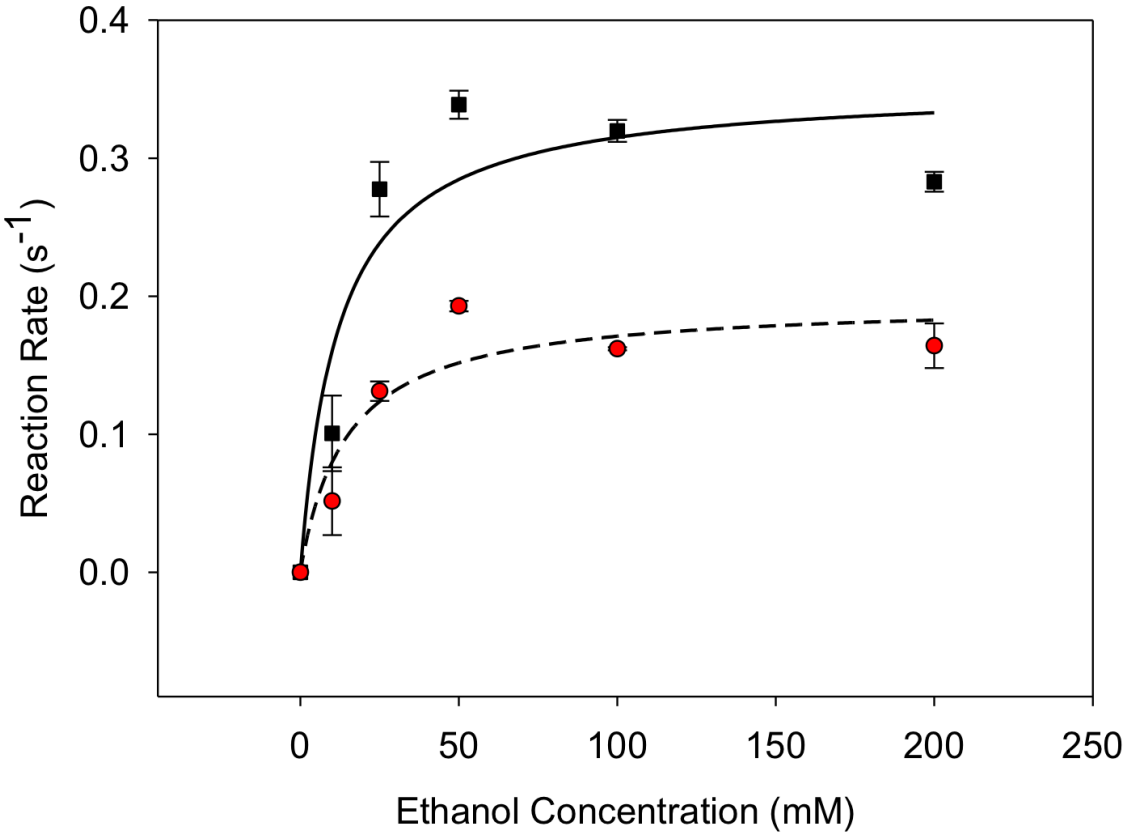

Figure 30. Steady state analysis of ADH catalyzed oxidation of ethanol. Filled squares represent the initial velocities of NADH production, and open circles indicate the same for NADD. After fitting to the Michaelis−Menten equation, the data yield a $^{D}(V/K)$ value of 2.19 ± 0.05. Error bars are from 5 replicates.

It is worth noting that some of this ambiguity arises from an inability to directly detect enzyme complexes that are populated in the steady state (i.e., the E·NAD(H/D) complex, where E = enzyme) or the pre-steady state (e.g., the ternary $E{\cdot}NAD^{+}{\cdot}CH_3C(H/D)_2OH$ complex). In the case of ADH, the detection of active enzyme complexes is complicated by the presence of NAD^{+} as discussed earlier; however, this challenge may prove surmountable with careful adjustment of solvent and ionization conditions. The challenge of distinguishing labeled from unlabeled complexes in competition experiments, on the other hand (i.e., a 2−8 Da difference on a roughly 148 kDa complex), would be daunting even on an ultrahigh resolution instrument. Nonetheless, for smaller proteins, direct measurement of microscopic KIEs via enzyme complex intermediates is possible using TRESI-MS, as demonstrated in the following section.

4.4.2 Primary $^{12}C/^{13}C$ KIE in Chymotrypsin Acylation

In contrast to KIEs involving isotopes of protium, heavy atom KIEs rarely exceed more than a few percent and are therefore much more challenging to measure in terms of achieving the necessary level of precision. Chymotrypsin catalyzed hydrolysis of para-nitrophenyl acetate (mechanism shown in Figure B3, Appendix B) is among the relatively few enzymatic reactions for which a heavy atom KIE has been reported.[461] This reaction also includes an observable pre-steady state characterized by the population of an acyl-enzyme intermediate. Acylation of the enzyme is fully rate limiting in the pre-steady state, and isotopic substitution at the carbonyl carbon has no impact on the substrate binding equilibrium.[461] The primary $^{12}C/^{13}C$ KIE associated with acyl-enzyme formation is therefore attributable specifically to the irreversible acylation step.

The release of chromophoric para-nitrophenolate upon acylation makes the chymotrypsin/p-NPA pre-steady state accessible to optical analysis; however, the optical equivalency of labeled and unlabeled para-nitrophenol rules out a competition approach for measuring KIEs. By TRESI-

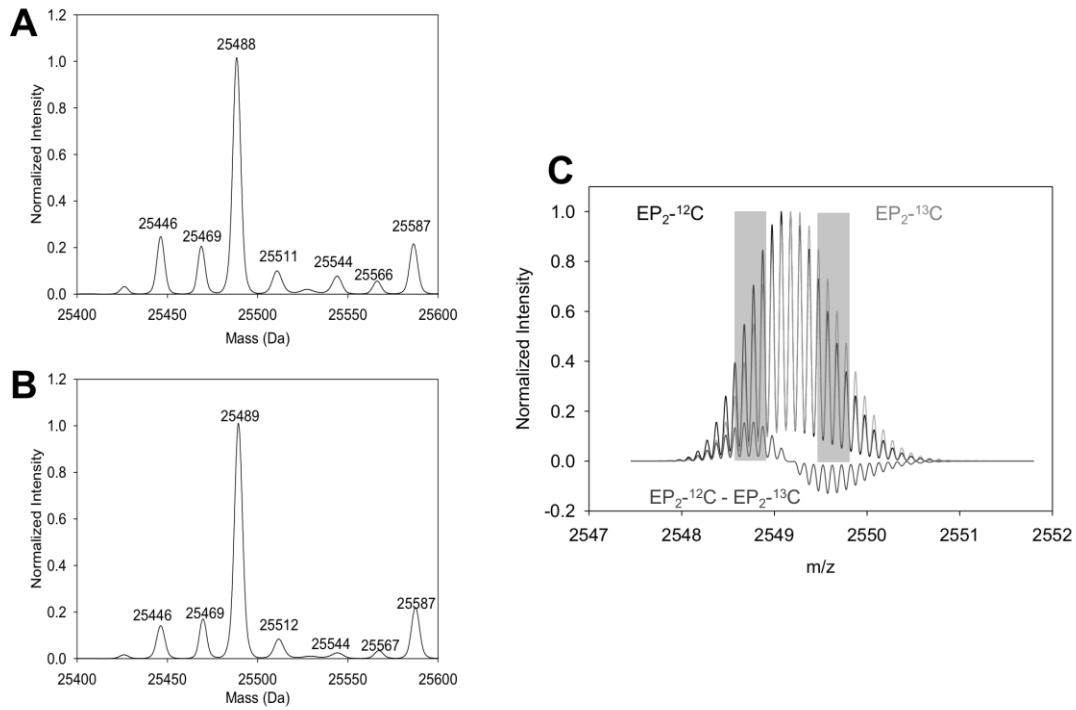

Figure 31. Matched pair of deconvoluted mass distributions for labeled and unlabeled acyl-chymotrypsin. (A) unlabeled; (B) labeled. The peak at 25 446 Da corresponds to free δ′-chymotrypsin while the acyl-enzyme is observed at 25 488 Da in the case of the unlabeled substrate and 25 489 Da in the case of the labeled substrate. The spectra also include a number of sodium and potassium adducts common in commercially supplied samples. (C) A model of the 10+ *m/z* peak for labeled and unlabeled acyl-chymotrypsin (50/50 mixture) illustrating the challenge of differentiating the two peaks at the *m/z* level due to overlap. Peaks for ^{12}C are shown in black, while the ^{13}C peaks are shown in gray. Small peaks appearing above and below the *m/z* axis are difference peaks (^{12}C–^{13}C). Shaded areas indicate the ion current extraction window for ^{12}C acyl-enzyme (left) and ^{13}C acyl-enzyme (right), resulting in a 60% contribution from the desired species.

MS, pre-steady state acylation of chymotrypsin is monitored by direct detection of the acyl-enzyme intermediate.[449] Competition experiments are therefore possible in principle but will require the differentiation of a 1 Da difference on a 25 kDa protein, complicated still further by overlapping natural abundance ^{13}C isotope distributions. In terms of full-width half-maximum (FWHM) resolution, this requirement is well beyond the capabilities of a typical Q-TOF instrument; however, a competitive KIE can still be measured provided that the "labeled" and "unlabeled" peaks are distinguishable and the extent of overlap between the peaks is known. To determine if the labeled and unlabeled enzyme complex were distinguishable, we collected mass spectra of chymotrypsin in the presence of unlabeled (Figure 31A) and labeled substrate (Figure31B). In both cases, the free enzyme appears at 25446 ± 2 Da after deconvolution, corresponding to the δ' form of the enzyme.[449] The mass of the acyl-enzyme, however, was 25488 ± 3 Da for the unlabeled substrate and 25489 ± 3 Da for the labeled substrate. In terms of absolute mass, these values are identical to within error; however, in each matched set of measurements (n = 5), acylation with labeled substrate resulted in a mass difference that was always 1 Da more than acylation with unlabeled substrate. This is a testament to the power of deconvolution over multiple peaks to measure mass differences in the absence of an internal standard, and it confirms that there is a measurable difference in peak position between labeled and unlabeled acyl-chymotrypsin.

The challenge in differentiating the labeled and unlabeled acyl-enzyme in individual *m/z* peaks is illustrated in Figure 31C, in which the labeled and unlabeled 10+ peaks are modeled at 100 000 FWHM. Kinetics taken from overlapping regions of the distribution will yield a weighted average rate for the two species (see Appendix B). It is therefore desirable to acquire kinetics from regions of the peak where overlap is lowest, corresponding to the outer edges of the distribution. However, this must be balanced with the need for sufficient signal-to-noise. Ultimately, a region

corresponding to 60% contribution from the desired species (Figure 31C, shaded regions) was selected. Effectively, this means that the observed KIE will be only 20% of the actual KIE (see Appendix B for details), which makes for a very challenging measurement. Nonetheless, the enhanced precision of measuring the KIE in a single competitive assay appears to outweigh the challenges; TRESI-based experiments in which the labeled and unlabeled rates were measured separately failed to yield a reliable KIE (i.e., the measurement error was greater than the measurement; data not shown).

Extracted ion currents (XICs) from the appropriate regions of the *m/z* peaks yield intensity−time profiles dominated by either ^{12}C- or ^{13}C-acylated chymotrypsin as described above (also see methods and Figure B2, Appendix B). After normalization to the total ion current (TIC) to remove artifacts from sensitivity drift, and averaging over all *m/z* peaks with sufficient signal-to-noise, we obtain low-dispersion kinetic profiles, an example of which is shown in Figure 32A. To ensure that the observed small rate difference was not the result of systematically changing peak shape or interference from nearby peaks, we performed control experiments in which an identical procedure was used to generate "left-side-of-peak" and "right-side-of-peak" kinetic profiles from samples containing only unlabeled substrate, shown in Figure 32B. These control profiles were identical to within error.

Least-squares fits to the data using a single exponential expression yielded an average ^{12}C acylation rate of 1.10 ± 0.21 s^{-1} and an average ^{13}C acylation rate of 1.06 ± 0.19 s^{-1}, based on five independent runs. The error associated with these independent measurements is too great to allow for the extraction of a reliable KIE; however, this is largely a consequence of run-to-run variability in the absolute rates. Since in a competition experiment KIEs are calculated from matched rates (i.e., paired ^{12}C and ^{13}C rates extracted from individual runs), the issue of run-to-run variability is

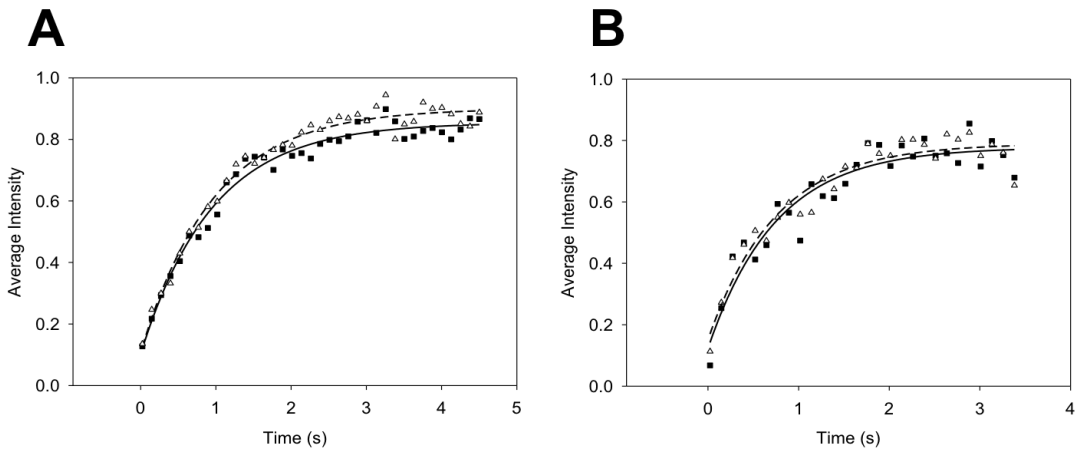

Figure 32. Intensity−time profiles drawn from acyl-chymotrypsin ion currents extracted as shown in Figure 31. Filled squares represent intensities taken from the right side of the peak; open triangles correspond to the intensity on the left side. (A) A typical $^{12}C/^{13}C$ profile for KIE measurement yielding an intrinsic acylation KIE_{obs} of 1.017 ± 0.008, which is 20% of the actual value due to peak overlap (details on the data analysis are provided in the Appendix). (B) A $^{12}C/^{12}C$ negative control to ensure that KIE measurements are not an artifact from time-dependent changes in peak shape. The data are fit using least-squares to a single exponential expression yielding a "KIE" of 1.00 ± 0.005.

eliminated, resulting in a substantial decrease in the error. After adjusting for peak overlap, the average KIE derived from these experiments (n = 5) is 1.09 ± 0.02. To the best of our knowledge, this represents the first competitive heavy-atom KIE measurement in the pre-steady state. While there are no directly comparable measurements in the literature, this value is within the range determined for deacylation of chymotrypsin using a single-turnover approach (≤1.08,depending on ethanol concentration).[462] The value is significantly higher than the 1.030 ± 0.002 steady state ^{13}(V/K) value reported by Hess and co-workers;[461] however, that measurement would have been a convolution of the primary KIEs for acylation and deacylation and would also have been influenced by any change in the ratio of the acylation/deacylation rates resulting from isotopic substitution. The magnitude of our acylation-specific KIE measurement indicates a late transition state for loss of paranitrophenolate from the tetrahedral acyl-enzyme complex, consistent with strong stabilization of the oxyanion.

4.5 Conclusions

We have demonstrated a novel TRESI-MS-based approach for the measurement of kinetic isotope effects in enzyme catalyzed reactions. The main advantage of TRESI-MS in this context is that is allows for competition experiments in a broad range of systems without the need for radioactive labeling or large amounts of material. Interpretation of the data may also be simplified in many cases, particularly when an enzyme complex is directly observable. Finally, by enabling competition experiments in the pre-steady state, TRESI-MS greatly increases the number of enzymatic reactions in which it is possible to measure microscopic KIEs (i.e., KIEs that are attributable to a single step in the reaction mechanism). The competition approach was found to be essential in achieving the necessary level of precision for heavy atom KIE measurements. In

summary, TRESI-MS represents a powerful alternative for measuring KIEs, with the potential to yield new insights into enzymatic mechanisms, transition states, and catalysis-linked dynamics.

Chapter 5

Correlating Dynamic Conformational Sampling to Enzyme Catalysis: A Millisecond Timescale Hydrogen/Deuterium Exchange Mass Spectrometry Approach

5.1 Summary

Characterizing the myriad of conformations that are directly related to catalysis has proven extremely challenging and has largely required a multidisciplinary approach involving x-ray crystallography[463], fluorescence[464], and relaxation dispersion NMR techniques.[465] Hydrogen/deuterium exchange mass spectrometry represents a unique alternative, as it is unaffected by size-limitations and can monitor "NMR inaccessible" reactions on the millisecond timescale. In this work, we apply a strategy combining time-resolved electrospray ionization H/D exchange (TRESI-HDX) and kinetic isotope effects to directly link conformational dynamics of yeast alcohol dehydrogenase (ADH) with its catalytic reaction co-ordinate. ADH reaction kinetics monitored in the presence of isotopically labeled (ethanol-1,1-D_2) or unlabeled ethanol. The deuterium label on ethanol participates exclusively in enzymatic hydrogen transfer; therefore when compared to unlabeled ethanol, any difference in catalytic turnover is the result of a kinetic isotope effect (KIE). Shifts in the statistical distribution of ADH-cofactor bound species upon ethanol binding are surprising and may provide evidence for cooperativity in the ADH mechanism. Global H/D exchange rates show that, on average, ADH takes up deuterium 1.27 ± 0.07 s^{-1} times faster when catalyzing hydrogen transfer compared to deuterium transfer, and provides evidence for an induced-fit model of catalysis-linked dynamics. These decreased dynamics correlate with a kinetic isotope effect of 2.14 ± 0.42 for the catalytic reaction.

5.2 Introduction

The physical basis for enzyme function is closely associated with dynamic flexibility.[466] In the past, enzymes have been viewed as largely rigid molecules proceeding by 'lock and key' mechanisms of catalysis that disregard molecular motions within an enzymes structure.[467] Several studies have now shown that enzyme catalysis is based upon a long-range network of amino acids

that participate in catalytically relevant conformational changes.[468] The hierarchy of timescales relevant to enzyme catalysis-linked dynamics is vast, spanning the range of 10^{-12} to 10^{2} seconds, with some cases extending to years (Figure 33).[469] Techniques such as X-ray diffraction are critical for establishing a high-resolution baseline 'snapshot' of protein structure and sub-states, and time-resolved methods typically provide dynamic information with 100 ps time resolution.[470471] Usually X-ray data is supplemented with low-resolution high-precision spectroscopic (ie: Raman, IR, Circular Dichroism, and single-molecule fluorescence) information on the dynamics of one or a few sites of interest.[472–475] Much of the experimental data on catalysis-linked dynamics has come from CPMG relaxation dispersion NMR methods.[476–478] This is unsurprising because NMR delivers atomic level resolution at ^{1}H, ^{2}H, ^{13}C and ^{15}N sites on timescales ranging from picoseconds to seconds, all while following solution-phase dynamics under steady-state conditions.[479] High magnetic field NMR with cryogenically cooled probes is capable of studying the dynamics of proteins up to 100 kDa, and sometimes even larger depending on the system.[479–482] Despite being able to characterize the complete ensemble of conformations that are directly related to catalysis[483,300], NMR methods find themselves confined to a small set of reversible enzyme systems in order to circumvent substrate depletion.[484–486] Mass spectrometry-based approaches for investigating enzyme catalysis are capable of probing both steady-state and pre-steady state mechanisms that are 'out of reach' for NMR methods so to speak.[487,488] This is primarily achieved through time-resolved methods such as TRESI-MS which offer analogous timescales to that of stopped-flow optical spectroscopy.[281–283,489] TRESI-MS-coupled H/D exchange is a powerful method for probing the conformational dynamics of enzymes undergoing catalysis, and has provided a new model for catalysis-linked dynamics in the 'CPMG-inaccessible' chymotrypsin catalyzed hydrolysis of p-nitrophenyl acetate.[169]

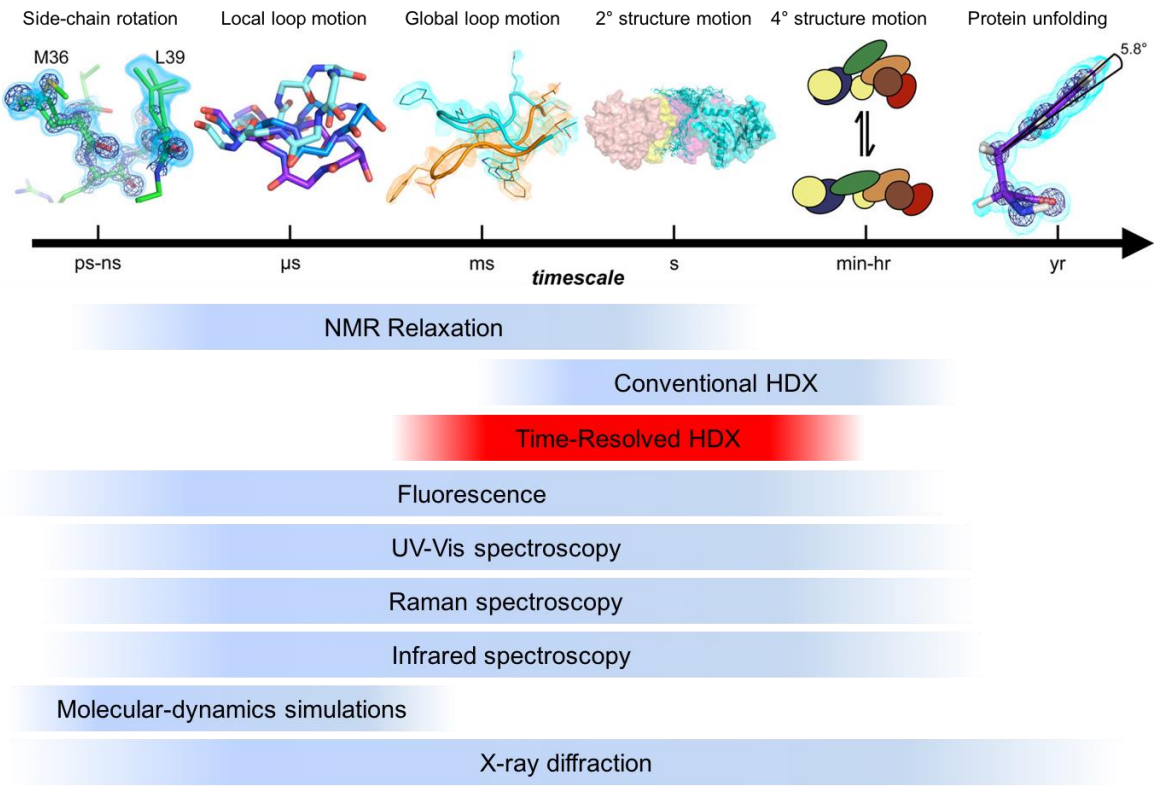

Figure 33. Timescales for the conformational dynamics of proteins. Picosecond-nanosecond motions involve small changes in torsion angles[483], with localized loop motions occurring on the microsecond timescale as seen with residual dipolar coupling NMR on the β1β2 loop of Ubiquitin.[490] Global loop motions occur in milliseconds and are in some cases rate-limiting for catalysis, which is the case protein tyrosine phosphatase 1B loop opening and closing.[491] Access to the central pore of the archaeal proteasome is dependent on movement of an N-terminal arm at a per seconds rate determined by NMR.[492] The Son of Sevenless protein complex when bound to two Ras molecules exhibits rearrangements that occur on the min-hour timescale in its protein-protein interfaces to modulate distinctly different catalytic states.[493] A kinetically trapped α-lytic protease structure stable on the timescale of years, will unfold on the scale of weeks with only a 6º deviation from planarity on Phe228.[494] This figure was adapted from Henzler-Wildman et. al.[495] and Bhabha et. al.[469]

In this work, we apply a similar TRESI-HDX-MS based approach to identify how dynamics influences the enormous rate enhancements associated with hydride transfers in yeast alcohol dehydrogenase (ADH).[452] This enzyme has been implicated in multiple studies to undergo quantum-mechanical tunneling via hydride transfer to nicotnamide adenine dinucleotide (NAD^+) during ethanol oxidation.[452,496] Hydrogen tunneling is a phenomenon where a particle can ignore a reaction energy barrier.[497] As is not typically seen with the heavier isotope deuterium, we exploit this by comparing the rates of reaction of ethanol turnover to deuterated ethanol, which yields a sizeable kinetic isotope effect. Time-resolved measurements of KIE's on ADH have previously been reported by Liuni et. al[489]; briefly they are measured by observing the appearance of NADH (666 *m/z*) and NADD (667 *m/z*) over the course of the reaction. Our new approach involves the addition of D_2O for HDX measurements on the ADH tetramer (147 kDa) as the enzyme turns over isotopically labeled and unlabeled ethanol, which may provide insights into the catalysis-linked dynamics associated with hydride transfers.

5.3 Experimental

5.3.1 Materials

Yeast alcohol dehydrogenase (A3263) , β-nicotinamide adenine dinucleotide hydrate (N7004), LC-MS grade ammonium hydroxide (44273), LC-MS grade ammonium acetate (73594), and Deuterium Oxide (99.99% D_2O) were purchased from Sigma Aldrich (St. Louis, MO) . Ethanol-1,1-D_2 was purchased from Cambridge Isotope Laboratories (Andover, MA). HPLC-grade methanol, ethanol, acetonitrile and hydrochloric acid were purchased from Fisher Scientific (Ottawa, ON). Ultrapure water was generated in-house using a Millipore Milli-Q Advantage A10 system (Billerica, MA). All solutions were pH adjusted using the S20 SevenEasy pH meter (Denver Instruments, Bohemia, NY).

5.3.2 Time-Resolved Device Fabrication

The time-resolved interface was constructed as per Liuni et al.[489] with some minor modifications. A 33 gauge stainless steel metal capillary (I.D. = 132.6 μm, O.D. = 203.2 μm, length = 18 cm, McMaster-Carr, Aurora, OH) served as both the outer capillary and electrospray capillary. The inner glass capillary (I.D. = 40 μm, O.D. =109.2 μm, length = 40 cm, Polymicro Technologies, Phoenix, AZ) was sealed and a notch was cut 2mm downstream from the sealed end using a CO_2-powered laser (*Versa*Laser™ Universal Laser Systems, Scottsdale, AZ). Upchurch PEEK fittings 1/16", a PEEK 3-way MicroTEE, and FEP tubing (1/16" OD x 0.009" ID and 1/32" OD x 0.005" ID) were purchased from IDEX (Oak Harbor, WA).

5.3.3 TRESI-MS of ADH

The TRESI device was interfaced directly into the commercial heated probe spray assembly of a Waters Synapt G1 HDMS Mass Spectrometer (Manchester, UK) equipped with an 8k quadrupole. Nitrogen gas was used for both the source and IMS region, and argon gas was used in the trap region of the mass spectrometer. Solutions were infused into the TRESI setup using two 1 mL Hamilton Gastight glass syringes (Reno, NV) by two Harvard 11 Elite syringe pumps (Holliston, Massachusetts). For all experiments, protein solutions were infused via 'syringe 1' into the inner capillary at a rate of 4 μL per minute. Deuterium oxide substrate solutions were infused at 16 μL per minute using 'syringe 2' for 80% deuterium labeling conditions. ADH was initially prepared as a 20 μM stock solution in 100 mM ammonium acetate (pH 7.0) and spin-desalted using a 7K MWCO zeba column (ThermoFisher Scientific, Grand Island, NY). A 10 μM ADH solution in the same buffer was then electrosprayed via syringe 1, with 100mM ammonium acetate buffer in syringe 2, resulting in a 2 μM effective ADH concentration. Source conditions were optimized to ensure maximal transmission of the apo-ADH tetramer providing a baseline for all

other experiments. A number of excellent reviews were used and outline the guidelines for electrospraying high molecular weight proteins.[498,499] The resulting source conditions were as follows: capillary 3.5 kV, sample cone 200 V, extraction cone 1.0 V, source temperature 125 °C, desolvation temperature 100 °C, desolvation gas flow 250 L h^{-1}, cone gas flow 25 L h^{-1}. The pressure in the source region was increased to 5 mBar . The trap and transfer collision energies were set to 6V and 2V respectively with a Trap pressure of $7.75x10^{-3}$ Bar. An enhanced duty cycle (EDC) mass value of 4000 was used to increase signal of the protein complex. Spectra were acquired from 2000-10,000 *m/z* for 3 minutes with a 2 second scan duration. All spectra were recorded in triplicate and mass spectral data was processed using MassLynx 4.1

5.3.4 Global TRESI-HDX-MS Measurements for ADH Catalysis

Global HDX studies were carried out on apo-ADH, holo-ADH, catalytically active ADH with ethanol, and with ethanol-1,1-D_2 independently of one another. All data was acquired for 10 time points with a reaction time range of 40 ms to 5 s. A baseline deuterium exchange dataset was acquired for apo-ADH using D_2O in 100mM ammonium acetate buffer. For holo-ADH 10 µM protein was incubated with 400 µM NAD^+ (80 µM effective concentration) and infused and mixed with D_2O in 100mM ammonium acetate buffer. For catalytically active ADH experiments, ethanol substrate at 250 mM (200 mM effective concentration) was added to the D_2O buffer and infused in syringe 2, while ADH preincubated with NAD^+ was in syringe 1. All kinetic runs were initiated after a 15 minute pre-equilibration period. This was established after observing a steady rise in mass on the protein upon initiating deuterium infusion, and is the result of the syringe pumps taking 15 minutes to reach stable optimal pressure.

5.4 Results

The apo-ADH TRESI mass spectrum (green overlay Figure 34) shows a tetramer distribution between 5000-6000 *m/z* with visible protein charge-states at 28^{+}-25^{+}, which is in line with other native ADH ESI-MS studies.[500] ADH at 10 µM was preincubated with 400 µM NAD^{+} and the resulting 40-fold excess of NAD^{+} co-factor yielded protein mass spectra populated by $ADH(NAD^{+})_{1\text{-}5}$, with the specific-binding state $ADH(NAD^{+})_{2}$, being the most intense (Figure 34 (top)). Previous studies investigating co-operative effects of NAD^{+} binding show a similar trend for a solutions containing 2 and 3 NAD^{+} per tetramer of ADH.[501] Once D_2O and substrate was introduced into the TRESI source, the flow was allowed to equilibrate at the 0mm position prior to starting a kinetic run. Mass spectra were acquired during this phase and a shift in mass is observed for both holo-ADH and catalytically active ADH, which is normally observed during pre-equilibration. This was done by plotting the shift in *m/z* versus scan number (Figure 34, bottom). The distribution and intensity for the catalytically active ADH-NAD^{+}-Ethanol complex however, experiences a shift with the maximum specific-binding state, $ADH(NAD^{+})_{4}$, becoming the most intense. No intensity shift was observed for holo-ADH.

Global HDX kinetics were measured at 0 mm to 5 mm, 10 mm, 20 mm, 50 mm, and 100 mm pullback of the inner capillary corresponding to reaction times of 40 ms, 87 ms 135 ms, 183 ms, 231 ms, 279 ms, 518 ms, 996 ms, 2431 ms, and 4823 ms. Figure 35 A-D depicts the observed mass shifts for apo-ADH, holo-ADH, active ADH with ethanol, and active ADH with ethanol-1,1-D_2 plotted as the change in mass:

$$\Delta Mass = Mass_{ADH}^{Deuterated} - Mass_{ADH}^{Native} \quad (23)$$

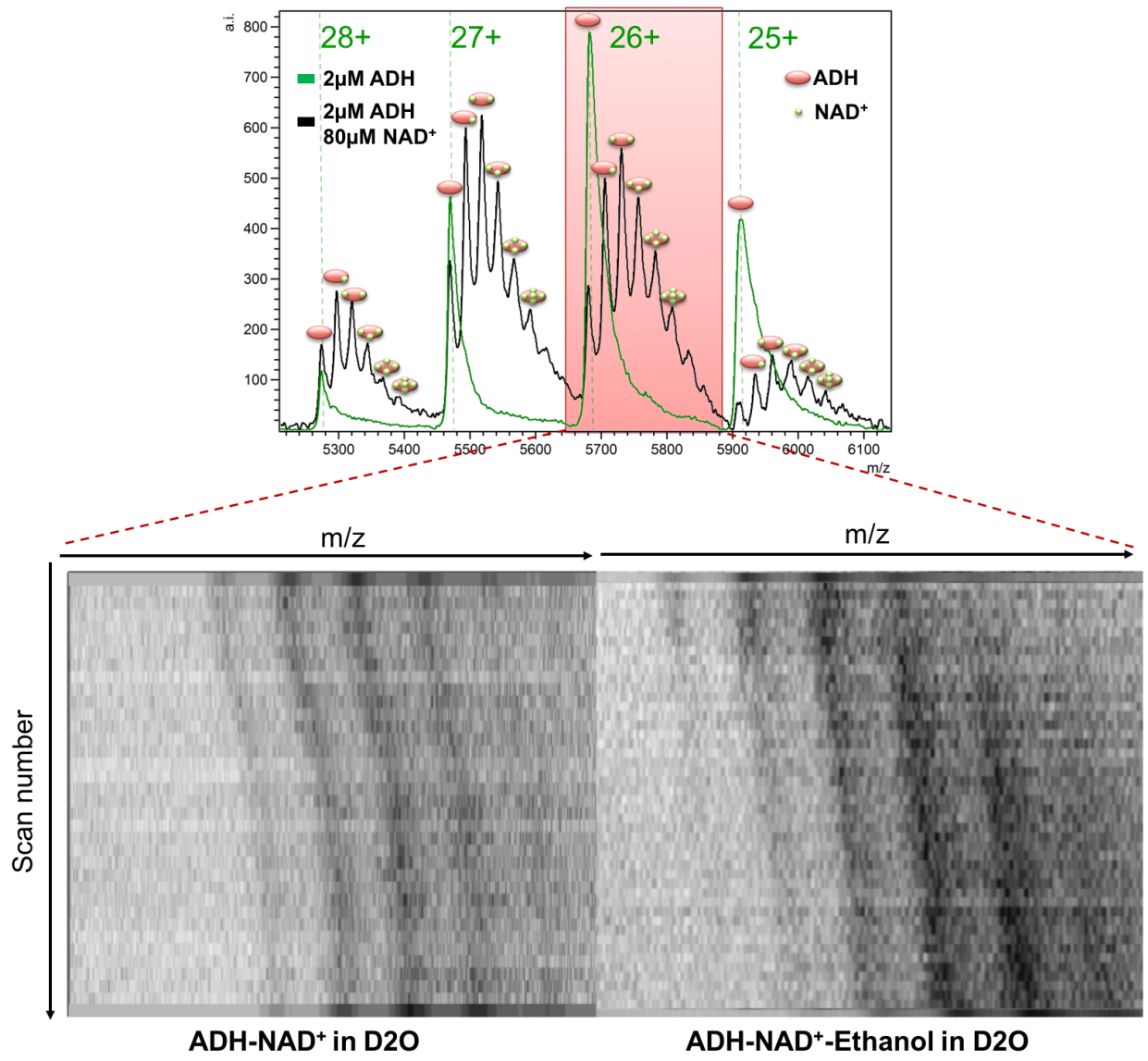

Figure 34. (Top) Overlaid spectra of apo-ADH and holo-ADH where red circles indicate the enzyme and green circles indicate the cofactor. Any enzyme-cofactor complexes with greater than 4 cofactor bound are attributed to nonspecific binding. (Bottom) Heat-maps for mass spectra acquired of the 26^+ charge state as D_2O equilibrates into the TRESI source (X-axis = *m/z*, Y-axis = scan number, Z-axis = intensity). Preferential population of the maximum specific binding state of $ADH(NAD^+)_4$ occurs only with the addition of ethanol. Deuterium-shifted ADH-NAD^+ distributions show no shift.

Kinetic curves were generated by fitting the data to a single exponential plus a line:

$$f(t) = y_0 + a(1 - exp(-k_{obs}^{amide}t) + (y_1 + (k_{obs}^{side-chain}t)) \quad (24)$$

where k_{obs}^{amide} is the contribution of backbone amide exchange, $k_{obs}^{side-chain}$ is the contribution of side-chain exchange, t is time in seconds, y_0 and y_1 are intercept values, and a is the amplitude. No $(NAD^+)_5$-bound data is shown for holo-ADH since signal intensities for that species were too low.

Visually interpreting the differences in rates from Figure 35 is challenging, therefore the HDX rates of all species are reported as fold-change values:

$$Fold\ Change_{Global\ HDX} = \frac{k_{obs}^{Global\ HDX}}{k_{ref}^{Global\ HDX}} - 1 \quad (25)$$

where $k_{obs}^{Global\ HDX}$ are the observed rates from holo-ADH, ethanol-ADH, and 1,1-D_2-ethanol-ADH . The observed global HDX rate for apo-ADH is used as $k_{ref}^{Global\ HDX}$. Figure 36 shows fold-change Global HDX rates for apo-,holo-, ethanol-, and 1,1-D_2-ethanol-ADH species. No bar is present for apo-ADH as it used as the reference rate. The amount of deuterium uptake for the initial timepoint in the Global HDX series is defined as the 'burst'. Figure 37A depicts fold-change bursts for all species, with colours representing the individual experiments. Similarly in Figure 37B fold-change amplitudes, which refers to the total amount of deuterium uptake from the first point to the last point, are reported. Values from Figures 36, and 37 are summarized in Table 2.

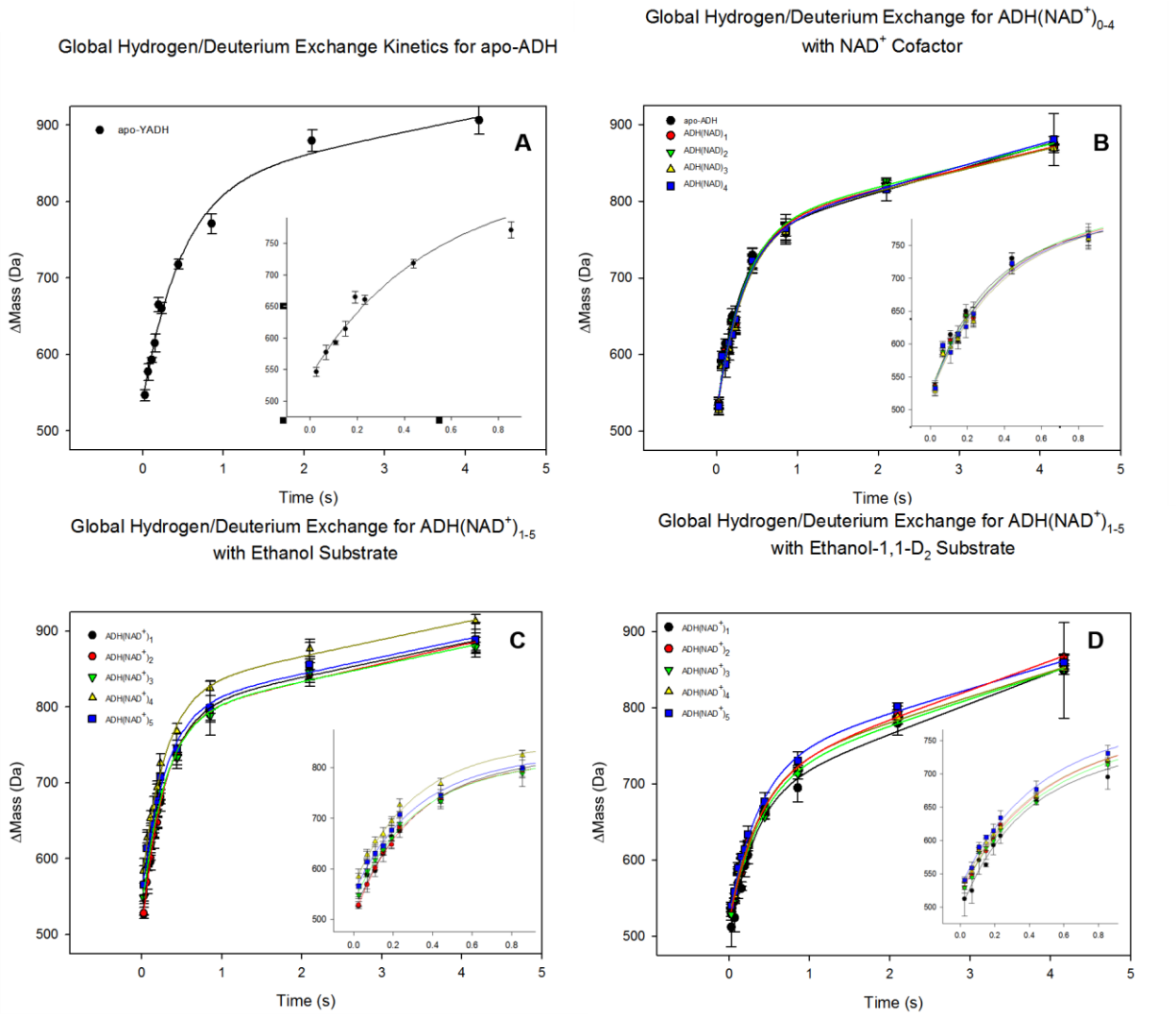

Figure 35. Global HDX rate curves. Each point represents three 3 minute acquisition of ADH at a specific reaction corresponding to positional pullback of the inner capillary in the TRESI source. Insets show early reaction kinetics. (A) HDX kinetics for apo-ADH. (B) HDX kinetics for holo-ADH. At 80μM NAD^+, kinetics were measured for up to 4-bound protein-cofactor complexes. The "apo"-ADH in this plot is not truly free enzyme, as binding and release of cofactor still occurs. (C) HDX kinetics for active ADH with ethanol shows differences in rate as the bound –state of ADH increases from 1-4. (D) HDX kinetics for active ADH with Ethanol-1,1-D_2 shows an overall decreased rate when compared to unlabeled ethanol.

		NAD_0	NAD_1	NAD_2	NAD_3	NAD_4	NAD_5
Apo-ADH	Rate (s^{-1})	2.10±0.40	-	-	-	-	-
	Amplitude	360±20	-	-	-	-	-
	Burst	546±7	-	-	-	-	-
holo-ADH	Rate (s^{-1})	3.52±0.63	2.97±0.61	3.00±0.63	2.96±0.60	3.14±0.82	-
	Amplitude	339±12	334±6	339±7	341±8	348±36	-
	Burst	537±8	536±5	535±7	528±6	532±11	-
ADH-ethanol	Rate (s^{-1})	-	3.44±0.68	3.79±0.29	3.42±0.33	3.45±1.52	3.41±0.64
	Amplitude	-	358±13	355 ±11	330±8	328±19	323±34
	Burst	-	526±1	528±7	548±4	584±16	566±25
ADH-ethanol-1,1-D_2	Rate (s^{-1})	-	3.23±0.54	2.73±0.35	2.57±0.29	2.59±0.20	2.63±0.36
	Amplitude	-	337±68	337±5	322±10	315±6	319±10
	Burst	-	512±26	529±3	529±8	537±5	541±5

Table 1. Global HDX rates, amplitudes, and bursts for apo-, holo-, ADH-ethanol, and ADH-ethanol-1,1-D_2 taken from data in Figure 35

5.5 Discussion

Yeast alcohol dehydrogenase is a homo-tetramer with 347 amino acids and has a calculated mass of 147 396 Da.[502] Added to this are 8 Zn atoms, 4 of which are involved in catalysis and the other 4 are structural. The enzyme can accommodate 4 nicotinamide adenine dinucleotide co-factors, each are 664 Da and bind to the carboxy-terminal end of the Rossman fold near the center of the tetramer.[503] We report a deconvoluted mass of 147839±185 Da for the ADH tetramer observed on the Synapt. When 8 Zinc atoms are subtracted, the deconvoluted mass is 147316±185 Da which correlates quite well to the calculated mass reported above. In a previous study by Liuni et. al.[489] high NAD^+ concentrations thwarted any prospect of measuring steady-state reaction kinetics on the native enzyme due to the deleterious effects of NAD-adduction on the ADH charge-state dustribution. Here, we circumvent this problem by lowering the effective concentration of NAD^+ to 80 µM, maintaining a 10–fold excess of cofactor per tetramer. Under these conditions, mass spectral quality was only slightly impacted, as seen in Figure 34. The effect of NAD^+-binding on ADH in Figure 34 is that of a statistical distribution with $ADH(NAD^+)_2$ being the most intense species. Recent crystallographic data on ADH (2.4 Å resolution, PDB entry 4W6Z) raises questions on the possibility of cooperativity in the catalytic mechanism due to a never-before-seen asymmetry between the dimeric units; with one in an open and one in a closed conformation in the NAD-binding domain.[504] With no evidence of negative cooperativity from coenzyme binding or during catalysis[505,506], the different subunit structures represent energetically accessible conformations that could be visited during catalysis. Mass spectrometry has a distinct advantage for probing cooperativity because all the ligation states can be monitored simultaneously.[501] In Figure 34 (bottom) the addition of ethanol caused the statistical distribution to shift from $ADH(NAD^+)_2$ to $ADH(NAD^+)_4$, possibly providing evidence for a cooperative effect caused by

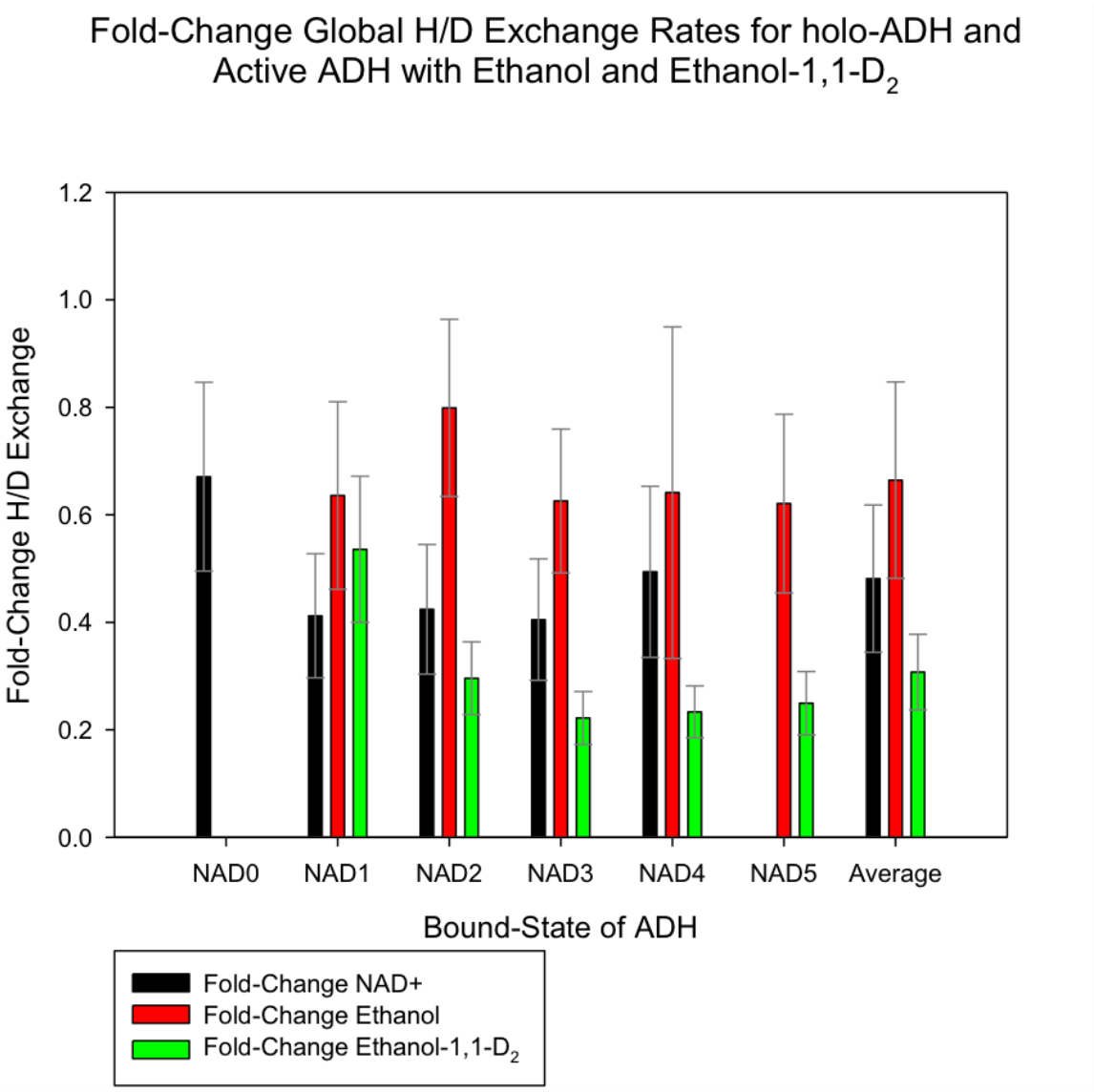

Figure 36. Fold-change Global HDX rates for holo-ADH, active ADH with ethanol, and active ADH with ethanol-1,1-D_2. Overall, dynamics for ethanol catalysis remained similar for each bound-state, while ethanol-1,1-D_2 rates decreased incrementally for each NAD^+-bound. Differences for all three cases are also apparent in their average fold-change.

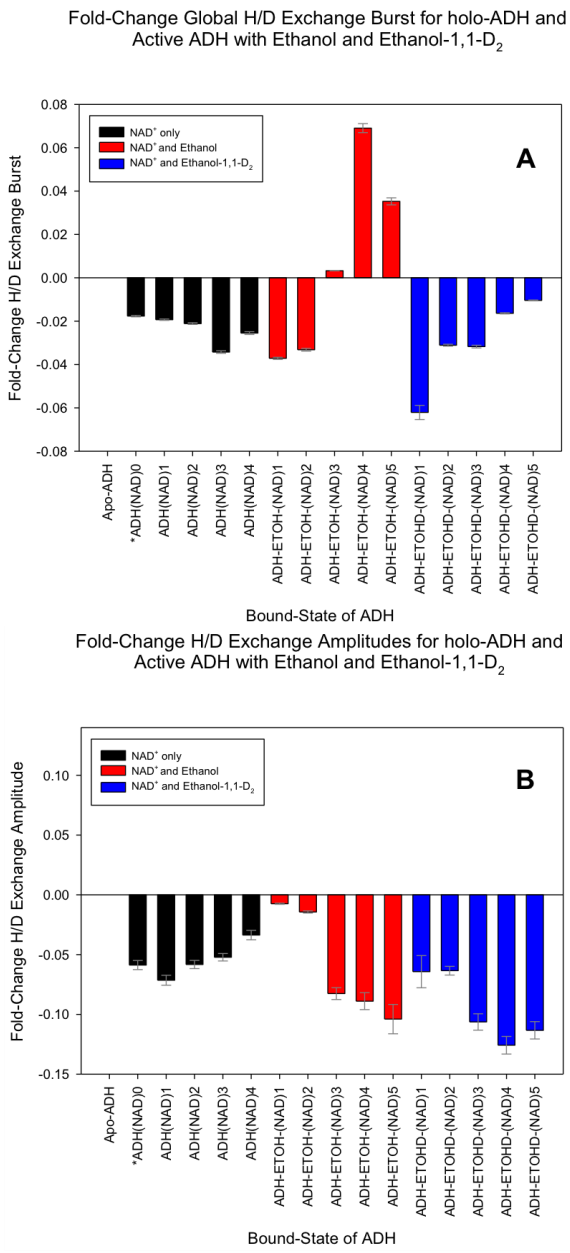

Figure 37. Fold-change plots for HDX Burst and Amplitude. (A) The initial deuterium uptake for the 'NAD only' series (black) shows a decreasing trend in the initial dynamics associated with cofactor binding. The 'NAD+ and Ethanol' series shows a drastic increase in initial deuterium uptake with the maximum specific binding state ADH-ETOH(NAD^+)$_4$ being the most dynamic. The 'NAD+ and Ethanol-1,1-D_2' series shows an increasing trend, but displays markedly less initial dynamics than ethanol catalysis. (B) Fold-change amplitudes for 'NAD only' shows incremental increase in deuterium exchange, while 'NAD+ and Ethanol' and 'NAD+ and Ethanol-1,1-D_2' series decrease drastically relative to apo-ADH.

		NAD_0	NAD_1	NAD_2	NAD_3	NAD_4	NAD_5
Apo-ADH	F-C Rate	0	-	-	-	-	-
	F-C Amplitude	0	-	-	-	-	-
	F-C Burst	0	-	-	-	-	-
holo-ADH	F-C Rate	0.67±0.18	0.41±0.12	0.42±0.12	0.40±0.11	0.49±0.16	-
	F-C Amplitude	-0.0587± 3.83E-03	-0.0715± 4.17E-03	-0.0583± 3.44E-03	-0.0522± 3.14E-03	-0.0337± 3.93E-03	-
	F-C Burst	-0.0177± 3.39E-04	-0.0193± -3.19E-04	-0.0211± 3.89E-04	-0.0343± 5.99E-04	-0.0255± 6.39E-04	-
caADH-ethanol	F-C Rate	-	0.64±0.17	0.80±0.16	0.63±0.13	0.64±0.31	0.62±0.17
	F-C Amplitude	-	-0.0075± 4.91E-04	-0.0143± 6.36E-04	-0.0826± 4.83E-05	-0.0889± 2.09E-03	-0.1040± 1.62E-03
	F-C Burst	-	-0.0372± 4.91E-04	-0.0332± 6.36E-04	0.0032± 4.83E-05	0.0690± 2.09E-03	0.0353± 1.62E-03
caADH-1,1-D_2 ethanol	F-C Rate	-	0.54±0.14	0.30±0.07	0.22±0.05	0.23±0.05	0.25±0.06
	F-C Amplitude	-	-0.0643± -1.35E-02	-0.0635± -3.65E-03	-0.1064± -6.82E-03	-0.1258± -7.38E-03	-0.1133± -7.22E-03
	F-C Burst	-	-0.0621± -3.27E-03	-0.0311± -4.51E-04	-0.0318± -6.27E-04	-0.0164± -2.71E-04	-0.0104± -1.64E-04

Table 2. Fold-Change ("F-C") rates, amplitudes and bursts for apo-, holo-, caADH-ethanol, and caADH-1,1-D_2-ethanol (ca. stands for catalytically active) taken from data in Figure 36 and 37 (n=3).

ethanol binding. This was seen across all charge states, and best displayed using the 26^{+} ion as it was the most intense. To our knowledge there are no reports on positive cooperativity for ADH. Cooperativity studies are typically done by titrations, and would need to be applied here for more conclusive evidence.

The criteria for interpreting the conformational dynamics of catalytically active enzymes from global hydrogen deuterium exchange data was already described previously.[169] Briefly, the global HDX rate is in averaged measure of the frequency of hydrogen bond breaking, which translates into how fast the enzyme is sampling conformational space. The amplitude describes the number of sites that become available for exchange on the timescale of the measurement, which is the size of the conformational space or 'landscape'. A new parameter introduced here is the initial deuterium uptake at the start of the measurement, or 'burst'. This can be attributed to very fast exchanging amides or side chains that become available during catalysis, and is thus a measure of the initial dynamics of the system.

Figure 35 A-D represents the 'standard' way of plotting Global HDX data. A notable feature is the faster rate of exchange for ADH$(NAD^{+})_4$ with ethanol in comparison to all other enzyme-cofactor species (Figure 35C). Deuterium transfer also shows an overall depressed global rate of exchange (Figure 35D). In Figure 35B, there is also a substantial decrease in deuterium uptake for the enzyme-cofactor complexes. Parameters such as exchange rate, amplitude and burst are extracted and shown in Table 1. Fold-change analysis (Figure 36, Figure 37AB), of the extracted parameters allows a comparison between native state ADH with catalytically active ADH, offering an opportunity to gauge the subtle differences in dynamics between 'acitve' and 'inactive' enzyme.

5.5.1 The Dynamics of the ADH-NAD^+ Complex

Building on the conformational changes of cofactor binding discussed above, as well as a previous conventional H/D exchange study which reported substantial 'rigidification' of the ADH-NAD complex when compared to free enzyme owing to decreased deuterium uptake[507], our results show a similar behavior. Fold-change global HDX rates for the ADH-$(NAD^+)_n$ (n=0-4) species shows on average a higher rate of conformational sampling than free-enzyme (Figure 36). This can be attributed to a rapid equilibrium between free enzyme and cofactor, noting the high dissociation constant for NAD^+ (920μM).[504] The n=0 species also experiences this rapid equilibrium and is not entirely free enzyme which can explain its difference in dynamics. The number of sites that become available initially for enzyme-cofactor binding is markedly lower than free-enzyme. In Figure 37A the ADH-$(NAD^+)_n$ (n=0-4) series experiences a downward sloping trend with the n=3 and n=4 species being the least dynamic initially. This supports the observed rigidfication seen by conventional measurements (minutes to hours timescale) but on a millisecond-timescale measurement. Measurements on the millisecond-timescale are sensitive enough to report on loop dynamics in relatively large proteins.[303] The observations here suggest fast exchangers such as side-chains and amides are less available for HDX and are being sequestered more often in the closed-state. In Figure 37B amplitudes for the enzyme-cofactor series are all lower than free-enzyme showing a slight negative trend (n=0,1) followed by a more positive trend (n=2-4).

5.5.2 The Dynamics of Catalytically Active ADH

Global H/D exchange rates show that on average, ADH takes up deuterium 1.27 ± 0.07 s^{-1} times faster when catalyzing hydrogen transfer compared to deuterium transfer and can be seen in Figure 36. These dynamics correlate with a measured kinetic isotope effect of 2.14 ± 0.42 for the

catalytic reaction (data not shown). The most notable feature in Figure 36 is the sharp downward trend in fold-change as the enzyme-cofactor occupancy increases for the ADH-$(NAD+)_n$-1,1-D_2-Ethanol from 1-5. This is a direct measure of catalysis-linked dynamics for yeast alcohol dehydrogenase, owing to a single heavy-atom isotopic substitution in the active site. The magnitude of measured KIE is is still quite substantial, imparting a 2-fold reduction in catalytic rate on ADH, even though the rate-determining release of NADH/D cofactor masks the true intrinsic KIE. Amide hydrogens and side-chains in highly open and available conformations for deuterium exchange are abundant for ethanol catalysis, imparting a maximum overall burst for the n=4 species of ADH-$(NAD+)_n$-Ethanol. The ADH-$(NAD+)_n$-1,1-D_2-Ethanol series trends higher, but is much lower in comparison to ethanol catalysis, which is consistent with the KIE measurements made. Fold-change amplitudes for ethanol and ethanol-1,1-D_2 describe a decreasing trend in conformational space as seen in Figure 37B. Overall, the differences in dynamics between the substrate-free and catalytically active substrate-bound states along with a decreasing size of the conformational space on ligand binding provides compelling evidence for an induced-fit model of catalysis-linked dynamics in ADH.

5.6 Conclusions

These data provide unambiguous evidence that the conformational dynamics of ADH are directly linked to the catalytic reaction coordinate, representing a key piece of evidence in the long-standing debate about the role (or lack thereof) for conformational dynamics in enzyme catalysis. The induced fit nature of ADH catalysis is especially pronounced for Ethanol-1,1-D_2. Previous studies have shown with great detail that in order for hydrogen tunneling to occur the enzyme must adopt a tunneling ready state owing to donor-acceptor-distance sampling.[508] This sampling rate is much more pronounced for deuterium than hydrogen, owing to differences in the zero-point energy

for the bond. Localizing specific areas undergoing H/D exchange could provide a discrete measure of the dynamics of tunneling. Also peptide level H/D exchange on cofactor binding should shed more light on recent evidence that suggests the possibility for cooperative conformational transitions caused by cofactor biding.[504] Averaging all catalytically active states and enzyme cofactor species still show remarkable differences in dynamics. In order elevate mass spectrometry to that of near-NMR status for catalysis-linked dynamic studies, a spatially resolved approach must be taken.

Chapter 6

Conclusions and Future Work

6.1 Summary and Impact

The work presented here displays the versatility of coupling front-end analytical methods to mass spectrometers for uncovering new and exciting insights in narcotics detection, protein folding, enzyme catalysis, and catalysis-linked dynamics. In Chapter 1 fundamental techniques such as HPLC, Ion mobility, and hybrid mass spectrometers are introduced and categorized into three significant zones: pre-ionization, in-ionization, and post ionization, representing areas on a mass spectrometer where the bulk of analytical advancements have occurred. Focus is given to such front-end methods as ion mobility – specifically pertaining to trace-compound detectors, and time-resolved methods for characterizing proteins and enzymes.

In Chapter 2, a commercially available TCD-IMS was interfaced to a triple quadrupole mass spectrometer, providing a second dimension to previously poorly characterized opium samples on standalone-TCD-IMS instruments. This IMS-coupled-MS method identified a novel marker for opium detection in negative ion mode, a mode typically used for explosives detection. Full-characterization of the highly complex opium solutions in sub-par matrices demonstrates the robustness of a TCD-IMS-MS system. The impact of these results highlights the usefulness of a front-end ion mobility method to national security and law-enforcement agencies. The unambiguous linking of IMS detection with mass-specific assignment of illicit substances negates an often argued ‘grey area’ during prosecutions on whether TCD’s are capable confirming the identity of illegal narcotics. A small bench top IMS-MS placed at high-volume nodes of entry into

Canada such as airports, border crossings, and seaports adds an additional layer of detection for illicit substances, decreasing their ability to do harm in Canadian society.

In Chapter 3, time-resolved ESI coupled with traveling-wave ion mobility was used to settle a long-standing debate on whether kinetic unfolding intermediates or equilibrium unfolding intermediates are distinctly different for the well-characterized model protein cytochrome c. Substantially different kinetic behavior could be determined from deviations in IMS peak height from peak intensity vs reaction time profiles for the 10^+ and 8^+ species. High, intermediate, and low charge states for both kinetic and equilibrium unfolding showed identical structural similarities when compared side-by-side, suggesting that equilibrium and kinetic species are identical. The TRESI-IMS-MS method uniquely delivers structural information for species that are transiently populated, providing critical insights to cytochrome c unfolding landscapes, and is a valuable new technology for protein folding studies. The impact of this method adds an additional tool to help shed light on the mechanisms for proteopathies such as Alzheimer's, Parkinson's and a wide range of other disorders; which are thought to gain pathogeny through misfolded proteins. This also has impact on the cattle industry for understanding and preventing mad cow disease, which can save millions of dollars and avoid economic catastrophes.

Cumbersome analytical methods for measuring kinetic isotope effects have led to a decline in this remarkably powerful technique - which can infer upon enzyme mechanism and transition state structure. In Chapter 4, a TRESI-MS method was applied to illustrate the simplistic measurement of kinetic isotope effects in enzyme reactions. A large deuterium isotope effect of 2.19 ± 0.05 for yeast alcohol dehydrogenase oxidation of ethanol demonstrated the methods usefulness in characterizing a predominantly steady-state reaction. The precision of an internal competition approach for measuring an intrinsic $^{12}C/^{13}C$ KIE associated with the pre-steady state acylation of

chymotrypsin during hydrolysis of pNPA proved to be essential, achieving a KIE of 1.09 ± 0.02. With characterization of steady-state and pre-steady state systems, TRESI-MS has established itself as versatile tool for measuring KIE's with the potential for higher-level characterization of enzyme mechanism, transition states, and catalysis-linked dynamics. The impact of these results play an important role in moving towards a rational-based approach for drug design. With knowledge of a biological targets transition state structure, molecules complimentary in shape can be used as highly effective inhibitors, which in turn results in desired therapeutic effects with reduced side effects and less financial strain on clinical trials development.

In Chapter 5, a significant contribution is made in the long-standing debate on whether or not enzyme catalysis is modulated by conformational dynamics. Ascribing to the results in the previous chapter it was thought that if a single isotopic substitution could impart an enormous depression on the catalytic rate, there should be an appreciable change in dynamics as well if catalysis and dynamics are in fact linked. The TRESI-HDX-MS approach was applied, which monitored the global dynamics of yeast alcohol dehydrogenase during catalysis, revealed significant differences between the dynamics for ethanol and ethanol-1,1-D_2. Global H/D exchange rates showed on average ADH takes up deuterium 1.27 ± 0.07 s^{-1} times faster when catalyzing hydrogen transfer compared to deuterium transfer. Overall amplitudes for deuterium exchange showed marked decreases for catalytically active species in both cases, providing compelling evidence for an induced-fit model of catalysis linked dynamics in ADH. A surprising observation to add was the apparent cooperative effect for ethanol binding, which demonstrates the usefulness of a TRESI-MS based approach for monitoring enzyme catalysis. The impact of these results aids in our fundamental understanding of enzymes. High-throughput computer docking incorporating dynamic information will increase the likely hood of finding better lead

compounds for drug-development. Understanding the link between catalysis and dynamics may help humans design new and improved enzymes, which could revolutionize food manufacturing, brewing, and therapeutics.

6.2 Future Work

The application of front-end mass spectrometric methods for enhancing the analytical throughput of mass spectrometers is described in multiple areas of this dissertation. In pertaining to ion mobility of narcotics, several improvements to the method can be made. When applying the dual-gating technique peaks that are not visible due to the low resolution analysis of ion mobility, become visible in the mass spectrometer. Scanning through the time domain across a peak in dual-gate mode reveals both major and minor components. The intensities of these minor components can be used to reconstruct drift times from *m/z* peak intensities, providing a new way to characterize mobility of low-level interferences or analytes of interest. The system is also capable of rapid classification of new and emerging narcotics and explosives, reducing downtime for countermeasures and convictions for law-enforcement agencies. The TCD-IMS-MS system would also benefit from a high resolution mass spectrometer for increased sensitivity and selectivity.

For time-resolved ESI a number of fundamental improvements can be made to elevate the technique for greater understanding of protein folding, protein-protein interactions and catalysis linked dynamic studies. Populating transient kinetic intermediates during protein folding is a salient feature of the TRESI method, however, not much can be said about these intermediates without additional measurable factors. Temperature for one is a missing link that would connect theses intermediates to key thermodynamic factors such as ΔG (change in free energy), ΔH (change in enthalpy), and ΔS (change in entropy) and energies of activation; providing unprecedented detail of the protein folding energy landscape. A thermostated time-resolved Electrospray ionization

source is relatively simple to craft, by way of a closed loop liquid bath that surrounds the electrospray capillary, allowing for discrete biological zone (5-50°C) temperature controlled reactions. Shi et. al has recently shown a similar application for probing conformational changes in substance p by ion mobility spectrometry, but was only able to monitor transitions from seconds to minutes[509]. A thermostated-TRESI combined with ion mobility separation offers the added benefit studying transiently populated protein conformers on the millisecond timescale, for a more coarse-grained physical and energetic landscape of protein folding.

Chapter 3 noted that a pH jump unfolding HDX-MS experiment would not be suitable for probing the conformations of cytochrome c, owing to conventional HDX thinking, which is loss of dynamic information at higher pH due to back-exchange. This is true and only if the rate of exchange is faster than the rate at which you are measuring – or in the case of the TRESI source – mixing. A review of fundamental HDX manuscripts[148,152,510] details the rates at which HDX occurs on unstructured model peptides and polypeptides as a function of pH. The plots in Figure 38A and 38B show exchange rates (s^{-1}) for amide backbones as well as side-chains from the literature and associated threshold TRESI mixing rates (s^{-1}) at neutral pH for two fixed positions, 0mm and 5mm.This shows that for the most part, initial global hydrogen deuterium exchange dynamics are governed by backbone amides and most side chains. As the reaction proceeds backbone amide hydrogens become susceptible to back exchange and loss of the label, while some side-chains remain well within range for longer mixing times. The implications for this impact all global HDX measurements that employ a continuous labeling approach with no quenching. This hypothesis can be tested by performing global hydrogen deuterium exchange on a small protein that is susceptible to ETD/ECD non-ergotic fragmentation yielding a high-sequence coverage peptide map where the deuterium label can be mapped.

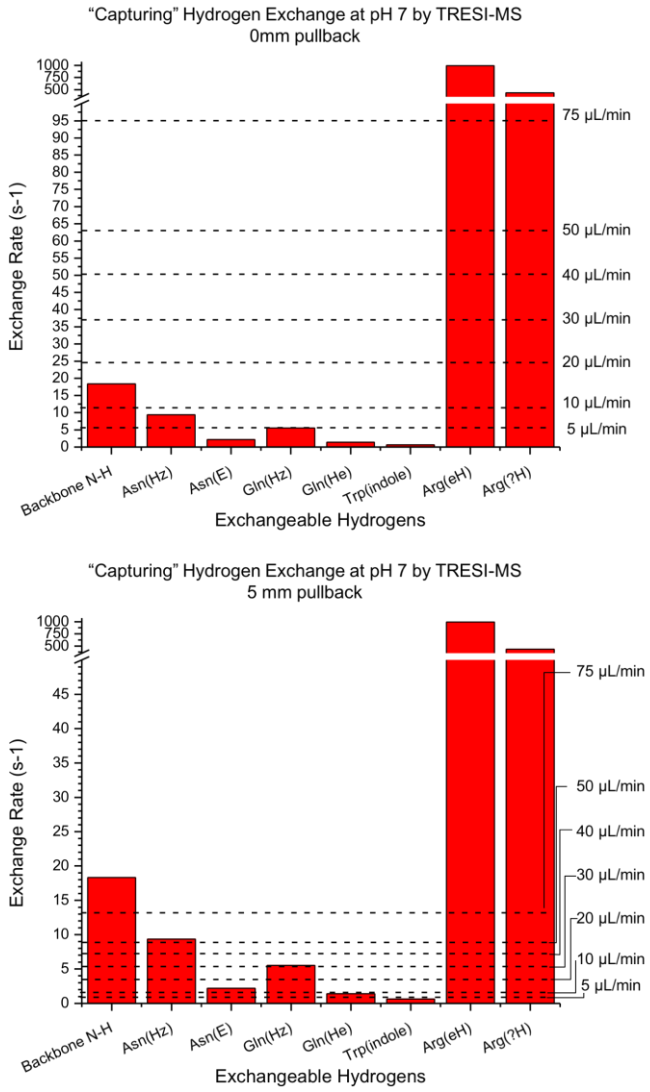

Figure 38. Threshold mixing values for measuring levels of hydrogen deuterium exchange (pH 7.0, 25°C) on several sites with known intrinsic exchange rates. (A) At 0mm pullback, the time-resolved mixer offers the highest resolution mixing, capturing most side-chains and backbone amide hydrogens at values above 20µL/min. At 10µL/min the ability to properly measure hydrogen exchange at backbone amides is lost, as the rate of mixing is less than the intrinsic rate of exchange. (B) TRESI mixing for 5mm pullback. At this stage back-exchange on unstructured amide hydrogens is likely and as well as most side chains except for Gln and Trp.

References

(1) Thomson, J. J. *Rays of Positive Electricity and Their Application to Chemical Analyses*; Longmans, Green and Company, 1921; Vol. 1.

(2) Fenn, J. B. Electrospray Wings for Molecular Elephants (Nobel Lecture). *Angew. Chem. Int. Ed.* **2003**, *42* (33), 3871–3894.

(3) McKay, A. R.; Ruotolo, B. T.; Ilag, L. L.; Robinson, C. V. Mass Measurements of Increased Accuracy Resolve Heterogeneous Populations of Intact Ribosomes. *J. Am. Chem. Soc.* **2006**, *128* (35), 11433–11442.

(4) Snijder, J.; Rose, R. J.; Veesler, D.; Johnson, J. E.; Heck, A. J. R. Studying 18 MDa Virus Assemblies with Native Mass Spectrometry. *Angew. Chem. Int. Ed.* **2013**, *52* (14), 4020–4023.

(5) Pandey, A.; Mann, M. Proteomics to Study Genes and Genomes. *Nature* **2000**, *405* (6788), 837–846.

(6) Chace, D. H. Mass Spectrometry in the Clinical Laboratory. *Chem. Rev.* **2001**, *101* (2), 445–478.

(7) Eller, K.; Schwarz, H. Organometallic Chemistry in the Gas Phase. *Chem. Rev.* **1991**, *91* (6), 1121–1177.

(8) Hillenkamp, F.; Peter-Katalinic, J. *MALDI MS: A Practical Guide to Instrumentation, Methods and Applications*; John Wiley & Sons, 2013.

(9) Knochenmuss, R.; Zenobi, R. MALDI Ionization: The Role of In-Plume Processes. *Chem. Rev.* **2003**, *103* (2), 441–452.

(10) Soltwisch, J.; Jaskolla, T. W.; Hillenkamp, F.; Karas, M.; Dreisewerd, K. Ion Yields in UV-MALDI Mass Spectrometry As a Function of Excitation Laser Wavelength and Optical and Physico-Chemical Properties of Classical and Halogen-Substituted MALDI Matrixes. *Anal. Chem.* **2012**, *84* (15), 6567–6576.

(11) Cohen, S. L.; Chait, B. T. Influence of Matrix Solution Conditions on the MALDI-MS Analysis of Peptides and Proteins. *Anal. Chem.* **1996**, *68* (1), 31–37.

(12) Shevchenko, A.; Jensen, O. N.; Podtelejnikov, A. V.; Sagliocco, F.; Wilm, M.; Vorm, O.; Mortensen, P.; Shevchenko, A.; Boucherie, H.; Mann, M. Linking Genome and Proteome by Mass Spectrometry: Large-Scale Identification of Yeast Proteins from Two Dimensional Gels. *Proc. Natl. Acad. Sci.* **1996**, *93* (25), 14440–14445.

(13) Turnbull, J. E.; Field, R. A. Emerging Glycomics Technologies. *Nat. Chem. Biol.* **2007**, *3* (2), 74–77.

(14) Schiller, J.; Suss, R.; Fuchs, B.; Muller, M.; Zschornig, O.; Arnold, K. MALDI-TOF MS in Lipidomics. *Front. Biosci.-Landmark* **2007**, *12*, 2568–2579.

(15) Larsen, M. R.; Thingholm, T. E.; Jensen, O. N.; Roepstorff, P.; Jørgensen, T. J. D. Highly Selective Enrichment of Phosphorylated Peptides from Peptide Mixtures Using Titanium Dioxide Microcolumns. *Mol. Cell. Proteomics MCP* **2005**, *4* (7), 873–886.

(16) Beavis, R. C.; Chait, B. T. Rapid, Sensitive Analysis of Protein Mixtures by Mass Spectrometry. *Proc. Natl. Acad. Sci.* **1990**, *87* (17), 6873–6877.

(17) Cornett, D. S.; Reyzer, M. L.; Chaurand, P.; Caprioli, R. M. MALDI Imaging Mass Spectrometry: Molecular Snapshots of Biochemical Systems. *Nat. Methods* **2007**, *4* (10), 828–833.

(18) Williams, T. L.; Andrzejewski, D.; Lay Jr., J. O.; Musser, S. M. Experimental Factors Affecting the Quality and Reproducibility of MALDI TOF Mass Spectra Obtained from Whole Bacteria Cells. *J. Am. Soc. Mass Spectrom.* **2003**, *14* (4), 342–351.
(19) Demeure, K.; Quinton, L.; Gabelica, V.; De Pauw, E. Rational Selection of the Optimum MALDI Matrix for Top-Down Proteomics by In-Source Decay. *Anal. Chem.* **2007**, *79* (22), 8678–8685.
(20) Chen, G.; Pramanik, B. N. LC-MS for Protein Characterization: Current Capabilities and Future Trends. *Expert Rev. Proteomics* **2008**, *5* (3), 435–444.
(21) Wang, H.; Hanash, S. Multi-Dimensional Liquid Phase Based Separations in Proteomics. *J. Chromatogr. B* **2003**, *787* (1), 11–18.
(22) Whitehouse, C. M.; Dreyer, R. N.; Yamashita, M.; Fenn, J. B. Electrospray Interface for Liquid Chromatographs and Mass Spectrometers. *Anal. Chem.* **1985**, *57* (3), 675–679.
(23) Peschke, M.; Verkerk, U. H.; Kebarle, P. Features of the ESI Mechanism That Affect the Observation of Multiply Charged Noncovalent Protein Complexes and the Determination of the Association Constant by the Titration Method. *J. Am. Soc. Mass Spectrom.* **2004**, *15* (10), 1424–1434.
(24) Kebarle, P.; Verkerk, U. H. On the Mechanism of Electrospray Ionization Mass Spectrometry (ESIMS). In *Electrospray and MALDI Mass Spectrometry*; Cole, R. B., Ed.; John Wiley & Sons, Inc., 2010; pp 1–48.
(25) Taylor, G. I.; McEwan, A. D. The Stability of a Horizontal Fluid Interface in a Vertical Electric Field. *J. Fluid Mech.* **1965**, *22* (01), 1–15.
(26) Lord Rayleigh F.R.S. On the Equilibrium of Liquid Conducting Masses Charged with Electricity. *Philos. Mag. Ser. 5* **1882**, *14* (87), 184–186.
(27) Smith, J. N.; Flagan, R. C.; Beauchamp, J. L. Droplet Evaporation and Discharge Dynamics in Electrospray Ionization†. *J. Phys. Chem. A* **2002**, *106* (42), 9957–9967.
(28) Gomez, A.; Tang, K. Charge and Fission of Droplets in Electrostatic Sprays. *Phys. Fluids 1994-Present* **1994**, *6* (1), 404–414.
(29) Taflin, D. C.; Ward, T. L.; Davis, E. J. Electrified Droplet Fission and the Rayleigh Limit. *Langmuir* **1989**, *5* (2), 376–384.
(30) Dole, M.; Mack, L. L.; Hines, R. L.; Mobley, R. C.; Ferguson, L. D.; Alice, M. B. Molecular Beams of Macroions. *J. Chem. Phys.* **1968**, *49* (5), 2240–2249.
(31) Schmelzeisen-Redeker, G.; Bütfering, L.; Röllgen, F. W. Desolvation of Ions and Molecules in Thermospray Mass Spectrometry. *Int. J. Mass Spectrom. Ion Process.* **1989**, *90* (2), 139–150.
(32) Iribarne, J. V.; Thomson, B. A. On the Evaporation of Small Ions from Charged Droplets. *J. Chem. Phys.* **1976**, *64* (6), 2287–2294.
(33) Loscertales, I. G.; Mora, J. F. de la. Experiments on the Kinetics of Field Evaporation of Small Ions from Droplets. *J. Chem. Phys.* **1995**, *103* (12), 5041–5060.
(34) Fernandez de la Mora, J. Electrospray Ionization of Large Multiply Charged Species Proceeds via Dole's Charged Residue Mechanism. *Anal. Chim. Acta* **2000**, *406* (1), 93–104.
(35) Konermann, L. A Minimalist Model for Exploring Conformational Effects on the Electrospray Charge State Distribution of Proteins. *J. Phys. Chem. B* **2007**, *111* (23), 6534–6543.
(36) Liuni, P.; Wilson, D. J. Understanding and Optimizing Electrospray Ionization Techniques for Proteomic Analysis. *Expert Rev. Proteomics* **2011**, *8* (2), 197–209.

(37) Hogan, C. J.; Carroll, J. A.; Rohrs, H. W.; Biswas, P.; Gross, M. L. Combined Charged Residue-Field Emission Model of Macromolecular Electrospray Ionization. *Anal. Chem.* **2009**, *81* (1), 369–377.
(38) Konermann, L.; Ahadi, E.; Rodriguez, A. D.; Vahidi, S. Unraveling the Mechanism of Electrospray Ionization. *Anal. Chem.* **2013**, *85* (1), 2–9.
(39) Iribarne, J. V.; Thomson, B. A. On the Evaporation of Small Ions from Charged Droplets. *J. Chem. Phys.* **1976**, *64* (6), 2287–2294.
(40) Cech, N. B.; Enke, C. G. Selectivity in Electrospray Ionization Mass Spectrometry. In *Electrospray and MALDI Mass Spectrometry*; Cole, R. B., Ed.; John Wiley & Sons, Inc., 2010; pp 49–73.
(41) Cech, N. B.; Enke, C. G. Relating Electrospray Ionization Response to Nonpolar Character of Small Peptides. *Anal. Chem.* **2000**, *72* (13), 2717–2723.
(42) Kaltashov, I. A.; Mohimen, A. Estimates of Protein Surface Areas in Solution by Electrospray Ionization Mass Spectrometry. *Anal. Chem.* **2005**, *77* (16), 5370–5379.
(43) Iavarone, A. T.; Williams, E. R. Mechanism of Charging and Supercharging Molecules in Electrospray Ionization. *J. Am. Chem. Soc.* **2003**, *125* (8), 2319–2327.
(44) Winger, B. E.; Light-Wahl, K. J.; Ogorzalek Loo, R. R.; Udseth, H. R.; Smith, R. D. Observation and Implications of High Mass-to-Charge Ratio Ions from Electrospray Ionization Mass Spectrometry. *J. Am. Soc. Mass Spectrom.* **1993**, *4* (7), 536–545.
(45) Kebarle, P.; Verkerk, U. H. Electrospray: From Ions in Solution to Ions in the Gas Phase, What We Know Now. *Mass Spectrom. Rev.* **2009**, *28* (6), 898–917.
(46) Samalikova, M.; Grandori, R. Protein Charge-State Distributions in Electrospray-Ionization Mass Spectrometry Do Not Appear to Be Limited by the Surface Tension of the Solvent. *J. Am. Chem. Soc.* **2003**, *125* (44), 13352–13353.
(47) Allen, M. H.; Vestal, M. L. Design and Performance of a Novel Electrospray Interface. *J. Am. Soc. Mass Spectrom.* **1992**, *3* (1), 18–26.
(48) Bruins, A. P. Mass Spectrometry with Ion Sources Operating at Atmospheric Pressure. *Mass Spectrom. Rev.* **1991**, *10* (1), 53–77.
(49) Kebarle, P. A Brief Overview of the Present Status of the Mechanisms Involved in Electrospray Mass Spectrometry. *J. Mass Spectrom. JMS* **2000**, *35* (7), 804–817.
(50) Körner, R.; Wilm, M.; Morand, K.; Schubert, M.; Mann, M. Nano Electrospray Combined with a Quadrupole Ion Trap for the Analysis of Peptides and Protein Digests. *J. Am. Soc. Mass Spectrom.* **1996**, *7* (2), 150–156.
(51) Wilm, M.; Mann, M. Analytical Properties of the Nanoelectrospray Ion Source. *Anal. Chem.* **1996**, *68* (1), 1–8.
(52) Maziarz III, E. P.; Baker, G. A.; Mure, J. V.; Woodab, T. D. A Comparison of Electrospray versus Nanoelectrospray Ionization Fourier Transform Mass Spectrometry for the Analysis of Synthetic Poly(dimethylsiloxane)/poly(ethylene Glycol) Oligomer Blends. *Int. J. Mass Spectrom.* **2000**, *202* (1–3), 241–250.
(53) Wilm, M.; Shevchenko, A.; Houthaeve, T.; Breit, S.; Schweigerer, L.; Fotsis, T.; Mann, M. Femtomole Sequencing of Proteins from Polyacrylamide Gels by Nano-Electrospray Mass Spectrometry. *Nature* **1996**, *379* (6564), 466–469.
(54) Wood, T. D.; Moy, M. A.; Dolan, A. R.; Jr, P. M. B.; White, T. P.; Smith, D. R.; Higbee, D. J. Miniaturization of Electrospray Ionization Mass Spectrometry. *Appl. Spectrosc. Rev.* **2003**, *38* (2), 187–244.

(55) Davis, M. T.; Stahl, D. C.; Hefta, S. A.; Lee, T. D. A Microscale Electrospray Interface for Online, Capillary Liquid Chromatography/Tandem Mass Spectrometry of Complex Peptide Mixtures. *Anal. Chem.* **1995**, *67* (24), 4549–4556.
(56) Gatlin, C. L.; Kleemann, G. R.; Hays, L. G.; Link, A. J.; Yates, J. R. Protein Identification at the Low Femtomole Level from Silver-Stained Gels Using a New Fritless Electrospray Interface for Liquid Chromatography-Microspray and Nanospray Mass Spectrometry. *Anal. Biochem.* **1998**, *263* (1), 93–101.
(57) Gohlke, R. S. Time-of-Flight Mass Spectrometry and Gas-Liquid Partition Chromatography. *Anal. Chem.* **1959**, *31* (4), 535–541.
(58) Ryhage, R. Use of a Mass Spectrometer as a Detector and Analyzer for Effluent Emerging from High Temperature Gas Liquid Chromatography Columns. *Anal. Chem.* **1964**, *36* (4), 759–764.
(59) Dorsey, J. A.; Hunt, R. H.; O'Neal, M. J. Rapid-Scanning Mass Spectrometry. Continuous Analysis of Fractions from Capillary Gas Chromatography. *Anal. Chem.* **1963**, *35* (4), 511–515.
(60) Grayson, M. A. The Mass Spectrometer as a Detector for Gas Chromatography. *J. Chromatogr. Sci.* **1986**, *24* (12), 529–542.
(61) Sparkman, O. D.; Penton, Z.; Kitson, F. G. *Gas Chromatography and Mass Spectrometry: A Practical Guide: A Practical Guide*; Academic Press, 2011.
(62) Olivares, J. A.; Nguyen, N. T.; Yonker, C. R.; Smith, R. D. On-Line Mass Spectrometric Detection for Capillary Zone Electrophoresis. *Anal. Chem.* **1987**, *59* (8), 1230–1232.
(63) *Capillary Electrophoresis of Biomolecules: Methods and Protocols*; Volpi, N., Maccari, F., Eds.; Methods in molecular biology; Humana Press: New York, 2013.
(64) Lukacs, K.; Jorgenson, J. Capillary Zone Electrophoresis - Effect of Physical Parameters on Separation Efficiency and Quantitation. *J. High Resolut. Chromatogr. Chromatogr. Commun.* **1985**, *8* (8), 407–411.
(65) Moseley, M.; Deterding, L.; Tomer, K.; Jorgenson, J. Determination of Bioactive Peptides Using Capillary Zone Electrophoresis Mass-Spectrometry. *Anal. Chem.* **1991**, *63* (2), 109–114.
(66) Kannamkumarath, S. S.; Wrobel, K.; Wrobel, K.; B'Hymer, C.; Caruso, J. A. Capillary Electrophoresis-Inductively Coupled Plasma-Mass Spectrometry: An Attractive Complementary Technique for Elemental Speciation Analysis. *J. Chromatogr. A* **2002**, *975* (2), 245–266.
(67) Lu, J. J.; Zhu, Z.; Wang, W.; Liu, S. Coupling Sodium Dodecyl Sulfate–Capillary Polyacrylamide Gel Electrophoresis with MALDI-TOF-MS via a PTFE Membrane. *Anal. Chem.* **2011**, *83* (5), 1784–1790.
(68) Takada, Y.; Sakairi, M.; Koizumi, H. Atmospheric-Pressure Chemical-Ionization Interface for Capillary Electrophoresis Mass-Spectrometry. *Anal. Chem.* **1995**, *67* (8), 1474–1476.
(69) Barbula, G. K.; Safi, S.; Chingin, K.; Perry, R. H.; Zare, R. N. Interfacing Capillary-Based Separations to Mass Spectrometry Using Desorption Electrospray Ionization. *Anal. Chem.* **2011**, *83* (6), 1955–1959.
(70) Geiger, M.; Hogerton, A. L.; Bowser, M. T. Capillary Electrophoresis. *Anal. Chem.* **2012**, *84* (2), 577–596.
(71) Smith, R. D.; Barinaga, C. J.; Udseth, H. R. Improved Electrospray Ionization Interface for Capillary Zone Electrophoresis-Mass Spectrometry. *Anal. Chem.* **1988**, *60* (18), 1948–1952.

(72) Moini, M. Capillary Electrophoresis Mass Spectrometry and Its Application to the Analysis of Biological Mixtures. *Anal. Bioanal. Chem.* **2002**, *373* (6), 466–480.
(73) Schmitt-Kopplin, P.; Frommberger, M. Capillary Electrophoresis – Mass Spectrometry: 15 Years of Developments and Applications. *ELECTROPHORESIS* **2003**, *24* (22-23), 3837–3867.
(74) Moini, M. Simplifying CE−MS Operation. 2. Interfacing Low-Flow Separation Techniques to Mass Spectrometry Using a Porous Tip. *Anal. Chem.* **2007**, *79* (11), 4241–4246.
(75) Fonslow, B. R.; Yates, J. R. Capillary Electrophoresis Applied to Proteomic Analysis. *J. Sep. Sci.* **2009**, *32* (8), 1175–1188.
(76) Haselberg, R.; de Jong, G. J.; Somsen, G. W. Low-Flow Sheathless Capillary Electrophoresis-Mass Spectrometry for Sensitive Glycoform Profiling of Intact Pharmaceutical Proteins. *Anal. Chem.* **2013**, *85* (4), 2289–2296.
(77) Ramautar, R.; Somsen, G. W.; de Jong, G. J. CE-MS for Metabolomics: Developments and Applications in the Period 2010-2012. *Electrophoresis* **2013**, *34* (1), 86–98.
(78) Haselberg, R.; Ratnayake, C. K.; de Jong, G. J.; Somsen, G. W. Performance of a Sheathless Porous Tip Sprayer for Capillary Electrophoresis-Electrospray Ionization-Mass Spectrometry of Intact Proteins. *J. Chromatogr. A* **2010**, *1217* (48), 7605–7611.
(79) Hoffmann, T.; Martin, M. M. CE-ESI-MS/MS as a Rapid Screening Tool for the Comparison of Protein–ligand Interactions. *ELECTROPHORESIS* **2010**, *31* (7), 1248–1255.
(80) Pioch, M.; Bunz, S.-C.; Neusuess, C. Capillary Electrophoresis/mass Spectrometry Relevant to Pharmaceutical and Biotechnological Applications. *Electrophoresis* **2012**, *33* (11), 1517–1530.
(81) Kawai, M.; Iwamuro, Y.; Iio-Ishimaru, R.; Chinaka, S.; Takayama, N.; Hayakawa, K. Analysis of Phosphorus-Containing Amino Acid-Type Herbicides by Sheathless Capillary Electrophoresis/Electrospray Ionization-Mass Spectrometry Using a High Sensitivity Porous Sprayer. *Anal. Sci.* **2011**, *27* (8), 857–860.
(82) Bonvin, G.; Schappler, J.; Rudaz, S. Non-Aqueous Capillary Electrophoresis for the Analysis of Acidic Compounds Using Negative Electrospray Ionization Mass Spectrometry. *J. Chromatogr. A* **2014**, *1323*, 163–173.
(83) Manz, A.; Graber, N.; Widmer, H. Miniaturized Total Chemical-Analysis Systems - a Novel Concept for Chemical Sensing. *Sens. Actuators B-Chem.* **1990**, *1* (1-6), 244–248.
(84) Whitesides, G. M. The Origins and the Future of Microfluidics. *Nature* **2006**, *442* (7101), 368–373.
(85) Koster, S.; Verpoorte, E. A Decade of Microfluidic Analysis Coupled with Electrospray Mass Spectrometry: An Overview. *Lab. Chip* **2007**, *7* (11), 1394–1412.
(86) Harrison, D.; Glavina, P.; Manz, A. Towards Miniaturized Electrophoresis and Chemical-Analysis Systems on Silicon - an Alternative to Chemical Sensors. *Sens. Actuators B-Chem.* **1993**, *10* (2), 107–116.
(87) Harrison, D.; Manz, A.; Fan, Z.; Ludi, H.; Widmer, H. Capillary Electrophoresis and Sample Injection Systems Integrated on a Planar Glass Chip. *Anal. Chem.* **1992**, *64* (17), 1926–1932.
(88) McEnery, M.; Tan, A. M.; Alderman, J.; Patterson, J.; O'Mathuna, S. C.; Glennon, J. D. Liquid Chromatography on-Chip: Progression towards a Mu-Total Analysis System. *Analyst* **2000**, *125* (1), 25–27.

(89) Lazar, I. M.; Grym, J.; Foret, F. Microfabricated Devices: A New Sample Introduction Approach to Mass Spectrometry. *Mass Spectrom. Rev.* **2006**, *25* (4), 573–594.
(90) Henry, C. Micro Meets Macro: Interfacing Microchips and Mass Spectrometers. *Anal. Chem.* **1997**, *69* (11), 359A – 361A.
(91) Ramsey, R. S.; Ramsey, J. M. Generating Electrospray from Microchip Devices Using Electroosmotic Pumping. *Anal. Chem.* **1997**, *69* (6), 1174–1178.
(92) Xue, Q.; Foret, F.; Dunayevskiy, Y. M.; Zavracky, P. M.; McGruer, N. E.; Karger, B. L. Multichannel Microchip Electrospray Mass Spectrometry. *Anal. Chem.* **1997**, *69* (3), 426–430.
(93) Zhang, B.; Liu, H.; Karger, B. L.; Foret, F. Microfabricated Devices for Capillary Electrophoresis−Electrospray Mass Spectrometry. *Anal. Chem.* **1999**, *71* (15), 3258–3264.
(94) Figeys, D.; Ning, Y.; Aebersold, R. A Microfabricated Device for Rapid Protein Identification by Microelectrospray Ion Trap Mass Spectrometry. *Anal. Chem.* **1997**, *69* (16), 3153–3160.
(95) Oleschuk, R. D.; Harrison, D. J. Analytical Microdevices for Mass Spectrometry. *Trac-Trends Anal. Chem.* **2000**, *19* (6), 379–388.
(96) Bings, N. H.; Wang, C.; Skinner, C. D.; Colyer, C. L.; Thibault, P.; Harrison, D. J. Microfluidic Devices Connected to Fused-Silica Capillaries with Minimal Dead Volume. *Anal. Chem.* **1999**, *71* (15), 3292–3296.
(97) Kelly, R. T.; Page, J. S.; Marginean, I.; Tang, K.; Smith, R. D. Dilution-Free Analysis from Picoliter Droplets by Nano-Electrospray Ionization Mass Spectrometry. *Angew. Chem. Int. Ed.* **2009**, *48* (37), 6832–6835.
(98) Rob, T.; Wilson, D. J. A Versatile Microfluidic Chip for Millisecond Time-Scale Kinetic Studies by Electrospray Mass Spectrometry. *J. Am. Soc. Mass Spectrom.* **2009**, *20* (1), 124–130.
(99) Fortier, M.-H.; Bonneil, E.; Goodley, P.; Thibault, P. Integrated Microfluidic Device for Mass Spectrometry-Based Proteomics and Its Application to Biomarker Discovery Programs. *Anal. Chem.* **2005**, *77* (6), 1631–1640.
(100) Chambers, A. G.; Mellors, J. S.; Henley, W. H.; Ramsey, J. M. Monolithic Integration of Two-Dimensional Liquid Chromatography−Capillary Electrophoresis and Electrospray Ionization on a Microfluidic Device. *Anal. Chem.* **2011**, *83* (3), 842–849.
(101) Fuentes, H. V.; Woolley, A. T. Electrically Actuated, Pressure-Driven Liquid Chromatography Separations in Microfabricated Devices. *Lab. Chip* **2007**, *7* (11), 1524–1531.
(102) Yin, H.; Killeen, K.; Brennen, R.; Sobek, D.; Werlich, M.; van de Goor, T. Microfluidic Chip for Peptide Analysis with an Integrated HPLC Column, Sample Enrichment Column, and Nanoelectrospray Tip. *Anal. Chem.* **2005**, *77* (2), 527–533.
(103) Lee, J.; Soper, S. A.; Murray, K. K. Microfluidic Chips for Mass Spectrometry-Based Proteomics. *J. Mass Spectrom.* **2009**, *44* (5), 579–593.
(104) Krenkova, J.; Lacher, N. A.; Svec, F. Highly Efficient Enzyme Reactors Containing Trypsin and Endoproteinase LysC Immobilized on Porous Polymer Monolith Coupled to MS Suitable for Analysis of Antibodies. *Anal. Chem.* **2009**, *81* (5), 2004–2012.
(105) Zhu, S.; Shala, A.; Bezginov, A.; Sljoka, A.; Audette, G.; Wilson, D. J. Hyperphosphorylation of Intrinsically Disordered Tau Protein Induces an Amyloidogenic Shift in Its Conformational Ensemble. *PLoS ONE* **2015**, *10* (3), e0120416.

(106) Rob, T.; Gill, P. K.; Golemi-Kotra, D.; Wilson, D. J. An Electrospray Ms-Coupled Microfluidic Device for Sub-Second Hydrogen/deuterium Exchange Pulse-Labelling Reveals Allosteric Effects in Enzyme Inhibition. *Lab. Chip* **2013**, *13* (13), 2528–2532.
(107) Wheeler, A. R. Putting Electrowetting to Work. *Science* **2008**, *322* (5901), 539–540.
(108) Talroze, V.; Karpov, G.; GORODETS. IG; Skurat, V. Capillary System for Introduction of Liquid Mixtures into an Analytical Mass-Spectrometer. *Russ. J. Phys. Chem. USSR* **1968**, *42* (12), 1658.
(109) Carroll, D. I.; Dzidic, I.; Stillwell, R. N.; Haegele, K. D.; Horning, E. C. Atmospheric Pressure Ionization Mass Spectrometry. Corona Discharge Ion Source for Use in a Liquid Chromatograph-Mass Spectrometer-Computer Analytical System. *Anal. Chem.* **1975**, *47* (14), 2369–2373.
(110) Blakley, C.; McAdams, M.; Vestal, M. Crossed-Beam Liquid Chromatoraph—mass Spectrometer Combination. *J. Chromatogr. A* **1978**, *158*, 261–276.
(111) Yamashita, M.; Fenn, J. B. Electrospray Ion Source. Another Variation on the Free-Jet Theme. *J. Phys. Chem.* **1984**, *88* (20), 4451–4459.
(112) Whitehouse, C. M.; Dreyer, R. N.; Yamashita, M.; Fenn, J. B. Electrospray Interface for Liquid Chromatographs and Mass Spectrometers. *Anal. Chem.* **1985**, *57* (3), 675–679.
(113) Carroll, D. I.; Dzidic, I.; Stillwell, R. N.; Horning, M. G.; Horning, E. C. Subpicogram Detection System for Gas Phase Analysis Based upon Atmospheric Pressure Ionization (API) Mass Spectrometry. *Anal. Chem.* **1974**, *46* (6), 706–710.
(114) Henion, J. D.; Thomson, B. A.; Dawson, P. H. Determination of Sulfa Drugs in Biological Fluids by Liquid Chromatography/mass Spectrometry/mass Spectrometry. *Anal. Chem.* **1982**, *54* (3), 451–456.
(115) Yamashita, M.; Fenn, J. B. Negative Ion Production with the Electrospray Ion Source. *J. Phys. Chem.* **1984**, *88* (20), 4671–4675.
(116) Fenn, J. B.; Mann, M.; Meng, C. K.; Wong, S. F.; Whitehouse, C. M. Electrospray Ionization for Mass Spectrometry of Large Biomolecules. *Science* **1989**, *246* (4926), 64–71.
(117) Bogdanov, B.; Smith, R. D. Proteomics by FTICR Mass Spectrometry: Top down and Bottom up. *Mass Spectrom. Rev.* **2005**, *24* (2), 168–200.
(118) Flora, J. W.; Null, A. P.; Muddiman, D. C. Dual-Micro-ESI Source for Precise Mass Determination on a Quadrupole Time-of-Flight Mass Spectrometer for Genomic and Proteomic Applications. *Anal. Bioanal. Chem.* **2002**, *373* (7), 538–546.
(119) Gillet, L. C.; Navarro, P.; Tate, S.; Röst, H.; Selevsek, N.; Reiter, L.; Bonner, R.; Aebersold, R. Targeted Data Extraction of the MS/MS Spectra Generated by Data-Independent Acquisition: A New Concept for Consistent and Accurate Proteome Analysis. *Mol. Cell. Proteomics* **2012**, *11* (6), O111.016717.
(120) Chen, G.; Pramanik, B. N. LC-MS for Protein Characterization: Current Capabilities and Future Trends. *Expert Rev. Proteomics* **2008**, *5* (3), 435–444.
(121) Zhao, Y.-Y.; Lin, R.-C. UPLC–MSE Application in Disease Biomarker Discovery: The Discoveries in Proteomics to Metabolomics. *Chem. Biol. Interact.* **2014**, *215*, 7–16.
(122) Thurman, E. M.; Ferrer, I.; Barceló, D. Choosing between Atmospheric Pressure Chemical Ionization and Electrospray Ionization Interfaces for the HPLC/MS Analysis of Pesticides. *Anal. Chem.* **2001**, *73* (22), 5441–5449.
(123) Hernandez, F.; Sancho, J. V.; Pozo, O. J. Critical Review of the Application of Liquid Chromatography/mass Spectrometry to the Determination of Pesticide Residues in Biological Samples. *Anal. Bioanal. Chem.* **2005**, *382* (4), 934–946.

(124) Richardson, S. D.; Ternes, T. A. Water Analysis: Emerging Contaminants and Current Issues. *Anal. Chem.* **2005**, *77* (12), 3807–3838.
(125) Vanderford, B. J.; Pearson, R. A.; Rexing, D. J.; Snyder, S. A. Analysis of Endocrine Disruptors, Pharmaceuticals, and Personal Care Products in Water Using Liquid Chromatography/Tandem Mass Spectrometry. *Anal. Chem.* **2003**, *75* (22), 6265–6274.
(126) Lee, M. S.; Kerns, E. H. LC/MS Applications in Drug Development. *Mass Spectrom. Rev.* **1999**, *18* (3-4), 187–279.
(127) Mei, H.; Hsieh, Y.; Nardo, C.; Xu, X.; Wang, S.; Ng, K.; Korfmacher, W. A. Investigation of Matrix Effects in Bioanalytical High-Performance Liquid Chromatography/tandem Mass Spectrometric Assays: Application to Drug Discovery. *Rapid Commun. Mass Spectrom.* **2003**, *17* (1), 97–103.
(128) Dettmer, K.; Aronov, P. A.; Hammock, B. D. Mass Spectrometry-Based Metabolomics. *Mass Spectrom. Rev.* **2007**, *26* (1), 51–78.
(129) Mishur, R. J.; Rea, S. L. Applications of Mass Spectrometry to Metabolomics and Metabonomics: Detection of Biomarkers of Aging and of Age-Related Diseases. *Mass Spectrom. Rev.* **2012**, *31* (1), 70–95.
(130) Wenk, M. R. The Emerging Field of Lipidomics. *Nat. Rev. Drug Discov.* **2005**, *4* (7), 594–610.
(131) Hermansson, M.; Uphoff, A.; Kakela, R.; Somerharju, P. Automated Quantitative Analysis of Complex Lipidomes by Liquid Chromatography/mass Spectrometry. *Anal. Chem.* **2005**, *77* (7), 2166–2175.
(132) Yates, J. R.; Ruse, C. I.; Nakorchevsky, A. Proteomics by Mass Spectrometry: Approaches, Advances, and Applications. In *Annual Review of Biomedical Engineering*; Annual Reviews: Palo Alto, 2009; Vol. 11, pp 49–79.
(133) Roux, K. J.; Kim, D. I.; Raida, M.; Burke, B. A Promiscuous Biotin Ligase Fusion Protein Identifies Proximal and Interacting Proteins in Mammalian Cells. *J. Cell Biol.* **2012**, *196* (6), 801–810.
(134) Wasslen, K. V.; Tan, L. H.; Manthorpe, J. M.; Smith, J. C. Trimethylation Enhancement Using Diazomethane (TrEnDi): Rapid On-Column Quaternization of Peptide Amino Groups via Reaction with Diazomethane Significantly Enhances Sensitivity in Mass Spectrometry Analyses via a Fixed, Permanent Positive Charge. *Anal. Chem.* **2014**, *86* (7), 3291–3299.
(135) Pan, J.; Zhang, S.; Chou, A.; Hardie, D. B.; Borchers, C. H. Fast Comparative Structural Characterization of Intact Therapeutic Antibodies Using Hydrogen–Deuterium Exchange and Electron Transfer Dissociation. *Anal. Chem.* **2015**, *87* (12), 5884–5890.
(136) Underbakke, E. S.; Iavarone, A. T.; Chalmers, M. J.; Pascal, B. D.; Novick, S.; Griffin, P. R.; Marletta, M. A. Nitric Oxide-Induced Conformational Changes in Soluble Guanylate Cyclase. *Struct. Lond. Engl. 1993* **2014**, *22* (4), 602–611.
(137) Contrepois, K.; Ezan, E.; Mann, C.; Fenaille, F. Ultra-High Performance Liquid Chromatography-Mass Spectrometry for the Fast Profiling of Histone Post-Translational Modifications. *J. Proteome Res.* **2010**, *9* (10), 5501–5509.
(138) Zaia, J. Mass Spectrometry of Oligosaccharides. *Mass Spectrom. Rev.* **2004**, *23* (3), 161–227.
(139) Huber, C. G.; Oberacher, H. Analysis of Nucleic Acids by on-Line Liquid chromatography–Mass Spectrometry. *Mass Spectrom. Rev.* **2001**, *20* (5), 310–343.

(140) S W Englander; Mayne, L. Protein Folding Studied Using Hydrogen-Exchange Labeling and Two-Dimensional NMR. *Annu. Rev. Biophys. Biomol. Struct.* **1992**, *21* (1), 243–265.
(141) Krishna, M. M. G.; Hoang, L.; Lin, Y.; Englander, S. W. Hydrogen Exchange Methods to Study Protein Folding. *Methods* **2004**, *34* (1), 51–64.
(142) Neira, J. L. NMR as a Tool to Identify and Characterize Protein Folding Intermediates. *Arch. Biochem. Biophys.* **2013**, *531* (1–2), 90–99.
(143) Konermann, L.; Pan, J.; Liu, Y.-H. Hydrogen Exchange Mass Spectrometry for Studying Protein Structure and Dynamics. *Chem. Soc. Rev.* **2011**, *40* (3), 1224–1234.
(144) Katta, V.; Chait, B. Conformational-Changes in Proteins Probed by Hydrogen-Exchange Electrospray-Ionization Mass-Spectrometry. *Rapid Commun. Mass Spectrom.* **1991**, *5* (4), 214–217.
(145) Zhang, Z.; Smith, D. L. Determination of Amide Hydrogen Exchange by Mass Spectrometry: A New Tool for Protein Structure Elucidation. *Protein Sci.* **1993**, *2* (4), 522–531.
(146) Kan, Z.-Y.; Walters, B. T.; Mayne, L.; Englander, S. W. Protein Hydrogen Exchange at Residue Resolution by Proteolytic Fragmentation Mass Spectrometry Analysis. *Proc. Natl. Acad. Sci.* **2013**, *110* (41), 16438–16443.
(147) Eigen, M. Proton Transfer, Acid-Base Catalysis, and Enzymatic Hydrolysis. Part I: ELEMENTARY PROCESSES. *Angew. Chem. Int. Ed. Engl.* **1964**, *3* (1), 1–19.
(148) Dempsey, C. E. Hydrogen Exchange in Peptides and Proteins Using NMR Spectroscopy. *Prog. Nucl. Magn. Reson. Spectrosc.* **2001**, *39* (2), 135–170.
(149) Molday, R. S.; Englander, S. W.; Kallen, R. G. Primary Structure Effects on Peptide Group Hydrogen Exchange. *Biochemistry (Mosc.)* **1972**, *11* (2), 150–158.
(150) Perrin, C. L.; Arrhenius, G. M. L. Mechanisms of Acid-Catalyzed Proton Exchange in N-Methyl Amides. *J. Am. Chem. Soc.* **1982**, *104* (24), 6693–6696.
(151) Perrin, C. L. Proton Exchange in Amides: Surprises from Simple Systems. *Acc. Chem. Res.* **1989**, *22* (8), 268–275.
(152) Bai, Y.; Milne, J. S.; Mayne, L.; Englander, S. W. Primary Structure Effects on Peptide Group Hydrogen Exchange. *Proteins* **1993**, *17* (1), 75–86.
(153) Morgan, C. R.; Engen, J. R. Investigating Solution-Phase Protein Structure and Dynamics by Hydrogen Exchange Mass Spectrometry. In *Current Protocols in Protein Science*; John Wiley & Sons, Inc., 2009.
(154) Tüchsen, E. Mechanism of Surface Peptide Proton Exchange in Bovine Pancreatic Trypsin Inhibitor Salt Effects and O-Protonation. *J. Mol. Biol. 185* (2), 421–430.
(155) Perrin, C. L. Proton Exchange in Amides: Surprises from Simple Systems. *Acc. Chem. Res.* **1989**, *22* (8), 268–275.
(156) Resetca, D. Characterizing Protein Dynamics of Protein-Ligand Interactions by Hydrogen-Deuterium Exchange Mass Spectrometry. **2014**.
(157) Fogolari, F.; Esposito, G.; Viglino, P.; Briggs, J. M.; McCammon, J. A. pKa Shift Effects on Backbone Amide Base-Catalyzed Hydrogen Exchange Rates in Peptides. *J. Am. Chem. Soc.* **1998**, *120* (15), 3735–3738.
(158) Skinner, J. J.; Lim, W. K.; Bédard, S.; Black, B. E.; Englander, S. W. Protein Hydrogen Exchange: Testing Current Models. *Protein Sci. Publ. Protein Soc.* **2012**, *21* (7), 987–995.
(159) Li, R.; Woodward, C. The Hydrogen Exchange Core and Protein Folding. *Protein Sci. Publ. Protein Soc.* **1999**, *8* (8), 1571–1590.

(160) Pan, Y.; Briggs, M. S. Hydrogen Exchange in Native and Alcohol Forms of Ubiquitin. *Biochemistry (Mosc.)* **1992**, *31* (46), 11405–11412.
(161) Englander, S. W.; Sosnick, T. R.; Englander, J. J.; Mayne, L. Mechanisms and Uses of Hydrogen Exchange. *Curr. Opin. Struct. Biol.* **1996**, *6* (1), 18–23.
(162) McAllister, R. G.; Konermann, L. Challenges in the Interpretation of Protein H/D Exchange Data: A Molecular Dynamics Simulation Perspective. *Biochemistry (Mosc.)* **2015**, *54* (16), 2683–2692.
(163) Konermann, L. Protein Structure and Dynamics Studied by Mass Spectrometry: H/D Exchange, Hydroxyl Radical Labeling, and Related Approaches. *J. Mass Spectrom. 43* (8), 1021–1036.
(164) Khanal, A.; Pan, Y.; Brown, L. S.; Konermann, L. Pulsed Hydrogen/deuterium Exchange Mass Spectrometry for Time-Resolved Membrane Protein Folding Studies. *J. Mass Spectrom.* **2012**, *47* (12), 1620–1626.
(165) Houde, D.; Arndt, J.; Domeier, W.; Berkowitz, S.; Engen, J. R. Rapid Characterization of IgG1 Conformation and Conformational Dynamics by Hydrogen/deuterium Exchange Mass Spectrometry. *Anal. Chem.* **2009**, *81* (7), 2644–2651.
(166) Zhu, M. M.; Rempel, D. L.; Du, Z.; Gross, M. L. Quantification of Protein−Ligand Interactions by Mass Spectrometry, Titration, and H/D Exchange: PLIMSTEX. *J. Am. Chem. Soc.* **2003**, *125* (18), 5252–5253.
(167) Engen, J. R. Analysis of Protein Conformation and Dynamics by Hydrogen/Deuterium Exchange MS. *Anal. Chem.* **2009**, *81* (19), 7870–7875.
(168) Marcsisin, S. Hydrogen Exchange Mass Spectrometry: What Is It and What Can It Tell Us? *Anal. Bioanal. Chem.* **2010**, *397* (3), 967–972.
(169) Liuni, P.; Jeganathan, A.; Wilson, D. J. Conformer Selection and Intensified Dynamics During Catalytic Turnover in Chymotrypsin. *Angew. Chem.* **2012**, *124* (38), 9804–9807.
(170) Hoerner, J. K.; Xiao, H.; Dobo, A.; Kaltashov, I. A. Is There Hydrogen Scrambling in the Gas Phase? Energetic and Structural Determinants of Proton Mobility within Protein Ions. *J. Am. Chem. Soc.* **2004**, *126* (24), 7709–7717.
(171) Abzalimov, R. R.; Kaplan, D. A.; Easterling, M. L.; Kaltashov, I. A. Protein Conformations Can Be Probed in Top-Down HDX MS Experiments Utilizing Electron Transfer Dissociation of Protein Ions Without Hydrogen Scrambling. *J. Am. Soc. Mass Spectrom.* **2009**, *20* (8), 1514–1517.
(172) Venter, A.; Nefliu, M.; Cooks, R. G. Ambient Desorption Ionization Mass Spectrometry. *Trac-Trends Anal. Chem.* **2008**, *27* (4), 284–290.
(173) Chang, D.-Y.; Lee, C.-C.; Shiea, J. Detecting Large Biomolecules from High-Salt Solutions by Fused-Droplet Electrospray Ionization Mass Spectrometry. *Anal. Chem.* **2002**, *74* (11), 2465–2469.
(174) Chen, H. W.; Venter, A.; Cooks, R. G. Extractive Electrospray Ionization for Direct Analysis of Undiluted Urine, Milk and Other Complex Mixtures without Sample Preparation. *Chem. Commun.* **2006**, No. 19, 2042–2044.
(175) Chen, H.; Wortmann, A.; Zhang, W.; Zenobi, R. Rapid In Vivo Fingerprinting of Nonvolatile Compounds in Breath by Extractive Electrospray Ionization Quadrupole Time-of-Flight Mass Spectrometry. *Angew. Chem. Int. Ed.* **2007**, *46* (4), 580–583.
(176) Zhu, L.; Gamez, G.; Chen, H.; Chingin, K.; Zenobi, R. Rapid Detection of Melamine in Untreated Milk and Wheat Gluten by Ultrasound-Assisted Extractive Electrospray Ionization Mass Spectrometry (EESI-MS). *Chem. Commun.* **2009**, No. 5, 559–561.

(177) Zhu, L.; Gamez, G.; Chen, H. W.; Huang, H. X.; Chingin, K.; Zenobi, R. Real-Time, on-Line Monitoring of Organic Chemical Reactions Using Extractive Electrospray Ionization Tandem Mass Spectrometry. *Rapid Commun. Mass Spectrom. RCM* **2008**, *22* (19), 2993–2998.

(178) Marquez, C. A.; Wang, H.; Fabbretti, F.; Metzger, J. O. Electron-Transfer-Catalyzed Dimerization of Trans-Anethole: Detection of the Distonic Tetramethylene Radical Cation Intermediate by Extractive Electrospray Ionization Mass Spectrometry. *J. Am. Chem. Soc.* **2008**, *130* (51), 17208–17209.

(179) Law, W. S.; Chen, H.; Ding, J.; Yang, S.; Zhu, L.; Gamez, G.; Chingin, K.; Ren, Y.; Zenobi, R. Rapid Characterization of Complex Viscous Liquids at the Molecular Level. *Angew. Chem. Int. Ed.* **2009**, *48* (44), 8277–8280.

(180) Law, W. S.; Chen, H. W.; Balabin, R.; Berchtold, C.; Meier, L.; Zenobi, R. Rapid Fingerprinting and Classification of Extra Virgin Olive Oil by Microjet Sampling and Extractive Electrospray Ionization Mass Spectrometry. *Analyst* **2010**, *135* (4), 773–778.

(181) Shieh, I.-F.; Lee, C.-Y.; Shiea, J. Eliminating the Interferences from TRIS Buffer and SDS in Protein Analysis by Fused-Droplet Electrospray Ionization Mass Spectrometry. *J. Proteome Res.* **2005**, *4* (2), 606–612.

(182) Chen, H.; Yang, S.; Li, M.; Hu, B.; Li, J.; Wang, J. Sensitive Detection of Native Proteins Using Extractive Electrospray Ionization Mass Spectrometry. *Angew. Chem. Int. Ed.* **2010**, *49* (17), 3053–3056.

(183) Law, W. S.; Wang, R.; Hu, B.; Berchtold, C.; Meier, L.; Chen, H.; Zenobi, R. On the Mechanism of Extractive Electrospray Ionization. *Anal. Chem.* **2010**, *82* (11), 4494–4500.

(184) Shiea, J.; Chang, D.-Y.; Lin, C.-H.; Jiang, S.-J. Generating Multiply Charged Protein Ions by Ultrasonic Nebulization/Multiple Channel-Electrospray Ionization Mass Spectrometry. *Anal. Chem.* **2001**, *73* (20), 4983–4987.

(185) Koyanagi, G. K.; Blagojevic, V.; Bohme, D. K. Applications of Extractive Electrospray Ionization (EESI) in Analytical Chemistry. *Int. J. Mass Spectrom.* **2015**, *379*, 146–150.

(186) Schneider, B. B.; Covey, T. R.; Coy, S. L.; Krylov, E. V.; Nazarov, E. G. Planar Differential Mobility Spectrometer as a Pre-Filter for Atmospheric Pressure Ionization Mass Spectrometry. *Int. J. Mass Spectrom.* **2010**, *298* (1-3), 45–54.

(187) Kafle, A.; Coy, S. L.; Wong, B. M.; Jr, A. J. F.; Glick, J. J.; Vouros, P. Understanding Gas Phase Modifier Interactions in Rapid Analysis by Differential Mobility-Tandem Mass Spectrometry. *J. Am. Soc. Mass Spectrom.* **2014**, *25* (7), 1098–1113.

(188) Ross, S. K.; McDonald, G.; Marchant, S. The Use of Dopants in High Field Asymmetric Waveform Spectrometry. *Analyst* **2008**, *133* (5), 602–607.

(189) Kolakowski, B. M.; Mester, Z. Review of Applications of High-Field Asymmetric Waveform Ion Mobility Spectrometry (FAIMS) and Differential Mobility Spectrometry (DMS). *Analyst* **2007**, *132* (9), 842–864.

(190) Purves, R. W.; Guevremont, R.; Day, S.; Pipich, C. W.; Matyjaszczyk, M. S. Mass Spectrometric Characterization of a High-Field Asymmetric Waveform Ion Mobility Spectrometer. *Rev. Sci. Instrum.* **1998**, *69* (12), 4094–4105.

(191) Guevremont, R.; Barnett, D. A.; Purves, R. W.; Vandermey, J. Analysis of a Tryptic Digest of Pig Hemoglobin Using ESI-FAIMS-MS. *Anal. Chem.* **2000**, *72* (19), 4577–4584.

(192) Borysik, A. J. H.; Read, P.; Little, D. R.; Bateman, R. H.; Radford, S. E.; Ashcroft, A. E. Separation of β2-Microglobulin Conformers by High-Field Asymmetric Waveform Ion

Mobility Spectrometry (FAIMS) Coupled to Electrospray Ionisation Mass Spectrometry. *Rapid Commun. Mass Spectrom.* **2004**, *18* (19), 2229–2234.

(193) Brown, L. J.; Toutoungi, D. E.; Devenport, N. A.; Reynolds, J. C.; Kaur-Atwal, G.; Boyle, P.; Creaser, C. S. Miniaturized Ultra High Field Asymmetric Waveform Ion Mobility Spectrometry Combined with Mass Spectrometry for Peptide Analysis. *Anal. Chem.* **2010**, *82* (23), 9827–9834.

(194) Miller, R. A.; Eiceman, G. A.; Nazarov, E. G.; King, A. T. A Novel Micromachined High-Field Asymmetric Waveform-Ion Mobility Spectrometer. *Sens. Actuators B-Chem.* **2000**, *67* (3), 300–306.

(195) Nazarov, E. G.; Miller, R. A.; Eiceman, G. A.; Stone, J. A. Miniature Differential Mobility Spectrometry Using Atmospheric Pressure Photoionization. *Anal. Chem.* **2006**, *78* (13), 4553–4563.

(196) Levin, D. S.; Vouros, P.; Miller, R. A.; Nazarov, E. G.; Morris, J. C. Characterization of Gas-Phase Molecular Interactions on Differential Mobility Ion Behavior Utilizing an Electrospray Ionization-Differential Mobility-Mass Spectrometer System. *Anal. Chem.* **2006**, *78* (1), 96–106.

(197) Ells, B.; Barnett, D. A.; Froese, K.; Purves, R. W.; Hrudey, S.; Guevremont, R. Detection of Chlorinated and Brominated Byproducts of Drinking Water Disinfection Using Electrospray Ionization-High-Field Asymmetric Waveform Ion Mobility Spectrometry-Mass Spectrometry. *Anal. Chem.* **1999**, *71* (20), 4747–4752.

(198) Buryakov, I. A. Qualitative Analysis of Trace Constituents by Ion Mobility Increment Spectrometer. *Talanta* **2003**, *61* (3), 369–375.

(199) McCooeye, M.; Ding, L.; Gardner, G. J.; Fraser, C. A.; Lam, J.; Sturgeon, R. E.; Mester, Z. Separation and Quantitation of the Stereoisomers of Ephedra Alkaloids in Natural Health Products Using Flow Injection-Electrospray Ionization-High Field Asymmetric Waveform Ion Mobility Spectrometry-Mass Spectrometry. *Anal. Chem.* **2003**, *75* (11), 2538–2542.

(200) Hatsis, P.; Kapron, J. T. A Review on the Application of High-Field Asymmetric Waveform Ion Mobility Spectrometry (FAIMS) in Drug Discovery. *Rapid Commun. Mass Spectrom.* **2008**, *22* (5), 735–738.

(201) Bomers, M. K.; Menke, F. P.; Savage, R. S.; Vandenbroucke-Grauls, C. M. J. E.; van Agtmael, M. A.; Covington, J. A.; Smulders, Y. M. Rapid, Accurate, and On-Site Detection of C-Difficile in Stool Samples. *Am. J. Gastroenterol.* **2015**, *110* (4), 588–594.

(202) Manicke, N. E.; Belford, M. Separation of Opiate Isomers Using Electrospray Ionization and Paper Spray Coupled to High-Field Asymmetric Waveform Ion Mobility Spectrometry. *J. Am. Soc. Mass Spectrom.* **2015**, *26* (5), 701–705.

(203) McSheehy, S.; Mester, Z. Arsenic Speciation in Marine Certified Reference Materials - Part 1. Identification of Water-Soluble Arsenic Species Using Multidimensional Liquid Chromatography Combined with Inductively Coupled Plasma, Electrospray and Electrospray High-Field Asymmetric Waveform Ion Mobility Spectrometry with Mass Spectrometric Detection. *J. Anal. At. Spectrom.* **2004**, *19* (3), 373–380.

(204) Shvartsburg, A. A. Ultrahigh-Resolution Differential Ion Mobility Separations of Conformers for Proteins above 10 kDa: Onset of Dipole Alignment? *Anal. Chem.* **2014**, *86* (21), 10608–10615.

(205) Robinson, E. W.; Williams, E. R. Multidimensional Separations of Ubiquitin Conformers in the Gas Phase: Relating Ion Cross Sections to H/D Exchange Measurements. *J. Am. Soc. Mass Spectrom.* **2005**, *16* (9), 1427–1437.

(206) Zhao, W.; Wang, Y.; Li, J.; Li, L.; Wang, Q.; Han, K.; Zhang, Y.; Li, X.; Li, P.; Luo, J.; et al. Determination of Melamine in Milk and Dairy Products by Microchip-Based High-Field Asymmetric Ion Mobility Spectrometry Combined with Solid-Phase Extraction. *Food Chem.* **2015**, *188*, 489–495.
(207) Yates, J. R.; Ruse, C. I.; Nakorchevsky, A. Proteomics by Mass Spectrometry: Approaches, Advances, and Applications. *Annu. Rev. Biomed. Eng.* **2009**, *11* (1), 49–79.
(208) Chughtai, K.; Heeren, R. M. A. Mass Spectrometric Imaging for Biomedical Tissue Analysis. *Chem. Rev.* **2010**, *110* (5), 3237–3277.
(209) Glish, G. L.; Burinsky, D. J. Hybrid Mass Spectrometers for Tandem Mass Spectrometry. *J. Am. Soc. Mass Spectrom.* **2011**, *19* (2), 161–172.
(210) Brocchieri, L.; Karlin, S. Protein Length in Eukaryotic and Prokaryotic Proteomes. *Nucleic Acids Res.* **2005**, *33* (10), 3390–3400.
(211) Matthews, J. M.; Sunde, M. Dimers, Oligomers, Everywhere. In *Protein Dimerization and Oligomerization in Biology*; Matthews, J. M., Ed.; Advances in Experimental Medicine and Biology; Springer New York, 2012; pp 1–18.
(212) Tang, X.-J.; Fred Brewer, C.; Saha, S.; Chernushevich, I.; Ens, W.; Standing, K. G.; Chait, B. T. Investigation of Protein-Protein Noncovalent Interactions in Soybean Agglutinin by Electrospray Ionization Time-of-Flight Mass Spectrometry. *Rapid Commun. Mass Spectrom.* **1994**, *8* (9), 750–754.
(213) Sharon, M.; Robinson, C. V. The Role of Mass Spectrometry in Structure Elucidation of Dynamic Protein Complexes. *Annu. Rev. Biochem.* **2007**, *76* (1), 167–193.
(214) Chernushevich, I. V.; Thomson, B. A. Collisional Cooling of Large Ions in Electrospray Mass Spectrometry. *Anal. Chem.* **2004**, *76* (6), 1754–1760.
(215) Sobott, F.; Hernández, H.; McCammon, M. G.; Tito, M. A.; Robinson, C. V. A Tandem Mass Spectrometer for Improved Transmission and Analysis of Large Macromolecular Assemblies. *Anal. Chem.* **2002**, *74* (6), 1402–1407.
(216) Benesch, J. L. P.; Ruotolo, B. T.; Simmons, D. A.; Robinson, C. V. Protein Complexes in the Gas Phase: Technology for Structural Genomics and Proteomics. *Chem. Rev.* **2007**, *107* (8), 3544–3567.
(217) Brodbelt, J. S. Analytical Applications of Ion-Molecule Reactions. *Mass Spectrom. Rev.* **1997**, *16* (2), 91–110.
(218) Jones, C. M.; Beardsley, R. L.; Galhena, A. S.; Dagan, S.; Cheng, G.; Wysocki, V. H. Symmetrical Gas-Phase Dissociation of Noncovalent Protein Complexes via Surface Collisions. *J. Am. Chem. Soc.* **2006**, *128* (47), 15044–15045.
(219) Felitsyn, N.; Kitova, E. N.; Klassen, J. S. Thermal Dissociation of the Protein Homodimer Ecotin in the Gas Phase. *J. Am. Soc. Mass Spectrom.* **2002**, *13* (12), 1432–1442.
(220) Geels, R. B. J.; van der Vies, S. M.; Heck, A. J. R.; Heeren, R. M. A. Electron Capture Dissociation as Structural Probe for Noncovalent Gas-Phase Protein Assemblies. *Anal. Chem.* **2006**, *78* (20), 7191–7196.
(221) Mason, E. A.; McDaniel, E. W. *Transport Properties of Ions in Gases*; Wiley, 1988.
(222) Ewing, R. G.; Atkinson, D. A.; Eiceman, G. A.; Ewing, G. J. A Critical Review of Ion Mobility Spectrometry for the Detection of Explosives and Explosive Related Compounds. *Talanta* **2001**, *54* (3), 515–529.
(223) Ah, L.; L, E. Application of Air Sampling and Ion-Mobility Spectrometry to Narcotics Detection: A Feasibility Study. *Bull. Narc.* **1984**, *37* (1), 3–16.

(224) Meng, Q.; Karpas, Z.; Eiceman, G. A. Monitoring Indoor Ambient Atmospheres for Volatile Organic Compounds Using an Ion Mobility Analyzer Array with Selective Chemical Ionization. *Int. J. Environ. Anal. Chem.* **1995**, *61* (2), 81–94.
(225) Karpas, Z.; Tilman, B.; Gdalevsky, R.; Lorber, A. Determination of Volatile Biogenic Amines in Muscle Food Products by Ion Mobility Spectrometry. *Anal. Chim. Acta* **7**, *463* (2), 155–163.
(226) Roehl, J. E. Environmental and Process Applications for Ion Mobility Spectrometry. *Appl. Spectrosc. Rev.* **1991**, *26* (1-2), 1–57.
(227) Eiceman, G. A.; Karpas, Z.; Jr, H. H. H. *Ion Mobility Spectrometry, Third Edition*; CRC Press, 2013.
(228) Cohen, M. J.; Karasek, F. W. Plasma Chromatography^{TM}—A New Dimension for Gas Chromatography and Mass Spectrometry. *J. Chromatogr. Sci.* **1970**, *8* (6), 330–337.
(229) Kozole, J.; Stairs, J. R.; Cho, I.; Harper, J. D.; Lukow, S. R.; Lareau, R. T.; DeBono, R.; Kuja, F. Interfacing an Ion Mobility Spectrometry Based Explosive Trace Detector to a Triple Quadrupole Mass Spectrometer. *Anal. Chem.* **2011**, *83* (22), 8596–8603.
(230) Liuni, P.; Romanov, V.; Binette, M.-J.; Zaknoun, H.; Tam, M.; Pilon, P.; Hendrikse, J.; Wilson, D. J. Unambiguous Characterization of Analytical Markers in Complex, Seized Opiate Samples Using an Enhanced Ion Mobility Trace Detector-Mass Spectrometer. *Anal. Chem.* **2014**, *86* (21), 10772–10779.
(231) McAfee, K. B.; Sipler, D.; Edelson, D. Mobilities and Reactions of Ions in Argon. *Phys. Rev.* **1967**, *160* (1), 130–135.
(232) McKnight, L. G.; McAfee, K. B.; Sipler, D. P. Low-Field Drift Velocities and Reactions of Nitrogen Ions in Nitrogen. *Phys. Rev.* **1967**, *164* (1), 62–70.
(233) McCullough, B. J.; Kalapothakis, J.; Eastwood, H.; Kemper, P.; MacMillan, D.; Taylor, K.; Dorin, J.; Barran, P. E. Development of an Ion Mobility Quadrupole Time of Flight Mass Spectrometer. *Anal. Chem.* **2008**, *80* (16), 6336–6344.
(234) Creaser, C. S.; Benyezzar, M.; Griffiths, J. R.; Stygall, J. W. A Tandem Ion Trap/Ion Mobility Spectrometer. *Anal. Chem.* **2000**, *72* (13), 2724–2729.
(235) Bluhm, B. K.; Gillig, K. J.; Russell, D. H. Development of a Fourier-Transform Ion Cyclotron Resonance Mass Spectrometer-Ion Mobility Spectrometer. *Rev. Sci. Instrum.* **2000**, *71* (11), 4078–4086.
(236) Donohoe, G. C.; Maleki, H.; Arndt, J. R.; Khakinejad, M.; Yi, J.; McBride, C.; Nurkiewicz, T. R.; Valentine, S. J. A New Ion Mobility–Linear Ion Trap Instrument for Complex Mixture Analysis. *Anal. Chem.* **2014**, *86* (16), 8121–8128.
(237) Steiner, W. E.; Klopsch, S. J.; English, W. A.; Clowers, B. H.; Hill, H. H. Detection of a Chemical Warfare Agent Simulant in Various Aerosol Matrixes by Ion Mobility Time-of-Flight Mass Spectrometry. *Anal. Chem.* **2005**, *77* (15), 4792–4799.
(238) Borsdorf, H.; Rudolph, M. Gas-Phase Ion Mobility Studies of Constitutional Isomeric Hydrocarbons Using Different Ionization Techniques. *Int. J. Mass Spectrom.* **2001**, *208* (1-3), 67–72.
(239) Sielemann, S.; Baumbach, J. I.; Schmidt, H.; Pilzecker, P. Quantitative Analysis of Benzene, Toluene, and M-Xylene with the Use of a UV-Ion Mobility Spectrometer. *Field Anal. Chem. Technol.* **2000**, *4* (4), 157–169.
(240) Waltman, M. J.; Dwivedi, P.; Hill, H. H.; Blanchard, W. C.; Ewing, R. G. Characterization of a Distributed Plasma Ionization Source (DPIS) for Ion Mobility Spectrometry and Mass Spectrometry. *Talanta* **2008**, *77* (1), 249–255.

(241) Lee, J.; Park, S.; Cho, S. G.; Goh, E. M.; Lee, S.; Koh, S.-S.; Kim, J. Analysis of Explosives Using Corona Discharge Ionization Combined with Ion Mobility Spectrometry-Mass Spectrometry. *Talanta* **2014**, *120*, 64–70.
(242) Kozole, J.; Levine, L. A.; Tomlinson-Phillips, J.; Stairs, J. R. Gas Phase Ion Chemistry of an Ion Mobility Spectrometry Based Explosive Trace Detector Elucidated by Tandem Mass Spectrometry. *Talanta* **2015**, *140*, 10–19.
(243) Valentine, S. J.; Anderson, J. G.; Ellington, A. D.; Clemmer, D. E. Disulfide-Intact and -Reduced Lysozyme in the Gas Phase: Conformations and Pathways of Folding and Unfolding. *J. Phys. Chem. B* **1997**, *101* (19), 3891–3900.
(244) McLean, J. A.; Ruotolo, B. T.; Gillig, K. J.; Russell, D. H. Ion Mobility–mass Spectrometry: A New Paradigm for Proteomics. *Int. J. Mass Spectrom.* **January 2**, *240* (3), 301–315.
(245) Vonhelden, G.; Wyttenbach, T.; Bowers, M. Conformation of Macromolecules in the Gas-Phase - Use of Matrix-Assisted Laser-Desorption Methods in Ion Chromatography. *Science* **1995**, *267* (5203), 1483–1485.
(246) Ruotolo, B. T.; Giles, K.; Campuzano, I.; Sandercock, A. M.; Bateman, R. H.; Robinson, C. V. Evidence for Macromolecular Protein Rings in the Absence of Bulk Water. *Science* **2005**, *310* (5754), 1658–1661.
(247) Wyttenbach, T.; vonHelden, G.; Bowers, M. T. Gas-Phase Conformation of Biological Molecules: Bradykinin. *J. Am. Chem. Soc.* **1996**, *118* (35), 8355–8364.
(248) Scott, D.; Layfield, R.; Oldham, N. J. Ion Mobility-Mass Spectrometry Reveals Conformational Flexibility in the Deubiquitinating Enzyme USP5. *Proteomics* **2015**, *15* (16), 2835–2841.
(249) Shi, L.; Holliday, A. E.; Khanal, N.; Russell, D. H.; Clemmer, D. E. Configurationally-Coupled Protonation of Polyproline-7. *J. Am. Chem. Soc.* **2015**, *137* (27), 8680–8683.
(250) Clemmer, D.; Hudgins, R.; Jarrold, M. Naked Protein Conformations - Cytochrome-C in the Gas-Phase. *J. Am. Chem. Soc.* **1995**, *117* (40), 10141–10142.
(251) Liu, X.; Valentine, S. J.; Plasencia, M. D.; Trimpin, S.; Naylor, S.; Clemmer, D. E. Mapping the Human Plasma Proteome by SCX-LC-IMS-MS. *J. Am. Soc. Mass Spectrom.* **2007**, *18* (7), 1249–1264.
(252) Uetrecht, C.; Rose, R. J.; van Duijn, E.; Lorenzen, K.; Heck, A. J. R. Ion Mobility Mass Spectrometry of Proteins and Protein Assemblies. *Chem. Soc. Rev.* **2010**, *39* (5), 1633–1655.
(253) Merenbloom, S. I.; Koeniger, S. L.; Valentine, S. J.; Plasencia, M. D.; Clemmer, D. E. IMS−IMS and IMS−IMS−IMS/MS for Separating Peptide and Protein Fragment Ions. *Anal. Chem.* **2006**, *78* (8), 2802–2809.
(254) Kurulugama, R. T.; Valentine, S. J.; Sowell, R. A.; Clemmer, D. E. Development of a High-Throughput IMS-IMS-MS Approach for Analyzing Mixtures of Biomolecules. *J. Proteomics* **2008**, *71* (3), 318–331.
(255) Cottingham, K. Ion Mobility Spectrometry Rediscovered. *Anal. Chem.* **2003**, *75* (19), 435A – 439A.
(256) Cumeras, R. Review on Ion Mobility Spectrometry. Part 2: Hyphenated Methods and Effects of Experimental Parameters. *The Analyst* **2015**, *140* (5), 1391–1410.
(257) Cumeras, R. Review on Ion Mobility Spectrometry. Part 1: Current Instrumentation. *The Analyst* **2015**, *140* (5), 1376–1390.
(258) Mason, E. A.; McDaniel, E. W. *Transport Properties of Ions in Gases*; Wiley, 1988.

(259) Shvartsburg, A. A. *Differential Ion Mobility Spectrometry: Nonlinear Ion Transport and Fundamentals of FAIMS*; CRC Press, 2008.
(260) Bush, M. F.; Hall, Z.; Giles, K.; Hoyes, J.; Robinson, C. V.; Ruotolo, B. T. Collision Cross Sections of Proteins and Their Complexes: A Calibration Framework and Database for Gas-Phase Structural Biology. *Anal. Chem.* **2010**, *82* (22), 9557–9565.
(261) Bohrer, B. C.; Merenbloom, S. I.; Koeniger, S. L.; Hilderbrand, A. E.; Clemmer, D. E. Biomolecule Analysis by Ion Mobility Spectrometry. *Annu. Rev. Anal. Chem.* **2008**, *1* (1), 293–327.
(262) Revercomb, H. E.; Mason, E. A. Theory of Plasma Chromatography/gaseous Electrophoresis. Review. *Anal. Chem.* **1975**, *47* (7), 970–983.
(263) Dugourd, P.; Hudgins, R. R.; Clemmer, D. E.; Jarrold, M. F. High-Resolution Ion Mobility Measurements. *Rev. Sci. Instrum.* **1997**, *68* (2), 1122–1129.
(264) Clemmer, D. E.; Jarrold, M. F. Ion Mobility Measurements and Their Applications to Clusters and Biomolecules. *J. Mass Spectrom.* **1997**, *32* (6), 577–592.
(265) Giles, K.; Pringle, S. D.; Worthington, K. R.; Little, D.; Wildgoose, J. L.; Bateman, R. H. Applications of a Travelling Wave-Based Radio-Frequency-Only Stacked Ring Ion Guide. *Rapid Commun. Mass Spectrom. RCM* **2004**, *18* (20), 2401–2414.
(266) Thalassinos, K.; Grabenauer, M.; Slade, S. E.; Hilton, G. R.; Bowers, M. T.; Scrivens, J. H. Characterization of Phosphorylated Peptides Using Traveling Wave-Based and Drift Cell Ion Mobility Mass Spectrometry. *Anal. Chem.* **2009**, *81* (1), 248–254.
(267) Scarff, C. A.; Thalassinos, K.; Hilton, G. R.; Scrivens, J. H. Travelling Wave Ion Mobility Mass Spectrometry Studies of Protein Structure: Biological Significance and Comparison with X-Ray Crystallography and Nuclear Magnetic Resonance Spectroscopy Measurements. *Rapid Commun. Mass Spectrom.* **2008**, *22* (20), 3297–3304.
(268) Ruotolo, B. T.; Benesch, J. L. P.; Sandercock, A. M.; Hyung, S.-J.; Robinson, C. V. Ion Mobility–mass Spectrometry Analysis of Large Protein Complexes. *Nat. Protoc.* **2008**, *3* (7), 1139–1152.
(269) Li, H.; Giles, K.; Bendiak, B.; Kaplan, K.; Siems, W. F.; Hill, H. H. Resolving Structural Isomers of Monosaccharide Methyl Glycosides Using Drift Tube and Traveling Wave Ion Mobility Mass Spectrometry. *Anal. Chem.* **2012**, *84* (7), 3231–3239.
(270) Niu, S.; Rabuck, J. N.; Ruotolo, B. T. Ion Mobility-Mass Spectrometry of Intact Protein--Ligand Complexes for Pharmaceutical Drug Discovery and Development. *Curr. Opin. Chem. Biol.* **2013**, *17* (5), 809–817.
(271) Zhou, M.; Politis, A.; Davies, R. B.; Liko, I.; Wu, K.-J.; Stewart, A. G.; Stock, D.; Robinson, C. V. Ion Mobility–mass Spectrometry of a Rotary ATPase Reveals ATP-Induced Reduction in Conformational Flexibility. *Nat. Chem.* **2014**, *6* (3), 208–215.
(272) Pringle, S. D.; Giles, K.; Wildgoose, J. L.; Williams, J. P.; Slade, S. E.; Thalassinos, K.; Bateman, R. H.; Bowers, M. T.; Scrivens, J. H. An Investigation of the Mobility Separation of Some Peptide and Protein Ions Using a New Hybrid Quadrupole/travelling Wave IMS/oa-ToF Instrument. *Int. J. Mass Spectrom.* **2007**, *261* (1), 1–12.
(273) Chait, B. T.; Kent, S. B. Weighing Naked Proteins: Practical, High-Accuracy Mass Measurement of Peptides and Proteins. *Science* **1992**, *257* (5078), 1885–1894.
(274) Dill, K. A.; Ozkan, S. B.; Shell, M. S.; Weikl, T. R. The Protein Folding Problem. *Annu. Rev. Biophys.* **2008**, *37*, 289–316.

(275) Johnson, K. A. Rapid Quench Kinetic Analysis of Polymerases, Adenosinetriphosphatases, and Enzyme Intermediates. *Methods Enzymol.* **1995**, *249*, 38–61.
(276) Lipman, E. A.; Schuler, B.; Bakajin, O.; Eaton, W. A. Single-Molecule Measurement of Protein Folding Kinetics. *Science* **2003**, *301* (5637), 1233–1235.
(277) Kelly, S. M.; Price, N. C. The Use of Circular Dichroism in the Investigation of Protein Structure and Function. *Curr. Protein Pept. Sci.* **2000**, *1* (4), 349–384.
(278) Zitzewitz, J. A.; Bilsel, O.; Luo, J.; Jones, B. E.; Matthews, C. R. Probing the Folding Mechanism of a Leucine Zipper Peptide by Stopped-Flow Circular Dichroism Spectroscopy. *Biochemistry (Mosc.)* **1995**, *34* (39), 12812–12819.
(279) Kolakowski, B. M.; Simmons, D. A.; Konermann, L. Stopped-Flow Electrospray Ionization Mass Spectrometry: A New Method for Studying Chemical Reaction Kinetics in Solution. *Rapid Commun. Mass Spectrom.* **2000**, *14* (9), 772–776.
(280) Konermann, L.; Collings, B. A.; Douglas, D. J. Cytochrome c Folding Kinetics Studied by Time-Resolved Electrospray Ionization Mass Spectrometry. *Biochemistry (Mosc.)* **1997**, *36* (18), 5554–5559.
(281) Wilson, D. J.; Konermann, L. A Capillary Mixer with Adjustable Reaction Chamber Volume for Millisecond Time-Resolved Studies by Electrospray Mass Spectrometry. *Anal. Chem.* **2003**, *75* (23), 6408–6414.
(282) Lento, C.; Audette, G. F.; Wilson, D. J. Time-Resolved Electrospray Mass Spectrometry — a Brief History. *Can. J. Chem.* **2014**, *93* (1), 7–12.
(283) Wilson, D. J.; Konermann, L. Mechanistic Studies on Enzymatic Reactions by Electrospray Ionization MS Using a Capillary Mixer with Adjustable Reaction Chamber Volume for Time-Resolved Measurements. *Anal. Chem.* **2004**, *76* (9), 2537–2543.
(284) Cook, P.; Cleland, W. W. *Enzyme Kinetics and Mechanism*; Garland Science, 2007.
(285) Zechel, D. L.; Konermann, L.; Withers, S. G.; Douglas, D. J. Pre-Steady State Kinetic Analysis of an Enzymatic Reaction Monitored by Time-Resolved Electrospray Ionization Mass Spectrometry. *Biochemistry (Mosc.)* **1998**, *37* (21), 7664–7669.
(286) Head, M. B.; Mistry, K. S.; Ridings, B. J.; Smith, C. A.; Parker, M. J. Nucleophilic and Enzymic Catalysis of P-Nitrophenylacetate Hydrolysis. *J. Chem. Educ.* **1995**, *72* (2), 184.
(287) Gutfreund, H.; Sturtevant, J. M. The Mechanism of the Reaction of Chymotrypsin with P-Nitrophenyl Acetate. *Biochem. J.* **1956**, *63* (4), 656–661.
(288) Gutfreund, H.; Sturtevant, J. M. The Mechanism of the Reaction of Chymotrypsin with P-Nitrophenyl Acetate. *Biochem. J.* **1956**, *63* (4), 656–661.
(289) Cook, P.; Cleland, W. W. *Enzyme Kinetics and Mechanism*; Garland Science, 2007.
(290) Purich, D. L. *Enzyme Kinetics: Catalysis & Control: A Reference of Theory and Best-Practice Methods*; Elsevier, 2010.
(291) Berti, P. J. [14] Determining Transition States from Kinetic Isotope Effects; Enzymology, B.-M. in, Ed.; Enzyme kinetics and mechanism Part E: Energetics of Enzyme Catalysis; Academic Press, 1999; Vol. 308, pp 355–397.
(292) Northrop, D. B. Uses of Isotope Effects in the Study of Enzymes. *Methods* **2001**, *24* (2), 117–124.
(293) Blanchard, J. S.; Cleland, W. W. Kinetic and Chemical Mechanisms of Yeast Formate Dehydrogenase. *Biochemistry (Mosc.)* **1980**, *19* (15), 3543–3550.
(294) Roeske, C. A.; O'Leary, M. H. Carbon Isotope Effects on Enzyme-Catalyzed Carboxylation of Ribulose Bisphosphate. *Biochemistry (Mosc.)* **1984**, *23* (25), 6275–6284.

(295) Northrop, D. B. The Expression of Isotope Effects on Enzyme-Catalyzed Reactions. *Annu. Rev. Biochem.* **1981**, *50* (1), 103–131.
(296) Cleland, W. W. The Use of Isotope Effects to Determine Enzyme Mechanisms. *Arch. Biochem. Biophys.* **2005**, *433* (1), 2–12.
(297) Rodgers, J.; Femec, D. A.; Schowen, R. L. Isotopic Mapping of Transition-State Structural Features Associated with Enzymic Catalysis of Methyl Transfer. *J. Am. Chem. Soc.* **1982**, *104* (12), 3263–3268.
(298) Boehr, D. D.; Dyson, H. J.; Wright, P. E. An NMR Perspective on Enzyme Dynamics. *Chem. Rev.* **2006**, *106* (8), 3055–3079.
(299) Daniel, R. M.; Dunn, R. V.; Finney, J. L.; Smith, J. C. The Role of Dynamics in Enzyme Activity. *Annu. Rev. Biophys. Biomol. Struct.* **2003**, *32*, 69–92.
(300) Henzler-Wildman, K. A.; Lei, M.; Thai, V.; Kerns, S. J.; Karplus, M.; Kern, D. A Hierarchy of Timescales in Protein Dynamics Is Linked to Enzyme Catalysis. *Nature* **2007**, *450* (7171), 913–916.
(301) Eisenmesser, E. Z.; Bosco, D. A.; Akke, M.; Kern, D. Enzyme Dynamics During Catalysis. *Science* **2002**, *295* (5559), 1520–1523.
(302) Labeikovsky, W.; Eisenmesser, E. Z.; Bosco, D. A.; Kern, D. Structure and Dynamics of Pin1 during Catalysis by NMR. *J. Mol. Biol.* **2007**, *367* (5), 1370–1381.
(303) Rob, T.; Liuni, P.; Gill, P. K.; Zhu, S.; Balachandran, N.; Berti, P. J.; Wilson, D. J. Measuring Dynamics in Weakly Structured Regions of Proteins Using Microfluidics-Enabled Subsecond H/D Exchange Mass Spectrometry. *Anal. Chem.* **2012**, *84* (8), 3771–3779.
(304) Resetca, D.; Haftchenary, S.; Gunning, P. T.; Wilson, D. J. Changes in Signal Transducer and Activator of Transcription 3 (STAT3) Dynamics Induced by Complexation with Pharmacological Inhibitors of Src Homology 2 (SH2) Domain Dimerization. *J. Biol. Chem.* **2014**, *289* (47), 32538–32547.
(305) Rob, T.; Gill, P. K.; Golemi-Kotra, D.; Wilson, D. J. An Electrospray Ms-Coupled Microfluidic Device for Sub-Second Hydrogen/deuterium Exchange Pulse-Labelling Reveals Allosteric Effects in Enzyme Inhibition. *Lab. Chip* **2013**, *13* (13), 2528–2532.
(306) Grünberg, R.; Leckner, J.; Nilges, M. Complementarity of Structure Ensembles in Protein-Protein Binding. *Struct. Lond. Engl. 1993* **2004**, *12* (12), 2125–2136.
(307) Boehr, D. D.; Nussinov, R.; Wright, P. E. The Role of Dynamic Conformational Ensembles in Biomolecular Recognition. *Nat. Chem. Biol.* **2009**, *5* (11), 789–796.
(308) UNDOC. *Addiction, Crime and Insurgency*; 2009.
(309) CBSA. *Annual Statistics - Seizures*; Canada Border Services Agency: Ottawa, Canada, 2013.
(310) Vincent, P. G.; Engelke, B. F. High Pressure Liquid Chromatographic Determination of the Five Major Alkaloids in Papaver Somniferum L. and Thebaine in Papaver Bracteatum Lindl. Capsular Tissue. *J Assoc Anal Chem* **1979**, *62* (2), 310–314.
(311) Brenneisen, R.; Borner, S. [Psychotropic drugs. IV. The morphinan alkaloid content of Papaver somniferum and Papaver bracteatum]. *Pharm Acta Helv* **1985**, *60* (11), 302–310.
(312) Rajananda, V.; Nair, N. K.; Navaratnam, V. An Evaluation of TLC Systems for Opiate Analysis. *B Narc.* **1985**, *37* (1), 35–47.
(313) Lim, H. Y.; Kwok, S. F. Differentiation and Comparison of Raw, Prepared and Dross Opium. *B Narc.* **1981**, *33* (1), 31–41.

(314) Baggi, T. R.; Rama Rao, N. V.; Murty, H. R. Visualisation of Opium Alkaloids on TLC Plates by Gibbs Reagent Spray. *Forensic Sci* **1976**, *8* (3), 265–267.
(315) Thielemann, H.; Groh, F. [Thin layer chromatographic separation and identification of main opium alkaloids]. *Pharmazie* **1975**, *30* (4), 255–256.
(316) Ashour, A.; Hegazy, M. A.; Moustafa, A. A.; Kelani, K. O.; Fattah, L. E. Validated Stability-Indicating TLC Method for the Determination of Noscapine. *Drug Test Anal* **2009**, *1* (7), 327–338.
(317) Narayanaswami, K.; Golani, H. C.; Dua, R. D. Assay of Major and Minor Constituents of Opium Samples and Studies of Their Origin. *Forensic Sci Int* **1979**, *14* (3), 181–190.
(318) Furmanec, D. Quantitative Gas Chromatographic Determination of the Major Alkaloids in Gum Opium. *J Chromatogr* **1974**, *89* (1), 76–79.
(319) Ayyangar, N. R.; Bhide, S. R. Separation of Eight Alkaloids and Meconic Acid and Quantitation of Five Principal Alkaloids in Gum Opium by Gradient Reversed-Phase High-Performance Liquid Chromatography. *J Chromatogr* **1988**, *436* (3), 455–465.
(320) Ziegler, H. W.; Beasley, T. H., Sr.; Smith, D. W. Simultaneous Assay for Six Alkaloids in Opium, Using High-Performance Liquid Chromatography. *J Assoc Anal Chem* **1975**, *58* (5), 888–897.
(321) Beasley, T. H.; Smith, D. W.; Ziegler, H. W.; Charles, R. L. Liquid Chromatographic System for Separating Opium Alkaloids. *J Assoc Ana Chem* **1974**, *57* (1), 85–90.
(322) Trenerry, V. C.; Wells, R. J.; Robertson, J. Determination of Morphine and Related Alkaloids in Crude Morphine, Poppy Straw and Opium Preparations by Micellar Electrokinetic Capillary Chromatography. *J Chromatogr A* **1995**, *718* (1), 217–225.
(323) Bjornsdottir, I.; Hansen, S. H. Determination of Opium Alkaloids in Crude Opium Using Non-Aqueous Capillary Electrophoresis. *J Pharm. Biomed* **1995**, *13* (12), 1473–1481.
(324) Hodges, C. C.; Rapoport, H. Morphinan Alkaloids in Callus-Cultures of Papaver-Somniferum. *J Nat Prod* **1982**, *45* (4), 481–485.
(325) Matz, L. M.; Hill, H. H., Jr. Evaluation of Opiate Separation by High-Resolution Electrospray Ionization-Ion Mobility Spectrometry/mass Spectrometry. *Anal Chem* **2001**, *73* (8), 1664–1669.
(326) Eatherton, R. L.; Morrissey, M. A.; Hill, H. H. Comparison of Ion Mobility Constants of Selected Drugs after Capillary Gas Chromatography and Capillary Supercritical Fluid Chromatography. *Anal Chem* **1988**, *60* (20), 2240–2243.
(327) Khayamian, T.; Tabrizchi, M.; Jafari, M. T. Quantitative Analysis of Morphine and Noscapine Using Corona Discharge Ion Mobility Spectrometry with Ammonia Reagent Gas. *Talanta* **2006**, *69* (4), 795–799.
(328) Schmidt, J.; Boettcher, C.; Kuhnt, C.; Kutchan, T. M.; Zenk, M. H. Poppy Alkaloid Profiling by Electrospray Tandem Mass Spectrometry and Electrospray FT-ICR Mass Spectrometry after [ring-13C6]-Tyramine Feeding. *Phytochemistry* **2007**, *68* (2), 189–202.
(329) Kikura-Hanajiri, R.; Kaniwa, N.; Ishibashi, M.; Makino, Y.; Kojima, S. Liquid Chromatographic-Atmospheric Pressure Chemical Ionization Mass Spectrometric Analysis of Opiates and Metabolites in Rat Urine after Inhalation of Opium. *J Chromatogr B* **2003**, *789* (1), 139–150.
(330) Morley, S. R.; Forrest, A. R.; Galloway, J. H. Validation of Meconin as a Marker for Illicit Opiate Use. *J Anal Toxicol* **2007**, *31* (2), 105–108.
(331) El-Haj, B. M.; Ali, H. S.; Hamoudi, N. M. Oripavine as a New Marker of Opiate Product Use. *Forensic Toxicol* **2011**, *29* (2), 152–158.

(332) Eiceman, G. A.; Karpas, Z. *Ion Mobility Spectrometry, Second Edition*; Taylor & Francis, 2005.
(333) Eiceman, G. A.; Stone, J. A. Peer Reviewed: Ion Mobility Spectrometers in National Defense. *Anal Chem* **2004**, *76* (21), 390 A – 397 A.
(334) Cottingham, K. Product Review: Ion Mobility Spectrometry Rediscovered. *Anal Chem* **2003**, *75* (19), 435 A – 439 A.
(335) Verkouteren, J. R.; Staymates, J. L. Reliability of Ion Mobility Spectrometry for Qualitative Analysis of Complex, Multicomponent Illicit Drug Samples. *Forensic Sci Int* **2011**, *206* (1-3), 190–196.
(336) Karasek, F. W.; Karasek, D. E.; Kim, S. H. Detection of Lysergic Acid Diethylamide, Delta-9-Tetrahydrocannabinol and Related Compounds by Plasma Chromatography. *J Chromatogr* **1975**, *105* (2), 345–352.
(337) Elias, L.; Lawrence, A. H. Portable Trace Narcotics Detector For Field Use. *Can J Spectrosc* **1987**, *32* (2), A14–A15.
(338) Lawrence, A. H. Ion Mobility Spectrometry Mass-Spectrometry of Some Prescription and Illicit Drugs. *Anal Chem* **1986**, *58* (6), 1269–1272.
(339) St. Louis, R. H.; Hill Jr, H. H.; Eiceman, G. A. Ion Mobility Spectrometry in Analytical Chemistry. *Crc Cr Rev Anal Chem* **1990**, *21* (5), 321–355.
(340) Nanji, A. A.; Lawrence, A. H.; Mikhael, N. Z. Use of Skin Surface Sampling and Ion Mobility Spectrometry as a Preliminary Screening Method for Drug Detection in an Emergency Room. *Clin Toxicol* **1987**, *25* (6), 501–515.
(341) Poziomek, E. J.; Eiceman, G. A. Solid-Phase Enrichment, Thermal-Desorption, and Ion Mobility Spectrometry for Field Screening of Organic Pollutants in Water. *Env. Sci Technol* **1992**, *26* (7), 1313–1318.
(342) Kanu, A. B.; Dwivedi, P.; Tam, M.; Matz, L.; Hill, H. H., Jr. Ion Mobility-Mass Spectrometry. *J Mass Spectrom* **2008**, *43* (1), 1–22.
(343) Revercomb, H. E.; Mason, E. A. Theory of Plasma Chromatography Gaseous Electrophoresis - Review. *Anal Chem* **1975**, *47* (7), 970–983.
(344) Karasek, F. W.; Hill, H. H., Jr.; Kim, S. H. Plasma Chromatography of Heroin and Cocaine with Mass-Identified Mobility Spectra. *J Chromatogr* **1976**, *117* (2), 327–336.
(345) Lawrence, A. H. Characterization of Benzodiazepine Drugs by Ion Mobility Spectrometry. *Anal Chem* **1989**, *61* (4), 343–349.
(346) Borsdorf, H.; Rudolph, M. Gas-Phase Ion Mobility Studies of Constitutional Isomeric Hydrocarbons Using Different Ionization Techniques. *Int J Mass Spectrom* **2001**, *208* (1-3), 67–72.
(347) Sielemann, S.; Baumbach, J.; Schmidt, H.; Pilzecker, P. Quantitative Analysis of Benzene, Toluene, and M-xylene with the Use of a UV–ion Mobility Spectrometer. *Field Anal Chem Tech* **2000**, *4* (4), 157–169.
(348) Wu, C.; Siems, W. F.; Hill, H. H., Jr. Secondary Electrospray Ionization Ion Mobility Spectrometry/mass Spectrometry of Illicit Drugs. *Anal Chem* **2000**, *72* (2), 396–403.
(349) von Helden, G.; Kemper, P. R.; Gotts, N. G.; Bowers, M. T. Isomers of Small Carbon Cluster Anions: Linear Chains with up to 20 Atoms. *Science* **1993**, *259* (5099), 1300–1302.
(350) Gillig, K. J.; Ruotolo, B.; Stone, E. G.; Russell, D. H.; Fuhrer, K.; Gonin, M.; Schultz, A. J. Coupling High-Pressure MALDI with Ion Mobility/orthogonal Time-of-Flight Mass Spectrometry. *Anal Chem* **2000**, *72* (17), 3965–3971.

(351) Stauber, J.; MacAleese, L.; Franck, J.; Claude, E.; Snel, M.; Kaletas, B. K.; Wiel, I. M.; Wisztorski, M.; Fournier, I.; Heeren, R. M. On-Tissue Protein Identification and Imaging by MALDI-Ion Mobility Mass Spectrometry. *J Am Soc Mass Spectrom* **2010**, *21* (3), 338–347.

(352) Weston, D. J.; Bateman, R.; Wilson, I. D.; Wood, T. R.; Creaser, C. S. Direct Analysis of Pharmaceutical Drug Formulations Using Ion Mobility Spectrometry/quadrupole-Time-of-Flight Mass Spectrometry Combined with Desorption Electrospray Ionization. *Anal Chem* **2005**, *77* (23), 7572–7580.

(353) Campuzano, I.; Bush, M. F.; Robinson, C. V.; Beaumont, C.; Richardson, K.; Kim, H.; Kim, H. I. Structural Characterization of Drug-like Compounds by Ion Mobility Mass Spectrometry: Comparison of Theoretical and Experimentally Derived Nitrogen Collision Cross Sections. *Anal Chem* **2011**, *84* (2), 1026–1033.

(354) Cohen, M. J.; Karasek, F. W. Plasma Chromatography - a New Dimension for Gas Chromatography and Mass Spectrometry. *J Chromatogr Sci* **1970**, *8* (6), 330 – &.

(355) Kozole, J.; Stairs, J. R.; Cho, I.; Harper, J. D.; Lukow, S. R.; Lareau, R. T.; DeBono, R.; Kuja, F. Interfacing an Ion Mobility Spectrometry Based Explosive Trace Detector to a Triple Quadrupole Mass Spectrometer. *Anal Chem* **2011**, *83* (22), 8596–8603.

(356) Eiceman, G. A.; Karpas, Z.; Hill Jr, H. H. *Ion Mobility Spectrometry*; CRC press, 2013.

(357) Ritchie, R. K.; Thomson, P. C.; DeBono, R. F.; Danylewich-May, L. L.; Kim, L. Detection of Explosives, Narcotics, and Taggant Vapors by an Ion Mobility Spectrometry Particle Detector; 1994; Vol. 2092, pp 87–93.

(358) Galella, E.; Jennings, S.; Srikoti, M.; Bonasso, E. Cleaning Verification: Method Development and Validation Using Ion Mobility Spectrometry. *Pharm Technol* **2009**, *33* (7), 60–63.

(359) Hill, C. A.; Thomas, C. L. A Pulsed Corona Discharge Switchable High Resolution Ion Mobility Spectrometer-Mass Spectrometer. *Analyst* **2003**, *128* (1), 55–60.

(360) Giles, K.; Grimsrud, E. P. The Kinetic Ion Mobility Mass-Spectrometer - Measurements of Ion Molecule Reaction-Rate Constants at Atmospheric-Pressure. *J Phys Chem-US* **1992**, *96* (16), 6680–6687.

(361) Eiceman, G.; Nazarov, E.; Miller, R. A Micro-Machined Ion Mobility Spectrometer-Mass Spectrometer. *IJIMS* **2000**, *3* (1), 15–27.

(362) Kaur-Atwal, G.; O'Connor, G.; Aksenov, A. A.; Bocos-Bintintan, V.; Paul Thomas, C. L.; Creaser, C. S. Chemical Standards for Ion Mobility Spectrometry: A Review. *Int J Ion Mobil Spec* **2009**, *12* (1), 1–14.

(363) Eiceman, G. A.; Nazarov, E. G.; Stone, J. A. Chemical Standards in Ion Mobility Spectrometry. *Anal Chim Acta* **2003**, *493* (2), 185–194.

(364) Raith, K.; Neubert, R.; Poeaknapo, C.; Boettcher, C.; Zenk, M. H.; Schmidt, J. Electrospray Tandem Mass Spectrometric Investigations of Morphinans. *J Am Soc Mass Spectrom* **2003**, *14* (11), 1262–1269.

(365) Poeaknapo, C.; Fisinger, U.; Zenk, M. H.; Schmidt, J. Evaluation of the Mass Spectrometric Fragmentation of Codeine and Morphine after 13C-Isotope Biosynthetic Labeling. *Phytochemistry* **2004**, *65* (10), 1413–1420.

(366) Fabre, N.; Claparols, C.; Richelme, S.; Angelin, M. L.; Fouraste, I.; Moulis, C. Direct Characterization of Isoquinoline Alkaloids in a Crude Plant Extract by Ion-Pair Liquid Chromatography-Electrospray Ionization Tandem Mass Spectrometry: Example of Eschscholtzia Californica. *J Chromatogr A* **2000**, *904* (1), 35–46.

(367) Zhu, L.; Chen, X.; Zhang, Y.; Yu, H.; Zhong, D. Simultaneous Determination of Methylephedrine and Noscapine in Human Plasma by Liquid Chromatography-Tandem Mass Spectrometry. *J Chromatogr B* **2005**, *820* (2), 175–182.
(368) Wickens, J. R.; Sleeman, R.; Keely, B. J. Atmospheric Pressure Ionisation Mass Spectrometric Fragmentation Pathways of Noscapine and Papaverine Revealed by Multistage Mass Spectrometry and in-Source Deuterium Labelling. *Rapid Commun Mass Spectrom* **2006**, *20* (3), 473–480.
(369) Desgagne-Penix, I.; Facchini, P. J. Systematic Silencing of Benzylisoquinoline Alkaloid Biosynthetic Genes Reveals the Major Route to Papaverine in Opium Poppy. *Plant J* **2012**, *72* (2), 331–344.
(370) Schmidt, J.; Raith, K.; Boettcher, C.; Zenk, M. H. Analysis of Benzylisoquinoline-Type Alkaloids by Electrospray Tandem Mass Spectrometry and Atmospheric Pressure Photoionization. *Eur J Mass Spectrom* **2005**, *11* (3), 325–333.
(371) Staba, E. J.; Zito, S.; Amin, M. Alkaloid Production from Papaver Tissue-Cultures. *J Nat Prod* **1982**, *45* (3), 256–262.
(372) Desgagne-Penix, I.; Farrow, S. C.; Cram, D.; Nowak, J.; Facchini, P. J. Integration of Deep Transcript and Targeted Metabolite Profiles for Eight Cultivars of Opium Poppy. *Plant Mol Biol* **2012**, *79* (3), 295–313.
(373) Soparawalla, S.; Salazar, G. A.; Sokol, E.; Perry, R. H.; Cooks, R. G. Trace Detection of Non-Uniformly Distributed Analytes on Surfaces Using Mass Transfer and Large-Area Desorption Electrospray Ionization (DESI) Mass Spectrometry. *Analyst* **2010**, *135* (8), 1953–1960.
(374) Smith, C. A.; Maille, G. O.; Want, E. J.; Qin, C.; Trauger, S. A.; Brandon, T. R.; Custodio, D. E.; Abagyan, R.; Siuzdak, G. METLIN: A Metabolite Mass Spectral Database. *Ther Drug Monit* **2005**, *27* (6), 747–751.
(375) Fairbairn, J. W.; Williamson, E. M. Meconic Acid as a Chemotaxonomic Marker in the Papaveraceae. *Phytochemistry* **1978**, *17* (12), 2087–2089.
(376) Awade, A. C.; Cleuziat, P.; Gonzales, T.; Robert-Baudouy, J. Pyrrolidone Carboxyl Peptidase (Pcp): An Enzyme That Removes Pyroglutamic Acid (pGlu) from pGlu-Peptides and pGlu-Proteins. *Proteins.* **1994**, *20* (1), 34–51.
(377) Roessner, U.; Wagner, C.; Kopka, J.; Trethewey, R. N.; Willmitzer, L. Technical Advance: Simultaneous Analysis of Metabolites in Potato Tuber by Gas Chromatography-Mass Spectrometry. *Plant J* **2000**, *23* (1), 131–142.
(378) Abraham, G. N.; Podell, D. N. Pyroglutamic Acid. Non-Metabolic Formation, Function in Proteins and Peptides, and Characteristics of the Enzymes Effecting Its Removal. *Mol Cell Biochem* **1981**, *38 Spec No* (Pt 1), 181–190.
(379) Wold, J. K.; Smestad, B.; Winsnes, R.; Resser, D. The Water-Soluble Polysaccharide of Opium Poppy (Papaver Somniferum L.). *Acta Chem Scand* **1970**, *24* (4), 1262–1270.
(380) Daggett, V.; Fersht, A. The Present View of the Mechanism of Protein Folding. *Nat Rev Mol Cell Biol* **2003**, *4* (6), 497–502.
(381) Englander, S. W.; Mayne, L.; Krishna, M. M. G. Protein Folding and Misfolding: Mechanism and Principles. *Q. Rev. Biophys.* **2007**, *40* (04), 287–326.
(382) Matthews, C. R. Pathways of Protein Folding. *Annu. Rev. Biochem.* **1993**, *62* (1), 653–683.

(383) Zhu, L.; Fan, Y.-X.; Perrett, S.; Zhou, J.-M. Relationship between Kinetic and Equilibrium Folding Intermediates of Creatine Kinase. *Biochem. Biophys. Res. Commun.* **7**, *285* (4), 857–862.
(384) Udgaonkar, J. B. Multiple Routes and Structural Heterogeneity in Protein Folding. *Annu. Rev. Biophys.* **2008**, *37* (1), 489–510.
(385) Morris, E. R.; Searle, M. S. Overview of Protein Folding Mechanisms: Experimental and Theoretical Approaches to Probing Energy Landscapes. In *Current Protocols in Protein Science*; John Wiley & Sons, Inc., 2001.
(386) Ptitsyn, O. B. Kinetic and Equilibrium Intermediates in Protein Folding. *Protein Eng.* **1994**, *7* (5), 593–596.
(387) Ptitsyn, O. B.; Bychkova, V. E.; Uversky, V. N. *Kinetic and Equilibrium Folding Intermediates*; 1995; Vol. 348.
(388) Enoki, S.; Maki, K.; Inobe, T.; Takahashi, K.; Kamagata, K.; Oroguchi, T.; Nakatani, H.; Tomoyori, K.; Kuwajima, K. The Equilibrium Unfolding Intermediate Observed at pH 4 and Its Relationship with the Kinetic Folding Intermediates in Green Fluorescent Protein. *J. Mol. Biol.* **January 9**, *361* (5), 969–982.
(389) Dai, S. Y.; Fitzgerald, M. C. A Mass Spectrometry-Based Probe of Equilibrium Intermediates in Protein-Folding Reactions†. *Biochemistry (Mosc.)* **2006**, *45* (42), 12890–12897.
(390) Roy, S.; Basu, S.; Datta, A. K.; Bhattacharyya, D.; Banerjee, R.; Dasgupta, D. Equilibrium Unfolding of Cyclophilin from Leishmania Donovani: Characterization of Intermediate States. *Int. J. Biol. Macromol.* **8**, *69* (0), 353–360.
(391) Ayuso-Tejedor, S.; García-Fandiño, R.; Orozco, M.; Sancho, J.; Bernadó, P. Structural Analysis of an Equilibrium Folding Intermediate in the Apoflavodoxin Native Ensemble by Small-Angle X-Ray Scattering. *J. Mol. Biol.* **April 3**, *406* (4), 604–619.
(392) Neira, J. L. NMR as a Tool to Identify and Characterize Protein Folding Intermediates. *Arch. Biochem. Biophys.* **3**, *531* (1–2), 90–99.
(393) Haezebrouck, P.; Noyelle, K.; Joniau, M.; Van Dael, H. Kinetic and Equilibrium Intermediate States Are Different in LYLA1, a Chimera of Lysozyme and α-lactalbumin1. *J. Mol. Biol.* **10**, *293* (3), 703–718.
(394) Chen, K.-C.; Xu, M.; Wedemeyer, W. J.; Roder, H. Microsecond Unfolding Kinetics of Sheep Prion Protein Reveals an Intermediate That Correlates with Susceptibility to Classical Scrapie. *Biophys. J.* **July 9**, *101* (5), 1221–1230.
(395) Yamada, S.; Bouley Ford, N. D.; Keller, G. E.; Ford, W. C.; Gray, H. B.; Winkler, J. R. Snapshots of a Protein Folding Intermediate. *Proc. Natl. Acad. Sci.* **2013**, *110* (5), 1606–1610.
(396) Chen, Y.-C.; Urban, P. L. Time-Resolved Mass Spectrometry. *TrAC Trends Anal. Chem.* **3**, *44* (0), 106–120.
(397) Rob, T.; Wilson, D. Time-Resolved Mass Spectrometry for Monitoring Millisecond Time-Scale Solution-Phase Processes. *Eur. J. Mass Spectrom.* **2012**, *18* (2), 205–214.
(398) Wilson, D. J.; Konermann, L. A Capillary Mixer with Adjustable Reaction Chamber Volume for Millisecond Time-Resolved Studies by Electrospray Mass Spectrometry. *Anal. Chem.* **2003**, *75* (23), 6408–6414.
(399) Roberts, A.; Furdui, C.; Anderson, K. S. Observation of a Chemically Labile, Noncovalent Enzyme Intermediate in the Reaction of Metal-Dependent Aquifex Pyrophilus

KDO8PS by Time-Resolved Mass Spectrometry. *Rapid Commun. Mass Spectrom.* **2010**, *24* (13), 1919–1924.

(400) Li, Z.; Song, F.; Zhuang, Z.; Dunaway-Mariano, D.; Anderson, K. S. Monitoring Enzyme Catalysis in the Multimeric State: Direct Observation of Arthrobacter 4-Hydroxybenzoyl–coenzyme A Thioesterase Catalytic Complexes Using Time-Resolved Electrospray Ionization Mass Spectrometry. *Anal. Biochem.* **11**, *394* (2), 209–216.

(401) Konermann, L.; Collings, B. A.; Douglas, D. J. Cytochrome c Folding Kinetics Studied by Time-Resolved Electrospray Ionization Mass Spectrometry. *Biochemistry (Mosc.)* **1997**, *36* (18), 5554–5559.

(402) Konermann, L.; Rosell, F. I.; Mauk, A. G.; Douglas, D. J. Acid-Induced Denaturation of Myoglobin Studied by Time-Resolved Electrospray Ionization Mass Spectrometry. *Biochemistry (Mosc.)* **1997**, *36* (21), 6448–6454.

(403) Vahidi, S.; Stocks, B. B.; Liaghati-Mobarhan, Y.; Konermann, L. Submillisecond Protein Folding Events Monitored by Rapid Mixing and Mass Spectrometry-Based Oxidative Labeling. *Anal. Chem.* **2013**, *85* (18), 8618–8625.

(404) Pan, J.; Rintala-Dempsey, A. C.; Li, Y.; Shaw, G. S.; Konermann, L. Folding Kinetics of the S100A11 Protein Dimer Studied by Time-Resolved Electrospray Mass Spectrometry and Pulsed Hydrogen−Deuterium Exchange†. *Biochemistry (Mosc.)* **2006**, *45* (9), 3005–3013.

(405) Rob, T.; Liuni, P.; Gill, P. K.; Zhu, S.; Balachandran, N.; Berti, P. J.; Wilson, D. J. Measuring Dynamics in Weakly Structured Regions of Proteins Using Microfluidics-Enabled Subsecond H/D Exchange Mass Spectrometry. *Anal. Chem.* **2012**, *84* (8), 3771–3779.

(406) Pan, J.; Han, J.; Borchers, C. H.; Konermann, L. Characterizing Short-Lived Protein Folding Intermediates by Top-Down Hydrogen Exchange Mass Spectrometry. *Anal. Chem.* **2010**, *82* (20), 8591–8597.

(407) Lanucara, F.; Holman, S. W.; Gray, C. J.; Eyers, C. E. The Power of Ion Mobility-Mass Spectrometry for Structural Characterization and the Study of Conformational Dynamics. *Nat Chem* **2014**, *6* (4), 281–294.

(408) Ruotolo, B. T.; Benesch, J. L. P.; Sandercock, A. M.; Hyung, S.-J.; Robinson, C. V. Ion Mobility-Mass Spectrometry Analysis of Large Protein Complexes. *Nat Protoc.* **2008**, *3* (7), 1139–1152.

(409) Michaelevski, I.; Kirshenbaum, N.; Sharon, M. T-Wave Ion Mobility-Mass Spectrometry: Basic Experimental Procedures for Protein Complex Analysis. **2010**, No. 41, e1985.

(410) Salbo, R.; Bush, M. F.; Naver, H.; Campuzano, I.; Robinson, C. V.; Pettersson, I.; Jørgensen, T. J. D.; Haselmann, K. F. Traveling-Wave Ion Mobility Mass Spectrometry of Protein Complexes: Accurate Calibrated Collision Cross-Sections of Human Insulin Oligomers. *Rapid Commun. Mass Spectrom.* **2012**, *26* (10), 1181–1193.

(411) Chawner, R.; McCullough, B.; Giles, K.; Barran, P. E.; Gaskell, S. J.; Eyers, C. E. QconCAT Standard for Calibration of Ion Mobility-Mass Spectrometry Systems. *J. Proteome Res.* **2012**, *11* (11), 5564–5572.

(412) Smith, D.; Giles, K.; Bateman, R.; Radford, S.; Ashcroft, A. Monitoring Copopulated Conformational States during Protein Folding Events Using Electrospray Ionization-Ion Mobility Spectrometry-Mass Spectrometry. *J. Am. Soc. Mass Spectrom.* **2007**, *18* (12), 2180–2190.

(413) Smith, D. P.; Knapman, T. W.; Campuzano, I.; Malham, R. W.; Berryman, J. T.; Radford, S. E.; Ashcroft, A. E. Deciphering Drift Time Measurements from Travelling Wave Ion Mobility Spectrometry-Mass Spectrometry Studies. *Eur J Mass Spectrom Chichester Eng* **2009**, *15* (2), 113–130.

(414) Lento, C.; Audette, G. F.; Wilson, D. J. Time-Resolved Electrospray Mass Spectrometry — a Brief History. *Can. J. Chem.* **2015**, *93* (1), 7–12.

(415) Liuni, P.; Olkhov-Mitsel, E.; Orellana, A.; Wilson, D. J. Measuring Kinetic Isotope Effects in Enzyme Reactions Using Time-Resolved Electrospray Mass Spectrometry. *Anal Chem* **2013**, *85* (7), 3758–3764.

(416) Eaton, W. A.; Muñoz, V.; Hagen, S. J.; Jas, G. S.; Lapidus, L. J.; Henry, E. R.; Hofrichter, J. Fast Kinetics and Mechanisms in Protein Folding. *Annu. Rev. Biophys. Biomol. Struct.* **2000**, *29* (1), 327–359.

(417) Bhuyan, A. K.; Udgaonkar, J. B. Folding of Horse Cytochrome c in the Reduced State. *J. Mol. Biol.* **2001**, *312* (5), 1135–1160.

(418) Simmons, D. A.; Wilson, D. J.; Lajoie, G. A.; Doherty-Kirby, A.; Konermann, L. Subunit Disassembly and Unfolding Kinetics of Hemoglobin Studied by Time-Resolved Electrospray Mass Spectrometry†. *Biochemistry (Mosc.)* **2004**, *43* (46), 14792–14801.

(419) Pan, J.; Wilson, D. J.; Konermann, L. Pulsed Hydrogen Exchange and Electrospray Charge-State Distribution as Complementary Probes of Protein Structure in Kinetic Experiments: Implications for Ubiquitin Folding†. *Biochemistry (Mosc.)* **2005**, *44* (24), 8627–8633.

(420) Wilson, D. J.; Rafferty, S. P.; Konermann, L. Kinetic Unfolding Mechanism of the Inducible Nitric Oxide Synthase Oxygenase Domain Determined by Time-Resolved Electrospray Mass Spectrometry†. *Biochemistry (Mosc.)* **2005**, *44* (7), 2276–2283.

(421) Silveira, J. A.; Fort, K. L.; Kim, D.; Servage, K. A.; Pierson, N. A.; Clemmer, D. E.; Russell, D. H. From Solution to the Gas Phase: Stepwise Dehydration and Kinetic Trapping of Substance P Reveals the Origin of Peptide Conformations. *J. Am. Chem. Soc.* **2013**, *135* (51), 19147–19153.

(422) Northrop, D. B. Uses of Isotope Effects in the Study of Enzymes. *Methods* **2001**, *24* (2), 117–124.

(423) Mahler, H. R.; Douglas, J. Mechanisms of Enzyme-Catalyzed Oxidation-Reduction Reactions. I. An Investigation of the Yeast Alcohol Dehydrogenase Reaction by Means of the Isotope Rate Effect1,2. *J. Am. Chem. Soc.* **1957**, *79* (5), 1159–1166.

(424) Whittaker, M. M.; Ballou, D. P.; Whittaker, J. W. Kinetic Isotope Effects as Probes of the Mechanism of Galactose Oxidase. *Biochemistry (Mosc.)* **1998**, *37* (23), 8426–8436.

(425) Papajak, E.; Kwiecien, R. A.; Rudzinski, J.; Sicinska, D.; Kaminski, R.; Szatkowski, L.; Kurihara, T.; Esaki, N.; Paneth, P. Mechanism of the Reaction Catalyzed by DL-2-Haloacid Dehalogenase as Determined from Kinetic Isotope Effects. *Biochemistry (Mosc.)* **2006**, *45* (19), 6012–6017.

(426) Nesheim, J. C.; Lipscomb, J. D. Large Kinetic Isotope Effects in Methane Oxidation Catalyzed by Methane Monooxygenase: Evidence for C-H Bond Cleavage in a Reaction Cycle Intermediate. *Biochemistry (Mosc.)* **1996**, *35* (31), 10240–10247.

(427) Rendina, A. R.; Hermes, J. D.; Cleland, W. W. Use of Multiple Isotope Effects to Study the Mechanism of 6-Phosphogluconate Dehydrogenase. *Biochemistry (Mosc.)* **1984**, *23* (25), 6257–6262.

(428) Kim, K. H.; Isin, E. M.; Yun, C. H.; Kim, D. H.; Guengerich, F. P. Kinetic Deuterium Isotope Effects for 7-Alkoxycoumarin O-Dealkylation Reactions Catalyzed by Human Cytochromes P450 and in Liver Microsomes - Rate-Limiting C-H Bond Breaking in Cytochrome P450 1A2 Substrate Oxidation. *Febs J.* **2006**, *273* (10), 2223–2231.
(429) Knapp, M. J.; Klinman, J. P. Environmentally Coupled Hydrogen Tunneling - Linking Catalysis to Dynamics. *Eur. J. Biochem.* **2002**, *269* (13), 3113–3121.
(430) Sikorski, R. S.; Wang, L.; Markham, K. A.; Rajagopalan, P. T. R.; Benkovic, S. J.; Kohen, A. Tunneling and Coupled Motion in the Escherichia Coli Dihydrofolate Reductase Catalysis. *J. Am. Chem. Soc.* **2004**, *126* (15), 4778–4779.
(431) Hay, S.; Sutcliffe, M. J.; Scrutton, N. S. Promoting Motions in Enzyme Catalysis Probed by Pressure Studies of Kinetic Isotope Effects. *Proc. Natl. Acad. Sci. U. S. A.* **2007**, *104* (2), 507–512.
(432) Swanwick, R. S.; Maglia, G.; Tey, L.; Allemann, R. K. Coupling of Protein Motions and Hydrogen Transfer during Catalysis by Escherichia Coli Dihydrofolate Reductase. *Biochem. J.* **2006**, *394*, 259–265.
(433) Schramm, V. L.; Horenstein, B. A.; Kline, P. C. Transition State Analysis and Inhibitor Design for Enzymatic Reactions. *J. Biol. Chem.* **1994**, *269* (28), 18259–18262.
(434) Schramm, V. L. Enzymatic Transition States and Transition State Analogues. *Curr. Opin. Struct. Biol.* **2005**, *15* (6), 604–613.
(435) Berti, P. J. Determining Transition States from Kinetic Isotope Effects. *Enzyme Kinet. Mech. Pt E* **1999**, *308*, 355–397.
(436) Northrop, D. B. Steady-State Analysis of Kinetic Isotope Effects in Enzymic Reactions. *Biochemistry (Mosc.)* **1975**, *14* (12), 2644–2651.
(437) Glowacki, D. R.; Harvey, J. N.; Mulholland, A. J. Protein Dynamics and Enzyme Catalysis: The Ghost in the Machine? *Biochem. Soc. Trans.* **2012**, *40*, 515–521.
(438) McCann, J. A. B.; Berti, P. J. Transition State Analysis of Acid-Catalyzed dAMP Hydrolysis. *J. Am. Chem. Soc.* **2007**, *129* (22), 7055–7064.
(439) Kohen, A. Kinetic Isotope Effects as Probes for Hydrogen Tunneling, Coupled Motion and Dynamics Contributions to Enzyme Catalysis. *Prog. React. Kinet. Mech.* **2003**, *28* (2), 119–156.
(440) Sutcliffe, M. J.; Masgrau, L.; Roujeinikova, A.; Johannissen, L. O.; Hothi, P.; Basran, J.; Ranaghan, K. E.; Mulholland, A. J.; Leys, D.; Scrutton, N. S. Hydrogen Tunnelling in Enzyme-Catalysed H-Transfer Reactions: Flavoprotein and Quinoprotein Systems. *Philos. Trans. R. Soc. B-Biol. Sci.* **2006**, *361* (1472), 1375–1386.
(441) Klinman, J. P. Isotope Effects and Structure-Reactivity Correlations in the Yeast Alcohol Dehydrogenase Reaction. A Study of the Enzyme-Catalyzed Oxidation of Aromatic Alcohols. *Biochemistry (Mosc.)* **1976**, *15* (9), 2018–2026.
(442) Bates, C.; Kendrick, Z.; McDonald, N.; Kline, P. C. Transition State Analysis of Adenosine Nucleosidase from Yellow Lupin (Lupinus Luteus). *Phytochemistry* **2006**, *67* (1), 5–12.
(443) Hunt, C.; Gillani, N.; Farone, A.; Rezaei, M.; Kline, P. C. Kinetic Isotope Effects of Nucleoside Hydrolase from Escherichia Coli. *Biochim. Biophys. Acta-Proteins Proteomics* **2005**, *1751* (2), 140–149.
(444) Brecker, L.; Kogl, M. F.; Tyl, C. E.; Kratzer, R.; Nidetzky, B. NMR Study of C-13-Kinetic Isotope Effects at C-13 Natural Abundance to Characterize Oxidations and an Enzyme-Catalyzed Reduction. *Tetrahedron Lett.* **2006**, *47* (24), 4045–4049.

(445) Chan, J.; Lewis, A. R.; Gilbert, M.; Karwaski, M.-F.; Bennet, A. J. A Direct NMR Method for the Measurement of Competitive Kinetic Isotope Effects. *Nat. Chem. Biol.* **2010**, *6* (6), 405–407.
(446) Singleton, D. A.; Thomas, A. A. High-Precision Simultaneous Determination of Multiple Small Kinetic Isotope Effects at Natural Abundance. *J. Am. Chem. Soc.* **1995**, *117* (36), 9357–9358.
(447) Werner, R. A.; Brand, W. A. Referencing Strategies and Techniques in Stable Isotope Ratio Analysis. *Rapid Commun. Mass Spectrom.* **2001**, *15* (7), 501–519.
(448) Wilson, D. J.; Konermann, L. A Capillary Mixer with Adjustable Reaction Chamber Volume for Millisecond Time-Resolved Studies by Electrospray Mass Spectrometry. *Anal. Chem.* **2003**, *75* (23), 6408–6414.
(449) Wilson, D. J.; Konermann, L. Mechanistic Studies on Enzymatic Reactions by Electrospray Ionization MS Using a Capillary Mixer with Adjustable Reaction Chamber Volume for Time-Resolved Measurements. *Anal. Chem.* **2004**, *76* (9), 2537–2543.
(450) Powell, M. F.; Bruice, T. C. Effect of Isotope Scrambling and Tunneling on the Kinetic and Product Isotope Effects for Reduced Nicotinamide Adenine Dinucleotide Model Hydride Transfer Reactions. *J. Am. Chem. Soc.* **1983**, *105* (24), 7139–7149.
(451) Northrop, D. B.; Cho, Y. K. Effect of Pressure on Deuterium Isotope Effects of Yeast Alcohol Dehydrogenase: Evidence for Mechanical Models of Catalysis. *Biochemistry (Mosc.)* **2000**, *39* (9), 2406–2412.
(452) Cha, Y.; Murray, C. J.; Klinman, J. P. Hydrogen Tunneling in Enzyme Reactions. *Science* **1989**, *243* (4896), 1325–1330.
(453) Bahnson, B. J.; Colby, T. D.; Chin, J. K.; Goldstein, B. M.; Klinman, J. P. A Link between Protein Structure and Enzyme Catalyzed Hydrogen Tunneling. *Proc. Natl. Acad. Sci. U. S. A.* **1997**, *94* (24), 12797–12802.
(454) Kohen, A.; Cannio, R.; Bartolucci, S.; Klinman, J. P. Enzyme Dynamics and Hydrogen Tunnelling in a Thermophilic Alcohol Dehydrogenase. *Nature* **1999**, *399* (6735), 496–499.
(455) Hay, S.; Johannissen, L. O.; Hothi, P.; Sutcliffe, M. J.; Scrutton, N. S. Pressure Effects on Enzyme-Catalyzed Quantum Tunneling Events Arise from Protein-Specific Structural and Dynamic Changes. *J. Am. Chem. Soc.* **2012**, *134* (23), 9749–9754.
(456) Dickinson, F. M.; Monger, G. P. A Study of the Kinetics and Mechanism of Yeast Alcohol Dehydrogenase with a Variety of Substrates. *Biochem. J.* **1973**, *131* (2), 261–270.
(457) Zhang, H.; Cui, W.; Wen, J.; Blankenship, R. E.; Gross, M. L. Native Electrospray and Electron-Capture Dissociation in FTICR Mass Spectrometry Provide Top-Down Sequencing of a Protein Component in an Intact Protein Assembly. *J. Am. Soc. Mass Spectrom.* **2010**, *21* (12), 1966–1968.
(458) Loo, J. A. Observation of Large Subunit Protein Complexes by Electrospray Ionization Mass Spectrometry. *J. Mass Spectrom.* **1995**, *30* (1), 180–183.
(459) Klinman, J. P. The Mechanism of Enzyme-Catalyzed Reduced Nicotinamide Adenine Dinucleotide-Dependent Reductions. Substituent and Isotope Effects in the Yeast Alcohol Dehydrogenase Reaction. *J. Biol. Chem.* **1972**, *247* (24), 7977–7987.
(460) Park, H.; Kidman, G.; Northrop, D. B. Effects of Pressure on Deuterium Isotope Effects of Yeast Alcohol Dehydrogenase Using Alternative Substrates. *Arch. Biochem. Biophys.* **2005**, *433* (1), 335–340.

(461) Hess, R. A.; Hengge, A. C.; Cleland, W. W. Isotope Effects on Enzyme-Catalyzed Acyl Transfer from P-Nitrophenyl Acetate: Concerted Mechanisms and Increased Hyperconjugation in the Transition State. *J. Am. Chem. Soc.* **1998**, *120* (12), 2703–2709.
(462) Mishra, A. K.; Klapper, M. H. Permeable Membrane/mass Spectrometric Measurement of Solvent 1H/2H, 12C/13C, and 16O/18O Kinetic Isotope Effects Associated with Alpha-Chymotrypsin Deacylation: Evidence for Reaction Mechanism Plasticity. *Biochemistry (Mosc.)* **1986**, *25* (23), 7328–7336.
(463) Fraser, J. S.; Clarkson, M. W.; Degnan, S. C.; Erion, R.; Kern, D.; Alber, T. Hidden Alternative Structures of Proline Isomerase Essential for Catalysis. *Nature* **2009**, *462* (7273), 669–673.
(464) Homouz, D.; Sanabria, H.; Waxham, M. N.; Cheung, M. S. Modulation of Calmodulin Plasticity by the Effect of Macromolecular Crowding. *J. Mol. Biol.* **2009**, *391* (5), 933–943.
(465) Boehr, D. D.; McElheny, D.; Dyson, H. J.; Wright, P. E. Millisecond Timescale Fluctuations in Dihydrofolate Reductase Are Exquisitely Sensitive to the Bound Ligands. *Proc. Natl. Acad. Sci.* **2010**, *107* (4), 1373–1378.
(466) Nestl, B. M.; Hauer, B. Engineering of Flexible Loops in Enzymes. *ACS Catal.* **2014**, *4* (9), 3201–3211.
(467) Benkovic, S. J.; Hammes-Schiffer, S. A Perspective on Enzyme Catalysis. *Science* **2003**, *301* (5637), 1196–1202.
(468) Callender, R.; Dyer, R. B. The Dynamical Nature of Enzymatic Catalysis. *Acc. Chem. Res.* **2014**.
(469) Bhabha, G.; Biel, J. T.; Fraser, J. S. Keep on Moving: Discovering and Perturbing the Conformational Dynamics of Enzymes. *Acc. Chem. Res.* **2014**.
(470) Schotte, F.; Lim, M.; Jackson, T. A.; Smirnov, A. V.; Soman, J.; Olson, J. S.; Phillips, G. N.; Wulff, M.; Anfinrud, P. A. Watching a Protein as It Functions with 150-Ps Time-Resolved X-Ray Crystallography. *Science* **2003**, *300* (5627), 1944–1947.
(471) Bourgeois, D.; Royant, A. Advances in Kinetic Protein Crystallography. *Curr. Opin. Struct. Biol.* **2005**, *15* (5), 538–547.
(472) Peng, H.-L.; Deng, H.; Dyer, R. B.; Callender, R. Energy Landscape of the Michaelis Complex of Lactate Dehydrogenase: Relationship to Catalytic Mechanism. *Biochemistry (Mosc.)* **2014**, *53* (11), 1849–1857.
(473) Kukura, P.; McCamant, D. W.; Yoon, S.; Wandschneider, D. B.; Mathies, R. A. Structural Observation of the Primary Isomerization in Vision with Femtosecond-Stimulated Raman. *Science* **2005**, *310* (5750), 1006–1009.
(474) Henzler-Wildman, K. A.; Thai, V.; Lei, M.; Ott, M.; Wolf-Watz, M.; Fenn, T.; Pozharski, E.; Wilson, M. A.; Petsko, G. A.; Karplus, M.; et al. Intrinsic Motions along an Enzymatic Reaction Trajectory. *Nature* **2007**, *450* (7171), 838–844.
(475) Myong, S.; Stevens, B. C.; Ha, T. Bridging Conformational Dynamics and Function Using Single-Molecule Spectroscopy. *Struct. Lond. Engl. 1993* **2006**, *14* (4), 633–643.
(476) Eisenmesser, E. Z.; Bosco, D. A.; Akke, M.; Kern, D. Enzyme Dynamics During Catalysis. *Science* **2002**, *295* (5559), 1520–1523.
(477) Mulder, F. A. A.; Mittermaier, A.; Hon, B.; Dahlquist, F. W.; Kay, L. E. Studying Excited States of Proteins by NMR Spectroscopy. *Nat. Struct. Mol. Biol.* **2001**, *8* (11), 932–935.

(478) Korzhnev, D. M.; Salvatella, X.; Vendruscolo, M.; Di Nardo, A. A.; Davidson, A. R.; Dobson, C. M.; Kay, L. E. Low-Populated Folding Intermediates of Fyn SH3 Characterized by Relaxation Dispersion NMR. *Nature* **2004**, *430* (6999), 586–590.
(479) Palmer, A. G. NMR Characterization of the Dynamics of Biomacromolecules. *Chem. Rev.* **2004**, *104* (8), 3623–3640.
(480) Sprangers, R.; Kay, L. E. Quantitative Dynamics and Binding Studies of the 20S Proteasome by NMR. *Nature* **2007**, *445* (7128), 618–622.
(481) Christodoulou, J.; Larsson, G.; Fucini, P.; Connell, S. R.; Pertinhez, T. A.; Hanson, C. L.; Redfield, C.; Nierhaus, K. H.; Robinson, C. V.; Schleucher, J.; et al. Heteronuclear NMR Investigations of Dynamic Regions of Intact Escherichia Coli Ribosomes. *Proc. Natl. Acad. Sci. U. S. A.* **2004**, *101* (30), 10949–10954.
(482) Rennella, E.; Huang, R.; Velyvis, A.; Kay, L. E. (CHD2)-C-13-CEST NMR Spectroscopy Provides an Avenue for Studies of Conformational Exchange in High Molecular Weight Proteins. *J. Biomol. Nmr* **2015**, *63* (2), 187–199.
(483) Mittermaier, A.; Kay, L. E. New Tools Provide New Insights in NMR Studies of Protein Dynamics. *Science* **2006**, *312* (5771), 224–228.
(484) Villali, J.; Kern, D. Choreographing an Enzyme's Dance. *Curr. Opin. Chem. Biol.* **2010**, *14* (5), 636–643.
(485) Labeikovsky, W.; Eisenmesser, E. Z.; Bosco, D. A.; Kern, D. Structure and Dynamics of Pin1 During Catalysis by NMR. *J. Mol. Biol.* **2007**, *367* (5), 1370–1381.
(486) Wolf-Watz, M.; Thai, V.; Henzler-Wildman, K.; Hadjipavlou, G.; Eisenmesser, E. Z.; Kern, D. Linkage between Dynamics and Catalysis in a Thermophilic-Mesophilic Enzyme Pair. *Nat. Struct. Mol. Biol.* **2004**, *11* (10), 945–949.
(487) Vocadlo, D. J.; Davies, G. J.; Laine, R.; Withers, S. G. Catalysis by Hen Egg-White Lysozyme Proceeds via a Covalent Intermediate. *Nature* **2001**, *412* (6849), 835–838.
(488) Bothner, B.; Chavez, R.; Wei, J.; Strupp, C.; Phung, Q.; Schneemann, A.; Siuzdak, G. Monitoring Enzyme Catalysis with Mass Spectrometry. *J. Biol. Chem.* **2000**, *275* (18), 13455–13459.
(489) Liuni, P.; Olkhov-Mitsel, E.; Orellana, A.; Wilson, D. J. Measuring Kinetic Isotope Effects in Enzyme Reactions Using Time-Resolved Electrospray Mass Spectrometry. *Anal. Chem.* **2013**, *85* (7), 3758–3764.
(490) Lange, O. F.; Lakomek, N.-A.; Farès, C.; Schröder, G. F.; Walter, K. F. A.; Becker, S.; Meiler, J.; Grubmüller, H.; Griesinger, C.; de Groot, B. L. Recognition Dynamics up to Microseconds Revealed from an RDC-Derived Ubiquitin Ensemble in Solution. *Science* **2008**, *320* (5882), 1471–1475.
(491) Whittier, S. K.; Hengge, A. C.; Loria, J. P. Conformational Motions Regulate Phosphoryl Transfer in Related Protein Tyrosine Phosphatases. *Science* **2013**, *341* (6148), 899–903.
(492) Latham, M. P.; Sekhar, A.; Kay, L. E. Understanding the Mechanism of Proteasome 20S Core Particle Gating. *Proc. Natl. Acad. Sci.* **2014**, *111* (15), 5532–5537.
(493) Iversen, L.; Tu, H.-L.; Lin, W.-C.; Christensen, S. M.; Abel, S. M.; Iwig, J.; Wu, H.-J.; Gureasko, J.; Rhodes, C.; Petit, R. S.; et al. Molecular Kinetics. Ras Activation by SOS: Allosteric Regulation by Altered Fluctuation Dynamics. *Science* **2014**, *345* (6192), 50–54.
(494) Kelch, B. A.; Salimi, N. L.; Agard, D. A. Functional Modulation of a Protein Folding Landscape via Side-Chain Distortion. *Proc. Natl. Acad. Sci. U. S. A.* **2012**, *109* (24), 9414–9419.

(495) Henzler-Wildman, K.; Kern, D. Dynamic Personalities of Proteins. *Nature* **2007**, *450* (7172), 964–972.
(496) Huskey, W. P.; Schowen, R. L. Reaction-Coordinate Tunneling in Hydride-Transfer Reactions. *J. Am. Chem. Soc.* **1983**, *105* (17), 5704–5706.
(497) Steinfeld, J. I.; Francisco, J. S.; Hase, W. L. *Chemical Kinetics and Dynamics*; Prentice Hall, 1999.
(498) Hernández, H.; Robinson, C. V. Determining the Stoichiometry and Interactions of Macromolecular Assemblies from Mass Spectrometry. *Nat. Protoc.* **2007**, *2* (3), 715–726.
(499) Kirshenbaum, N.; Michaelevski, I.; Sharon, M. Analyzing Large Protein Complexes by Structural Mass Spectrometry. *J. Vis. Exp. JoVE* **2010**, No. 40.
(500) Zhang, H.; Cui, W.; Wen, J.; Blankenship, R. E.; Gross, M. L. Native Electrospray and Electron-Capture Dissociation in FTICR Mass Spectrometry Provide Top-Down Sequencing of a Protein Component in an Intact Protein Assembly. *J. Am. Soc. Mass Spectrom.* **2010**, *21* (12), 1966–1968.
(501) Rogniaux, H.; Sanglier, S.; Strupat, K.; Azza, S.; Roitel, O.; Ball, V.; Tritsch, D.; Branlant, G.; Van Dorsselaer, A. Mass Spectrometry as a Novel Approach to Probe Cooperativity in Multimeric Enzymatic Systems. *Anal. Biochem.* **2001**, *291* (1), 48–61.
(502) Bennetzen, J. L.; Hall, B. D. The Primary Structure of the Saccharomyces Cerevisiae Gene for Alcohol Dehydrogenase. *J. Biol. Chem.* **1982**, *257* (6), 3018–3025.
(503) Rossman, M. G.; Liljas, A.; Brändén, C.-I.; Banaszak, L. J. Evolutionary and Structural Relationships among Dehydrogenases. In *The Enzymes*; Boyer, P. D., Ed.; Academic Press, 1975; Vol. 11, pp 61–102.
(504) Raj, S. B.; Ramaswamy, S.; Plapp, B. V. Yeast Alcohol Dehydrogenase Structure and Catalysis. *Biochemistry (Mosc.)* **2014**, *53* (36), 5791–5803.
(505) Dickenson, C. J.; Dickinson, F. M. A Study of the pH- and Temperature-Dependence of the Reactions of Yeast Alcohol Dehydrogenase with Ethanol, Acetaldehyde and Butyraldehyde as Substrates. *Biochem. J.* **1975**, *147* (2), 303–311.
(506) Ganzhorn, A. J.; Green, D. W.; Hershey, A. D.; Gould, R. M.; Plapp, B. V. Kinetic Characterization of Yeast Alcohol Dehydrogenases. Amino Acid Residue 294 and Substrate Specificity. *J. Biol. Chem.* **1987**, *262* (8), 3754–3761.
(507) De Weck, Z.; Pande, J.; Kaegi, J. H. R. Interdependence of Coenzyme-Induced Conformational Work and Binding Potential in Yeast Alcohol and Porcine Heart Lactate Dehydrogenases: A Hydrogen-Deuterium Exchange Study. *Biochemistry (Mosc.)* **1987**, *26* (15), 4769–4776.
(508) Klinman, J. P.; Kohen, A. Hydrogen Tunneling Links Protein Dynamics to Enzyme Catalysis. *Annu. Rev. Biochem.* **2013**, *82* (1), 471–496.
(509) Shi, L.; Holliday, A. E.; Shi, H.; Zhu, F.; Ewing, M. A.; Russell, D. H.; Clemmer, D. E. Characterizing Intermediates Along the Transition from Polyproline I to Polyproline II Using Ion Mobility Spectrometry-Mass Spectrometry. *J. Am. Chem. Soc.* **2014**, *136* (36), 12702–12711.
(510) Englander, S. W.; Kallenbach, N. R. Hydrogen Exchange and Structural Dynamics of Proteins and Nucleic Acids. *Q. Rev. Biophys.* **1983**, *16* (04), 521–655.

Appendices

Appendix A: Unambiguous Characterization of Analytical Markers in Complex, Seized Opiate Samples Using an Enhanced Ion Mobility Trace Detector-Mass Spectrometer

A version of this appendix was published as Supporting Information in Analytical Chemistry:

Liuni, P.; Romanov, V.; Binette, M.-J.; Zaknoun, H.; Tam, M.; Pilon, P.; Hendrikse, J.; Wilson, D. J. Unambiguous Characterization of Analytical Markers in Complex, Seized Opiate Samples Using an Enhanced Ion Mobility Trace Detector-Mass Spectrometer. *Anal. Chem.* **2014**, *86* (21), 10772–10779.

Note: Opium samples A, B, C and D are now referred to as Opium 99, 168, 169, and 170 respectively. Original analysis was done using the numbered sample names, which were renamed to A, B, C, and D in the manuscript for simplicity.

Table A1 IMS spectral data from unmodified IONSCAN 400B and IMS mounted on API 2000, with reduced mobility and mass-to-charge values for the standard alkaloids in positive ion mode

Compound	400B Reduced Mobility ($cm^2V^{-1}s^{-1}$)	400B Resolving power	IMS-MS Reduced Mobility ($cm^2V^{-1}s^{-1}$)	IMS-MS Resolving power	Ion (*m/z*)	Ion Formula	Literature
Morphine	1.224	33	1.199	19	286	$[M+H]^+$	1.22[1], 1.214[2]
Morphine	1.262	32	1.256	33	268	$[M-H_2O]^+$	1.26[1], 1.254[2]
Codeine	1.186	29	1.153	19	300	$[M+H]^+$	1.18[1]
Codeine	1.209	27	1.200	36	282	$[M-H_2O]^+$	1.21[1]
Thebaine	1.142	33	1.146	24	312	$[M+H]^+$	1.14[1], Raith, e.t al [3]
Papaverine	1.044	34	1.042	24	340	$[M+H]^+$	Fabre et.al. [4]
Noscapine	0.985	39	0.984	21	414	$[M+H]^+$	Zhu, et.al [5]
Noscapine	1.443	37	1.437	27	220	$[M-194]^+$	Wickens, et.al.[6]

Table A2 Identification and verification of mobility peaks for opium in positive ion mode

K_0 Compound ID	*m/z* Mass	MS/MS	EIS-FTMS	Elemental Composition	Error (ppm)	ESI-FTMS/MS	Literature
0.985 Noscapine	414	179 (7), 206 (3), 220 (100), 353 (9), 365 (3), 414 (13)	414.15370	$C_{22}H_{23}NO_7$	-2.5	179.07100 (1), 205.07400 (1), 220.09736 (100), 248.09236 (1), 353.10247 (4), 365.10241 (3), 396.14465 (3), 414.15527 (19),	Ziegler et. al[7]
1.040 Papaverine	340	171 (16), 202 (100), 324 (38), 340 (93)	340.15481	$C_{20}H_{21}NO_4$	-2.8	171.06796 (6), 176.07069 (1), 187.06284 (1), 202.08625 (100), 296.12808 (4), 308.12810 (1), 310.10738 (2), 322.10735 (6), 324.12292 (24), 325.13072 (25), 340.15413 (47),	Ziegler et. al[7]
1.142 Thebaine	312	58 (33), 195 (10), 209 (17), 221 (100), 237 (55), 251 (17), 266 (20), 281 (27), 312 (29)	312.15993	$C_{19}H_{21}NO_3$	-2.3	221.09618 (2), 223.07545 (4), 237.09110 (2), 249.09105 (56), 253.08600 (1), 255.10164 (19), 266.09380 (38), 269.11730 (7), 280.13331 (16), 281.11731 (100), 283.13286 (1), 297.13598 (10), 312.15947 (15),	Ziegler et. al[7]
1.443 Noscapine [M-196]	220	See Figure	220.09726	$C_{12}H_{14}NO_3$	N/A	162.09129 (1), 179.07019 (1), 190.08616 (1), 192.05687 (1), 205.07313 (100), 220.09662 (5),	Ziegler et. al[7]

Table A3 400B Reduced mobility and mass to charge values for the standard acids in negative ion mode

Compound	400B Reduced Mobility ($cm^2V^{-1}s^{-1}$)	400B Resolution (FWHM)	Ion (*m/z*)
Pyroglutamic Acid	1.6002	42	128
Comenic Acid	1.6109	44	155
Meconic Acid	1.5235	44	199
Pyroglutamic acid dimer	1.2179	48	257
Comenic Acid•Pyroglutamic Acid	1.1870	56	284
Comenic Acid Dimer	1.1472	48	311
Meconic acid Dimer	1.0844	50	398

Table A4 Identification and verification of mobility peaks for opium in negative ion mode

K_0 Compound ID	*m/z* Mass	MS/MS	EIS-FTMS	Elemental Composition	Error (ppm)	ESI-FTMS/MS	Literature
1.18 Comenic Acid Pyroglutamic acid Dimer	284	69(2) 85(4) 111(100) 155(69) 311(1)	Not Present	$[C_6H_4O_5 \bullet C_6H_3O_5^-]$	N/A	N/A	Fairbairn et. al[8]
1.61 Comenic Acid	155	41(11) 69(11) 85(10) 111(100) 155(5)	154.998137	$C_6H_4O_5$	-3.0	N/A	Fairbairn et. al[8]

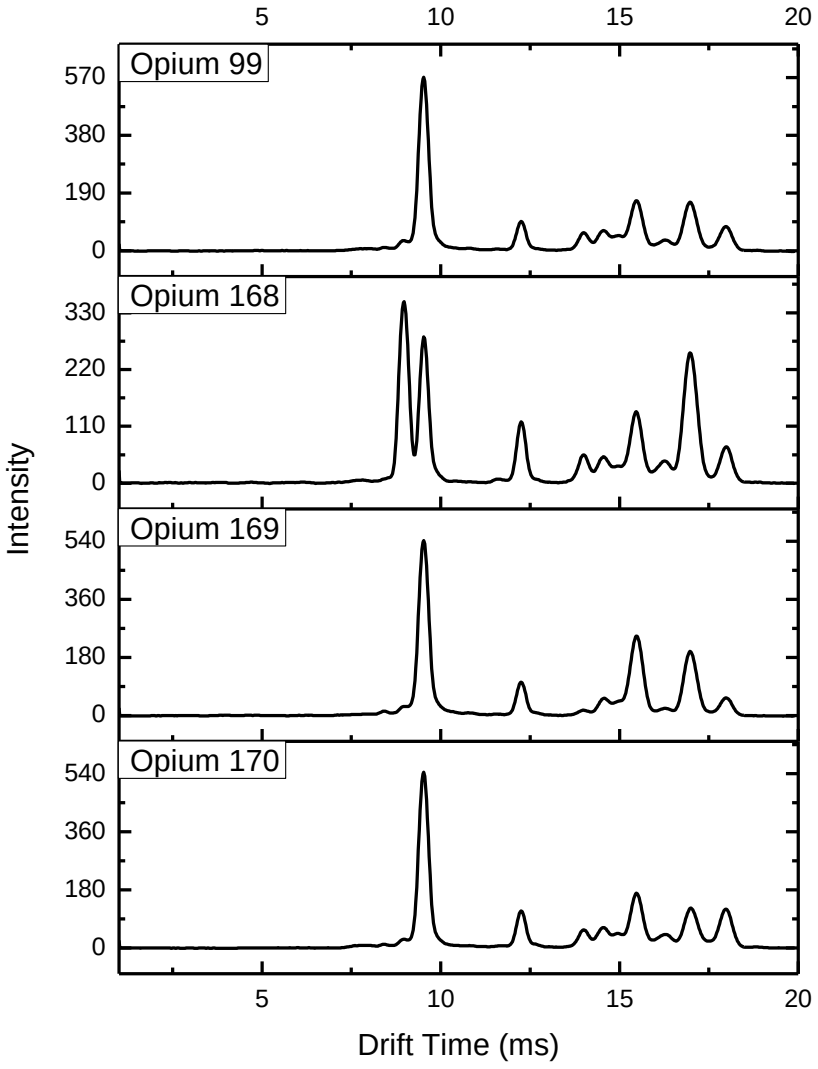

Figure A1 Positive ion mode 400B IMS of Opium samples.

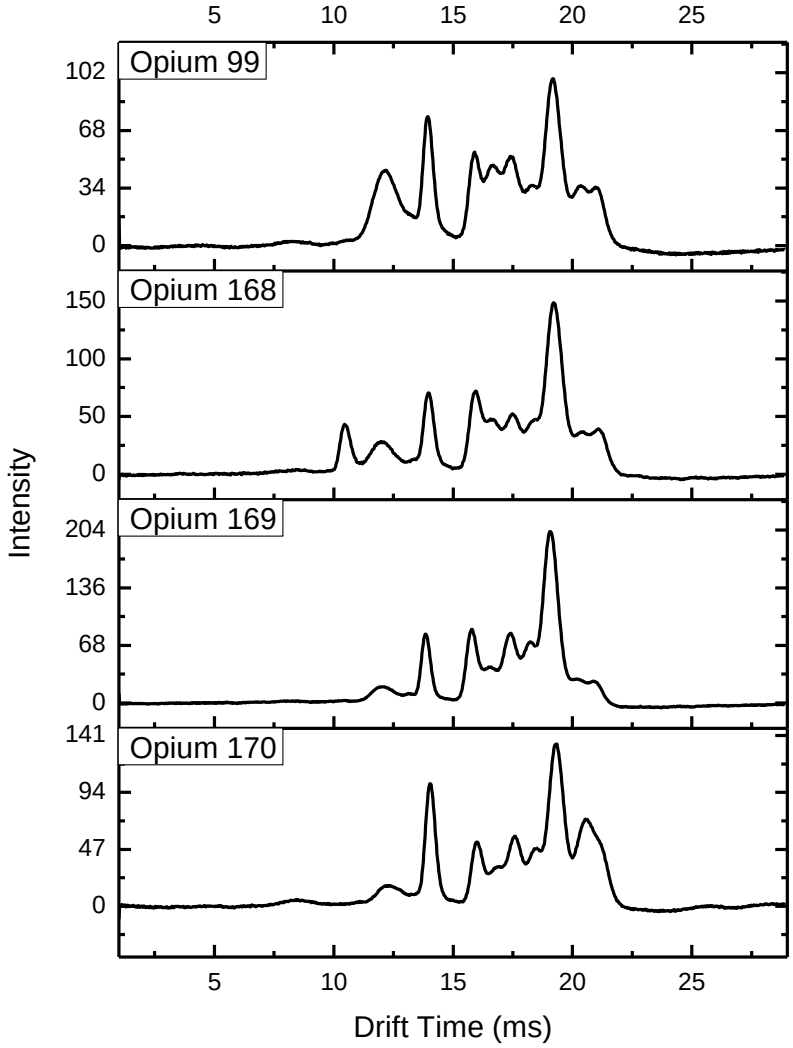

Figure A2 Positive ion mode mobility spectra of Opium samples run on the IMS-MS system.

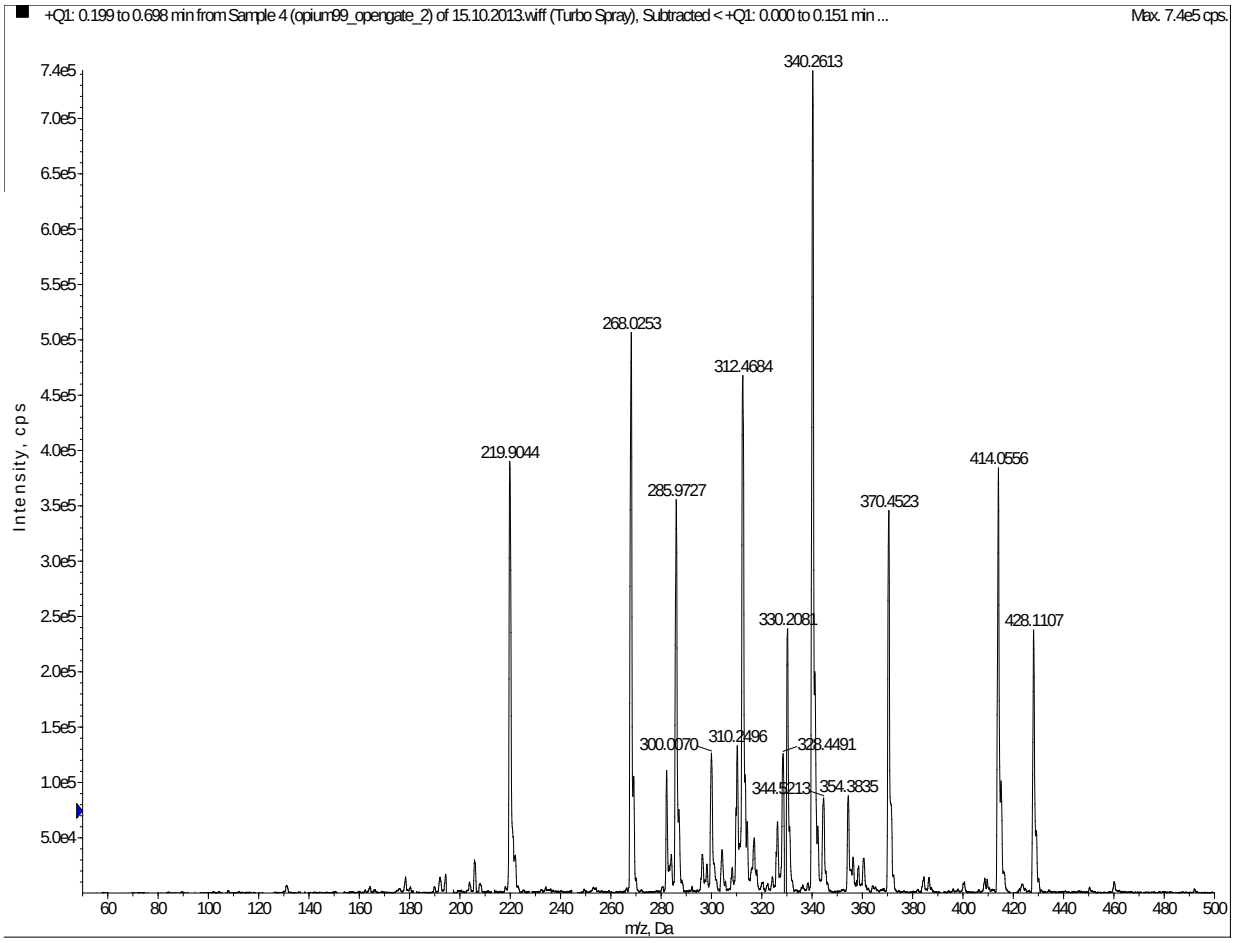

Figure A3 Opium 99 positive ion mode Open-gate mass spectrum.

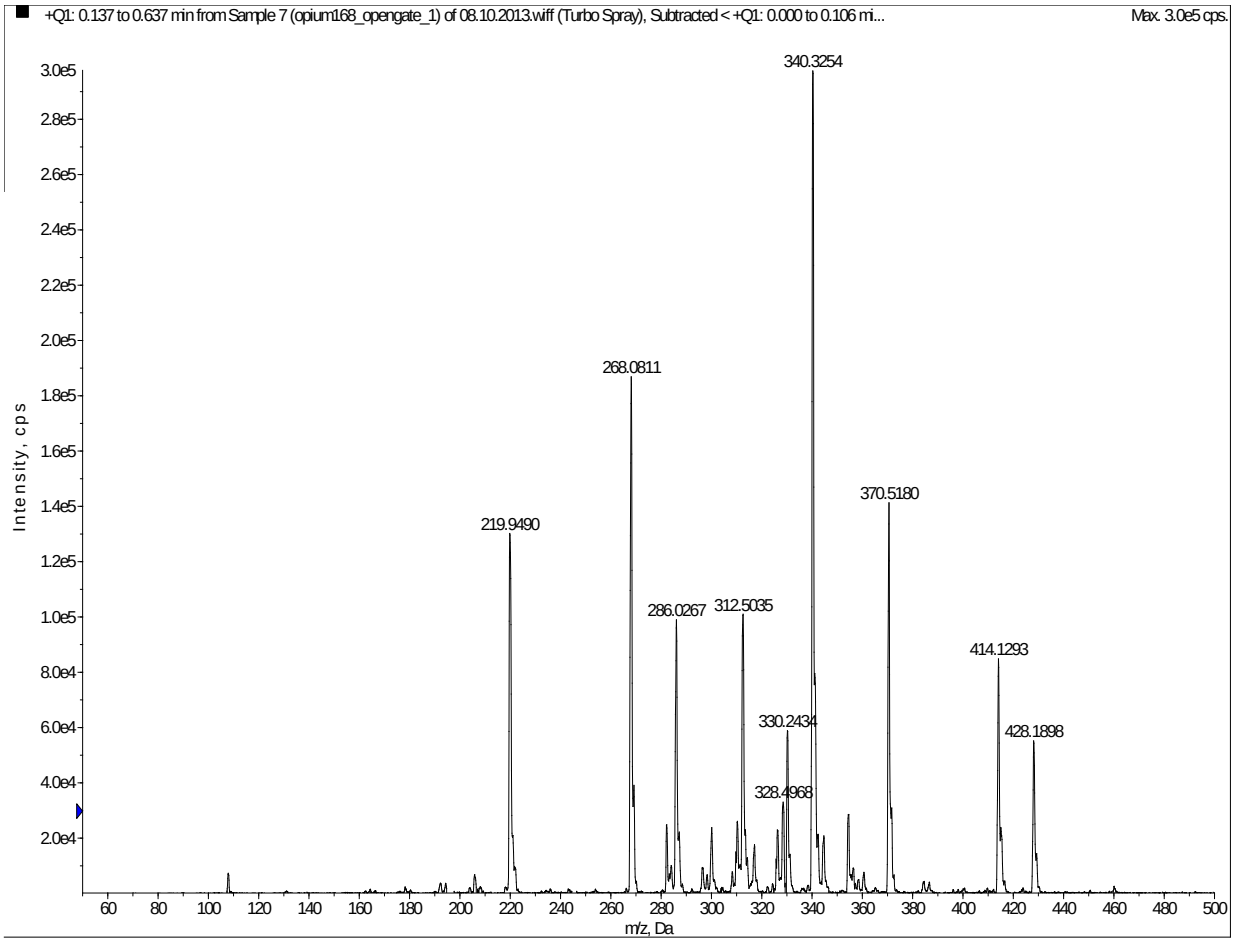

Figure A4 Opium 168 positive ion mode Open-gate mass spectrum.

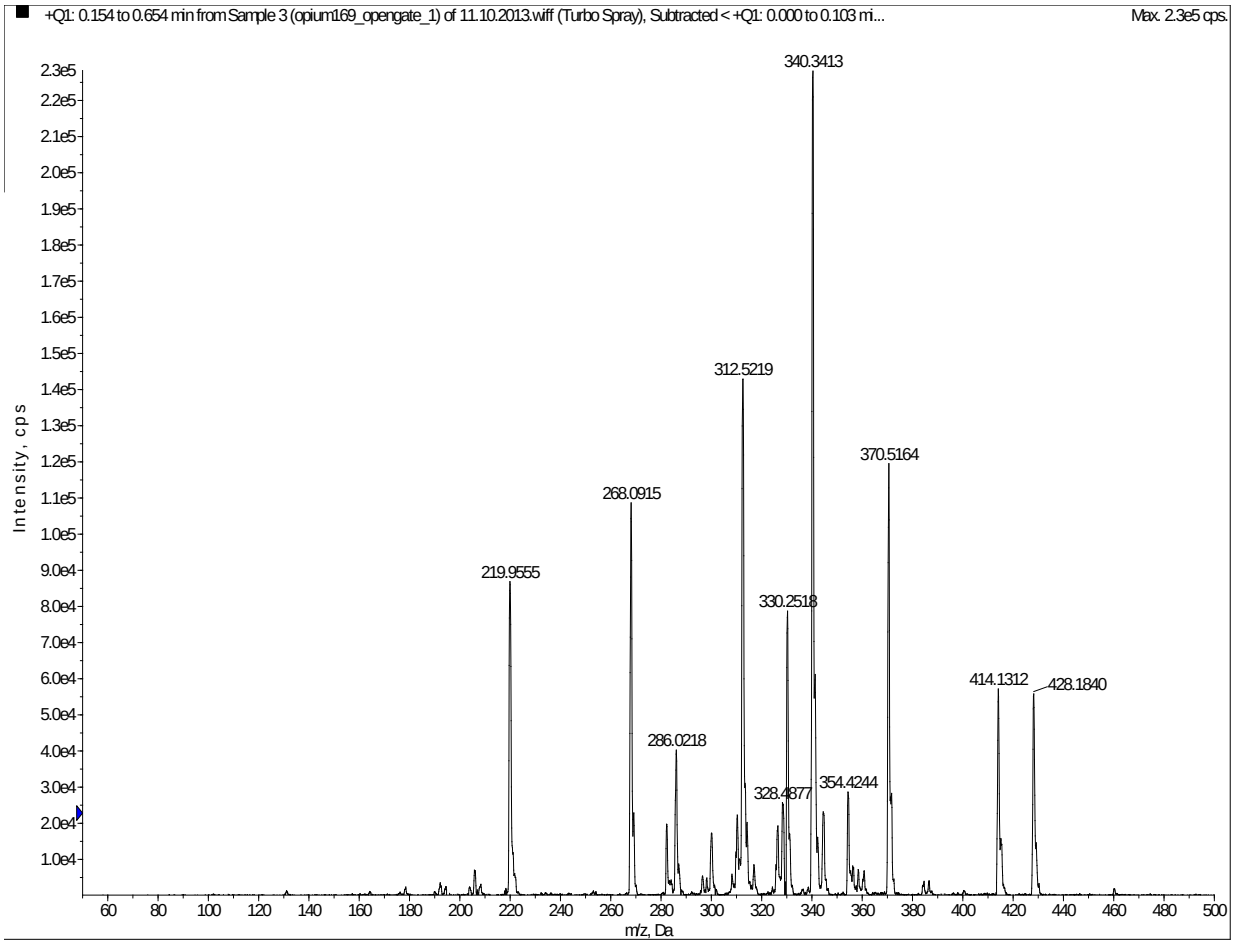

Figure A5 Opium 169 positive ion mode Open-gate mass spectrum.

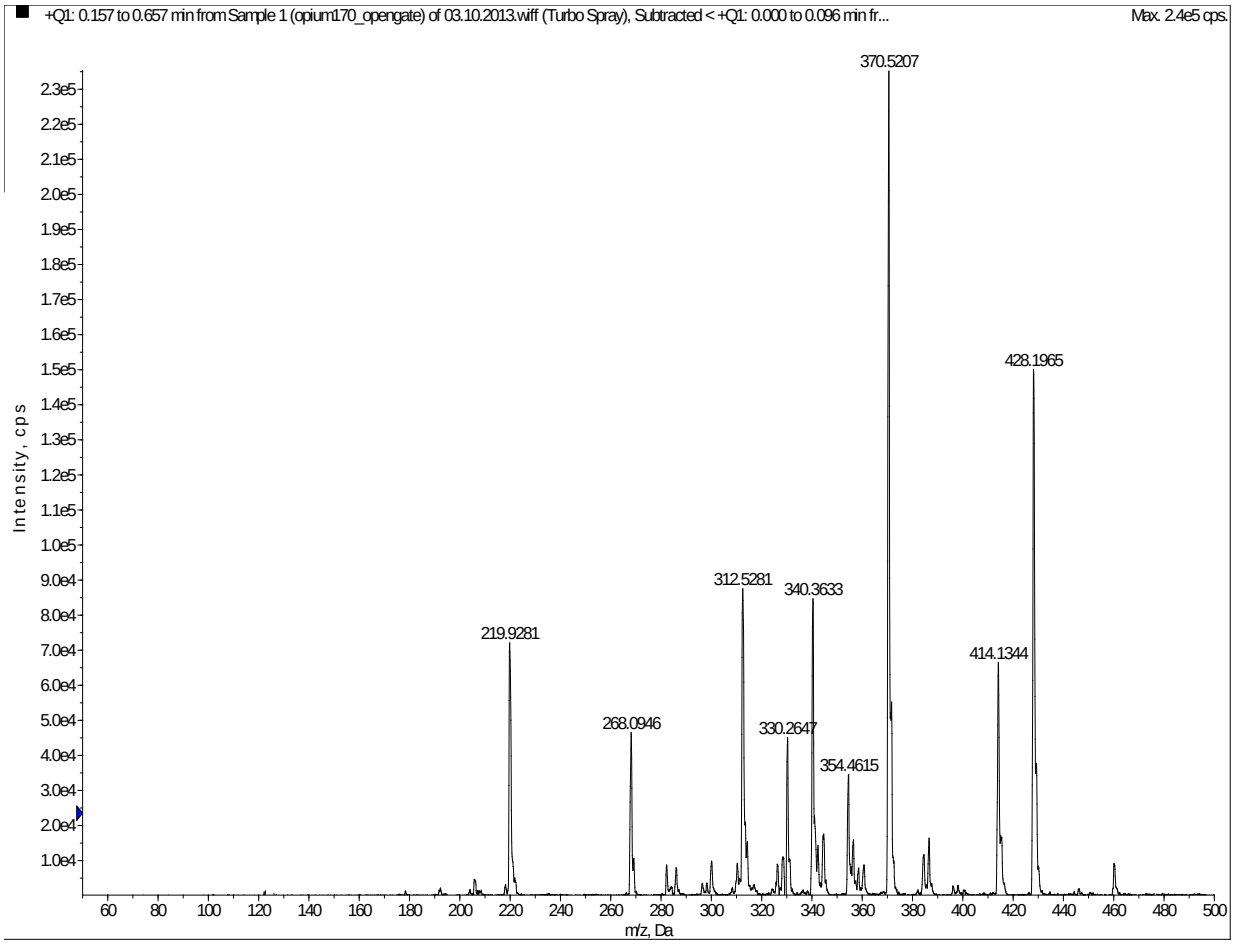

Figure A6 Opium 170 positive ion mode Open-gate mass spectrum.

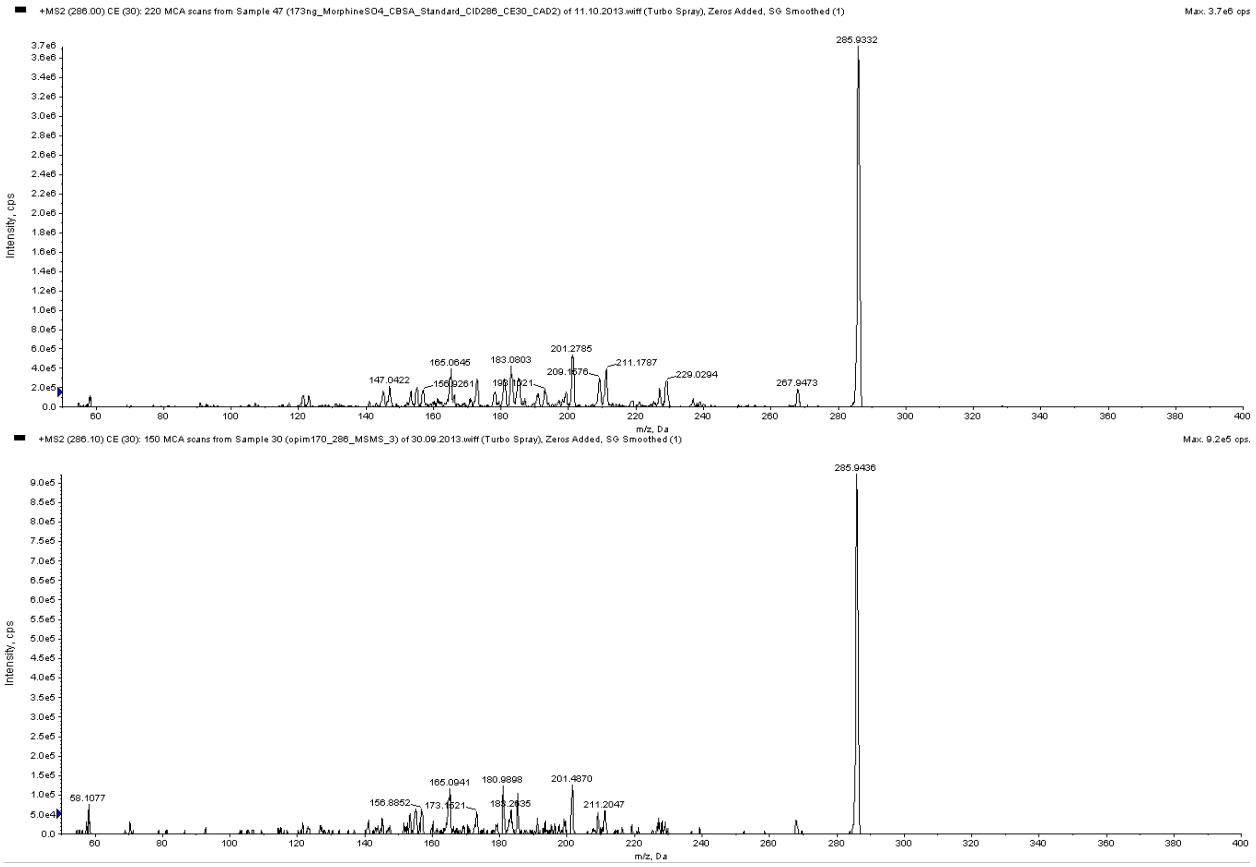

Figure A7 IMS-MS collision-induced dissociation (CE = 30) of morphine from opium and from the morphine standard solution.

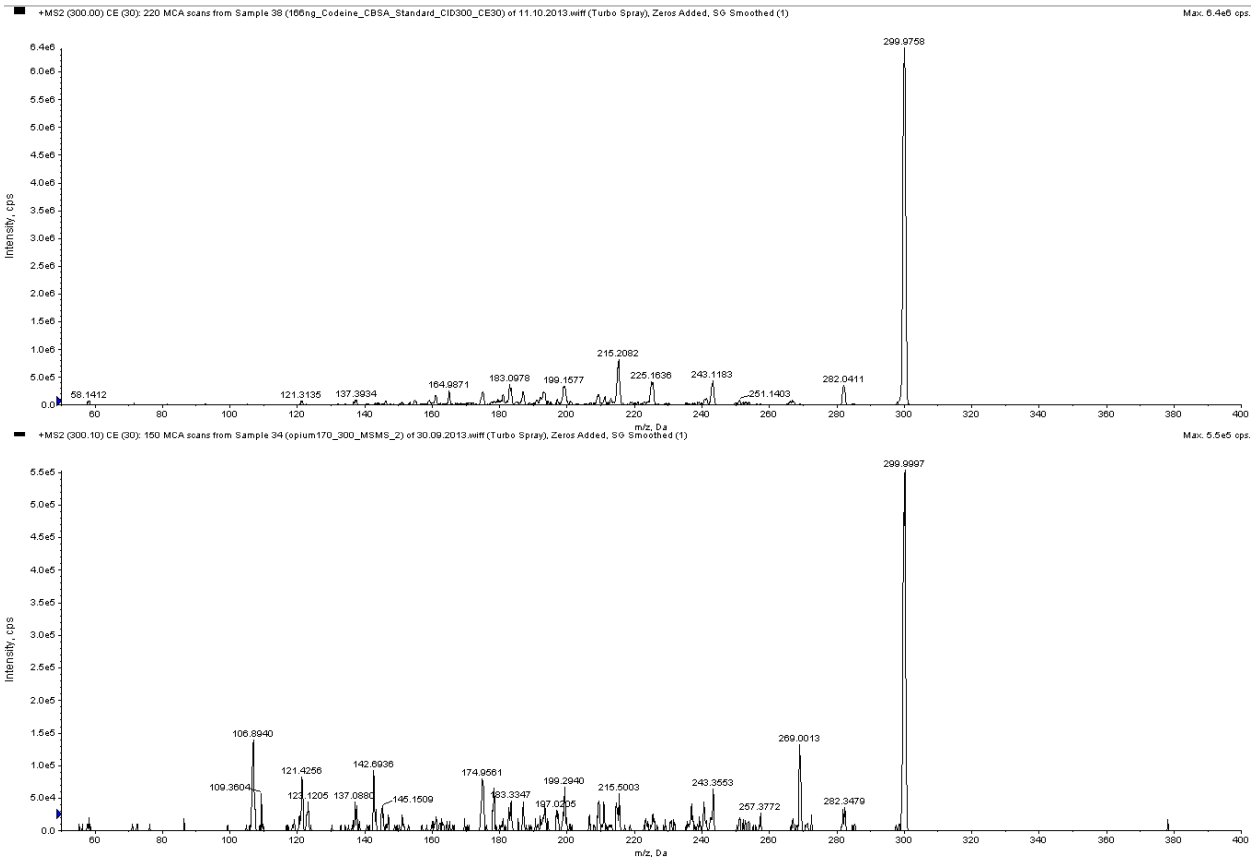

Figure A8 IMS-MS collision-induced dissociation (CE = 30) of codeine from opium and from the codeine standard solution.

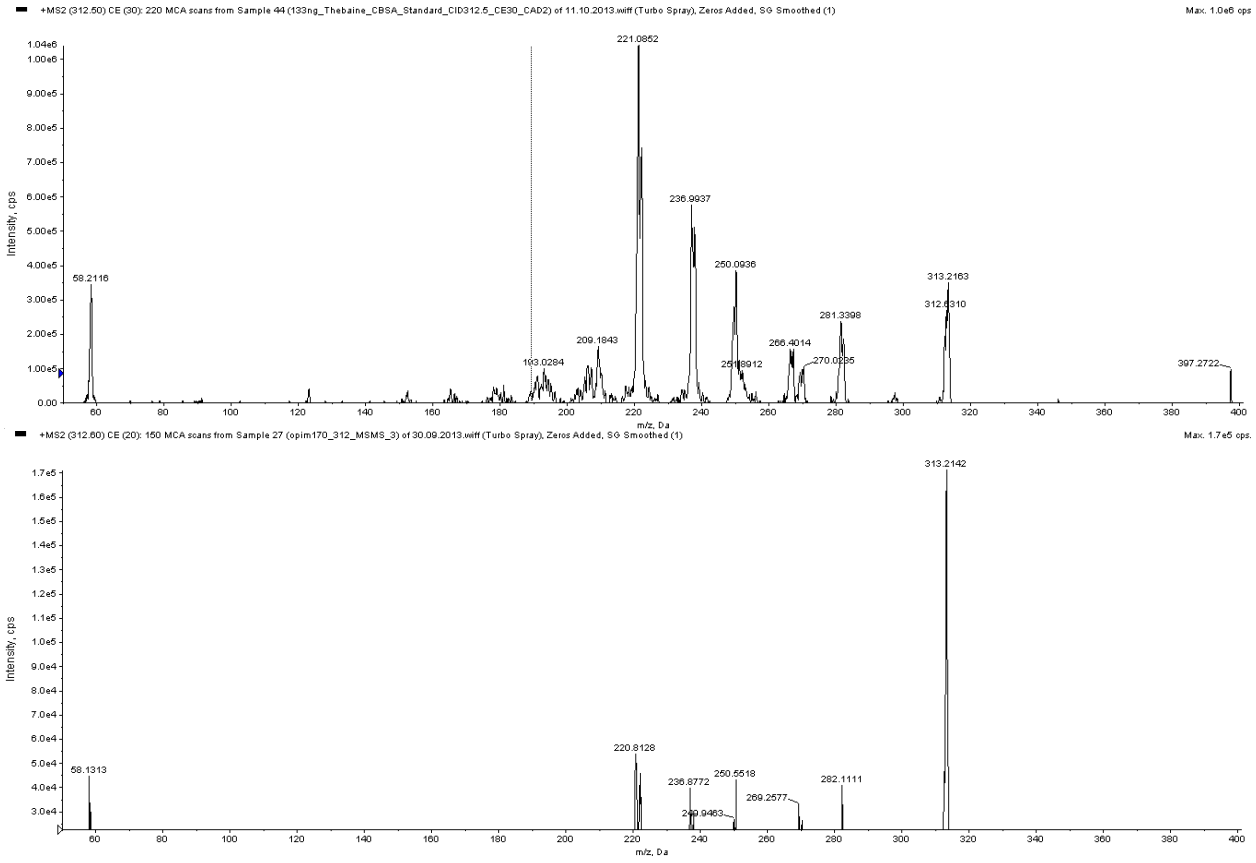

Figure A9 IMS-MS collision-induced dissociation of thebaine from opium (CE =20) and from the thebaine standard solution (CE=30).

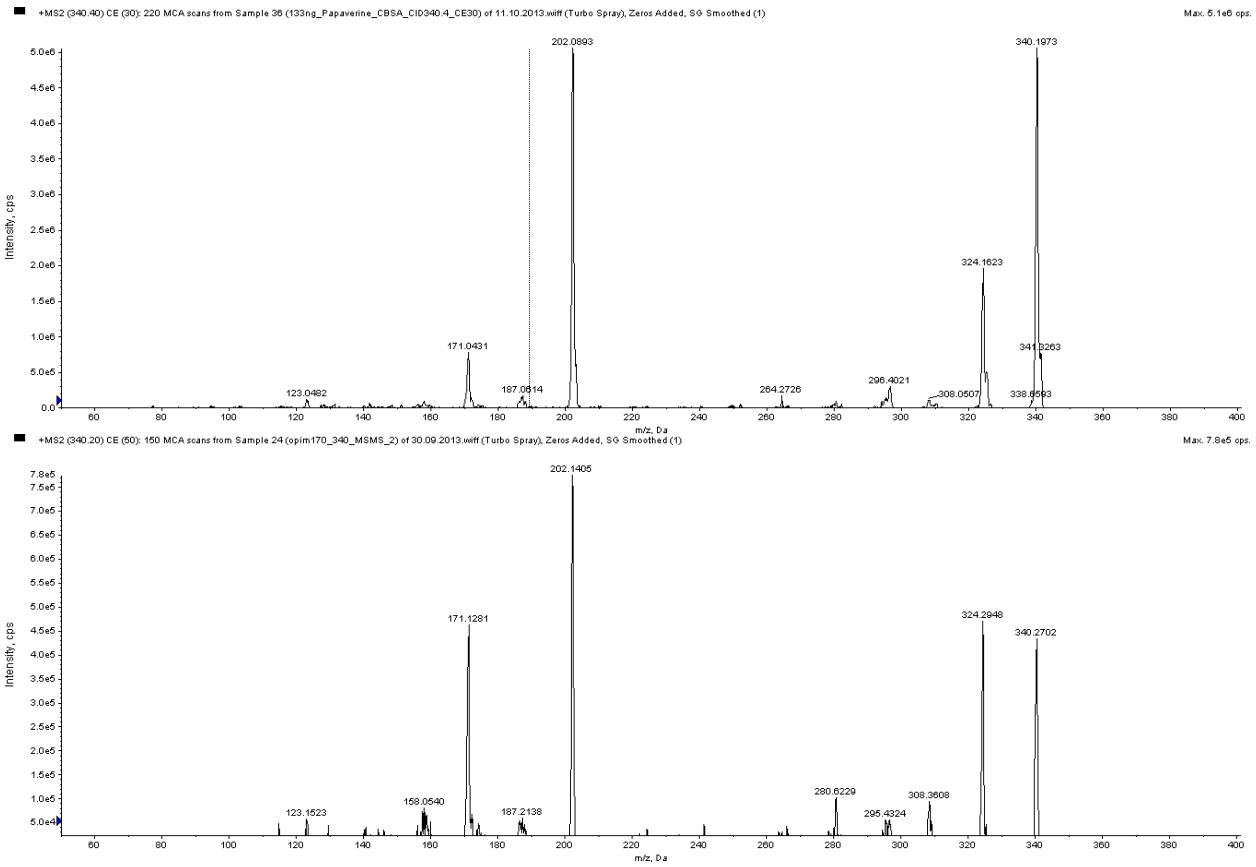

Figure A10 IMS-MS collision-induced dissociation of the papaverine standard solution (CE=50) and papaverine from opium (CE =30).

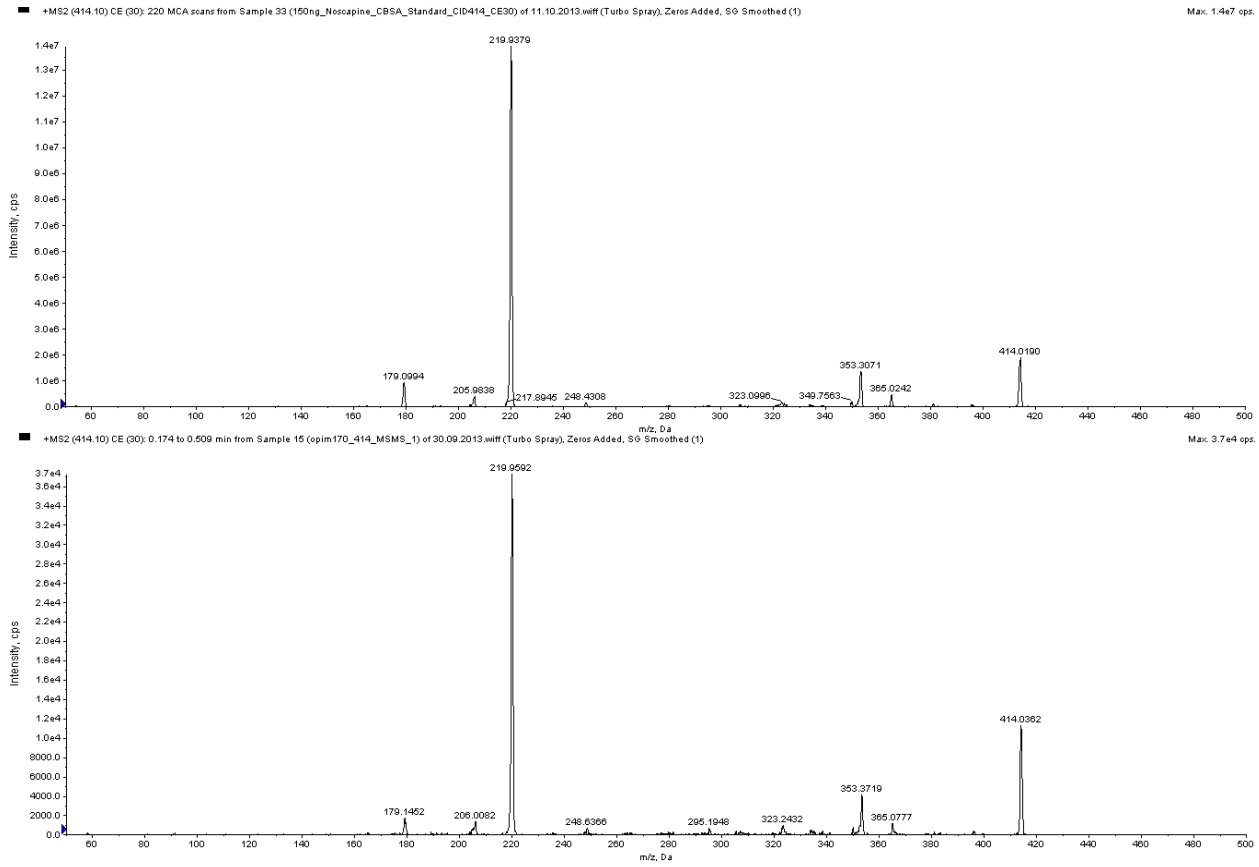

Figure A11 IMS-MS collision-induced dissociation of the noscapine standard solution and noscapine from opium (CE =30).

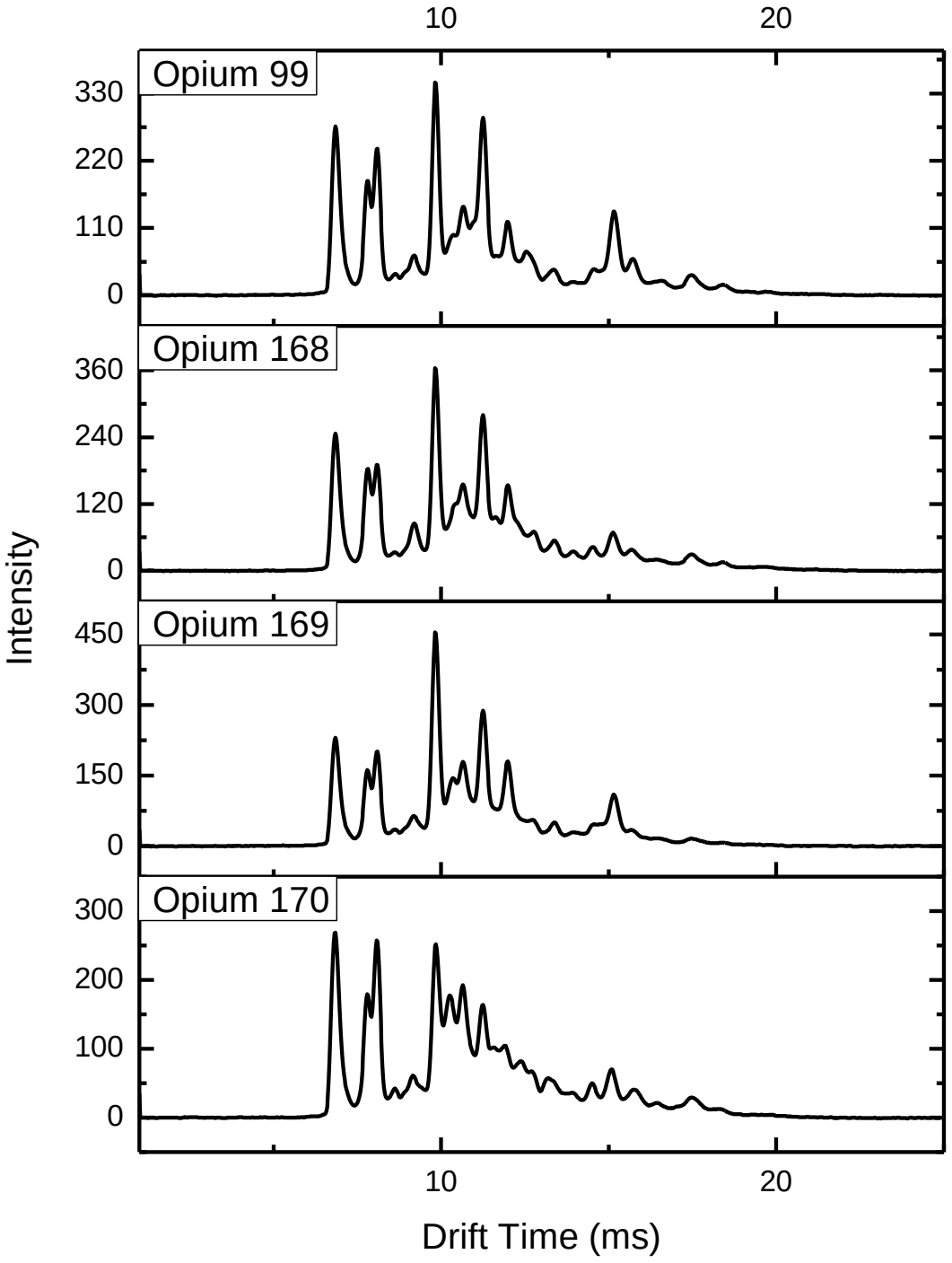

Figure A12 Negative ion mode mobility spectra of Opium on the stand-alone IONSCAN400B

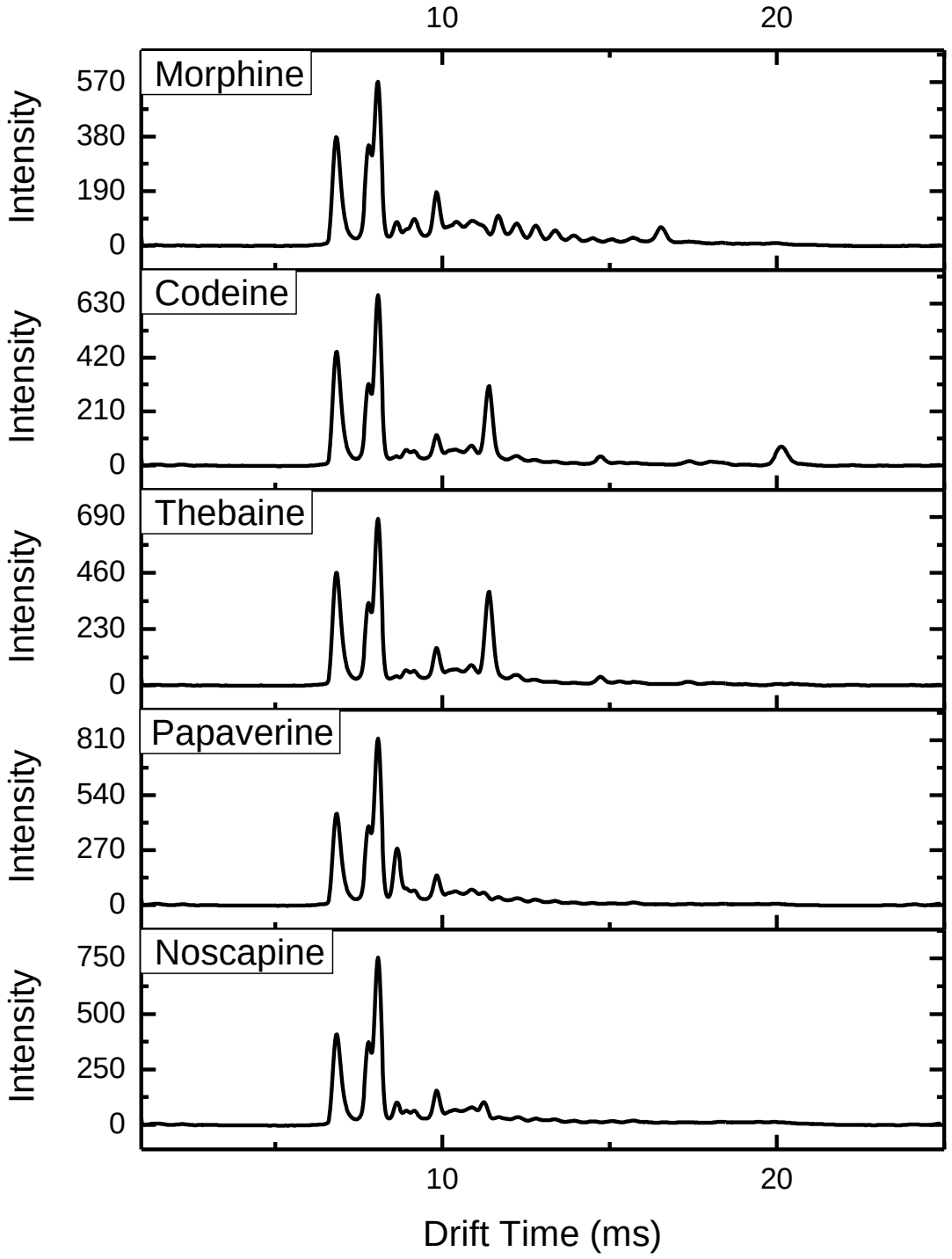

Figure A13 Negative ion mode mobility spectra of the alkaloid standards on the stand-alone IONSCAN400B.

Sample Preparation**.** Standards of morphine, were purchased from Cerilliant (Round Rock, Texas). Standards of codeine, noscapine, papaverine and thebaine were purchased from Toronto Research Chemicals (North York, Ontario, Canada). Standards of meconic acid were purchased from Synchem (Elk Grove Village, Illinois); comenic acid and pyroglutamic acid were purchased from Sigma (St. Louis, Missouri). All samples were prepared by depositing 1µL of diluted solution of opium and alkaloids standards onto a NOMEX swab (Smiths Detection, Mississauga, Ontario, Canada) and allowed to dry for at least 30 seconds prior to analysis. Typical concentrations of the compounds of interest varied from 100 ng/µL to 2000 ng/µL based on the response of the IMS-MS system.

Diluted solutions of seized opium samples were obtained from Canada Border Services Agency. Seized opium samples were dissolved in one part methanol and three parts chloroform. The same solvent system was used for the alkaloid standards as well as for comenic, meconic and pyroglutamic acids standards. Cocaine and trinitrotoluene (TNT) standards (1000 ng/µL in acetonitrile) were obtained from AccuStandard and diluted to desired concentration in 1:1 ethanol: acetonitrile.

Instrumentation**.** In the IONSCAN 400B (Smiths Detection, Mississauga, Ontario, Canada), ions are generated using APCI driven by fast electrons produced from radioactive decay of ^{63}Ni. This ionization mechanism produces positively and negatively charged analytes, with an efficiency that is dependent on the absolute difference in proton affinity between the analyte and the activated reagent gas.[9] Nicotinamide, ammonia, and acetone are favored low-proton-affinity reagents for positive ion-mode studies, while negative ion mode experiments typically employ chloride-containing compounds.[9] In either case, sub-nanogram sensitivities have been demonstrated for a range of compounds including TNT,

PETN, and RDX.[9] Ions are then pulsed into the drift cell and detected using a Faraday plate.[9,10]

For this study, ion mobility spectra of all compounds were recorded on a standard IONSCAN 400B system as described before and used previously.[11,12] Swabs were introduced into the IONSCAN 400B IMS system and heated to 224°C, thermally desorbing the analytes present in the samples sequentially, according to their volatility. Samples were analyzed for a total of 8 s (positive ion mode) and 7.5 s (negative ion mode), and acquired using the standard 400B software.

All IMS/MS experiments were performed on a 400B IMS that was mounted directly in front of the orifice of an AB SCIEX API 2000 Triple quadrupole mass spectrometer. The custom-made mechanical interface between the two systems was similar to the interface described by Kozole.[10] A number of changes, shown in Figure 1, were made relative to the Kozole interface design to enable the use of native software for instrument control and data acquisition on the IMS system while it was connected to the MS system, which was in turn controlled by Analyst version 1.4.

Hardware Modifications**.** The collector of the IMS instrument, the portion of the IMS housing located after the guard grid and the curtain plate of the mass spectrometer were removed from their individual systems. The IMS was modified and the interface was used for coupling to the API 2000. Additional high-voltage cables were added through the side of the modified IMS housing to replace the originals. The guard grid in the IMS housing was fixed to a custom-made stainless steel interface flange, which was attached to the front end of the API 2000. A custom Faraday plate, constructed from gold-plated stainless steel was positioned after the IMS guard grid and was electrically-insulated using a Vespel®

gasket. The center of the Faraday plate had a 6-mm diameter opening to allow the ion beam to pass through towards the mass spectrometer orifice. The mass spectrometer's curtain plate was replaced by the custom-designed interface flange so that the opening in the Faraday plate was positioned concentric with and 4-mm away from the MS orifice. Both the IMS housing and interface flange were electrically grounded while the Faraday plate was contacted through the interface flange with a BNS connector mounted on the outside of modified interface plate. In order to permit optimization of the electric field strength between the skimmer and Q0 rods for ion transmission and fragmentation in the skimmer region, the skimmer was electrically insulated from the chamber of the mass spectrometer using a Teflon® gasket mounted at the back of skimmer.

The IMS instrument was controlled by the native IONSCAN 400B electronics and software. The temperature of the IMS housing was controlled separately using a home-built heater consisting of 20 resistance wires (0.6 V/inch) soldered in parallel, with a total resistance of 3.2 Ohm. Despite the use of this heater, a temperature difference between the IMS and MS subsystems may remain, and this would be a possible area of improvement of the system. Purified and dried air (humidity level less than 20 ppb) was used as drift gas and as sample carrier gas. The countercurrent drift gas flow of the IONSCAN 400B system was introduced through the interface region between the Faraday and orifice plates. The drift flow was optimized experimentally until IMS peak position and peak width of a set of test analytes were similar to those found on a standalone IONSCAN 400B. A flow of 650 cc/min (600 cc/min in positive mode) of dried and purified air was supplied to the original curtain gas inlet of the API 2000, of which 300 cc/min was pulled through the

orifice into the mass spectrometer, while 350 cc/min (300 cc/min in positive mode) flowed into the IMS drift tube to serve as the drift gas in negative mode.

Ion mobility mode (standard operation of IONSCAN 400B)**.** In the ion mobility mode (IMS mode), the first of two ion gates was opened for 200-µs to allow a packet of ions to move into the drift region of the IMS instrument and towards the Faraday plate. The Faraday plate was connected to the normal instrument preamplifier at ground potential to measure current signal. Earlier designs of IMS-MS instruments have made use of Faraday plate ion detection[13-15], however the previous IONSCAN 400B – Triple quadrupole MS system relied on the mass spectrometer in ion transmission mode to record a mobility spectrum.[10] In order to maintain the IMS resolution through the mass spectrometer interface, the skimmer orifice diameter had to be reduced significantly in size, reducing MS sensitivity by an estimated factor of 10.[10] On the other hand, in the Kozole design, using the mass spectrometer as the IMS detector allows the recording of single *m/z* mobility spectrum by isolating ions with that *m/z* in the mass spectrometer.

Continuous Ion Flow. In the continuous ion flow mode, both ion gates in the IMS instrument are open continuously. In negative mode the first ion gate is held at -1800 V and the collector which functions as the second ion gate is held at -100 V. The voltages for the instrument and the collector are 1570 V and 65 V in positive mode respectively, permitting the ions formed in the reaction region of the IMS instrument to pass into the mass spectrometer. This continuous flow of ions is analyzed by the mass spectrometer.

Selected Mobility Monitoring Dual Gate. In the selected mobility monitoring mode, the first ion gate is opened for 200 – 1000 µs to allow a packet of ions into the drift region of the IMS instrument while the second ion gate is opened for one ms after a specific time

delay. The time delay is selected to permit only a selected portion of the ion packet with a particular mobility range to pass into the mass spectrometer. This mobility-filtered ion population is analyzed by the mass spectrometer. The stopping potentials applied to the first and second gates were -1824 V and -120V in negative ion mode and 1590 V and 95V in positive ion mode respectively. The time delay between the opening of the first and second gate is controlled using an arbitrary waveform generator (TEGAM, Inc. Model 2720A, Geneva, OH) and a voltage-to-voltage amplifier (TEGAM, Inc. Model 2340).

In both the continuous and the dual gating modes, all MS methods normally available on a triple quadruple mass spectrometer are available. In the experiments described here, Q1 scan, MS/MS and precursor ion scan methods were used.

Orbitrap Elite. Samples and standards were analyzed on an Orbitrap elite mass spectrometer (Thermo Scientific, Massachusetts) in both positive and negative modes, using the standard commercial heated electrospray ionization (HESI) source. Samples were diluted 100 times from the samples used in the IMS experiments with 1:3 methanol/chloroform, and 0.1% ammonium hydroxide was added to aid ionization in negative mode. Samples were infused at a rate of 3 μL/min and electrosprayed at 3.4-3.8 kV. Spectra were generated using the Orbitrap mass analyzer at 240000 resolution. MS^2 and MS^3 experiments were done using the Orbitrap, while the linear ion trap was used for collision-induced dissociation (CID) experiments that required the mass window to start at 50 *m/z*. Ions were subjected to fragmentation using normalized collision energy, with instrument defined setting between 20% and 40%.[16,17]

Workflow. First, an ion mobility spectrum from the standalone IONSCAN 400B is used to verify the reduced mobility values and the associated alarms for opium. Prior to

analyzing samples on the IMS-MS system, an internal standard calibration is performed to account for any differences between the standalone IONSCAN 400B and the IMS-MS system. Cocaine (positive mode K_0 = 1.160 $cm^2V^{-1}s^{-1}$)[18] and TNT (negative mode K_0 = 1.451 $cm^2V^{-1}s^{-1}$)[19] are used as external calibrants and normalized to their respective K_0 literature values. The calibrated mobility is used to normalize the IMS drift time axis. This calibration procedure was repeated daily, prior to each experiment.

Next, an MS scan is acquired in Open-Gate mode revealing the compounds that are present in the sample. In many cases, useful hypotheses regarding the relationship between *m/z* and K_0 values were made based on how both signals develop as a function of the sample desorption time. Product ion and precursor ion scans were used at times for further characterization. Peaks of interest in the mobility spectrum are selected and corresponding ions are passed on to the mass spectrometer by operating the IMS in dual-gate mode, parking the second gate at a delay time associated with a selected range of drift time and associated K_0 value.

References

(1) Eatherton, R. L.; Morrissey, M. A.; Hill, H. H. *Anal. Chem.* **1988**, *60*, 2240-2243.
(2) Khayamian, T.; Tabrizchi, M.; Jafari, M. T. *Talanta* **2006**, *69*, 795-799.
(3) Raith, K.; Neubert, R.; Poeaknapo, C.; Boettcher, C.; Zenk, M. H.; Schmidt, J. *Journal of the American Society for Mass Spectrometry* **2003**, *14*, 1262-1269.
(4) Fabre, N.; Claparols, C.; Richelme, S.; Angelin, M. L.; Fouraste, I.; Moulis, C. *Journal of chromatography. A* **2000**, *904*, 35-46.
(5) Zhu, L.; Chen, X.; Zhang, Y.; Yu, H.; Zhong, D. *J. Chromatogr. B* **2005**, *820*, 175-182.
(6) Wickens, J. R.; Sleeman, R.; Keely, B. J. *Rapid Commun. Mass Spectom.* **2006**, *20*, 473-480.
(7) Ziegler, J.; Facchini, P. J.; Geissler, R.; Schmidt, J.; Ammer, C.; Kramell, R.; Voigtlander, S.; Gesell, A.; Pienkny, S.; Brandt, W. *Phytochemistry* **2009**, *70*, 1696-1707.
(8) Fairbairn, J. W.; Williamson, E. M. *Phytochemistry* **1978**, *17*, 2087-2089.
(9) Eiceman, G. A.; Karpas, Z.; Hill Jr, H. H. *Ion mobility spectrometry*; CRC press, 2013.
(10) Kozole, J.; Stairs, J. R.; Cho, I.; Harper, J. D.; Lukow, S. R.; Lareau, R. T.; DeBono, R.; Kuja, F. *Anal. Chem.* **2011**, *83*, 8596-8603.
(11) Ritchie, R. K.; Thomson, P. C.; DeBono, R. F.; Danylewich-May, L. L.; Kim, L. In *Proc. SPIE 2092, Substance Detection Systems*, 1994, pp 87-93.
(12) Galella, E.; Jennings, S.; Srikoti, M.; Bonasso, E. *Pharm. Technol.* **2009**, *33*, 60-63.
(13) Hill, C. A.; Thomas, C. L. *The Analyst* **2003**, *128*, 55-60.
(14) Giles, K.; Grimsrud, E. P. *J Phys Chem-Us* **1992**, *96*, 6680-6687.
(15) Eiceman, G.; Nazarov, E.; Miller, R. *IJIMS* **2000**, *3*, 15-27.
(16) Lopez, L. L.; Tiller, P. R.; Senko, M. W.; Schwartz, J. C. *Rapid Commun Mass Sp* **1999**, *13*, 663-668.
(17) Fredenhagen, A.; Derrien, C.; Gassmann, E. *J Nat Prod* **2005**, *68*, 385-391.
(18) Karasek, F. W.; Hill, H. H., Jr.; Kim, S. H. *Journal of chromatography* **1976**, *117*, 327-336.
(19) Kaur-Atwal, G.; O'Connor, G.; Aksenov, A. A.; Bocos-Bintintan, V.; Paul Thomas, C. L.; Creaser, C. S. *Int. J. Ion Mobil. Spec.* **2009**, *12*, 1-14.

Appendix B: Measuring Kinetic Isotope Effects In Enzyme Reactions Using Time-Resolved Electrospray Mass Spectrometry

A version of this appendix was published as Supporting Information in Analytical Chemistry:

Liuni, P.; Olkhov-Mitsel, E.; Orellana, A.; Wilson, D. J. Measuring Kinetic Isotope Effects in Enzyme Reactions Using Time-Resolved Electrospray Mass Spectrometry. *Anal. Chem.* **2013**, *85* (7), 3758–3764.

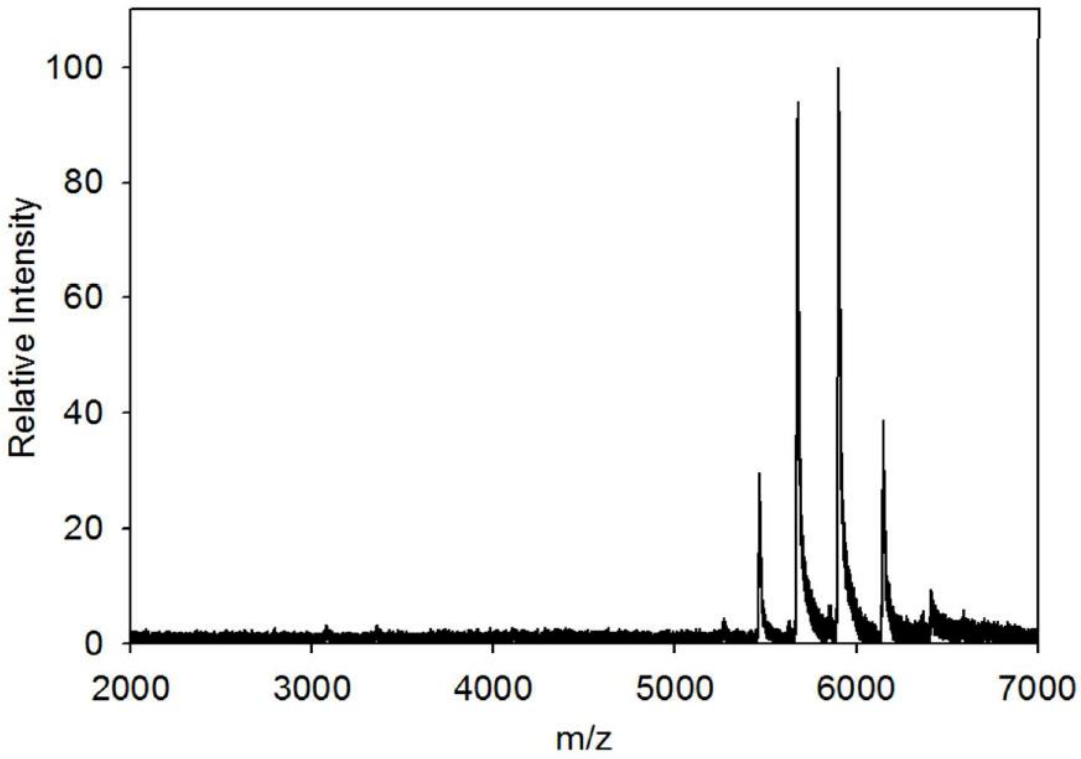

Figure B1. The native ADH mass spectrum, dominated by the tetramer.

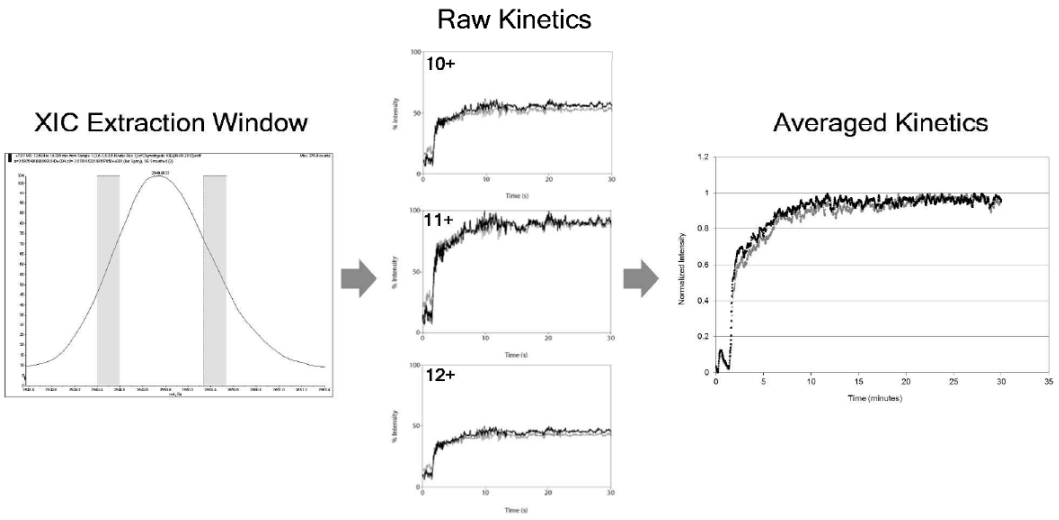

Figure B2. Schematic depiction of the process for extracting low dispersion kinetic profiles from a single run. (Left) Ion currents are extracted from the appropriate regions of all acyl-chymotrypsin *m/z* peaks with sufficient signal-to-noise. (Middle) Raw extracted ion currents from several charge states are normalized and averaged to generate low dispersion kinetic profiles (Right).

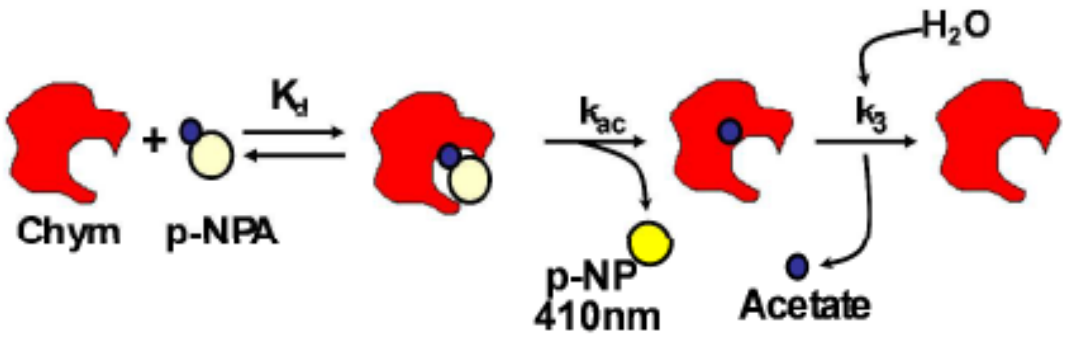

Figure B3. A schematic depiction of the Chymotrypsin mechanism. (Adapted from: D. J. Wilson and L. Konermann, Anal. Chem., 2004, 76, 2537-2543).

Data Analysis Details. By convention, KIEs are defined as the highest natural abundance isotope rate divided by the 'labeled' isotope rate. Thus, in the case of chymotrypsin acylation, the KIE would expressed as $KIE_{ac} = {}^{12}k_{ac}/{}^{13}k_{ac}$ where ${}^{12}k_{ac}$ and ${}^{13}k_{ac}$ correspond to the observed rates for unlabeled and ^{13}C carbonyl carbon-labeled substrate, respectively. In our measurements, the broad natural isotopic distribution of the protein creates substantial overlap between the labeled and unlabeled acyl enzyme. The overlap is minimized by selecting an XIC window that is in the region of greatest absolute difference in peak intensity, as shown in Figure B2, however, even in these regions, the undesired species contributes close to 40% of total intensity. In principle, this will generate a biphasic intensity-time profile from which both rates could be extracted by fitting to a double exponential expression. However, in practice the rates are much too similar to permit such an analysis. Instead, the data are fit to a single exponential and the extracted rate is the weighted average of the two contributing rates. In this case, the observed KIE becomes:

$$KIE_{obs} = [(0.6\times{}^{12}k_{ac})+(0.4\times{}^{13}k_{ac})] / [(0.4\times{}^{12}k_{ac})+(0.6\times{}^{13}k_{ac})]$$

The limit of this expression as $(12kac - 13kac) \rightarrow \infty$ is 0.6/0.4 = 1.5, corresponding to the maximum value for KIE_{obs}, no matter how great the differential between ${}^{12}k_{ac}$ and ${}^{13}k_{ac}$. This implies that for systems where there is a very large rate difference between labeled and unlabeled substrate, KIE_{obs} may be only a very small fraction of the actual KIE. This fraction can be obtained by comparing KIE_{obs} for a particular differential between ${}^{12}k_{ac}$ and ${}^{13}k_{ac}$ to the actual KIE (${}^{12}k_{ac}/{}^{13}k_{ac}$), which can be deconvoluted from the observed rates based on the known contributions of each species. In our case, where the differential is small, and KIE_{obs} is between 18% and 20% of the actual KIE.